Ultrafast Excited State Reaction Dynamics in Light-Driven Unidirectional Rotary Molecular Motors and Fluorescent Protein Chromophores

Jamie Conyard

School of Chemistry

University of East Anglia

Norwich

UK

2013

A thesis submitted in partial fulfilment of the requirements for the degree of Doctor of Philosophy at the University of East Anglia.

Declaration

I declare that the work contained in this thesis submitted by me for the degree of Doctor of Philosophy is my work, except where due reference is made to other authors, and has not previously been submitted by me for a degree at this or any other university.

Jamie Conyard

Acknowledgements

Firstly I would like to thank my supervisor, Prof. Steve Meech for his constant guidance and support over the duration of my time at UEA (as both a postgraduate and undergraduate). Without Steve's influence, I do not believe I would have had the confidence to even undertake a PhD. I am also indebted to Dr. Ismael Heisler for teaching me the background of ultrafast spectroscopy from the very basics, for his constant help with the experimental set-ups and data analysis, and for his general support with all aspects of my PhD studies. A huge thanks is also owed to Dr. Andras Lukacs for teaching me the transient absorption set-up and his continued support with the system long after he left UEA.

I also extend my thanks to all members of the Meech research group past and present: Kiri, Francesca, Kamila, Ismael, Andras, Leo, Minako and Mike for their friendship and support over the past 4 years.

I thank our collaborators on the molecular motor project: Prof. Ben Feringa and his research group, with special thanks to Arjen Cnossen for the synthesis of the samples and Dr. Wesley Browne for his advice and support on all aspects of the project. I also thank our collaborators on the GFP project: Dr. Kyril Solntsev and his research group, with special thanks to Anthony Baldridge for the synthesis of the HBDI samples.

Finally, I am infinitely grateful to my family and friends for their encouragement and support in everything that I do. In particular, my parents and sister – I would not have made it through the last few months of my studies without them.

Abstract

Excited state dynamics on an ultrafast timescale can provide insight into primary events in photochemical and photobiological processes. In this work, excited state dynamics of two important systems are characterized: unidirectional molecular rotary motors and HBDI derivatives (synthetic chromophores of the green fluorescent protein (GFP)). In both cases, the excited state is selectively probed by ultrafast fluorescence up-conversion with a time resolution better than 50 fs.

Molecular motors have biphasic (sub-picosecond and picosecond) fluorescence decays and oscillations attributed to excitation of coherently excited vibrational modes. The fluorescence data were contrasted with excited state decay and ground state recovery kinetics recorded using ultrafast transient absorption. Combining these experimental data with substituent dependence and solvent dependence studies, as well as existing calculations, we proposed a coupled two-state model for dynamics on the excited state potential energy surface. These data have implications for the design and optimisation of optically driven molecular motors. A ‘molecular propeller’ was also studied and shown to be more sensitive to medium friction than the motor.

The GFP experiments focused on determining the effect of alkyl substitution upon excited state dynamics of HBDI. HBDI in solution exhibits a very low quantum yield compared to the chromophore in its protein environment. Large alkyl substituents were found to shift the spectra but to exhibit only small retardation effects upon the excited state decay time, even in highly viscous solvents. This supports an assignment of a volume conserving isomerization mechanism promoting radiationless decay. Substituents which distort the planar structure of the chromophore lead to an enhanced radiationless decay. This provides further evidence for a link between radiationless decay of the excited state and twisting of HBDI.

Contents

1 Introduction

In this thesis we describe the excited state dynamics of two molecular systems: a synthetic molecular motor and the chromophore of a photoactive protein. Photoisomerization underpins the excited state dynamics of both of these systems. It is the aim of this work to gain a better understanding of the molecular dynamics on the excited state potential energy surface which facilitate isomerization in each system. To do so, ultrafast time resolved spectroscopy is employed.

1.1 Molecular Motors and Machines

Significant breakthroughs in molecular biology over the past two decades have revealed that biological motors drive numerous modes of movement throughout nature. For example, muscle contraction,[1,2] intracellular transport[3] and the movement of some bacteria (Flagella motor)[4,5] are just a small number of the processes in which biological motors are key. These motors typically convert chemical energy into mechanical energy thus fuelling movement at the molecular level. One of the most important motors is ATP synthase.[6,7] This protein acts as a biological molecular rotary motor and is intimately involved in the synthesis and hydrolysis of ATP, which is the primary method for storing and releasing chemical energy throughout nature.[8] A schematic representation of the motor function of ATP synthase is shown in Figure 1.1 (reproduced from Reference 9). Such discoveries have prompted extensive attempts to design synthetic systems capable of replicating the controllable molecular motion which is so elegantly employed by nature. Clearly, this is very challenging not least because it requires an input of energy into the system which selectively drives only specific motions out of the numerous possible degrees of freedom.[10] Despite these significant difficulties, remarkable progress has been made in this field over the past decade.

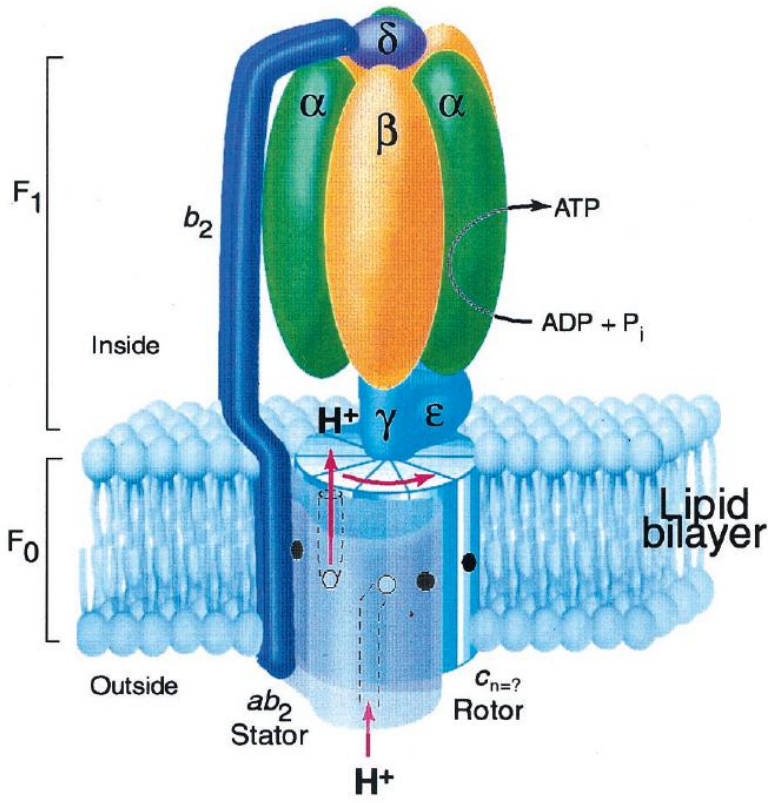

Figure 1.1 - *A schematic representation of the functioning of ATP synthase. The rotational motion facilitates conformational changes which allow sequential substrate binding, ATP formation and ATP release. This figure is reproduced from Reference 9.*

Numerous synthetic systems have been designed in which controllable molecular motion is achieved and functioning molecular switches, shuttles and motors have been developed.[11]

Molecular switches use input energy to undergo a selectively reversible structural change between two forms.[12] Light has proven to be the most commonly used source of energy for molecular switches. Photochromism (the light driven reversible change of a chemical species between two forms with different absorption spectra[13]) is the key principle behind the functionality of such switches. Photoisomerization is one of the key processes which facilitates photochromism in such molecular devices.[14] If each form of the switch exhibits a well resolved absorption spectrum, the irradiation wavelength can be tuned in order to selectively induce a photoisomerization reaction of one form to the other. Ideally, the reaction

occurs with a high photochemical quantum yield and is reversible so that the switch can be 'reset'. Light activated molecular switches have a number of potential applications including sensors and data storage. Numerous examples of molecular switches driven by light have been described.[12,14-16] Particular success has been found with switches based on the photoisomerization of azobenzene.[12,17,18] In this system it has been demonstrated that energy input can be harnessed to fuel controllable (and reversible) mechanical motion on a molecular scale.[12]

Molecular shuttles are supramolecular structures which use input energy to transfer 'cargo' (molecules, ions or electrons) from one location of the structure to another.[19] Although a variety of energy sources have been demonstrated including redox potential[20] and pH,[21] the most widely used is light.[11] Thus far, the most successful molecular shuttle design is based upon rotaxanes.[22-24] Rotoxanes are supramolecular structures which consist of a central macrocycle mechanically locked between two end groups (termed 'stations') along a linear thread (termed a 'track'). Figure 1.2[24] shows a schematic representation of a rotaxane molecular shuttle where naphthalimide (ni, grey), and succinamide (succ, green) are two 'stations' separated by an alkyl chain 'track'. In the ground state, naphthalimide has a poor hydrogen bond affinity for the central macrocycle. As a result the macrocycle ring is predominantly (>99 %) bound to the succinamide station. However, light is used to induce a significant increase in the hydrogen bond affinity of the macrocycle to the naphthalimide station. Excitation of the naphthalimide station results in intersystem crossing to form a triplet state. The triplet state is then reduced by an external electron donor group (1,4-Diazabicyclo[2.2.2]octane in this case) to form a radical anion state of the naphthalimide station. The hydrogen bond affinity of the macrocycle for the radical-anion naphthalimide station then surpasses that of the succinamide station.

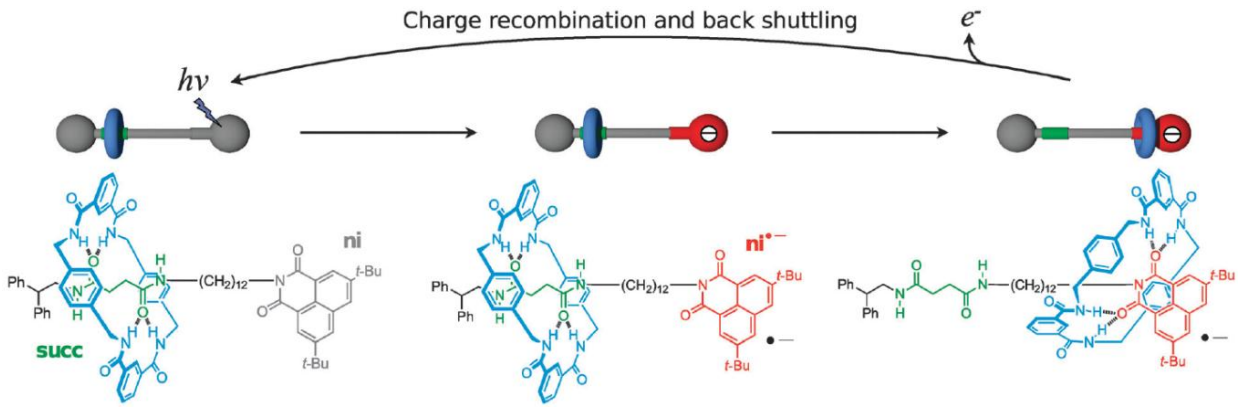

Figure 1.2 - *Schematic representation of the shuttling function of a rotaxane molecular shuttle. Excitation of the naphthalimide station (ni) leads to intersystem crossing to a triplet state. Reduction by an external electron donor (1,4-Diazabicyclo[2.2.2]octane) generates a radical anion state of the ni station. The macrocycle affinity is higher for the ni radical anionic compared to the succinimide station (si), resulting in shuttling from the si to the ni station. Charge recombination between the radical anion of ni and the radical cation of the electron donor results in the reversal of this process, with the macrocycle returning to the si station. This figure is reproduced from Reference 24.*

As a result, the macrocycle is shuttled along the 'track' from the succinamide 'station' to the naphthalimide 'station' on a 1μs timescale. Charge recombination between the radial anion of the naphthalimide station and the radical cation of the donor reverses this process with the macrocycle returning to the succinamide 'station' on a 100 μs timescale. This is yet another key example of utilising light as an energy source for controllable motion on a molecular scale.

The concept of driving molecular motion in a selective and controllable manner has been extended to the design of molecular motors. In order to mimic the motor action of biological motors such as ATP synthase, synthetic structures must harness input energy to fuel repetitive 360^{o} rotation of controllable directionality.[25] The design of such systems is clearly more

complex than that of molecular switches and shuttles, since the 'forward' reaction must always be favoured over the 'reverse' reaction. However, despite the significant challenges which exist to achieving this on a molecular scale, a number of successful cases have been reported.[25] The most promising designs of synthetic unidirectional molecular motors employ light as the source of energy.[11,25-27] Over the past decade the Feringa group have reported dramatic progress in this field,[28-30] such that molecular systems which undergo photochemically driven repetitive unidirectional rotary motion with MHz rotational speeds are now available.[31,32] These systems are based upon a sterically overcrowded alkene design, and exploit stereochemistry to achieve sequential excited state isomerization and ground state helix inversion steps to achieve unidirectional rotation (Figure 1.3).[30] A detailed description of the mechanism of motor action for this class of molecular motor is given in Chapter 3.

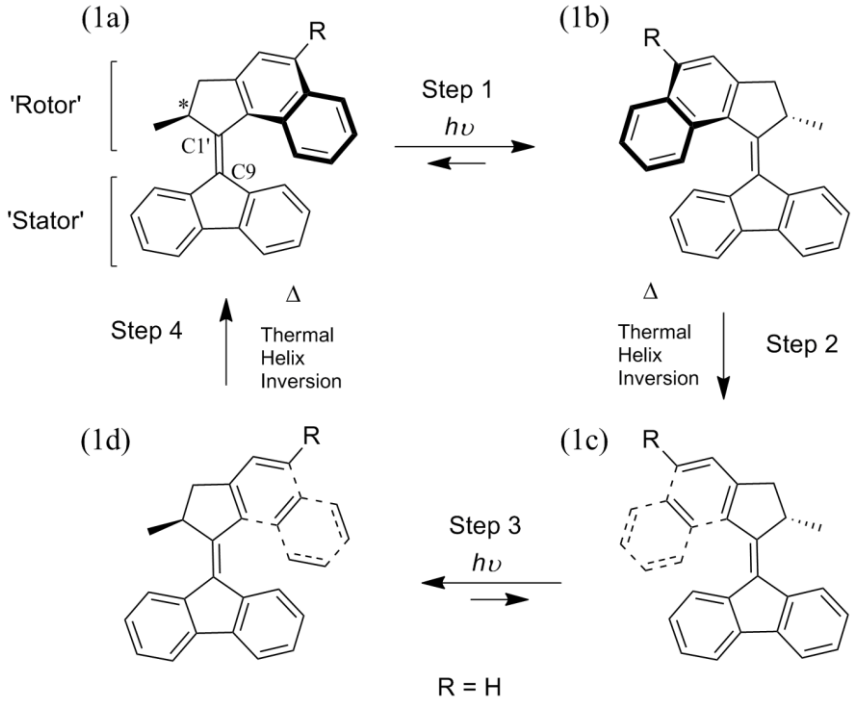

Figure 1.3 - *One full 360^o rotation of a Feringa molecular motor. A photochemical isomerization (Step 1) leads to a ground state structure which relaxes via a thermal helix inversion (Step 2). Each step is repeated (Step 3 and Step 4) to achieve a full revolution. Repetitive unidirectional rotation is achieved under constant irradiation.*

A common theme to all of the molecular switch, shuttle and motor devices described here is that light is the common choice of energy source and photochemical isomerization is exploited as the origin of the motion in the majority of cases. Photochemical isomerization is a fundamentally important excited state process and is discussed in detail in Section 1.3.1.

The principle goal of these molecular devices remains their successful incorporation in larger scale molecular machines which are capable of performing useful functions. However, to achieve this, significant optimisation of the molecular motor action is required. Significant research effort has been invested in order to understand and optimize the thermal processes on the ground state potential energy surface of the molecular motors through structural modifications.[33] In contrast, the mechanism of photoisomerization (the excited state step) is comparatively poorly understood. Therefore, it is the aim of this thesis to characterize the dynamics on the excited state potential energy surface of a unidirectional molecular rotary motor. In this way, a clearer insight into the molecular dynamics of the photochemical isomerization step which acts as the energy source for the unidirectional rotary motor motion will be gained. This work is described in Chapters 3 - 5.

1.2 The Green Fluorescent Protein

The green fluorescent protein (GFP) was first isolated from the jellyfish Aequorea Victoria by Shimomura and co-workers in 1962.[34] However, it was over 30 years after this initial discovery that Chalfie and co-workers first demonstrated the ability to clone and express GFP with specific proteins in living cells.[35] Fluorescence microscopy could then be used to detect the fluorescent protein, and hence the protein to which it was bound. Thus, the selective imaging of proteins in the cells of living organisms could be achieved. This discovery had a revolutionary effect upon the field of bioimaging and has fuelled the rapid development of technology in this area over the past 20 years. An important advance was made by Tsein and

co-workers who first demonstrated the ability to clone and express mutants of GFP.[36] This opened an entire new avenue of research in this field, greatly expanding the range of applications of GFP and leading to the recent production of a second generation of fluorescent proteins.[37-39] The fluorescent protein family exhibits emission profiles which span the entire visible region of the electromagnetic spectrum. In addition, many have more complicated photophysics than GFP itself, despite being derived from similar chromophores and having the same basic protein structure. For example, Dronpa is a FP with switchable fluorescent and non-fluorescent states,[40] whilst Kaede is a FP which undergoes a permanently shifted emission spectrum due to a photochemical reaction after excitation.[41] It has also been demonstrated that it is possible to exploit unnatural amino acid residues in order to directly modify the chromophore of a fluorescent protein.[42-44] This brings closer the tantalizing possibility of being able to tune the properties of fluorescent proteins by directly modifying the molecular structure of the chromophore. This would be an important development which could significantly expand the applications of FPs. Ultimately, the goal is to employ FPs to allow real time imaging of increasingly complex biological systems and processes. However, the significant level of control required over the photophysical properties of the FPs dictates that a detailed understanding of the excited state dynamics of these systems is required. In particular, the excited state dynamics of the chromophore and how they are affected by the protein environment is a fundamental consideration.

Niwa and co-workers[45] first identified the structure of the chromophore of GFP and synthesised the close analogue, *p*-hydroxybenzilideneimidazolinone (HBDI, Figure 1.4[38,46]). This led to the surprising discovery that HBDI in free solution is essentially non-fluorescent.[45] The fluorescence quantum yield of HBDI in a room temperature aqueous solution is approximately 2×10^{-4}. In stark contrast, the fluorescence quantum yield of the wild-type protein (wt-GFP) is ~0.8.[47]

(a)

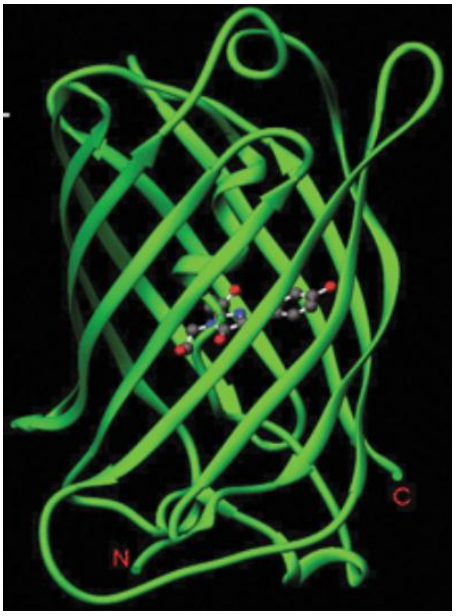

(b)

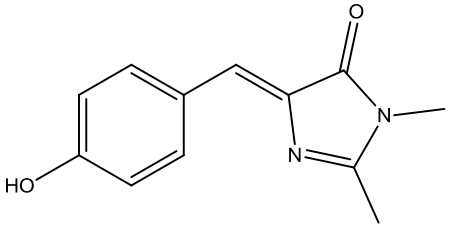

Figure 1.4 - *(a) The protein structure of GFP (reproduced from References [38] and [46]) and (b) The structure of HBDI, the synthetic model chromophore.*

Thus, the fluorescence of the GFP chromophore is significantly quenched in absence of the protein matrix. In addition, the absorption spectrum of neutral HBDI was found to be significantly blue shifted in comparison to wt-GFP.[48] This provides further evidence for a significant modification of the photophysics of HBDI induced by the protein environment.

The excited state decay of HBDI has been studied in detail by ultrafast spectroscopy. A sub-picosecond decay and ground state recovery was observed, thus leading to an assignment of ultrafast internal conversion as the mechanism of non-radiative decay.[49-51] The protein environment evidently acts to significantly suppress this radiationless relaxation pathway in the HBDI excited state. It has been established that internal conversion in HBDI occurs *via* torsional motion along a volume conserving and almost barrierless co-ordinate.[51,52] It is also known from NMR spectroscopy that HBDI undergoes an excited state isomerization reaction.[53,54] However, isomerization is typically regarded as a non-volume conserving processes. This has led to extensive debate regarding the mechanism of the volume

conserving excited state isomerization reaction which is undergone by HBDI. A more detailed discussion is given in Chapter 7.

The aim of this work is to investigate the substituent dependence of the excited state decay dynamics of HBDI. A series of alkyl substituted derivatives of HBDI will be studied (Chapter 7). Clearly, the study of excited state isomerization reactions is a key theme in this work and so some background is given in the next section.

1.3 Excited State Structural Dynamics

1.3.1 Excited State Isomerisation

An excited state cis/trans isomerisation reaction about a central double carbon bond (C=C) is one of the most common structural motifs for the conversion of light into mechanical energy. Indeed, a cis-trans photoisomerization of the retinal chromophore in rhodopsin is the fundamental photochemical process in vision.[55,56] As a result, understanding the molecular dynamics of such reactions has long been a focus of photochemical research. A general schematic representation of a photoisomerization reaction is shown in Figure 1.5. In the electronic ground state a significant energy barrier separates the cis and trans forms. However, electronic excitation leads to a π-π^* transition localised on the central double bond. As a result, the double bond character is significantly reduced, thus reducing (or even removing entirely, as in Figure 1.5) the barrier in the excited state. Rapid structural relaxation occurs along the reaction co-ordinate to a minimum on the excited state potential energy surface. The excited state population then undergoes ultrafast internal conversion directly to the ground state *via* an S_1/S_0 conical intersection.[57-61] A conical intersection is a molecular configuration in which multiple electronic states of a molecule are degenerate.

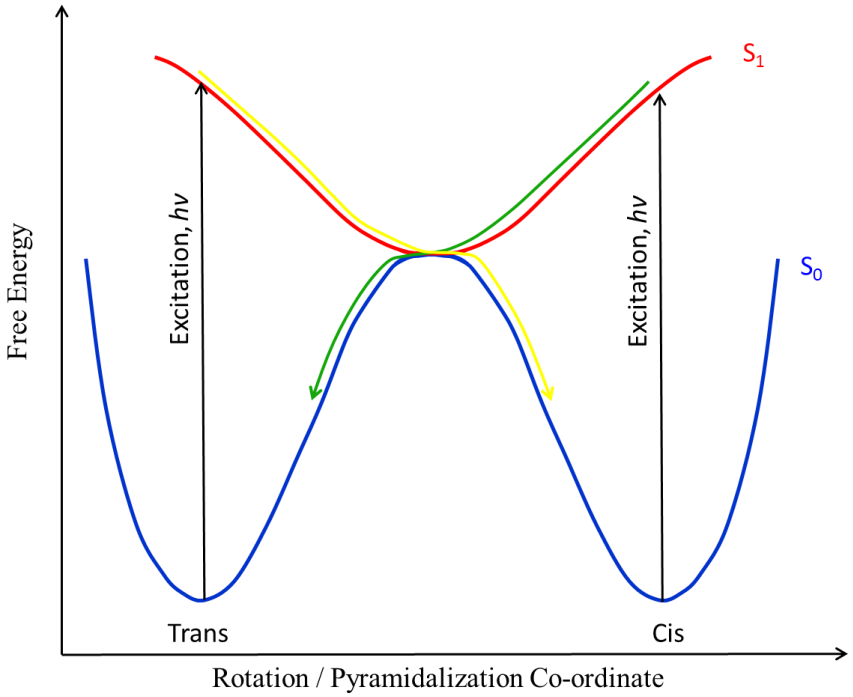

Figure 1.5 - *A schematic representation of an excited state cis/trans isomerization reaction.*

As a result, non-radiative transitions between different electronic states (non-adiabatic dynamics) can occur despite such transitions being forbidden by the Born-Oppenheimer approximation. [57,62,63] This pathway facilitates ultrafast internal conversion of electronically excited states (S_1) to the ground state (S_0) on an ultrafast timescale. A conical intersection is not an isolated point, but rather is a high-dimensional seam between the two intersecting potential energy surfaces.[57,59] Significant theoretical research has been conducted in a number of molecular systems in which conical intersections are involved in the excited state dynamics. However, a number of cases exist in which the excited state dynamics are found to lead a molecule through a conical intersection seam at a location which is significantly above the minimum energy geometry.[59] When applying conical intersections to the mechanisms of photochemical reactions, such as excited state isomerization, a minimum of two reactive co-ordinates are required to successfully describe the potential energy surfaces (often S_1 and S_0) which form the intersection.[57] Detailed quantum mechanical calculations on a number of

molecular systems which undergo photoisomerization reactions have revealed that both rotation about the central double bond and pyramidalization of the double bond atoms in the excited state form these co-ordinates.[57] Figure 1.5 is therefore an overly simplified picture in which the rotation and pyramidalization co-ordinates are represented by a single reaction co-ordinate in only one dimension.

A successful model for the description of the excited state molecular dynamics of a number of systems which undergo a barrierless (or near barrierless) excited state isomerization reaction was proposed by Bagchi, Fleming and Oxtoby[64] (BFO model). A detailed description of the BFO model is given in Section 1.3.2. The most widely studied (and structurally simple) example of such a system is stilbene. When considering the trans-cis and cis-trans photoisomerization reactions of stilbene, it was found that the mechanisms of these processes differ.[65] This is an important observation which provided a key insight into the molecular dynamics involved in the reaction. The cis-trans isomerization was reported to occur *via* barrierless structural evolution along the torsional co-ordinate of the central olefin, resulting in isomerization in less than 1 ps.[66] In contrast, a barrier was reported to exist to excited state structural evolution of the trans isomer along this co-ordinate.[67] This results in a slower timescale for the trans-cis isomerization. Further insight into the isomerization mechanism of stilbene was gained by studying the effects of solvent friction. Such considerations are described in Section 1.3.2.

Excited state isomerization reactions have also been reported for a number of other molecular systems. For example, azobenzene[68,69] (structurally analogous to stilbene, but with N=N replacing C=C) and triphenylmethane (TPM) dyes [70-72] are widely studied systems which undergo photoisomerization reactions. In each case, the role of excited state torsional motion was found to be important. As in the case of stilbene, the effect of solvent viscosity (friction) on the excited state dynamics has been shown to yield information on the nature of the

photoisomerization reactions. This is because high solvent friction is expected to retard torsional motion in such molecular systems.

1.3.2 Solvent Friction Effects upon Photoisomerization

One of the key considerations in probing excited state structural evolution is the effect of solvent friction. This is because isomerization coordinates which involve large scale molecular motion (such as the rotational motion of a phenyl ring in the isomerization of stilbene) are likely to be opposed by solvent friction. Thus, structural evolution along the co-ordinate which promotes internal conversion would be retarded, resulting in a longer excited state lifetime. This can be measured by ultrafast spectroscopic techniques. Therefore, the extent to which viscous media slow the decay of the excited state can be indicative of the extent to which large scale molecular motion is involved in the reactive co-ordinate.

The effect of solvent friction on the rate of a reaction was considered by Kramers.[73] His model assumed that molecular motion along the reaction co-ordinate required passage over an activation barrier. This was modelled by the escape of a particle over a one dimensional parabolic barrier.[74] The solvent friction parameter (ξ) reflects the effect of the medium on motion along the reaction co-ordinate. Kramers' theory makes two key predictions.[74,75] In the low friction regime, the rate of activation (and hence the rate of reaction) is governed by reactant – solvent energy transfer. Therefore, the frequency with which reactant-solvent collisions occur is rate limiting under low solvent friction conditions. Thus, the rate of reaction *increases* with increasing solvent friction. In the opposite case (high friction), reactant-solvent collisions are frequent such that energy transfer is no longer the rate limiting factor, and the friction resists motion. Under such conditions, the rate of the reaction is expected to decrease with increasing solvent friction. Therefore, Kramers' theory predicts an initial increase of the rate of reaction with increasing solvent friction, followed by a decrease.

This is termed ‘Kramer’s turnover’, the experimental observation of which was a focus of research in the last century.[75,76]

Kramer’s theory has been extensively tested and modified and applied to a number of reaction schemes. For example, the applicability of Kramers' theory to the dynamics of excited state isomerization reactions was widely studied. The trans-cis isomerization of stilbene is a particularly well characterised reaction.[65,67,77] In the low friction regime, increasing the solvent friction increases the isomerization rate. This is because the increasing friction results in more reactant-solvent collisions and hence a faster rate of activation. This was observed in gas phase measurements only.[74] In contrast, the higher friction regime exhibits the opposite trend. This is because reactant-solvent energy transfer is no longer rate limiting, instead retardation of torsional motion becomes the dominant factor. These observations are in good agreement with Kramers’ theory. However, several limitations of Kramers’ theory have been found, particularly with reference to excited state reactions which involve barrierless coordinates. For example, Kramers’ theory predicts a linear dependence of the rate of a reaction upon solvent friction.[74] However, the excited state relaxation of TPM dyes was found experimentally to only depend on $\zeta^{2/3}$.[70-72,78] A significant issue arises from the experimental definition of ‘solvent friction’. Typically, the shear viscosity of a solvent (η) is taken as a representation of solvent friction ($\zeta \propto \eta$)[79]. However, significant debate exists as to the validity of this relationship,[74] although it remains a frequently used approximation (and is used throughout this work). A commonly postulated alternative measure of microscopic solvent friction is the rotational correlation time ($\tau_{or)}$ of the isomerising molecule.[80] Although τ_{or} has been successfully used to describe the isomerization of stilbene,[81] it fails to provide a good fit to Kramers’ theory in other cases. [82] Thus, the complete description of solvent friction remains problematic.

Significant research has been devoted to the development of Kramer's model for application to barrierless (or almost barrierless) reaction co-ordinates. In the absence of a barrier to structural evolution, solvent friction represents the only force which opposes motion along the reaction co-ordinate. This was first considered by Oster and Nishijima,[83] whereby the fluorescence quantum yield (Φ_f) of Auramine O was studied as a function of solvent viscosity (η) and temperature (T). A linear relationship was suggested ($\Phi_f \propto \eta/T$) with the excited state reaction co-ordinate (leading to non-radiative decay) interpreted in terms of diffusive motion opposed by medium friction on a barrierless potential energy surface. Therefore, as the viscosity of the solvent is increased, the diffusive motion is retarded leading to an enhanced fluorescence quantum yield.

The treatment of barrierless excited state reaction co-ordinates was developed further by Bagchi, Fleming and Oxtoby (BFO model) in order to describe the effects of solvent friction upon the excited state decay of TPM dyes.[64] The ultrafast non-radiative decay of these molecules was proposed to occur *via* rotation of the phenyl groups along a strongly downhill barrierless co-ordinate.[70-72] It was proposed that this motion leads to an S_1-S_0 conical intersection, thus promoting ultrafast internal conversion. Therefore, the BFO model is based upon the motion of a solute particle on a potential surface with no barrier. The modelled surface is parabolic in nature, and the radiationless decay is represented by a position dependent sink (modelled as a pin hole, a Gaussian function and a Lorentzian function) on the potential surface. This sink function is used to describe a conical intersection (See Section 1.3.1 for a more detailed description of a conical intersection). Figure 1.6 shows a schematic representation of the excited state sink function employed by the BFO model. As the excited state population moves along the reaction co-ordinate, it approaches the vicinity of the sink and the ground state is repopulated *via* internal conversion.

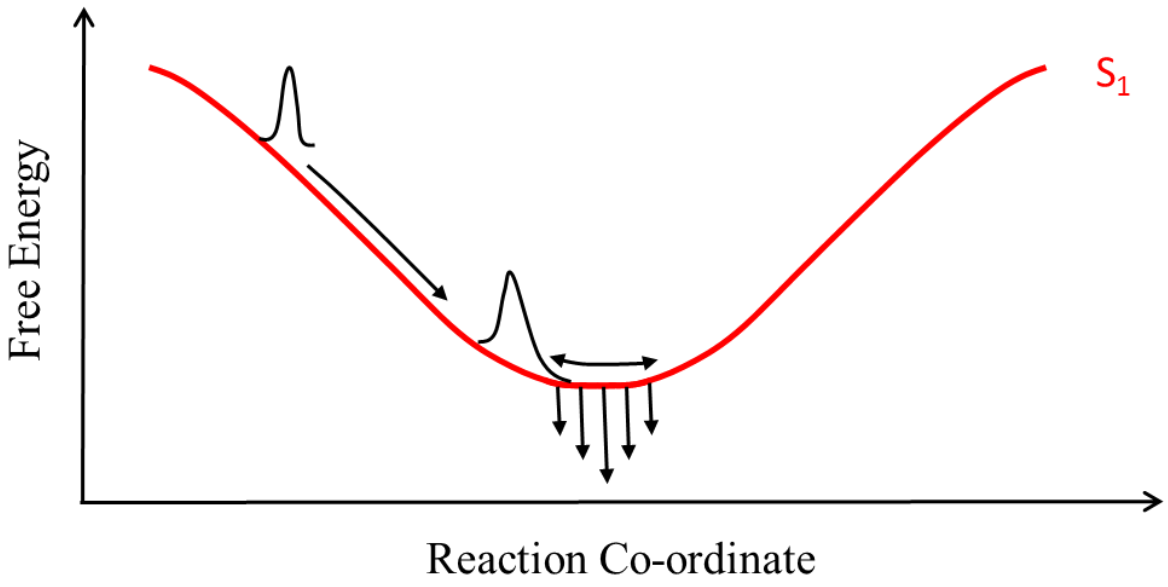

Figure 1.6 - *A schematic representation of the BFO model applied to barrierless excited state structural evolution. The initially populated excited state relaxes via structural motion along the reaction co-ordinate towards a position-dependent sink function from which direct relaxation to the ground state is possible.*

This model was able to account for the experimentally observed deviation from a linear dependence of the rate of isomerization upon solvent viscosity for TPM dyes. Thus, it was proposed that this model could be applied to various molecular systems in which radiationless decay is promoted by excited state structural evolution along a barrierless reaction co-ordinate. (e.g. photoisomerization, Section 1.3.1, Figure 1.5). A key conclusion from such studies is that the effects of solvent viscosity (as an approximation for solvent friction) upon excited state decay dynamics can be very revealing regarding the mechanisms of excited state reactions. Ultrafast spectroscopy allows real time measurement of excited state decay dynamics and thus an assessment of the nature of the molecular dynamics involved in the reaction co-ordinate is possible. The effects of solvent viscosity are important to the study of the excited state molecular dynamics of the molecular motor and fluorescent protein chromophore systems under investigation in this work.

1.3.3 Solvation Dynamics

The role of the solvent in ultrafast excited state molecular dynamics extends beyond the effects of viscosity. Of particular importance are molecular systems in which a charge separation exists between the ground and excited states or between initially excited and final states. In such cases, polar solvent molecules play a key role in the stabilisation of the charge separated state.[84] Figure 1.7 shows a schematic representation of the excitation of a molecule in which a charge separated state is populated. In the ground state, the solvent molecules are orientated so as to minimize electrostatic repulsion with the solute molecules.[84,85]

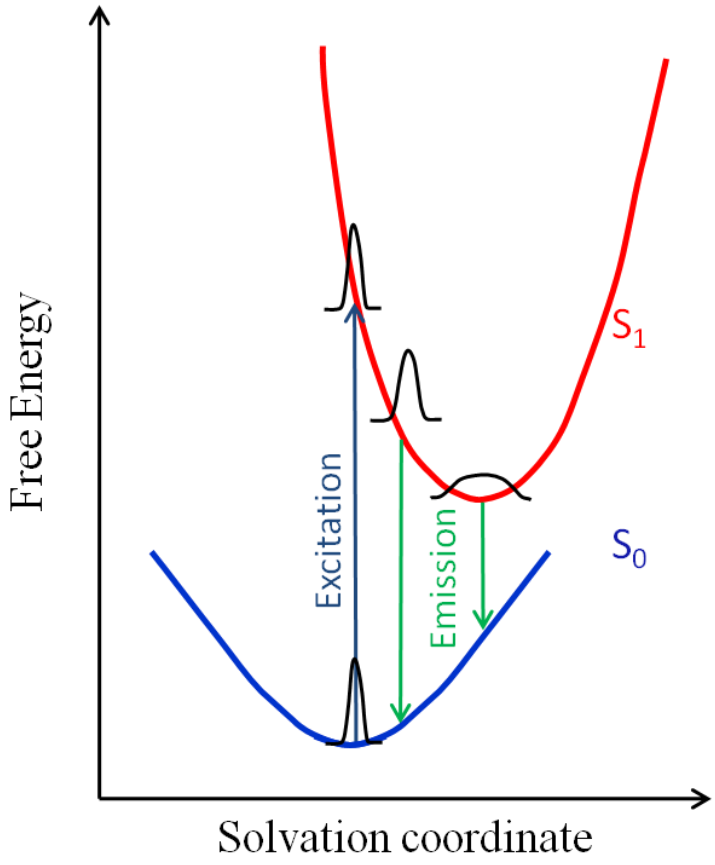

Figure 1.7 - *A schematic representation of excited state relaxation via solvation. The initial excited state molecular structure is formed instantaneously and is stabilised by the dynamic reorientation of solvent molecules. This corresponds to a dynamic red shift in the time-resolved fluorescence spectrum.*

This corresponds to the energetically optimal arrangement of the solvent. Thus, the ground state population is at the minimum on the ground state surface (Figure 1.7). However, upon excitation the electronic structure of the solute is instantaneously transformed to that of the excited state. If the excited state is of a different charge character, the solvent molecules are no longer in the lowest energy arrangement. Thus, the initially populated excited state is not at the minimum energy on the excited state surface (Figure 1.7) As a result, the solvent molecules re-orientate along the 'solvation' co-ordinate in order to re-establish equilibrium with the excited state solute molecules.

This dynamic rearrangement of the solvent thus reduces the energy of the excited state population to a position of minimum energy on the excited state surface (Figure 1.7). However, the movement of solvent molecules is not an instantaneous process. The timescale of solvent reorientation is therefore a key factor which can determine the rate of excited state stabilisation and hence the rates of excited state reactions.[86] Solvent dynamics are typically on the sub-pico to nanosecond timescale and so solvation can be measured in real time with ultrafast lasers. Time-resolved fluorescence spectroscopy has proven to be a useful tool for the experimental observation of solvation dynamics.[87-89] As shown in Figure 1.7, emission from the initially populated excited state structure is of a higher energy than emission from the stabilised state. This corresponds to a dynamic red shift of the emission spectrum.[84] This can be characterized by reconstruction of the time-dependent frequency domain emission spectrum from fluorescence decay curves measured at wavelengths spanning the emission spectrum.[84] This reconstruction process is discussed in detail in Chapter 2.

Ultrafast fluorescence spectroscopy has been used to probe experimentally the solvation dynamics of a number of molecular systems which undergo excited state reactions. For example, the rates of excited state electron transfer[90] and proton transfer[91] reactions have

been shown to depend upon the dynamics of solvation. Thus, the study of solvation dynamics can provide useful insights into the mechanisms of excited state reactions.

1.3.4 Vibrational Coherence

Ultrashort laser pulses for ultrafast spectroscopic measurements are of a broad energy bandwidth. As a result, electronic excitation can also lead to the excitation of many vibrational modes of a probe molecule.[92] If an excitation pulse is shorter than the period of a vibrationally active mode, this results in coherent impulsive excitation of the vibrational mode.[93] Thus, coherent motion of the nuclei of the vibrational mode is induced. Figure 1.8 shows a general schematic representation of coherent excitation of vibrational modes and the resulting coherent nuclear motion. Initial electronic excitation by an ultrashort pump pulse excites vibrational modes (υ = 1) which are displaced between the electronic ground and excited states. A coherent superposition of the υ = 1 and υ = 0 vibrational states is thus generated.

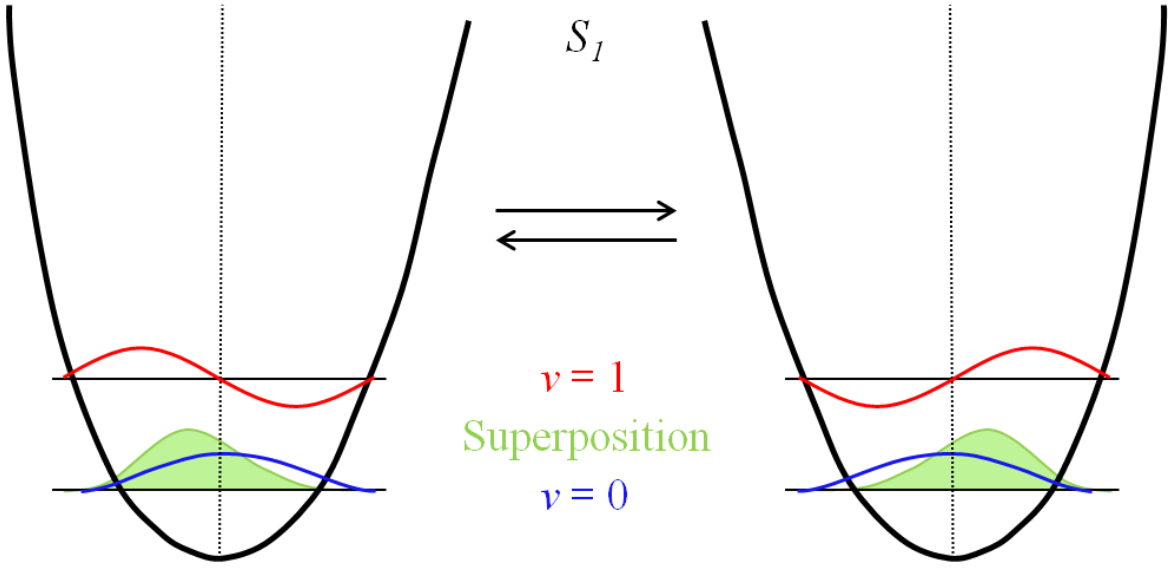

Figure 1.8 - *A schematic representation of the excited state coherent nuclear motion which results from the coherent excitation of vibrational modes by an ultrashort laser pulse.*

A wavepacket is launched on the excited state potential energy surface (S_1) with a frequency matching the frequency of the vibrational modes. Therefore, as the vibrationally coherent state evolves in time, coherent nuclear motion of the molecule is induced. The excited state population thus follows the coherent superposition as the coherently excited vibrational modes oscillate. During this evolution, a number of factors can lead to the loss of coherence and hence damping of the coherent nuclear motion. For example, the frequency of the mode may change during the course of the vibration (due to a strong intermolecular collision for example), the modes may become out of phase or the vibrational energy may be dissipated amongst lower frequency vibrational modes of the molecule (vibrational relaxation).This damping typically occurs on a significantly faster timescale (< 1 ps) in the excited state.

If a coherently excited vibrational mode is coupled to the electronic transition (S_0-S_1), the resulting coherent nuclear motion can be observed as oscillations in time-resolved experiments.[94] A number of oscillatory time-domain spectra have been observed by pump/probe transient absorption[95] and fluorescence up-conversion.[96] The temporal evolution of the oscillations can thus be followed as a real time representation of the coherent nuclear dynamics of a probe molecule. This is of particular potential significance for molecular systems which undergo ultrafast excited state reactions. A detailed insight into the mechanism of such reactions may be gained by following the nuclear dynamics involved in excited state structural evolution along the reaction co-ordinate. For example, ultrafast excited state isomerization,[95-97] proton transfer[92,98-100] and electron transfer[94,101] reactions have been found to exhibit coherent nuclear motion as revealed by oscillatory ultrafast spectroscopic signals. In each case, the relevance of the coherent nuclear motion to the molecular dynamics of the reaction co-ordinate can be assessed. Thus, such experimental characterisation, complemented by theoretical studies, has allowed assignment of vibrational modes which are directly involved in the co-ordinate of excited state reactions.

The study of coherent nuclear dynamics in excited state reactive systems by time resolved fluorescence spectroscopy has proven to be particularly useful. This is because oscillations observed by pump/probe transient absorption often involve coherent nuclear motion on both the ground and excited state surfaces. In contrast, since fluorescence unambiguously probes only the excited state, oscillations observed in time-resolved fluorescence can only reflect coherent nuclear motion in the excited state. The observation of such oscillations can provide an insight into the nature of the excited state surface. For example, a strongly damped oscillation suggests an anharmonic surface where weak re-phasing of the nuclear motion does occur leading to vibrational coherence, but with the loss of this coherence on a rapid timescale. Although coherent oscillations can only occur in a bound potential well (as shown in Figure 1.8) it is also possible to represent coherent nuclear motion on an adiabatic surface whereby two bound harmonic potential surfaces are coupled[102] (e.g. a bright excited state coupled to a dark excited state, Chapter 4, Figure 4.17). This approach is used in order to describe the coherent oscillations observed in the data presented in this thesis.

The challenge of these measurements is the time required resolution, which must be at least better than half of the vibrational period. In this work, ultrafast fluorescence up-conversion spectroscopy with a time resolution better than 50 fs will be used to measure excited state dynamics in unidirectional molecular rotary motors. This technique provides a suitably high time resolution such that coherent excitation of vibrational modes is possible. Thus, excited state low frequency modes which are coupled to the electronic transition moment are detected as oscillations in fluorescence decay profiles. Such coherent nuclear motion may provide additional insights into the mechanism of isomerization in the molecular motor systems under investigation in this work.

1.4 References

(1) Thomas, N.; Thornhill, R. A. *J. Phys. D: Appl. Phys.***1998**, *31*, 253.

(2) Kinbara, K.; Aida, T. *Chem. Rev.* **2005**, *105*, 1377.

(3) Veigel, C.; Schmidt, C. F. *Nat. Rev. Mol. Cell. Biol.* **2011**, *12*, 163.

(4) Berg, H. C.; Anderson, R. A. *Nature* **1973**, *245*, 380.

(5) Manson, M. D. *Proc. Natl. Acad. Sci. USA.* **2010**, *107*, 11151.

(6) Boyer, P. D. *Nature* **1999**, *402*, 247.

(7) Yoshida, M.; Muneyuki, E.; Hisabori, T. *Nat. Rev. Mol. Cell Biol.* **2001**, *2*, 669.

(8) Schliwa, M.; Woehlke, G. *Nature* **2003**, *422*, 759.

(9) Jiang, W. P.; Hermolin, J.; Fillingame, R. H. *Proc. Natl. Acad. Sci. USA.* **2001**, *98*, 4966.

(10) Miller, R. J. *Nat. Chem.* **2012**, *4*, 523.

(11) Balzani, V.; Credi, A.; Venturi, M. *Chem. Soc. Rev.* **2009**, *38*, 1542.

(12) Natali, M.; Giordani, S. *Chem. Soc. Rev.* **2012**, *41*, 4010.

(13) Hirshberg, Y.; Fischer, E. *J. Chem. Phys.* **1955**, *23*, 1723.

(14) Feringa, B. L. *Acc. Chem. Res.* **2001**, *34*, 504.

(15) Gust, D.; Moore, T. A.; Moore, A. L. *Chem. Commun.* **2006**, 1169.

(16) Pardo, R.; Zayat, M.; Levy, D. *Chem. Soc. Rev.* **2011**, *40*, 672.

(17) Robertus, J.; Reker, S. F.; Pijper, T. C.; Deuzeman, A.; Browne, W. R.; Feringa, B. L. *Phys. Chem. Chem. Phys.* **2012**, *14*, 4374.

(18) Altoe, P.; Bernardi, F.; Conti, I.; Garavelli, M.; Negri, F.; Orlandi, G. *Theor. Chem. Acc.* **2007**, *117*, 1041.

(19) Hess, H.; Vogel, V. *J. Biotechnol.* **2001**, *82*, 67.

(20) Saha, S.; Flood, A. H.; Stoddart, J. F.; Impellizzeri, S.; Silvi, S.; Venturi, M.; Credi, A. *J. Am. Chem. Soc.* **2007**, *129*, 12159.

(21) Sindelar, V.; Silvi, S.; Kaifer, A. E. *Chem. Commun.* **2006**, 2185.

(22) Brouwer, A. M.; Frochot, C.; Gatti, F. G.; Leigh, D. A.; Mottier, L.; Paolucci, F.; Roffia, S.; Wurpel, G. W. H. *Science* **2001**, *291*, 2124.

(23) Altieri, A.; Gatti, F. G.; Kay, E. R.; Leigh, D. A.; Martel, D.; Paolucci, F.; Slawin, A. M. Z.; Wong, J. K. Y. *J. Am. Chem. Soc.* **2003**, *125*, 8644.

(24) Panman, M. R.; Bodis, P.; Shaw, D. J.; Bakker, B. H.; Newton, A. C.; Kay, E. R.; Leigh, D. A.; Buma, W. J.; Brouwer, A. M.; Woutersen, S. *Phys. Chem. Chem. Phys.* **2012**, *14*, 1865.

(25) Browne, W. R.; Feringa, B. L. *Nat. Nanotechnol.* **2006**, *1*, 25.

(26) Ballardini, R.; Balzani, V.; Credi, A.; Gandolfi, M. T.; Venturi, M. *Acc. Chem. Res.* **2001**, *34*, 445.

(27) Kay, E. R.; Leigh, D. A.; Zerbetto, F. *Angew. Chem.-Int. Edit.* **2007**, *46*, 72.

(28) Koumura, N.; Zijlstra, R. W. J.; van Delden, R. A.; Harada, N.; Feringa, B. L. *Nature* **1999**, *401*, 152.

(29) Koumura, N.; Geertsema, E. M.; van Gelder, M. B.; Meetsma, A.; Feringa, B. L. *J. Am. Chem. Soc.* **2002**, *124*, 5037.

(30) Vicario, J.; Meetsma, A.; Feringa, B. L. *Chem. Commun.* **2005**, 5910.

(31) Pollard, M. M.; Klok, M.; Pijper, D.; Feringa, B. L. *Adv. Funct. Mater.* **2007**, *17*, 718.

(32) Klok, M.; Boyle, N.; Pryce, M. T.; Meetsma, A.; Browne, W. R.; Feringa, B. L. *J. Am. Chem. Soc.* **2008**, *130*, 10484.

(33) Pollard, M. M.; Meetsma, A.; Feringa, B. L. *Org. Biomol. Chem.*. **2008**, *6*, 507.

(34) Shimomura, O.; Johnson, F. H.; Saiga, Y. *J. Cell. Compar. Physl.* **1962**, *59*, 223.

(35) Chalfie, M.; Tu, Y.; Euskirchen, G.; Ward, W. W.; Prasher, D. C. *Science* **1994**, *263*, 802.

(36) Cubitt, A. B.; Heim, R.; Adams, S. R.; Boyd, A. E.; Gross, L. A.; Tsien, R. Y. *Trends. Biochem. Sci.* **1995**, *20*, 448.

(37) Shaner, N. C.; Campbell, R. E.; Steinbach, P. A.; Giepmans, B. N. G.; Palmer, A. E.; Tsien, R. Y. *Nat. Biotechnol.* **2004**, *22*, 1567.

(38) Tsien, R. Y. *Angew. Chem.-Int. Edit.* **2009**, *48*, 5612.

(39) Day, R. N.; Davidson, M. W. *Chem. Soc. Rev.* **2009**, *38*, 2887.

(40) Habuchi, S.; Ando, R.; Dedecker, P.; Verheijen, W.; Mizuno, H.; Miyawaki, A.; Hofkens, J. *Proc. Natl. Acad. Sci. USA.* **2005**, *102*, 9511.

(41) Ando, R.; Hama, H.; Yamamoto-Hino, M.; Mizuno, H.; Miyawaki, A. *Proc. Natl. Acad. Sci. USA.* **2002**, *99*, 12651.

(42) Kent, K. P.; Childs, W.; Boxer, S. G. *J. Am. Chem. Soc.* **2008**, *130*, 9664.

(43) Kent, K. P.; Oltrogge, L. M.; Boxer, S. G. *J. Am. Chem. Soc.* **2009**, *131*, 15988.

(44) Wang, L.; Xie, J. M.; Deniz, A. A.; Schultz, P. G. *J. Org. Chem.* **2003**, *68*, 174.

(45) Niwa, H.; Inouye, S.; Hirano, T.; Matsuno, T.; Kojima, S.; Kubota, M.; Ohashi, M.; Tsuji, F. I. *Proc. Natl. Acad. Sci. USA.* **1996**, *93*, 13617.

(46) Ormo, M.; Cubitt, A. B.; Kallio, K.; Gross, L. A.; Tsien, R. Y.; Remington, S. J. *Science* **1996**, *273*, 1392.

(47) Tsien, R. Y. *Annu. Rev. Biochem.* **1998**, *67*, 509.

(48) Meech, S. R. *Chem. Soc. Rev.* **2009**, *38*, 2922.

(49) Litvinenko, K. L.; Webber, N. M.; Meech, S. R. *Chem. Phys. Lett.* **2001**, *346*, 47.

(50) Webber, N. M.; Litvinenko, K. L.; Meech, S. R. *J. Phys. Chem. B.* **2001**, *105*, 8036.

(51) Litvinenko, K. L.; Webber, N. M.; Meech, S. R. *J. Phys. Chem. A.* **2003**, *107*, 2616.

(52) Mandal, D.; Tahara, T.; Meech, S. R. *J. Phys. Chem. B.* **2004**, *108*, 1102.

(53) Voliani, V.; Bizzarri, R.; Nifosi, R.; Abbruzzetti, S.; Grandi, E.; Viappiani, C.; Beltram, F. *J. Phys. Chem. B.* **2008**, *112*, 10714.

(54) Dong, J.; Abulwerdi, F.; Baldridge, A.; Kowalik, J.; Solntsev, K. M.; Tolbert, L. M. *J. Am. Chem. Soc.* **2008**, *130*, 14096.

(55) Yoshizawa, T.; Wald, G. *Nature* **1963**, *197*, 1279.

(56) Polli, D.; Altoe, P.; Weingart, O.; Spillane, K. M.; Manzoni, C.; Brida, D.; Tomasello, G.; Orlandi, G.; Kukura, P.; Mathies, R. A.; Garavelli, M.; Cerullo, G. *Nature* **2010**, *467*, 440.

(57) Levine, B. G.; Martinez, T. J. *Annu. Rev. Phys. Chem.* **2007**, *58*, 613.

(58) Domcke, W.; Yarkony, D. R. In *Annu. Rev. Phys. Chem., Vol 63*; Johnson, M. A., Martinez, T. J., Eds. 2012; Vol. 63, p 325.

(59) Toniolo, A.; Olsen, S.; Manohar, L.; Martinez, T. J. *Faraday Discuss.* **2004**, *127*, 149.

(60) Yarkony, D. R. *Acc. Chem. Res.* **1998**, *31*, 511.

(61) Matsika, S.; Krause, P. In In *Annu. Rev. Phys. Chem., Vol 62*; Leone, S. R., Cremer, P. S., Groves, J. T., Johnson, M. A., Eds. 2011; Vol. 62, p 621.

(62) Yarkony, D. R. *J. Phys. Chem. A.* **2001**, *105*, 6277.

(63) Worth, G. A.; Cederbaum, L. S. *Annu. Rev. Phys. Chem.* **2004**, *55*, 127.

(64) Bagchi, B.; Fleming, G. R.; Oxtoby, D. W. *J. Chem. Phys.* **1983**, *78*, 7375.

(65) Waldeck, D. H. *Chem. Rev.* **1991**, *91*, 415.

(66) Todd, D. C.; Jean, J. M.; Rosenthal, S. J.; Ruggiero, A. J.; Yang, D.; Fleming, G. R. *J. Chem. Phys.* **1990**, *93*, 8658.

(67) Kim, S. K.; Fleming, G. R. *J. Phys. Chem.* **1988**, *92*, 2168.

(68) Bandara, H. M. D.; Burdette, S. C. *Chem. Soc. Rev.* **2012**, *41*, 1809.

(69) Fujino, T.; Arzhantsev, S. Y.; Tahara, T. *J. Phys. Chem. A.* **2001**, *105*, 8123.

(70) Nagasawa, Y.; Ando, Y.; Kataoka, D.; Matsuda, H.; Miyasaka, H. *J. Phys. Chem. A.* **2002**, *106*, 2024.

(71) Bhasikuttan, A. C.; Sapre, A. V.; Okada, T. *J. Phys. Chem. A.* **2003**, *107*, 3030.

(72) Benamotz, D.; Harris, C. B. *J. Chem. Phys.* **1987**, *86*, 4856.

(73) Kramers, H. A. *Physica* **1940**, *7*, 284.

(74) Meech, S. R. *Annu. Rep. Prog. Chem., Sect. C: Phys. Chem.* **1990**, *87*, 199.

(75) Hynes, J. T. *Annu. Rev. Phys. Chem.* **1985**, *36*, 573.

(76) Lee, M. Y.; Holtom, G. R.; Hochstrasser, R. M. *Chem. Phys. Lett.* **1985**, *118*, 359.

(77) Todd, D. C.; Fleming, G. R. *J. Chem. Phys.* **1993**, *98*, 269.

(78) Sundstrom, V.; Gillbro, T. *J. Phys. Chem.* **1982**, *86*, 1788.

(79) Loughnane, B. J.; Scodinu, A.; Farrer, R. A.; Fourkas, J. T.; Mohanty, U. *J. Chem. Phys.* **1999**, *111*, 2686.

(80) Velsko, S. P. *J Chem Phys* **1983**, *78*, 249.

(81) Courtney, S. H.; Kim, S. K.; Canonica, S.; Fleming, G. R. *J. Chem. Soc., Faraday Trans.* **1986**, *82*, 2065.

(82) Barbara, P. F.; Jarzeba, W. *Acc. Chem. Res.* **1988**, *21*, 195.

(83) Oster, G.; Nishijima, Y. *J. Am. Chem. Soc.* **1956**, *78*, 1581.

(84) Maroncelli, M.; Fleming, G. R. *J. Chem. Phys.* **1987**, *86*, 6221.

(85) Glasbeek, M.; Zhang, H. *Chem. Rev.* **2004**, *104*, 1929.

(86) Rossky, P. J.; Simon, J. D. *Nature* **1994**, *370*, 263.

(87) Gustavsson, T.; Baldacchino, G.; Mialocq, J. C.; Pommeret, S. *Chem. Phys. Lett.* **1995**, *236*, 587.

(88) Horng, M. L.; Gardecki, J. A.; Papazyan, A.; Maroncelli, M. *J. Phys. Chem.* **1995**, *99*, 17311.

(89) Smith, N. A.; Meech, S. R.; Rubtsov, I. V.; Yoshihara, K. *Chem. Phys. Lett.* **1999**, *303*, 209.

(90) Maroncelli, M.; Macinnis, J.; Fleming, G. R. *Science* **1989**, *243*, 1674.

(91) Rini, M.; Kummrow, A.; Dreyer, J.; Nibbering, E. T. J.; Elsaesser, T. *Faraday Discuss.* **2003**, *122*, 27.

(92) Takeuchi, S.; Tahara, T. *J. Phys. Chem. A.* **2005**, *109*, 10199.

(93) Pollard, W. T.; Lee, S.-Y.; Mathies, R. A. *J. Chem. Phys.* **1990**, *92*, 4012.

(94) Rubtsov, I. V.; Yoshihara, K. *J. Phys. Chem. A.* **1999**, *103*, 10202.

(95) Ishii, K.; Takeuchi, S.; Tahara, T. *Chem. Phys. Lett.* **2004**, *398*, 400.

(96) Chosrowjan, H.; Taniguchi, S.; Mataga, N.; Unno, M.; Yamauchi, S.; Hamada, N.; Kumauchi, M.; Tokunago, F. *J. Phys. Chem. B.* **2004**, *108*, 2686.

(97) Nakamura, R.; Hamada, N.; Ichida, H.; Tokunaga, F.; Kanematsu, Y. *J. Chem. Phys.* **2007**, *127*, 215102.

(98) Chudoba, C.; Riedle, E.; Pfeiffer, M.; Elsaesser, T. *Chem. Phys. Lett.* **1996**, *263*, 622.

(99) Kim, C. H.; Joo, T. *Phys. Chem. Chem. Phys.* **2009**, *11*, 10266.

(100) Higashi, M.; Saito, S. *J. Phys. Chem. Lett.* **2011**, 2366.

(101) Nagasawa, Y.; Fujita, K.; Katayama, T.; Ishibashi, Y.; Miyasaka, H.; Takabe, T.; Nagao, S.; Hirota, S. *Phys. Chem. Chem. Phys.* **2010**, *12*, 6067.

(102) van der Meer, M. J.; Zhang, H.; Glasbeek, M. *J. Chem. Phys.* **2000**, *112*, 2878.

2 Experimental

In this chapter, the experimental procedures employed in this work will be outlined. A description of the ultrafast fluorescence up-conversion experiment will be presented first (Section 2.1), followed by a more detailed description of the transient absorption experiment (Section 2.2). The transient absorption description will also detail the software used to control the experiment and the key principles upon which the experiment is conducted (Sections 2.2.1 – 2.2.4). Finally, the data analysis procedures employed for each measurement will be described (Section 2.3), with particular focus placed upon the fitting of time domain data (Section 2.3.1.1 and Section 2.3.2.2 for fluorescence up-conversion and transient absorption measurements respectively) and the reconstruction of time-dependent fluorescence spectra from the fluorescence lifetime data (Section 2.3.1.2).

2.1 Ultrafast Time-resolved Fluorescence Up-conversion

Ultrafast fluorescence up-conversion is a method for measuring the fluorescence lifetime of a species with the time resolution limited only by the width of the laser pulse. Essentially, it is an ultrafast sampling method. Importantly, since it is fluorescence which is detected (a specifically excited state process), this method allows selective probing of the dynamics of only the excited state, which distinguishes it from transient absorption, for example. The apparatus described here has a time resolution better than 50 fs, thus allowing us to probe the very earliest dynamics on the excited state potential energy surface.

The general experimental set-up employed for ultrafast time-resolved fluorescence up-conversion is shown in Figure 2.1.[1-3] It is based on a commercially available titanium sapphire laser (Coherent Micra 10) which produces 18 fs laser pulses centred at 800 nm (tuneable from 780 nm – 830 nm) with a repetition rate of 80 MHz and output power of 1 W. In order to compensate for the highly chirped output of the Micra, a folded fused silica prism

arrangement was used to recompress the pulse after emergence from the oscillator cavity. The beam was then focused using spherical mirrors onto a β-barium borate (BBO) type I crystal (50 μm) to generate a 400 nm second harmonic 'pump' beam (up to 15 mW). The intensity of the pump pulse was controlled by an aperture placed in the beam path after the BBO crystal. The fundamental (gate) and pump beams were then separated by a dichroic mirror. The pump beam travelled a fixed distance to the sample cell (a 1 mm path length quartz flow cell) where it excited fluorescence. The 400 nm pulse was carefully recompressed by a pair of chirped mirrors (Femtolasers GSM012) in order to compensate for the pulse broadening effect of the sample cell windows.[4,5] The sample fluorescence, excited by the pump beam, was then collected with a reflective microscope objective and focused onto a BBO type I crystal (100 μm). The gate beam was directed to a delay stage, a pair of mirrors mounted on a motorised sub-micron resolution translation stage (Physik Instrumente M-515.22 with 0.1 μm resolution driven by LabView software), to introduce a controllable temporal delay of the gate pulse relative to the pump pulse with sub-fs accuracy. The gate beam was also carefully recompressed with a pair of chirped mirrors (Femtolasers GSM216) in order to compensate for the pulse broadening effects of transmission through the dichroic mirror and focusing lens. Finally, the gate beam was focused and crossed with the fluorescence beam in the BBO crystal.

At the correct crystal angle (where phase matching conditions are satisfied)[6], the gate pulse and fluorescence are combined (sum-frequency generation) to generate up-converted photons. This process occurs according to the following equation:

$$\frac{1}{\lambda_{SF}} = \frac{1}{\lambda_{gate}} + \frac{1}{\lambda_{fluor}} \qquad (2\text{-}1)$$

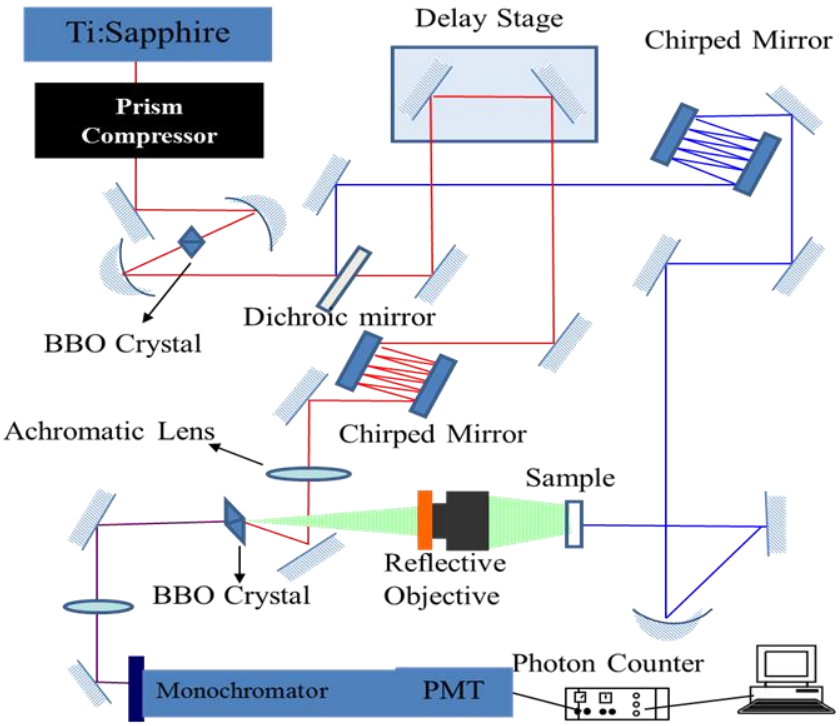

Figure 2.1 - *Femtosecond fluorescence upconversion experimental set-up.*

Where λ_{SF} represents the wavelength of the up-converted sum-frequency photons, λ_{gate} represents the wavelength of the gate photons (typically 800 nm) and λ_{fluor} represents the wavelength of the photons emitted by the sample. The sum frequency generation of the up-converted photons occurs from the instantaneous intensities of the gate and fluorescence in the crystal. The SFG samples the intensity of the fluorescence. The arrival time of the gate is then set by the delay line position. As a result, the fluorescence decay is mapped out with the time resolution of the experiment limited only by the width of the laser pulse. Thus, with proper recompression of the pulses to compensate for optical dispersion, very high experimental time resolution (sub 50 fs) is achievable. The width is mainly due to dispersion in the SFG crystal, which is kept as thin as possible. The intensity of the up-converted light was measured by a photomultiplier tube selected for low dark counts attached to a monochromator using a single photon counter (controlled by LabView software).

This allowed high sensitivity with minimal background thus resulting in a high signal to noise ratio (typically in the order of ~80:1 for the molecular motor system studied in this work). The emission wavelength at which the decay profile was measured was selected by the monochromator (as determined by the relationship between the wavelength of fluorescence and the wavelength of the corresponding up-converted photons). Each emission wavelength measured required tuning of the up-conversion BBO crystal angle in order to satisfy the phase matching conditions. To attenuate the strong scattering from the pump beam, a filter (Schott GG455) was placed after the objective (but before the up-conversion BBO crystal). In addition, a second filter (Schott UG11) was placed on the entrance slit of the monochromator to select the up-converted UV signal. The time resolution of the measurement is limited only by the cross-correlation width of the 400 nm and 800 nm pulses and was determined to be 45 fs by measuring the up-conversion of the instantaneous Raman scattering of pure heptane (Figure 2.2).

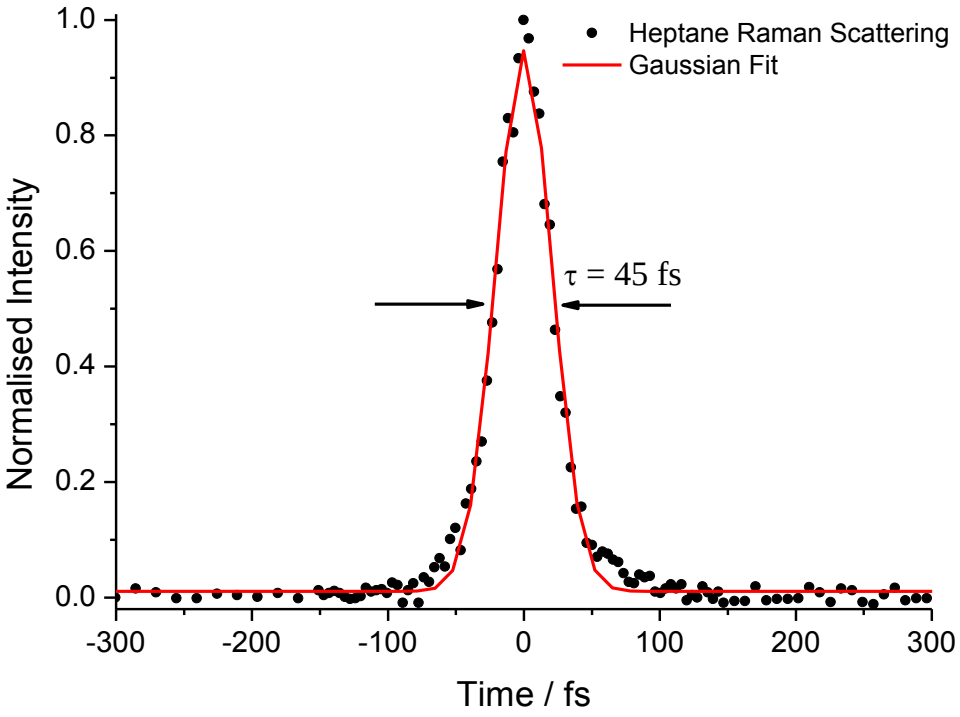

Figure 2.2 - *Cross correlation signal from Raman scattering of pure heptane at 475 nm fitted with a Gaussian function.*

2.2 Ultrafast Transient Absorption

The experimental set-up employed for ultrafast transient absorption measurements is shown in Figure 2.3. Pulses obtained from a commercial titanium sapphire laser (Clark MXR NJA-5) were amplified by a Clark-MXR ORC-1000 regenerative amplifier to provide 350 µJ pulses centred at 800 nm with a 1 kHz repetition rate. A beam-splitter (10/90 %) divided the amplified output. The 90% portion was focused into a BBO type I crystal (50 µm) to generate a 400 nm second harmonic pump beam. A bandpass filter (Schott BG40) was used to remove any remaining 800 nm light and the pump beam was directed to a delay stage (Physik Instrumente 505-4DG with 0.02 µm resolution controlled by LabView software) in order to introduce an adjustable temporal delay of the pump relative to the probe. The pump beam was then focused into the sample cell (a 1 mm path length quartz flow cell). The 10% portion of the amplified output was focussed into either a CaF_2 or sapphire window (2 mm thickness purchased from Crystran in each case) to generate a white light continuum probe (see Section 2.2.1). The CaF2 window was used for measurements in the 420 nm – 620 nm spectral region, where as the sapphire window allows access to a more red shifted spectral region (550 nm – 750 nm).

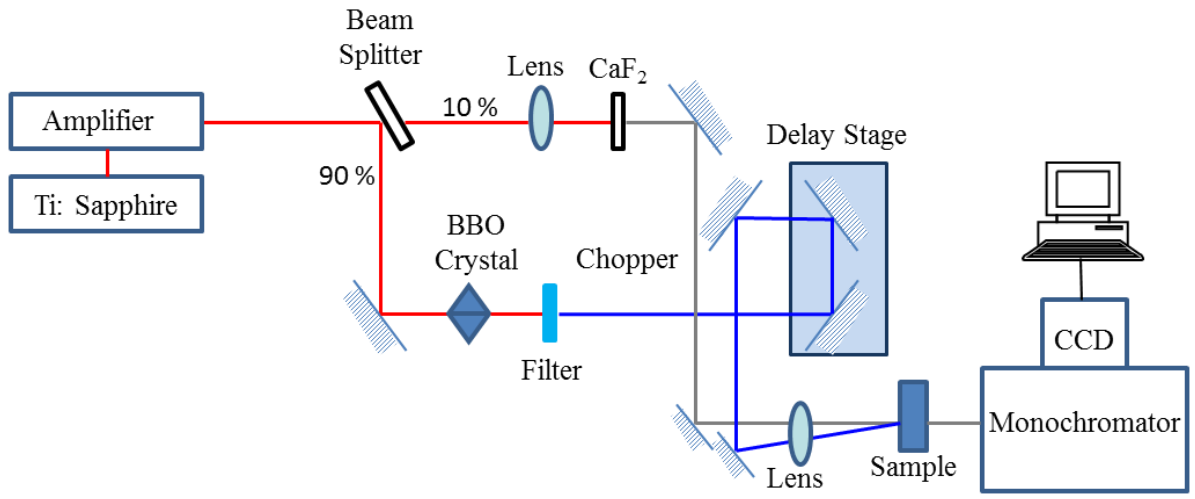

Figure 2.3 – *Femtosecond transient absorption experimental set-up.*

A half wave plate was inserted into the path of the beam used to generate the continuum in order to set the polarization of the probe at magic angle relative to the pump. This eliminates the contribution of solute rotational motion to the measured signal.[7] The continuum was then focused and spatially overlapped with the pump in the sample cell.

A chopper (Thor Labs MC1F10) was inserted in the path of the pump beam. The frequency of the chopper (500 Hz) was synchronised (Thor Labs MC2000) to exactly half the frequency of the amplified laser output (1 KHz) to allow the collection of probe only and pump-probe signals. The probe transmission was directed to a spectrometer (Jobin Yvon 270M) and the dispersed output detected by a CCD camera (Andor iXon DV885KCS-VP) chilled to -80 ^{o}C. The acquisition routine was written in LabView (see Section 2.2.2). A mechanical shutter was inserted into the beam path before the beam splitter and was synchronised to the CCD acquisition software in order to measure the background signal (in the absence of both the pump and probe achieved by closing the shutter) of the CCD for each time delay. The experimental time resolution was determined to be 300 fs by measuring the cross-correlation between the fundamental and second harmonic beams in an upconversion scheme.

2.2.1 White Light Continuum Generation

A key step in the experimental set-up for ultrafast transient absorption measurements is the generation of a white light continuum for use as a probe. Since the initial discovery of this phenomenon by Alfano and Shapiro,[8] a number of materials have been reported to generate a stable white light continuum when an intense laser pulse is focused into the material.[9,10] For example, water[12] and sapphire[11] have been used to generate white light. The continuum is generated in these materials primarily due to the nonlinear nature of the light-matter interaction where an intense laser pulse modifies the optical properties of the material and leads ultimately to self-phase modulation.[11,12] This results in a broadband output from the material in the visible region – a stable white light continuum is generated.

More recently, cubic fluoride crystals (CaF_2, LiF) have become popular materials for white light continuum generation. This is because the continuum generated by these materials covers the entire visible region and extends to around 350 nm, higher energy than can be obtained with other materials.[13,14] Such a wide wavelength range makes CaF_2 an ideal material to generate a broadband probe for transient absorption in the visible region.

However, continuous exposure to near-IR pulses results in accumulated optical damage to the surface of these CaF_2 (and sapphire) windows leading to unstable continuum generation. In order to prevent such damage, the crystal must be translated in a continuous manner. This introduces an extra complexity to the experimental set-up since the intensity of continuum generation depends significantly upon the focal point in the material.[11,13] Therefore, in order to maintain a stable continuum, the lateral translation must not result in the material moving out of the focus of the beam. To achieve this in the experimental set up employed here, the CaF_2 (and sapphire) window was mounted onto a motorised translation stage (Thor Labs Z825B Motorised Actuator). This stage was controlled by Thorlabs software (Thorlabs APT User) and programmed to translate 2 mm repetitively in each direction with 2 mm s^{-1} velocity. This resulted in almost no observable damage to the surface of the plate over weeks of measurements.

2.2.2 CCD Detection

Another key component of the transient absorption measurement was the recording, storage and reading out of spectral data by the CCD camera. Transient absorption spectra are generated by dividing the 'pump on' spectra by the 'pump off' spectra at a series of delay times (See Section 2.2.3). The highest signal/noise ratio is achieved when the change in absorption between the pump on and pump off condition is determined from adjacent pulses in the pulse train. This is because fluctuations in the intensity of the laser emission are smaller for adjacent pulses compared to summing several pump on then pump off pulses.

This is because short term stability is generally superior to long term stability in amplified lasers.[15] Usually, each individual spectrum is acquired, recorded and read out to the software before the acquisition of the next spectrum begins. However, this approach requires a CCD camera with an acquisition rate (frames per second (FPS)) which is higher than the repetition rate of the laser. The experimental set-up described in this work employed a CCD camera with a slower acquisition rate of 31 FPS, compared to the 1 kHz repetition rate of the laser. Thus, such an approach was impossible in our set-up. Instead, a "Fast Kinetics" acquisition mode of CCD operation was used in which all spectra were recorded in a single frame with the laser itself used to clock the acquisition process.

The CCD chip consisted of 1002 rows × 1004 columns of pixels. Instead of assigning the whole area of the chip to the measurement of a single pulse (as could occur with a fast readout chip), approximately 30 rows were used to image the stripe created by the dispersed white light probe beam on the CCD. The rows illuminated by the probe were termed the 'image area', and were confined to the very uppermost rows of the CCD chip. An example of the probe on the image area of the CCD chip, recorded with pure distilled water in the sample cell, can be seen in Figure 2.4. The remaining 970 rows were designated the 'storage area' and were kept completely dark. After the acquisition process was started, the next pulse from the amplifier triggered the CCD to measure the intensity of light on each pixel in the image area for the duration of the allotted exposure time (typically 300 microseconds). The same pulse also triggered the synchronisation of the chopper to the laser. The pump on/off condition of the first measured pulse was random and decided only by the position of the chopper when the synchronisation was initialised.

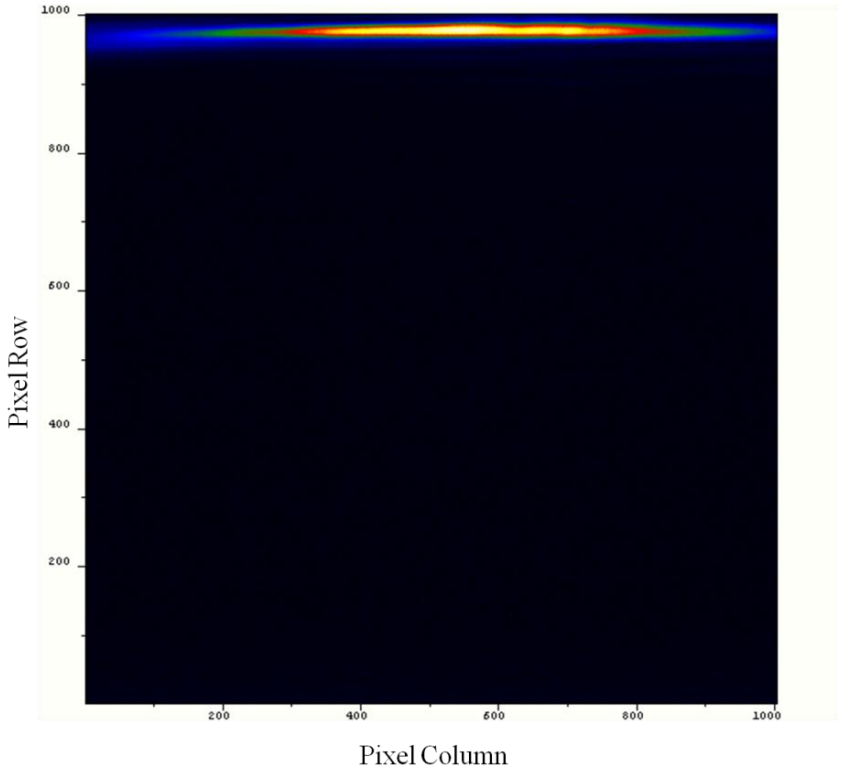

Figure 2.4 - *White light continuum probe on the 'image area' of the CCD chip.*

In order to determine the presence or absence of the pump for the first pulse measured, a photodiode was inserted into the path of the pump beam. This generated a voltage in the presence of the pump beam which was detected by an acquisition board (National Instruments Data Acquisition Board BNC 2110). The data acquisition software contained a voltage threshold, such that if this threshold was surpassed during the measurement of the first pulse, the software recorded that the pump was present. Conversely, if the voltage threshold was not reached, the software recorded that the first pulse was measured in the absence of the pump. Since the frequency of the chopper was synchronised to half the frequency of the laser, each subsequent pulse was measured alternately in pump on and pump off conditions. Thus, provided the pump on/off condition of the first pulse measured was known, the presence and absence of the pump for all subsequent pulses could be easily assigned.

After the 300 microsecond exposure time had elapsed, the data was shifted down from the image area into the first 30 rows of the storage area (in approximately 8 microseconds). This completed the acquisition of one 'shot' (the measurement sequence trigged by each pulse = one shot). The image area was then erased and the CCD remained idle until the acquisition of the next shot was triggered by the next pulse from the amplifier. The process was then repeated with each subsequent pulse measured in alternating pump on and off conditions. The data held in the storage area was repeatedly shifted down by 30 rows with the acquisition of each subsequent shot, until the capacity of the CCD chip was reached (approximately 60 shots). At this point, the CCD remained idle whilst the data was read out to the software (in approximately 60 milliseconds) and stored in matrix form (See Section 2.2.3). Upon completion of the read-out process, the storage area was wiped clean and the CCD acquisition process was resumed. Thus, the release of the next subsequent pulse from the amplifier served as a trigger to measure the first shot, and the entire process was repeated.

Each time domain data point consisted of the average of approximately 360 shots. Therefore, this entire process was repeated approximately 6 times for each time delay measured (6 x 60 shots). After completion of this sequence, the mechanical shutter was closed and a series of shots were acquired in order to measure the background signal on the CCD (in the absence of both the pump and probe beams). An identical procedure was followed to that described above, but in this case no laser light was able to reach the CCD. The resulting matrices were treated in the same manner to give a final average background spectrum for the given time delay point. This was subsequently subtracted from the final measured spectra as described in Section 2.2.3.

2.2.3 Data Readout

Once the capacity of the CCD storage area was reached, the data held had to be read out to the software in order to continue the measurement and to calculate the transient spectra. The

most suitable method to do so was by generation of a matrix, where each row represented a different shot and each column represented a different wavelength (determined by the calibration procedure described in Section 2.2.4). Since each time domain data point consisted of 360 individual shots and so required 6 complete read out procedures, this resulted in the formation of 6 separate matrices (each of 60 rows and 1004 columns) for each time delay measured. Alternating rows in each matrix represented pump on and pump off spectra measured by consecutive pulses in the pulse train. Each matrix was then decomposed into two separate matrices (each of 30 rows): a pump on matrix and a pump off matrix. The assignment of the pump on/off condition for the first shot (and so the first row) of each matrix, as determined by the photodiode (see Section 2.2.2), thus defined which rows form the decomposed pump on and pump off matrices. Now, identically numbered rows in each of the two separated matrices represented a pump on and pump off spectrum measured by adjacent pulses in the pulse train. The change in absorption (ΔOD) was then calculated at all wavelengths (each column) for each pair of rows by:

$$\Delta A = \log (I_0/I) \qquad (2\text{-}2)$$

Where I_0 is the intensity of the probe under pump off conditions and I is the intensity of the probe under pump on conditions. This process was repeated for each of the 6 matrices obtained from the CCD. This resulted in the formation of 6 time-intensity-ΔOD matrices (each of 30 rows). The average of these 6 matrices was then calculated to create a single matrix (of 30 rows). The overall average ΔOD of each column (each representing a particular wavelength) of this matrix was then calculated. Finally, the background spectrum (recorded with the shutter closed as described previously) was subtracted. This process was repeated for each time domain data point measured. The average spectrum at each time delay was then used to represent the change in absorption (ΔOD) in both the frequency (λ_i) and time domain (t_j) by construction of a time-intensity-ΔOD matrix [$(A_{ij}) = \Delta A(\lambda_i t_j)$].

2.2.4 CCD Calibration for Conversion of Pixel Column to Wavelength

After the white light continuum probe was directed to the spectrometer, the resulting spectrally dispersed light was focused onto the CCD chip. However, since the CCD chip is comprised of a grid of pixels, it was not possible to directly measure wavelength-resolved absorption spectra. To do so required a calibration procedure by which the CCD pixel column scale was converted to wavelength. The most suitable procedure to conduct such a calibration is by using a light source with well-defined emission lines. An Argon lamp was used in our set-up. When the light emitted from the lamp illuminated the CCD, characteristic emission lines were observed. Since the emission profile of an Argon lamp is well known,[16] it was possible to use two of these lines to accurately calculate the wavelength per pixel ratio of the CCD chip. Therefore, an accurate conversion of wavelength to pixel column was established. However, this also required the definition of the range of wavelengths illuminating the CCD for each measurement. Since a monochromator grating was used to disperse the white light continuum onto the CCD chip, calibration of this grating was also required in order to define the range of wavelengths which reached the CCD. A low dispersion grating was employed to ensure that the entire dispersed continuum was able to fit on the CCD chip. This calibration was performed using a monochromatic light source (a commercial laser pen with a centre wavelength of 532.4 nm). Since the CCD chip was known to consist of 1004 columns, it was possible to define the central wavelength of the CCD by adjusting the spectrometer grating such that the monochromatic light was centred exactly on the centre pixel column (column 502). An example of this can be seen in Figure 2.5. Thus, since the wavelength per pixel ratio was previously established, definition of the central pixel column defines the entire frequency range covered by the CCD. A central wavelength of 532.4 nm thus results in a measurement range of 420 nm to 620 nm. In order to extend the measured range further to the red, a sapphire window was used to generate the white light continuum (See Section 2.2.1).

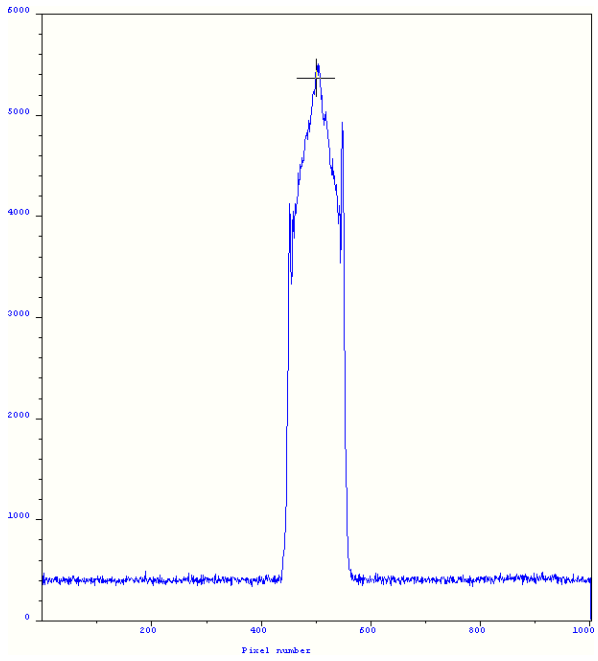

Figure 2.5- *Monochromatic laser pen emission (532.4 nm) on the central pixel row of the CCD chip*

In this case, the calibration procedure was then instead conducted using a laser pen with a central wavelength of 655 nm. Thus, by defining the central column of the CCD chip as 655 nm, the measurement range was shifted to approximately 550 nm to 750 nm.

The calibration of the CCD was checked routinely on a day to day basis by measuring the transient spectrum of flavin adenine dinucleotide (FAD) and comparing the maximum wavelengths of the ground state bleach, excited state absorption and stimulated emission transients to literature values (See Figure 2.14).

2.3 Data Analysis

2.3.1 Fluorescence Up-conversion

2.3.1.1 Fluorescence Decay Fitting

It is well documented that the time domain data obtained directly from time-resolved fluorescence up-conversion experiments do not provide an exact representation of the decay

dynamics.[17,18] Instead, the measured decays are convoluted with an instrument response function:[19]

$$I(t) = \int_0^t E(t-t')i(t')dt' \tag{2-3}$$

Where I(t) is the measured data, E(t) is the response from the sample and $i(t')$ is the instrument response function. Thus, in order to extract the true decay dynamics, the data must be subjected to a deconvolution procedure. This requires each measured decay curve $I(t)$ to be fitted to a mathematical decay function $F(t)$, convoluted with the instrument response function i(t'), where the accuracy of the fit determines the success of the $F(t)$.

In this work, the instrument response function was the cross-correlation of the pump and gate pulses at the sample. This was determined experimentally from measurements of the up-converted Raman scattering from heptane (see Figure 2.2), since Raman scattering is instantaneous and has the same spatial distribution as the fluorescence. Therefore, by fitting the measured data with a decay function convoluted with the measured instrument response function, it is possible to extract the true decay dynamics of the sample. In order to ensure the best possible fit to the experimental data, an evolutionary algorithm was used and residuals between the fitted function and the experimental data were generated.[20,21] An example of a measured fluorescence decay for HBDI (the synthetic chromophore of the green fluorescent protein) in ethanol (black circles), cross-correlation instrument response function (blue dashes) and convoluted decay function (red line) can be seen in Figure 2.6. In this case, a bi-exponential decay function was adequate to provide a good fit to the experimental data:

$$F(t) = \sum_{n=1}^{2} A_n e^{-t/\tau_n} \tag{2-4}$$

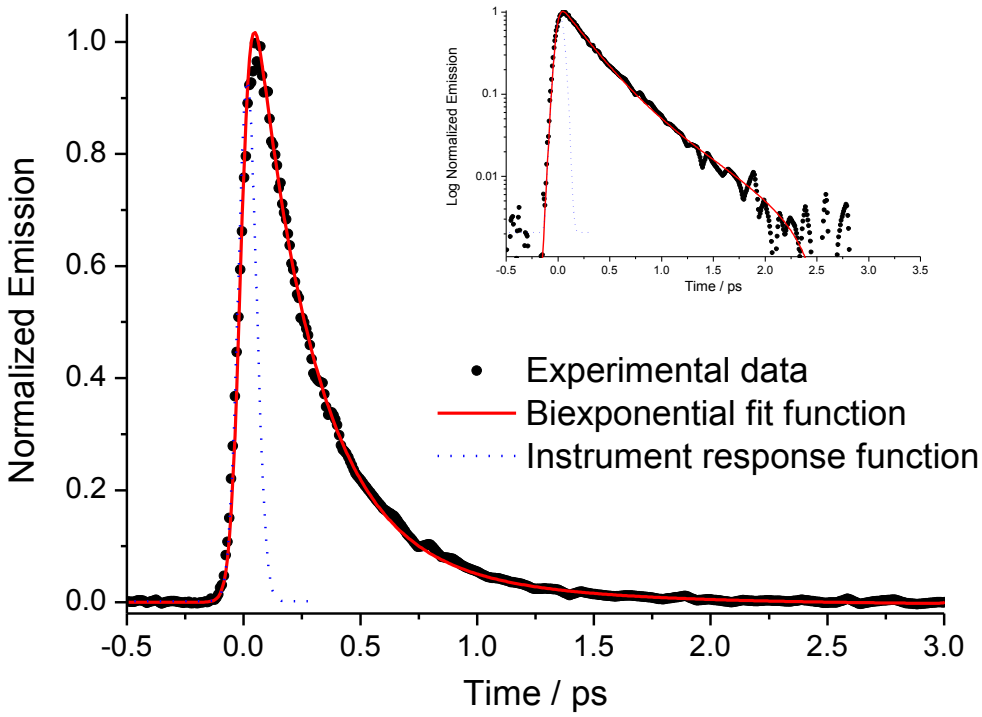

Figure 2.6 - *The fluorescence up-conversion decay profile of HBDI in ethanol (emission measured at 480 nm) fitted with a bi-exponential function. Inset shows the data on a log intensity scale.*

Where A_n is amplitude and τ_n is the time constant of the exponential decay. A detailed discussion of the fluorescence decay dynamics of HBDI and its derivatives can be found in Chapter 7. However, fluorescence decay dynamics which exhibit more complicated profiles may require a more complex function to provide an adequate fit. In the case of the molecular motor molecules discussed in this work (see Chapter 3, Chapter 4 and Chapter 5), simple exponential decay functions did not provide an adequate fit. Instead, it was found that for these data, a function comprising a sum of exponential components and one or more damped harmonic oscillators was required to achieve a good fit to the data:

$$F(t) = \sum_{n=1}^{2} A_n e^{-t/\tau_n} + A_{\omega n} \sin\left(\omega_n t + \phi_n\right) e^{-t/\tau_{Dn}} \qquad (2\text{-}5)$$

where A_n and $A_{\omega n}$ are the amplitudes of the exponential and oscillatory components respectively, τ_n is the time constant of the exponential decay, ω_n is the frequency, ϕ_n is the phase and τ_{Dn} is the damping constant of the oscillation. Figure 2.7a shows the fit quality of this function. A comparison of the residuals of several functions allowed an evaluation of the fit quality and determination of which function provided the best fit to the data. The residuals resulting from fitting the decay profile of molecular motor 1-H (Chapter 3, Figure 3.1) measured in dichloromethane at 556 nm with a bi-exponential only function (green), a bi-exponential combined with a single damped frequency oscillator (blue) and a bi-exponential combined with a two damped oscillator functions (red) are shown in Figure 2.7b. Clearly the best fit is achieved, with a near random residual, by the sum of a bi-exponential and two damped oscillator functions (red). The overall fit and the individual components which comprise the fitted function can be seen in Figure 2.8.

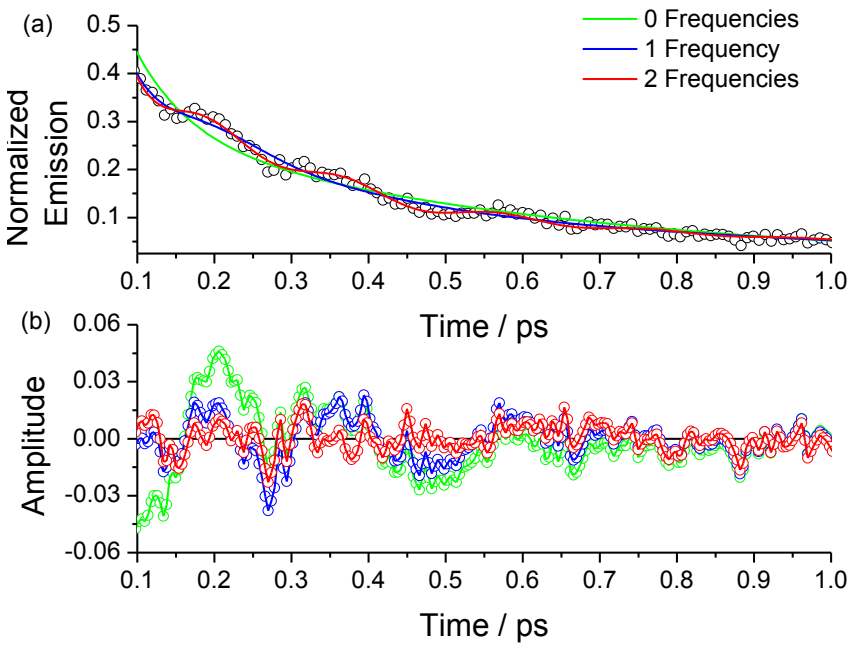

Figure 2.7 – *Time resolved fluorescence of molecular motor 1-H in DCM at 556 nm. Fit quality (a) and residuals (b) of experimental data (black) fitted to a bi-exponential function (green), a bi-exponential and a single damped harmonic oscillator function (blue) and a bi-exponential combined with two damped harmonic oscillator functions (red).*

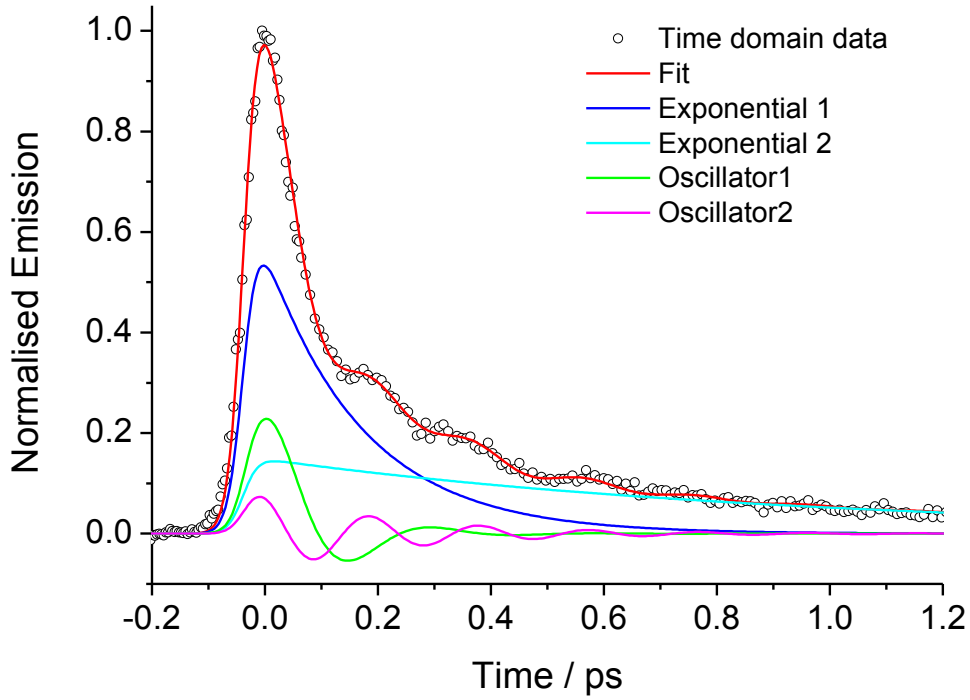

Figure 2.8 - *The individual components of the fit to the time domain data of molecular motor 1-H in DCM (emission measured at 556 nm). The overall fitting function (red line) is comprised of the sum of two exponential decay terms and two damped harmonic oscillator functions.*

2.3.1.2 Error Analysis

The experimental error of the fitting procedure was assessed by considering the fit of both repeated experiments and repeated fits to the same measurement. This analysis was performed for a selection of datasets presented in this work. An example of a repeated experiment is shown in Figure 2.9 for 1-H in DCM measured at an emission wavelength of 535 nm. These measurements were recorded 6 months apart and thus attest to the high reproducibility of the fluorescence up-conversion measurements. Each decay curve was fitted to a relatively complex function comprising the sum of two exponential terms and two damped harmonic oscillators. The standard deviation of each parameter of the fitted function between the repeated measurements was then calculated. This analysis was performed on a number of repeated experiments presented in this work. It was found that the error in the

exponential terms of the fitted functions (both the time constant τ and the amplitude A) were never larger than 10%. In contrast, the damped harmonic oscillator terms (the damping time τ_D, the frequency ω, the amplitude A_ω and the phase φ) exhibited an error which was larger but always less than 20%. The errors from repeated fits to the same measurements with different starting parameters were also collected. These errors were actually found to be slightly larger, with the exponential terms exhibiting an error always less than 15% and the damped harmonic oscillator terms less than 25%. Thus, the errors associated with repeated measurements fall within the error of the fitting procedure.

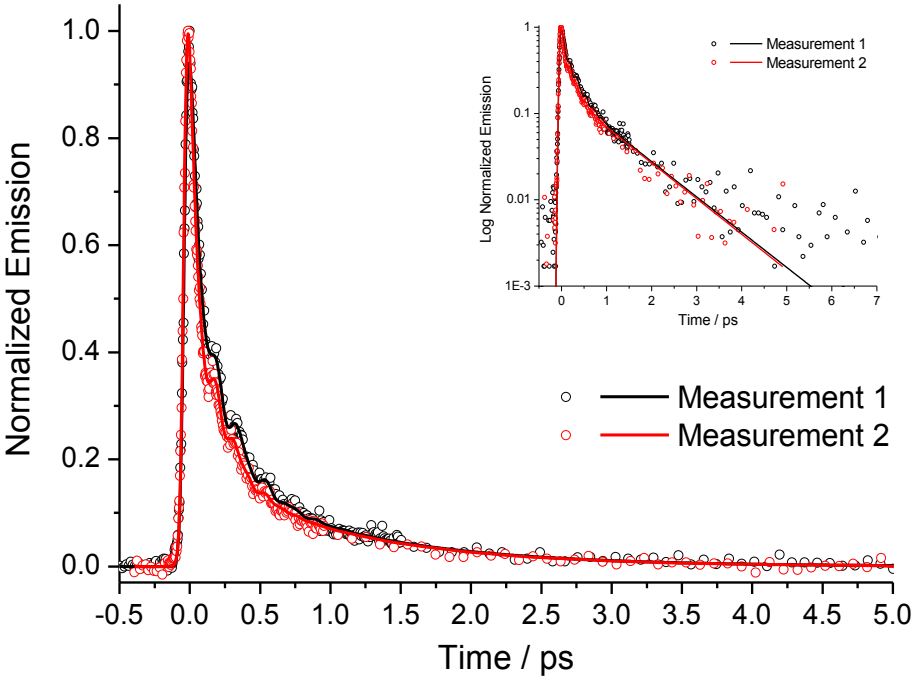

Figure 2.9 - *A comparison of repeated fluorescence up-conversion measurements of 1-H in DCM measured at 535 nm. The data are normalised at t = 0 ps. The raw data (points) were fitted to a function (lines) comprising the sum of two exponential decay terms and two damped harmonic oscillators. Each decay curve was recorded 6 months apart, thus attesting for the high reproducibility of the fluorescence up-conversion measurement. The exponential components were found to exhibit an error of less than 10%, compared to 20% for the oscillator components.*

This is a somewhat surprising conclusion which shows that the largest source of error in the measured data arises from the fitting procedure itself. One possible explanation for this observation is correlation between the pre-exponent (A_n in equation 2-5) and the time constant (τ_n in equation 2-5) of the exponential functions. Since these parameters are closely linked, it may be possible to obtain an adequate fit to the raw data with a combination of quite significantly different parameters. In such a case, the error of the average fluorescence lifetime (calculated from repeat fits to the same measurement) would be expected to be smaller than that of the individual components of the fitted function. This was found to be true for the data presented in this work. Therefore, it can be suggested that the origin of the fitting procedure error is the correlation between the individual parameters of the fitted functions. However, for the molecular motor samples studied in this work, the average fluorescence lifetime was determined to be a poor representation of the fluorescence decay dynamics (See Chapter 3) and so is excluded from the presented data.

Therefore, all fluorescence up-conversion data presented in this work are subject to the error bars as determined from repeated fits. Thus, the exponential components of the fitted functions are subject to an error of 15% whilst the damped harmonic oscillator terms are subject to an error of 25%.

2.3.1.3 Time Dependent Fluorescence Spectra

Fluorescence decay curves measured at individual emission wavelengths do not provide a full representation of the excited state decay dynamics. A more complete characterisation is given by the time dependence of the entire emission spectrum. By measuring the fluorescence decay profile at a series of emission wavelengths spanning the steady state emission spectrum, it is possible to reconstruct the time-dependent fluorescence spectra.[18] The integrated area of the deconvoluted fits to the experimental time domain data [$F(\lambda, t)$] were normalised to the amplitude of the corresponding wavelength in the steady state fluorescence

spectrum [$S_0(\lambda)$] to reconstruct the fluorescence spectrum at a given time after excitation [$S(\lambda,t)$] as follows:

$$S(\lambda,t) = \frac{F(\lambda,t)S_0(\lambda)}{\int_0^\infty F(\lambda,t)dt} \tag{2-6}$$

Although fluorescence spectra are usually recorded as a function of wavelength (λ / nm), a quantitative analysis requires conversion to an energy scale ($\tilde{\nu}$/ cm^{-1}).[21] The wavelength scale (nm) can be transformed to the wavenumber scale (cm^{-1}) *via* the following simple relationship:

$$\tilde{\nu} = \frac{10^7}{\lambda} \tag{2-7}$$

However, spectra recorded with constant wavelength resolution are non-linear as a function of wavenumber and so require an additional correction factor.[7] If the fluorescence spectrum as a function of wavelength is given by [17]:

$$I(\lambda) = \frac{dI}{d\lambda} \tag{2-8}$$

Then this can be expressed in terms of wavenumber by:

$$I(\tilde{\nu}) = \frac{dI}{d\tilde{\nu}} \tag{2-9}$$

The relation between $I(\lambda)$ and $I(\bar{\nu})$ can then be shown to be:

$$I(\tilde{\nu}) = \frac{dI}{d\lambda}\frac{d\lambda}{d\tilde{\nu}} \tag{2-10}$$

Since, from equation 2-7:

$$\frac{d\lambda}{d\tilde{\nu}} = \frac{10^7}{\tilde{\nu}^2} \tag{2-11}$$

Then equation 2-10 now becomes:

$$I(\tilde{\nu}) = \frac{10^7}{\tilde{\nu}^2} I(\lambda) \tag{2-12}$$

Thus, in order to convert the reconstructed time-dependent spectra from wavelength to wavenumber, a correction factor of $\tilde{\nu}^{-2}$ was applied.[20] Each spectrum then represents the fluorescence emission spectrum at a different time after excitation. However, since the reconstructed emission spectra comprised a discrete number of data points in the frequency domain (governed by the number of emission wavelengths at which the fluorescence decay curves were measured), each spectrum obtained was interpolated by fitting with a log-normal function[20]:

$$F(\tilde{\nu}) = h\left(\exp\left[-\ln(2)\{\ln(1+\alpha)/\gamma\}^2\right]\right) \quad \alpha > -1 \tag{2-13}$$

Where $\alpha \equiv 2\gamma(\tilde{\nu}\text{-}\tilde{\nu}_p)/\Gamma$. Thus, the spectrum at each time point can be described as a function of four parameters of the log-normal fit – the peak height (h), the peak frequency ($\tilde{\nu}_p$), the asymmetry (γ) and the width (Γ). However, the peak frequency is sensitive to evolution of the spectral shape and so a more suitable (and less shape sensitive) representation is found by calculating the first moment of the spectrum ($\tilde{\nu}_{FM}$):

$$\tilde{\nu}_{FM} = \frac{\int \tilde{\nu} I(\tilde{\nu}) d\nu}{\int I(\tilde{\nu}) d\nu} \tag{2-14}$$

Thus, if the log-normal function provides an adequate reflection of the shape of the reconstructed fluorescence spectrum, then the temporal evolution of these parameters provide a complete description of the time-dependence of the fluorescence emission spectrum. Indeed, the log-normal function provides an excellent fit to the experimental time-resolved spectra of the molecular motor samples created by this procedure. An example of the reconstructed time dependent fluorescence spectra of motor 1-H in dichloromethane, and the log-normal fits to the experimental data can be seen in Figure 2.10. This provides a complete representation of the fluorescence decay dynamics and can be used to generate a 3-dimensional fluorescence surface, where the fluorescence intensity as a function of both time and frequency can be viewed simultaneously. An example of such a surface, for motor 1-H in DCM, is shown in Figure 2.11. A more useful representation is in the form of a 2-dimensional contour plot in which the 3D surface is viewed along the intensity axis (Figure 2.12).

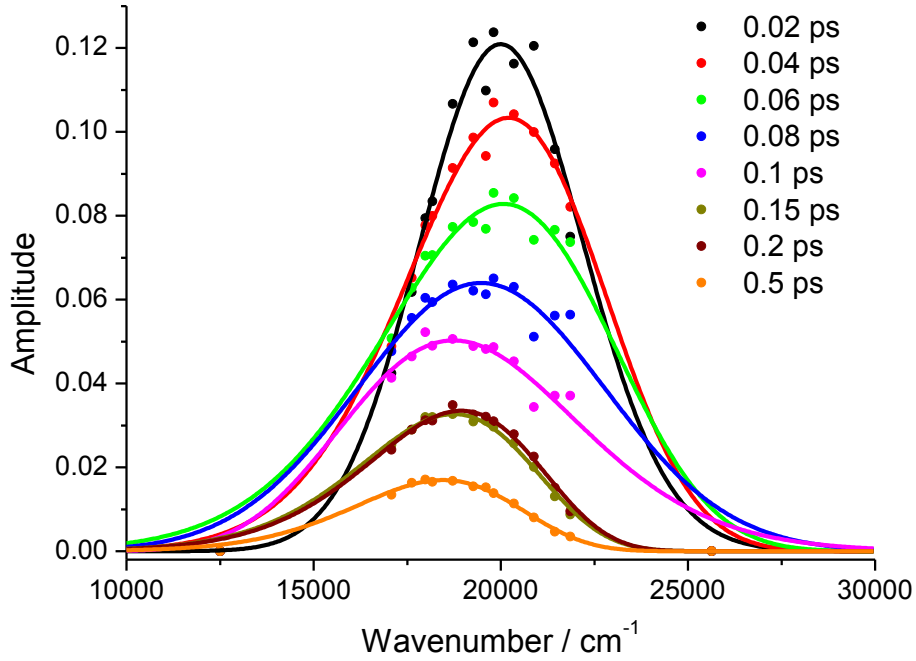

Figure 2.10 - *The reconstructed time-dependent emission spectra of molecular motor 1-H in dichloromethane. The experimental data (dots) is fit by a log-normal function (lines)*

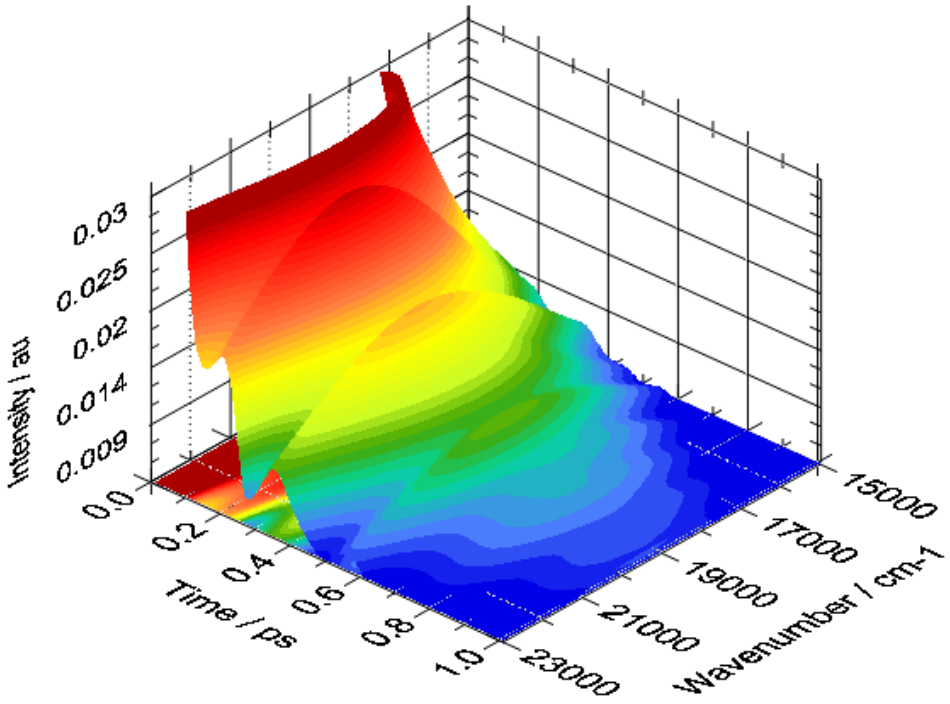

Figure 2.11 - *3-dimensional representation of the fluorescence decay dynamics of molecular motor 1-H in dichloromethane.*

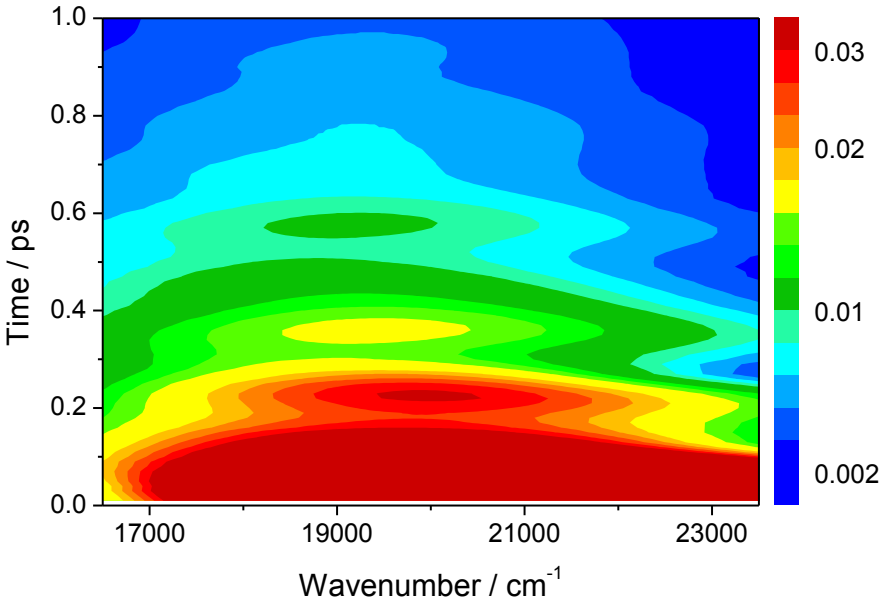

Figure 2.12 - *Contour plot representation of the 3-dimensional fluorescence surface of molecular motor 1-H in dichloromethane. This depicts the 3D surface viewed down the intensity axis.*

The time-dependent fluorescence emission spectra can then be accessed by taking slices through the surface at chosen time intervals whilst the time domain data can be accessed by taking slices through the surface at specific frequencies. Thus, creation of a 3D surface allows the complete temporal evolution of the decay dynamics to be mapped. The frequency domain data used to create the 3D surfaces is the log-normal fit to the time-resolved fluorescence spectra, reconstructed from the deconvoluted time-domain data. However, the raw time domain data, not subjected to the deconvolution procedure, can also be used to create time-resolved fluorescence spectra in the same manner.

Additionally, these spectra can be used directly to create a 3D surface, without being fitted to a log-normal function. In order to ensure that no artefacts were introduced to the data by the deconvolution and spectral fitting procedures, each 3D surface created from the deconvoluted data in this work was compared directly to a 3D surface generated from the raw time domain data. This comparison for motor 1-H in DCM is shown in Figure 2.13a (raw) and Figure 2.13b (deconvoluted data). This comparison shows that the features observed in the fitted data are also present in the raw data. This was observed for all 3D surfaces constructed in this work. Only the surfaces constructed from the deconvoluted and log-normal fitted data will be used for further analysis, as distortions due to convolution are removed for these surfaces.

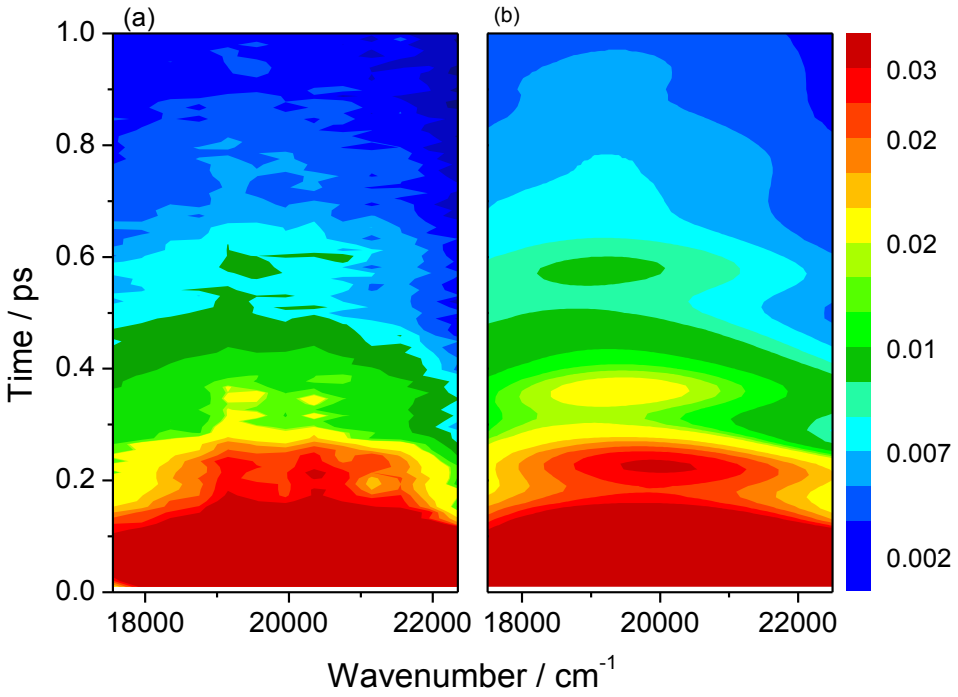

Figure 2.13 - *A comparison of the 3-dimensional fluorescence surface of molecular motor 1-H in dichloromethane created from (a) raw experimental time-domain data (with no deconvolution) and (b) log-normal fits to the deconvoluted time-domain data.*

2.3.2 Transient Absorption

Transient absorption spectroscopy is a useful tool for studying excited state dynamics. It complements ultrafast fluorescence, which provides unambiguous data on the initially excited and fluorescence states, because it provides access to the dynamics of dark states and the ground state recovery. Often, the electronically excited state of a molecule absorbs light at wavelengths where no absorption occurs in the ground state. This is characterized by positive amplitude in the transient absorption spectra (an excited state absorption band). In addition, since electronic excitation of a molecule also results in a reduction in the ground state population, this is characterized by a negative amplitude signal (ground state bleach). In some cases, the interaction between the probe and the excited electronic state leads to stimulated emission (gain) which also appears as a bleach. Thus, by time-resolving the relaxation of these transient features, it is possible to assess the complete dynamics following electronic

excitation. A particularly useful insight can be gained by comparing the timescales of excited state relaxation and ground state recovery. For example, a system in which the excited state absorption transient decays on a faster timescale than the recovery of the ground state suggests that an intermediate state is formed. Comparison of the relaxation dynamics associated with stimulated emission with the time resolved fluorescence data can also provide a useful insight into the excited state dynamics of a molecular system. Figure 2.14 shows an example of a typical transient absorption spectrum for Flavin adenine dinucleotide (FAD) *in* water, recorded at a series of time delays. The transient absorption of FAD is well known,[22,23] and so it was used as a routine reference measurement for the calibration of the CCD and spectrometer monochromator (see Section 2.2.4) in our laboratory.

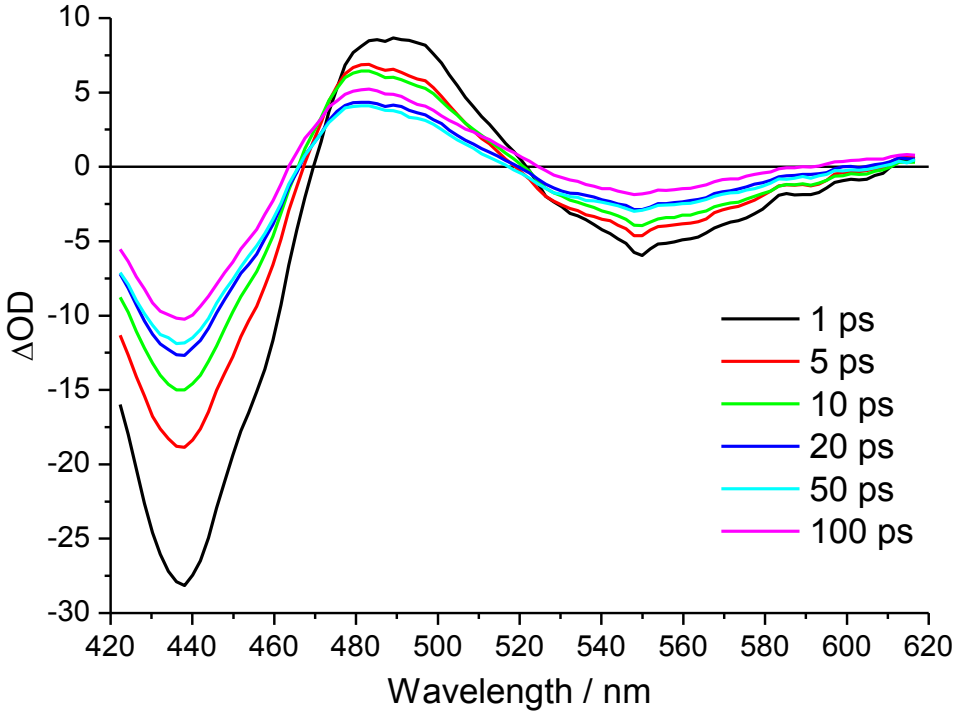

Figure 2.14 - *The time-dependent transient spectra of Flavin Adenine Dinucleotide (FAD) in water.*

Figure 2.14 reveals the ground state bleach (~440 nm), excited state absorption (~490 nm) and stimulated emission (~550 nm) of FAD in water. Thus, by assessing the time domain decay of each transient feature, it is possible to gain a detailed insight into the excited state dynamics of a molecular system of interest. Such an approach will be used in this work.

2.3.2.1 Coherent Artefact

One significant drawback to the ultrafast transient absorption is the generation of unwanted signals around zero delay time due to the overlap of the pump and probe pulses in the sample.[24,25] These signals, frequently referred to as a 'coherent artefact' or 'coherence spike', are detected in addition to the response of the molecular system and serve to obscure the dynamics observed at early delay times. The origin of the coherent artefact has been a matter of debate with a number of factors believed to contribute to the signal.[26-29] Pump-probe spectroscopy employs a high intensity pump pulse which is intended to induce changes in the sample (electronic excitation in the case of transient absorption spectroscopy). In contrast, the probe pulse is of sufficiently low intensity so as not to induce any changes in the sample, and is designed to monitor the evolution of the pump induced change. However, the high intensity of the pump pulse also induces changes in the optical response of the solvent through the non-linearity of the solvent refractive index.[24] Since the technique requires the pump and probe to be spatially overlapped in the sample around zero time delay, the probe pulse is then subjected to the non-linear refractive index induced by the pump. To add further problems, the coherent artefact is frequency dependent, so appears at different times for different frequencies within the probe pulse. However, this induced change in refractive index relaxes rapidly (typically < 1 ps) and so at longer delay times, the probe experiences the normal refractive index of the solvent. Therefore, around zero delay time, the probe is subjected to cross-phase modulation which is the major contributor to the generation of the coherent artefact.[24]

The coherent artefact has proven difficult to remove when measuring ultrafast time-resolved transient absorption spectra.[30] It has been shown that the coherent artefact can be significantly reduced by manipulating the polarization and incident angles of the pump and probe pulses in some more complex experimental set-ups.[31] The simpler solution we adopt involves careful removal of the spectra in which the coherent artefact is present from the dataset prior to analysis, although this limits the time resolution to times longer than the laser pulses. An example of the temporal evolution of the coherent artefact, measured for molecular motor 1-H in dichloromethane, can be seen in Figure 2.15.

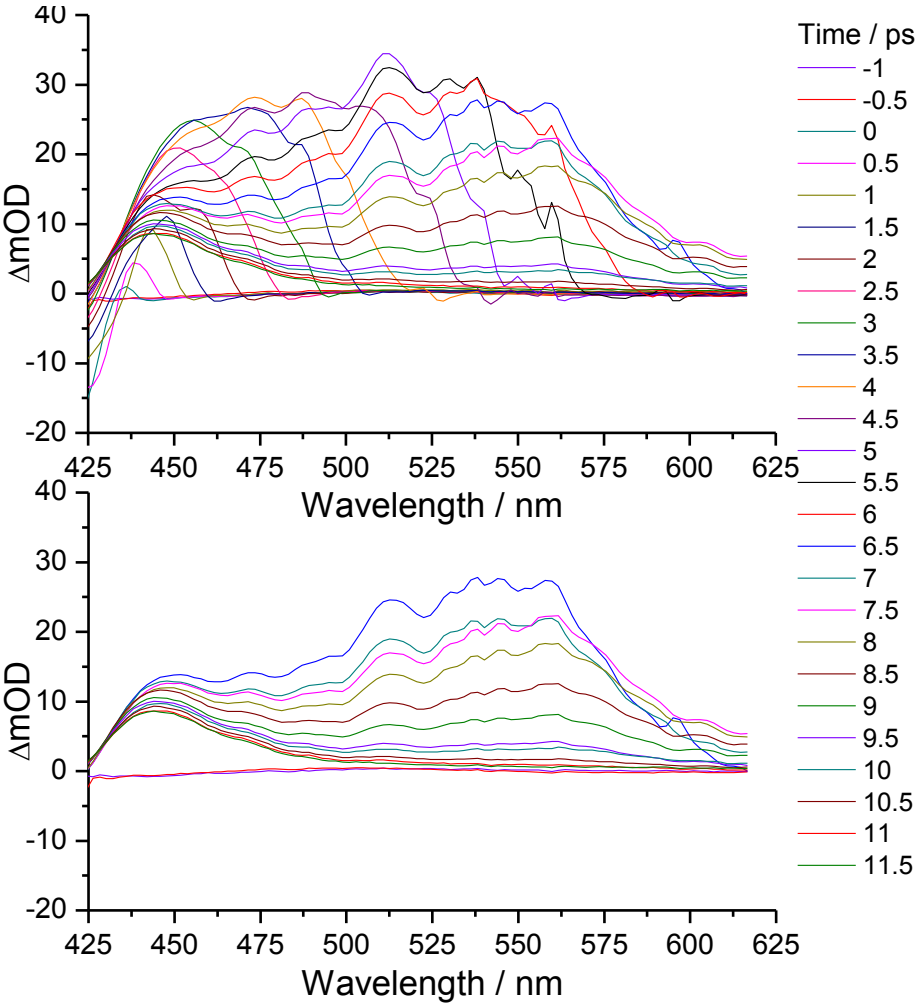

Figure 2.15 – *Transient absorption spectra of 1-H in DCM (a) before and (b) after subtraction of the coherent artefact.*

In order to analyse the time-domain dynamics at a particular wavelength, all spectra in which the coherent artefact was present at this wavelength were removed. All transient absorption data presented in this work were subjected to the subtraction of the coherent artefact in this manner.

2.3.2.2 Fitting of Time Domain Data

From the frequency domain transient absorption spectra recorded in this experiment, the time-domain relaxation of the transient absorption signal can be accessed by slicing along the time axis at any chosen wavelength. Fitting the time-domain spectra to a sum of exponentials yields more information regarding the relaxation dynamics of the transient absorption signal. Therefore, the time-domain transient absorption spectra presented in this work were subjected to the same fitting procedure described for the treatment of fluorescence decay curves (see Chapter 2.3.1.1). However, in the case of the transient absorption data the instrument response function used for deconvolution was defined as 300 fs (the time resolution of the measurement as determined experimentally from auto correlation measurements). Figure 2.16 shows an example of the frequency domain data (Figure 2.16a) for molecular motor 1-H in dichloromethane, sliced at 560 nm (indicated by arrow) and fitted with a bi-exponential function (Figure 2.16b).

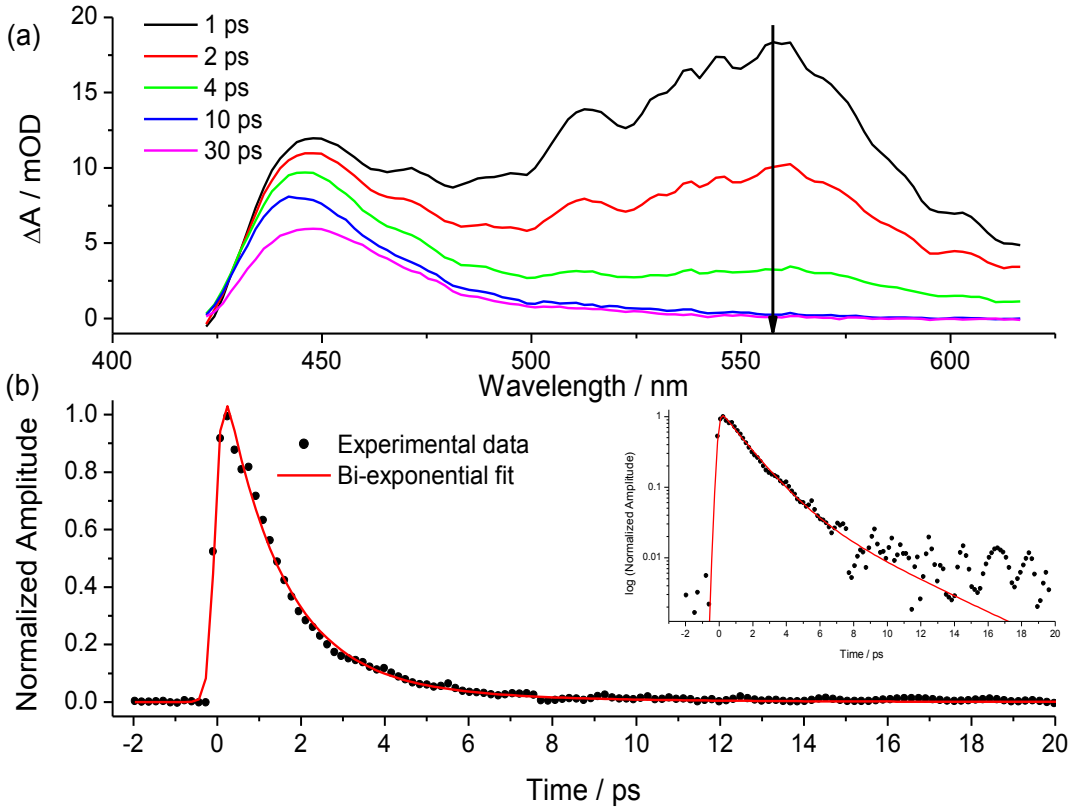

Figure 2.16 - *(a) Time-resolved transient absorption spectra of molecular motor 1-H in dichloromethane and (b) Time-domain relaxation of the transient absorption signal at 560 nm fitted with a biexponential function (log intensity scale is shown as inset).*

2.3.2.3 Error Analysis

As described previously for the treatment of the time-resolved fluorescence data (Section 2.3.1.2), an error analysis of the fitting procedure was conducted by considering the error associated with both repeat measurements and repeated fits to the same measurement. This was performed for a selection of transient absorption datasets throughout the work presented here. An example of transient decay curves obtained from repeat measurements of 1-H in Octanol measured at 560 nm, is shown in Figure 2.17. Clearly, the repeated measurements show good agreement. The raw data (points) was fitted to a bi-exponential function (lines) in each case. The error of each parameter was thus determined by calculating the standard deviation of each parameter of the fitted function between measurements. In every case, it

was found that each parameter exhibited an error no larger than 10% between repeated measurements. Each decay curve was also subjected to repeated fits in order to assess the error associated with the fitting procedure. In this case it was found that each parameter typically exhibited an error of less than 5%. Therefore, in the case of the transient absorption data (and in contrast to the fluorescence up-conversion data), the most significant source of error is the measurement. However, since the decay profiles of the transient absorption data are far less complex (no oscillation terms), it is not surprising that the fitting of the transient absorption time domain data is subject to a lesser degree of error. Thus, the parameters of the exponential functions fitted to each transient absorption decay curve in this work are subject to an error of 10%.

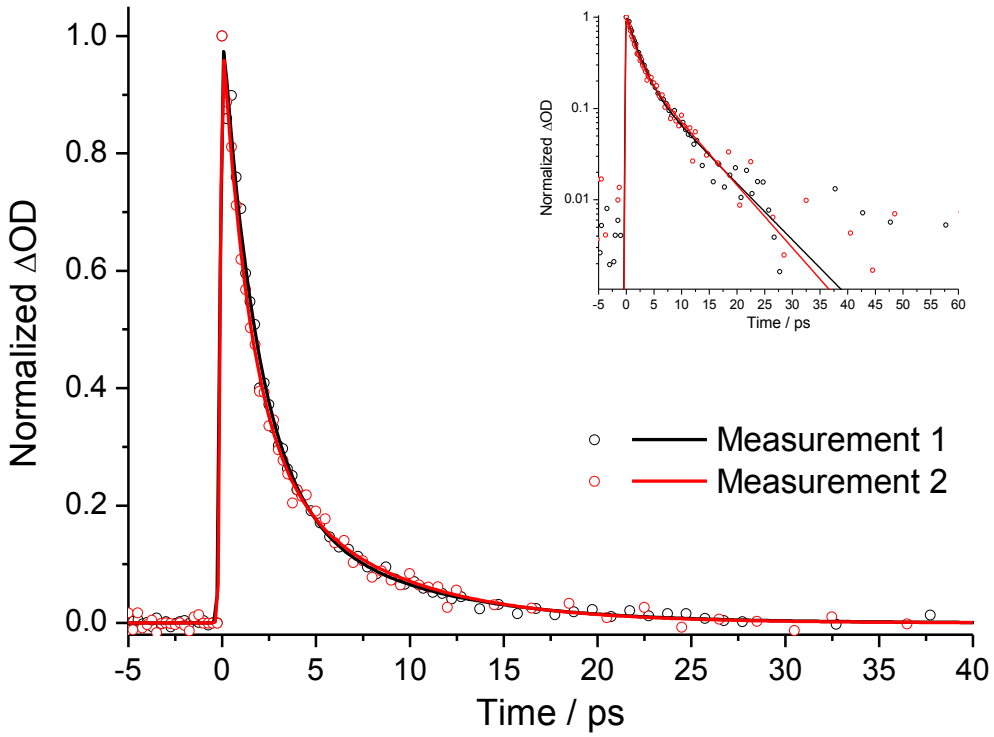

Figure 2.17 - *A comparison of transient decay curves measured for 1-H in octanol at 560 nm obtained by repeated measurements. The raw data (points) were fitted to a bi-exponential function (lines). Inset shows the data on a log intensity scale. Each parameter was found to exhibit an error of less than 10% between measurements.*

2.4 Sample Preparation

2.4.1 Molecular Motors

The synthesis of the molecular motor samples (See Chapter 4, Figure 4.1 and Chapter 5 Figure 5.1 for molecular structures) and 9,9'-Bifluorenylidene (See Chapter 6, Figure 6.1 for molecular structure) was conducted by the group of Prof. Ben Feringa (Stratingh Institute for Chemistry, University of Groningen, The Netherlands) and has been described in detail in a number of publications.[32-35] The samples were used as received and no further purification was required.

2.4.2 HBDI Derivatives

The synthesis of the HBDI derivative samples (See Chapter 7, Figure 7.3) for molecular structures) was conducted by the group of Prof. Laren Tolbert/Dr. Kyril Solntsev (School of Chemistry and Biochemistry, Georgia Institute of Technology, United States) according to the previously published procedure.[36] The samples were used as received and no further purification was required.

2.5 References

(1) Heisler, I. A.; Kondo, M.; Meech, S. R. *J. Phys. Chem. B.* **2009**, *113*, 1623.

(2) Shah, J. *IEEE J. Quantum Electron.* **1988**, *24*, 276.

(3) Rhee, H.; Joo, T. *Opt. Lett.* **2005**, *30*, 96.

(4) Szipocs, R.; Ferencz, K.; Spielmann, C.; Krausz, F. *Opt. Lett.* **1994**, *19*, 201.

(5) Szipocs, R.; KohaziKis, A. *Appl.Phys. B* **1997**, *65*, 115.

(6) Boyd, R. W. *Non Linear Optics (Third Edition)*.

(7) Lakowicz, J. R. *Principles of Fluorescence Spectroscopy*.

(8) Alfano, R. R.; Shapiro, S. L. *Phys. Rev. Lett.* **1970**, *24*, 584.

(9) Kovalenko, S. A.; Dobryakov, A. L.; Ruthmann, J.; Ernsting, N. P. *Phys. Rev. A.* **1999**, *59*, 2369.

(10) Berera, R.; van Grondelle, R.; Kennis, J. T. M. *Photosynth.. Res.* **2009**, *101*, 105.

(11) Kartazaev, V.; Alfano, R. R. *Opt. Commun.* **2008**, *281*, 463.

(12) De Boni, L.; Toro, C.; Hernandez, F. E. *Opt. Express* **2008**, *16*, 957.

(13) Johnson, P. J. M.; Prokhorenko, V. I.; Miller, R. J. D. *Opt. Express* **2009**, *17*, 21488.

(14) Huber, R.; Satzger, H.; Zinth, W.; Wachtveitl, J. *Opt.Commu.n* **2001**, *194*, 443.

(15) Polli, D.; Lueer, L.; Cerullo, G. *Rev. Sci. Instrum.* **2007**, *78*.

(16) *National Institute of Standards and Technology, http://physics.nist.gov/PhysRefData/Handbook/Tables/argontable2.htm*.

(17) Schanz, v. H. R., Femtosecond Broadband Fluorescence Upconversion, 2002.

(18) Smith, N. A.; Meech, S. R.; Rubtsov, I. V.; Yoshihara, K. *Chem. Phys. Lett.* **1999**, *303*, 209.

(19) *Least Squares Methods of Analysis - Convolution and Data Optimization*; B.K. Selinger, C. M. H. a. A. J. K., Ed.; Plenum: New York, 1983.

(20) Horng, M. L.; Gardecki, J. A.; Papazyan, A.; Maroncelli, M. *J. Phys. Chem.* **1995**, *99*, 17311.

(21) Maroncelli, M.; Fleming, G. R. *J. Chem. Phys.* **1987**, *86*, 6221.

(22) Brazard, J.; Usman, A.; Lacombat, F.; Ley, C.; Martin, M. M.; Plaza, P. *J. Phys. Chem. A.* **2011**, *115*, 3251.

(23) Zhao, R.-K.; Lukacs, A.; Haigney, A.; Brust, R.; Greetham, G. M.; Towrie, M.; Tonge, P. J.; Meech, S. R. *Phys. Chem. Chem. Phys.* **2011**, *13*, 17642.

(24) Dietzek, B.; Pascher, T.; Sundstrom, V.; Yartsev, A. *Laser. Phys. Lett.* **2007**, *4*, 38.

(25) Wang, C. R.; Luo, T.; Lu, Q. B. *Phys. Chem. Chem. Phys.* **2008**, *10*, 4463.

(26) Kovalenko, S. A.; Ernsting, N. P.; Ruthmann, J. *Chem. Phys. Lett.* **1996**, *258*, 445.

(27) Rasmusson, M.; Tarnovsky, A. N.; Akesson, E.; Sundstrom, V. *Chem. Phys. Lett.* **2001**, *335*, 201.

(28) Lian, T. Q.; Kholodenko, Y.; Locke, B.; Hochstrasser, R. M. *J. Phys. Chem.* **1995**, *99*, 7272.

(29) Lebedev, M. V.; Misochko, O. V.; Dekorsy, T.; Georgiev, N. *J. Exp. Theor. Phys* **2005**, *100*, 272.

(30) Ratner, J.; Steinmeyer, G.; Wong, T. C.; Bartels, R.; Trebino, R. *Opt. Lett.* **2012**, *37*, 2874.

(31) Luo, C. W.; Wang, Y. T.; Chen, F. W.; Shih, H. C.; Kobayashi, T. *Opt. Express* **2009**, *17*, 11321.

(32) Vicario, J.; Meetsma, A.; Feringa, B. L. *Chem. Commun.* **2005**, 5910.

(33) Pollard, M. M.; Meetsma, A.; Feringa, B. L. *Org.Biomol. Chem.* **2008**, *6*, 507.

(34) Pollard, M. M.; Wesenhagen, P. V.; Pijper, D.; Feringa, B. L. *Org.Biomol. Chem* **2008**, *6*, 1605.

(35) Cnossen, A., University of Groningen, 2013.

(36) Baldridge, A.; Kowalik, J.; Tolbert, L. M. *Synthesis-Stuttgart* **2010**, 2424.

3 Excited State Dynamics of a Unidirectional Molecular Rotary Motor

In this chapter, the excited state dynamics of a unidirectional molecular rotary motor will be studied. After a description of the experimental conditions employed (Section 3.2), the steady state spectroscopy of the motor molecule will be considered (Section 3.3.1). Following this, ultrafast fluorescence up-conversion measurements will be discussed (Section 3.3.2). A significant aspect of the fluorescence lifetime measurement is the reconstruction of the time domain evolution of the emission spectrum which will be described in Section 3.3.2.1. The time domain data and reconstructed fluorescence reveal a series of coherently excited vibrational modes. The assignment and significance of these are discussed. Transient absorption measurements will then be considered (Section 3.3.3). Finally, the solvent dependence of both fluorescence up-conversion and transient absorption measurements will be discussed (Section 3.3.4).

3.1 Introduction

The conversion of light into other forms of energy has been a major area of research for many years. A significant focus has been placed upon developing the ability to harness the energy of light for use in numerous applications. A number of such systems were described in Chapter 1. Light driven molecular motors are one particularly interesting class of system in which this is achieved with the conversion of light into mechanical energy through excited state reactions.[1] Nature employs molecular motors in a number of vital biological processes. Importantly, the biological functioning of many of these systems requires the motor motion to be unidirectional.[2] Such discoveries have prompted extensive attempts to synthesise molecules capable of mimicking light driven unidirectional rotation. This is difficult to achieve since unidirectional rotation requires an energy input (light in this case) to be harnessed such that motion in selected specific modes (rotation in this case) are favoured over all other possibilities.

On the molecular scale, where numerous independent degrees of freedom exist, all of which can be driven by this input of energy, the successful design of such a system would seem highly unlikely.[3] However, molecular motors based on chiral overcrowded alkenes have been shown to produce selective unidirectional motion in response to electronic excitation by light. These molecules, first reported by Feringa and co-workers[4-6] are comprised of a 'rotor' (upper part) attached to a 'stator' (lower part) *via* an 'axle' (a carbon-carbon double bond in the electronic ground state) as shown in Figure 3.1 (1-H). The absolute configuration of the stereogenic centre (marked by * in Figure 3.1) is key to achieving unidirectional motion. One full revolution of the rotor relative to the stator occurs *via* a four step mechanism (Figure 3.2). Firstly, a photoisomerization reaction leads to rotation of the rotor group relative to the stator group about the axle (Step 1, Figure 3.2).

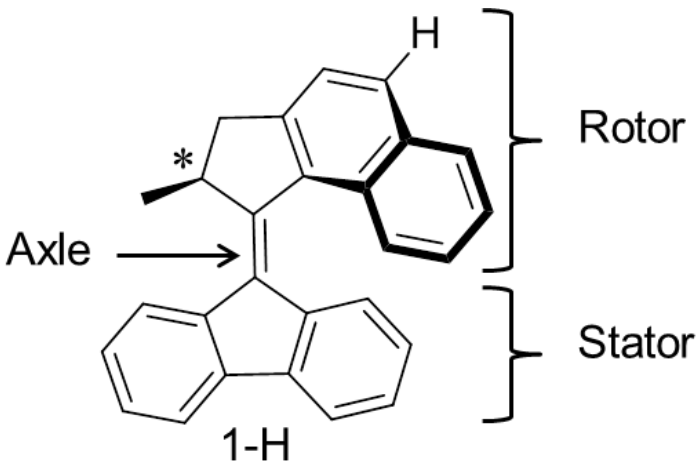

Figure 3.1 - *Structure of a unidirectional rotary molecular motor (1-H) based upon an overcrowded alkene design.*

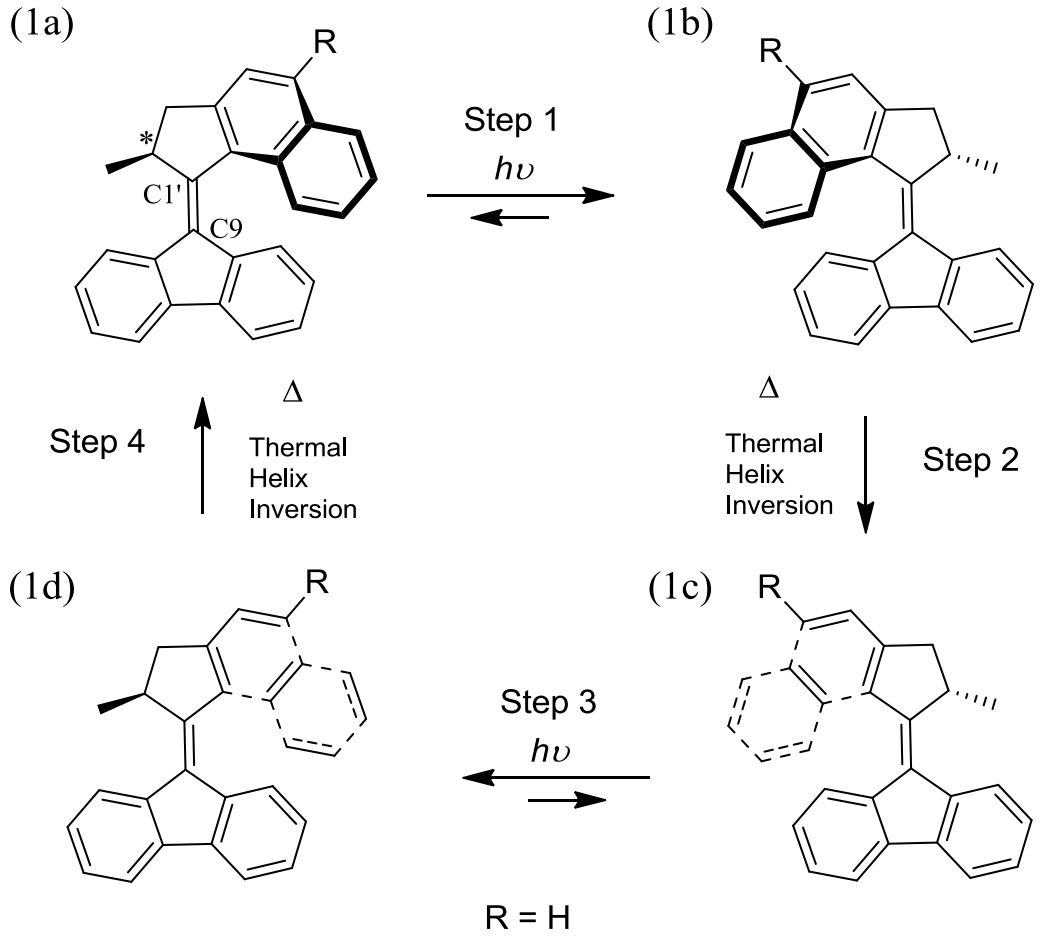

Figure 3.2 - *Reaction cycle of unidirectional molecular rotary motor **1**-H.*

Since this is a photochemical process, and represents the energy input for the entire motor cycle, this step is termed the 'power stroke'. The unidirectional nature of this step is governed by steric interaction between the phenyl groups of the rotor and stator. Following the power stroke, a thermal helix inversion takes place in the ground state on a far slower timescale (Step 2, Figure 3.2). In the initial structure (1a in Figure 3.2), the methyl group at the stereogenic centre adopts an axial conformation.[6] However, the product of the first photoisomerization (1b in Figure 3.2) is of inverted helicity with this methyl group adopting an equatorial conformation.[6] As a result, a thermally activated helix inversion occurs in the ground state to return the methyl group to the more energetically favourable axial orientation (1c in Figure 3.2). This reintroduces the steric barrier to rotation in the opposite direction.

Thus, the helix inversion acts as a 'lock' which forces each subsequent photoisomerization reaction to occur selectively in one direction. A second pair of photochemical isomerization and thermal helix inversion steps completes one full revolution of the rotor relative to the stator. Under constant irradiation, the cycle is continually repeated resulting in repetitive unidirectional rotation of the rotor relative to the stator. Thus, unidirectional motor action on a molecular scale is achieved.

In order to truly harness the mechanical energy of these molecular motors for applications in nanomachines, the stator must be attached to a surface. A surface provides a stationary anchor from which the unidirectional rotation of the rotor can be used to drive motion. Progress has been made in this regard in recent years. It has been shown that the stator of this molecular motor system can be covalently linked to the surface of gold nanoparticles.[7] The unidirectional rotation is retained and so rotation of the rotor proceeds in a unidirectional manner with respect to the surface. In order to continue to develop the applications of these systems, such that functional molecular machines are made a reality, a clearer understanding of the mechanism of motor action is required. Thus far, since it is the slowest step in the motor cycle and hence the rate limiting process, much attention has been devoted to understanding and improving the rate of the ground state thermal helix inversion. Indeed, optimisation of the molecular structure by chemical synthesis has resulted in a dramatically improved rate of rotation of these systems by a factor of over a million compared to the original motors.[8] In principle, these molecular motor systems can even achieve rotation frequencies in the region of MHz.[9]

However, comparatively little is known about the dynamics of the power stroke and how it depends upon the structure of the molecule and its environment.[10] This is surprising since a detailed understanding of the molecular dynamics on the excited state potential energy surface is vital for improving the quantum efficiency of these systems. Currently, for 1-H

(Figure 3.1), the photochemical quantum yield was found to be 0.14.[11] Thus, plenty of room remains for improvement. Progress in this direction will require a better understanding of the excited state dynamics of these molecules. In addition, in order to exploit the full potential of molecular motors in future applications such as molecular machines and nanodevices, a far better understanding of the excited state properties of these molecules is required. [1,12] Such applications will require a high level of control and ideally some tunability of the excited state molecular dynamics (for example using shaped laser pulses).[13,14] Such objectives can only be achieved by first understanding the mechanisms of excited state photoisomerization in unidirectional molecular motors. To begin to address these issues, ultrafast fluorescence up-conversion (with a sub 50 fs time resolution)[15] and transient absorption spectroscopies were employed to study the primary events which occur following photon absorption by 1-H. This allowed the characterisation of the excited state dynamics of the 'power stroke' which acts as the driving force for motor motion. Further insight was gained by studying the solvent dependence of the excited state dynamics.

3.2 Experimental

The molecular motor samples were provided to us by the group of Prof. Ben Feringa at the University of Groningen (Chapter 2). Steady state absorption spectra were recorded using a PerkinElmer XLS spectrophotometer. Steady state fluorescence spectra were recorded using a Jobin Yvon fluorometer with 3 nm excitation and emission bandwidths. The extremely weak nature of the emission caused severe distortion of the fluorescence spectra by Raman scattering of the solvent. Thus, the emission spectra were subjected to subtraction of the solvent Raman scattering, determined by measuring the spectra of pure solvent under identical conditions. All steady state measurements were made with a sample concentration ~10 μM (corresponding to ~0.3 OD at the wavelength of maximum absorption) in a 1 cm path length cell.

Time-resolved fluorescence decay curves were measured by fluorescence up-conversion as a function of emission wavelength. This set-up is described in detail in Chapter 2. The laser excitation pulse was centred at 400 nm and the excitation power was attenuated to 8.5 mW. All fluorescence up-conversion measurements were conducted with a sample concentration of 1 mM (corresponding to 2.5 OD at 400 nm) in a 1 mm path length cell. A peristaltic pump (Peri-Star Pro) was employed to ensure that the sample remained under continuous flow (60 mL / min) in order to prevent the formation of the photochemical product (1b in Figure 3.2). This was confirmed by the study of the excitation power dependence of the up-conversion signal which revealed that an excitation power of 8.5 mW under these flow conditions is in the linear regime (red line in Figure 3.3). In contrast, no flow revealed a non-linear power dependence at higher excitation powers (black line Figure 3.3). The possible contribution of the photoproduct to the measured data was assessed further by attempting to study the excited state dynamics of the photoproduct. To do so, a UV lamp (λ = 365 nm) was used to irradiate the reservoir of the flow cell to ensure the maximum concentration of the photoproduct. However, no significant differences were observed in the fluorescence decay curve under these conditions (green points in Figure 3.4) compared to that measured under the flow conditions with no lamp (red points in Figure 3.4). Thus, it was concluded that the fluorescence up-conversion experimental conditions employed in this work probed only the excited state dynamics of the initial structure of 1-H (1a in Figure 3.2).

Transient absorption measurements were conducted according to the procedure described in Chapter 2. The laser excitation was centred at 400 nm and the absorption was probed between 420 nm and 620 nm. All transient absorption measurements were conducted with a sample concentration of ~ 0.3 mM (corresponding to~ 0.8 OD at 400 nm) in a 1 mm path length cell. The same continuous flow conditions were employed as described for the fluorescence up-conversion measurements.

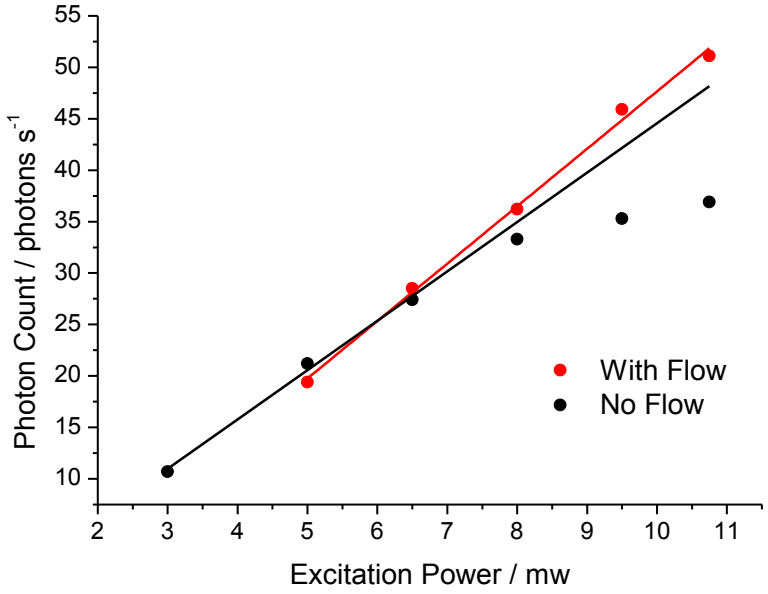

Figure 3.3 - *Excitation power dependence of the fluorescence up-conversion signal of 1-H measured in heptane.*

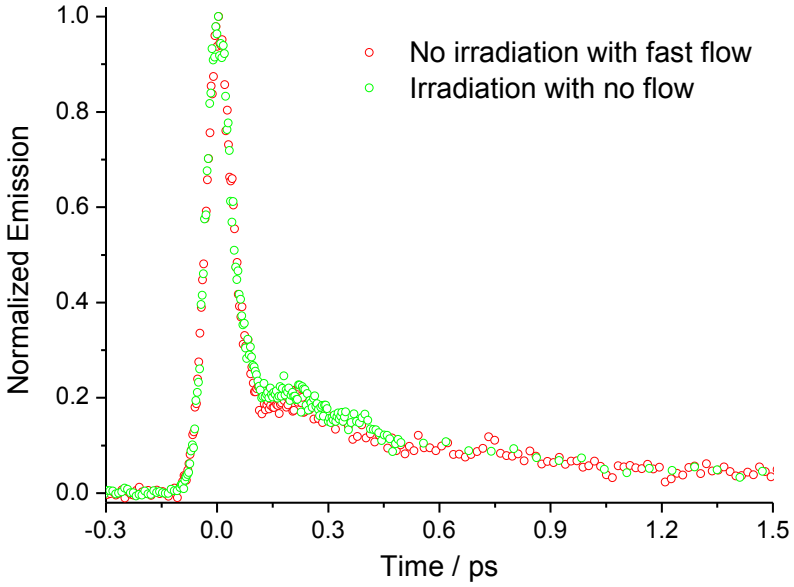

Figure 3.4 - *A comparison of the fluorescence decay curve of 1-H measured in heptane under flow with no irradiation (red points) and under no flow with irradiation at 365 nm (green line).*

3.3 Results and Discussion

3.3.1 Steady State Spectroscopy

The absorption and emission spectra of 1-H in dichloromethane (DCM) are shown in Figure 3.5. The absorption spectrum (maximum at 390 nm) is narrow with a strong transition moment (ε = 26000 $dm^3mol^{-1}cm^{-1}$) as reported previously.[16] The emission spectrum is weak (quantum yield estimated < 10^{-4}) and remarkably broad (stretching from 350 – 750 nm). The emission data presented in Figure 3.5 (black points) were recovered after subtraction of the solvent Raman scattering and fitted with a log normal function (red line). A weak and broad emission profile is indicative of a molecular system undergoing structural reorganisation in the excited state.[17]

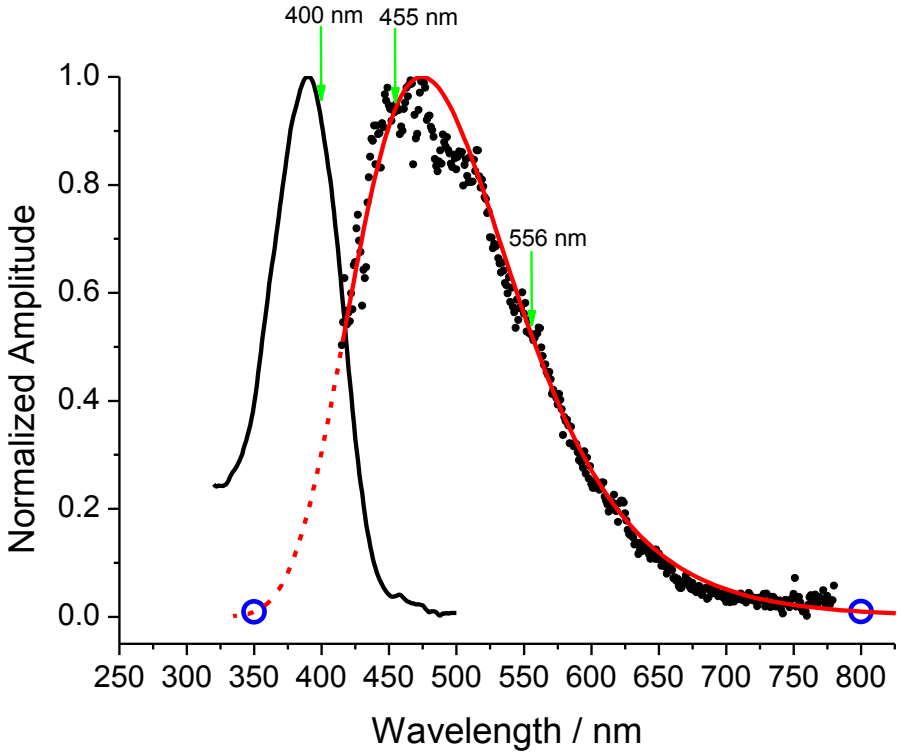

Figure 3.5 - *Steady state absorption and fluorescence spectra. The emission data (black points) was subjected to subtraction of the solvent Raman scattering signal and fitted with a log-normal function (red line).The blue circles represent the wavelengths at which the log-normal function fitted to the emission spectrum was constrained at zero intensity.*

The solvent dependence of the steady state spectra was also investigated. The absorption (Figure 3.6) and emission (Figure 3.7) spectra of 1-H were recorded in a series of solvents as a function of viscosity and polarity. The wavelengths of maximum absorption, emission and calculated Stokes shifts are summarized for each solvent in Table 3.1.

The absorption spectra reveal no significant solvent polarity dependence, with only a 2 nm red shift between polar acetonitrile (3.92 D) and non-polar cyclohexane (O D) solvents. Solvent viscosity also has little effect on the absorption spectra where no spectral shift was observed between ethanol (η = 1.1 mPa s) and octanol (η = 7.3 mPa s).

The emission spectra remain weak and broad in all solvents, and the data presented in Figure 3.7 were thus also subjected to the subtraction of solvent Raman scattering. The very weak nature of the emission precluded assessment of the effect of solvent viscosity upon the fluorescence quantum yield. Instead, ultrafast time-resolved spectroscopy was used to assess the effects of solvent viscosity upon the excited state decay dynamics of 1-H (Section 3.3.2). However, compared to the absorption spectra, a more substantial solvent polarity effect is observed for the fluorescence spectra. The emission of 1-H is red shifted in non-polar solvents (for example, by 24 nm in cyclohexane relative to acetonitrile). As a result, a larger Stokes shift is observed for 1-H in non-polar solvents (Table 3.1). However, solvation dynamics are often characterized by a larger Stoke's shift in polar solvent (See Chapter 1.3.3 for a more detailed discussion of solvent polarity effects). Since no such effect is observed, this suggests no significant difference in the dipole of the ground state and initial excited state structures of 1-H. Therefore, this suggests that 1-H does not exhibit any significant $S_0 - S_1$ charge transfer character. As a result, no significant solvation dynamics are expected in the excited state relaxation mechanism of 1-H. This was investigated further by ultrafast time resolved spectroscopy (Section 3.3.2).

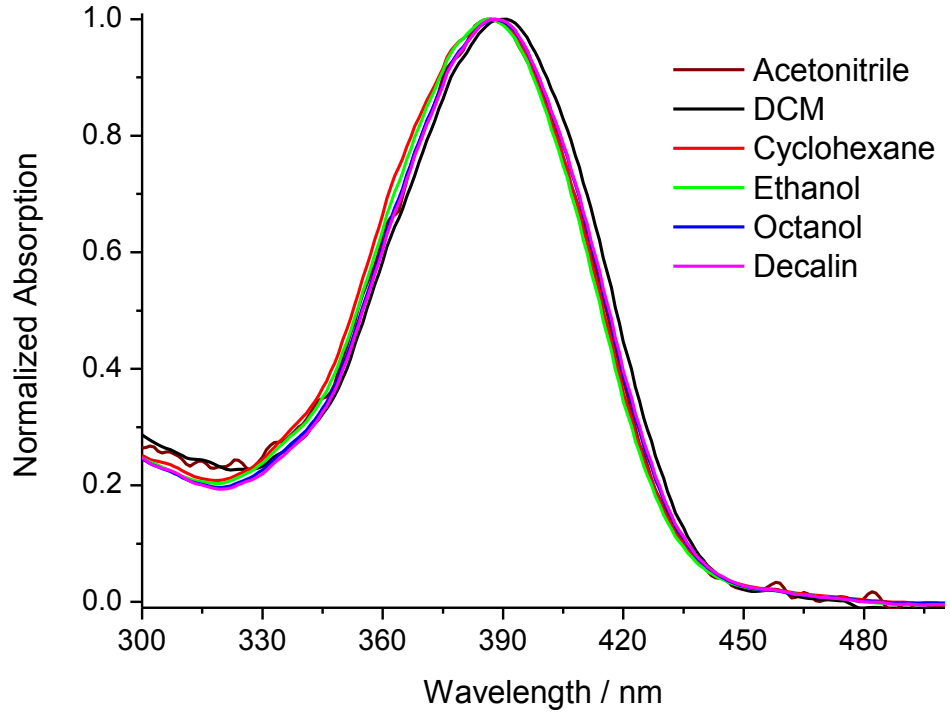

Figure 3.6 - *Solvent dependent steady-state absorption spectra of 1-H.*

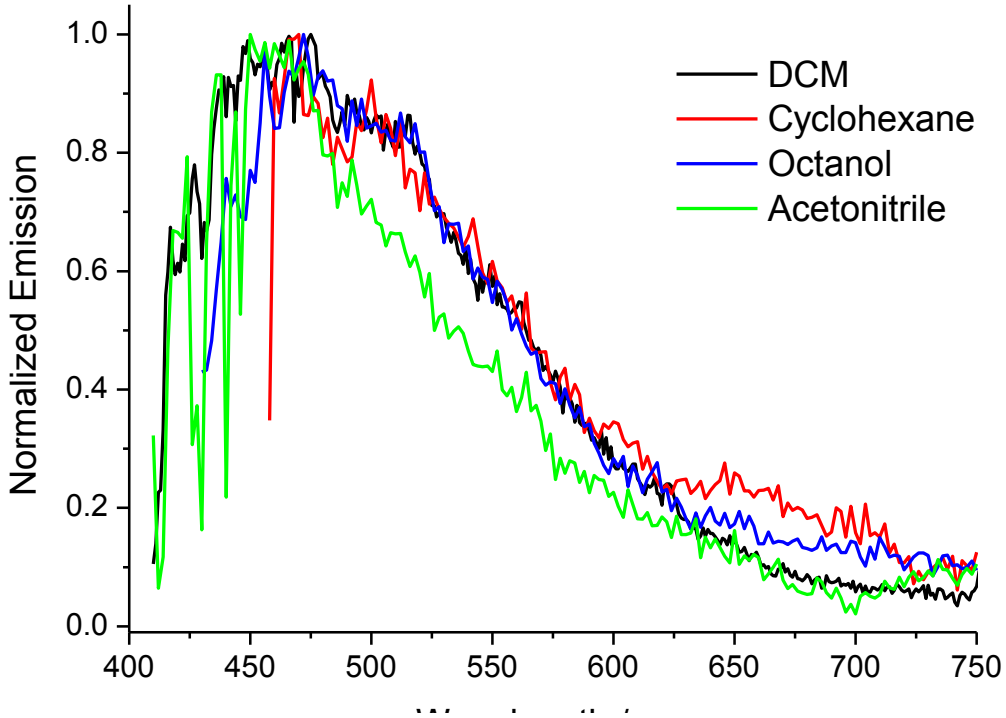

Figure 3.7 - *Solvent dependent steady-state fluorescence spectra of 1-H after subtraction of solvent Raman scattering. In each case, the excitation wavelength corresponds to the wavelength of maximum absorption. The spectra measured in acetonitrile and ethanol are omitted but the data is presented in Table 3.1.*

Table 3.1 - *Solvent dependent wavelengths of maximum absorption, emission and calculated Stokes shifts for 1-H.*

Solvent	Viscosity / mPa s	Absorption Maximum / nm	Emission Maximum / nm	Stoke's Shift / nm
Acetonitrile	0.37	386	465	79
DCM	0.43	390	475	85
Cyclohexane	0.89	387	489	102
Ethanol	1.07	386	470	84
Decalin	2.5	388	508	120
Octanol	7.29	388	472	84

3.3.2 Ultrafast Fluorescence Up-conversion

In order to probe the excited state dynamics of 1-H, we employed fluorescence up-conversion spectroscopy. The time-resolved emission profiles measured in DCM as a function of emission wavelength are shown in Figure 3.8. The excitation wavelength was 400 nm and the range over which the emission decay profiles were measured, shown by green arrows in Figure 3.5, was limited by scattered light.

The decay curves reveal an ultrafast wavelength-dependent decay superimposed with a series of oscillations. The excited state lifetime is shortest on the blue side of the emission spectrum, where the dominant feature is a ~100 fs decay component. As the emission wavelength is tuned to the red, the lifetime of the excited state becomes longer. The raw data (circles) were fitted to a function (solid lines) comprising the sum of two exponential relaxation terms and three damped harmonic oscillators (See Chapter 2 for details of the fitting procedure). An example of the individual components which comprise the fitting function is shown in Figure 3.9 (for data measured at 556 nm). The wavelength dependent exponential fitting parameters are shown in Table 3.2 and the corresponding parameters for the oscillator functions are shown in Table 3.3.

At all emission wavelengths, the bi-exponential decay is dominated by the faster component, which has the major amplitude (~80%). However, both components exhibit an emission wavelength dependence, where the faster component increases from 110 fs at 455 nm to 310 fs at 576 nm and the slower component from 0.9 ps to 1.3 ps over the same range. In contrast, the frequencies of the three damped harmonic oscillator functions are independent of emission wavelength within experimental error (Table 2). The frequency of the dominant oscillation was determined as 3.5 THz (113 cm^{-1}) whereas the frequencies of the minor oscillations were determined to be 5.4 THz (180 cm^{-1}) and 8.8 THz (294 cm^{-1}). The major oscillation (113 cm^{-1}) is most strongly damped with a damping constant of 95 fs compared to 220 fs (180 cm^{-1}) and 280 fs (294 cm^{-1}) for the minor oscillations. All three oscillations are damped more quickly as the emission wavelength is blue shifted (Table 3.3).

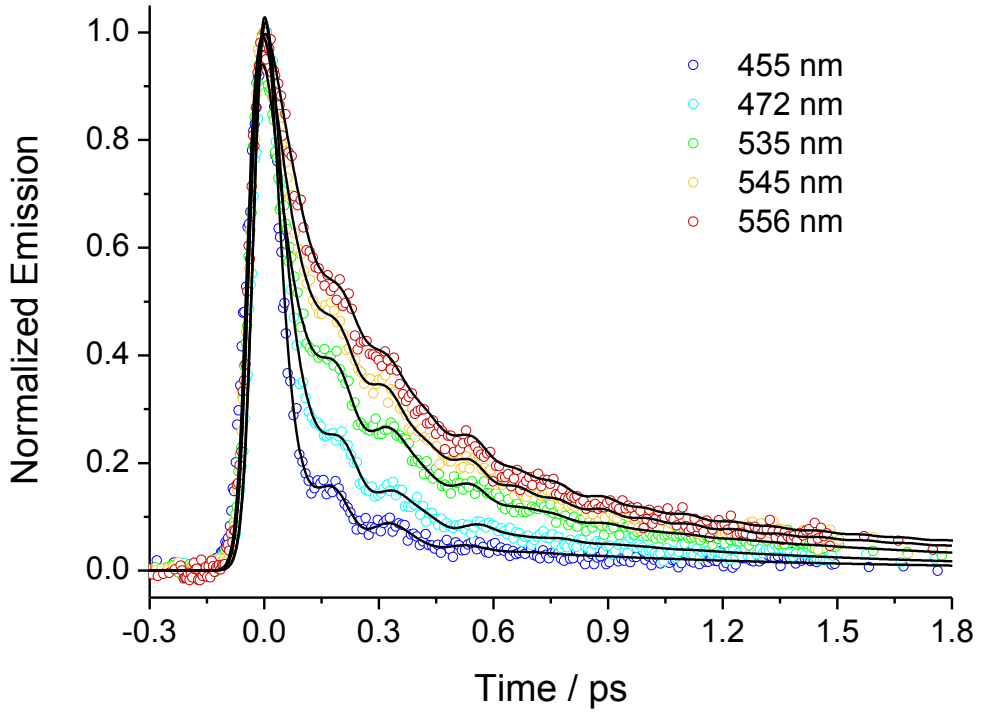

Figure 3.8 - *Time-resolved fluorescence decay curves of 1-H in DCM recorded as a function of emission wavelength. The raw data (circles) were fitted to a function comprising the sum of two exponential decay terms and two damped harmonic oscillators (lines).*

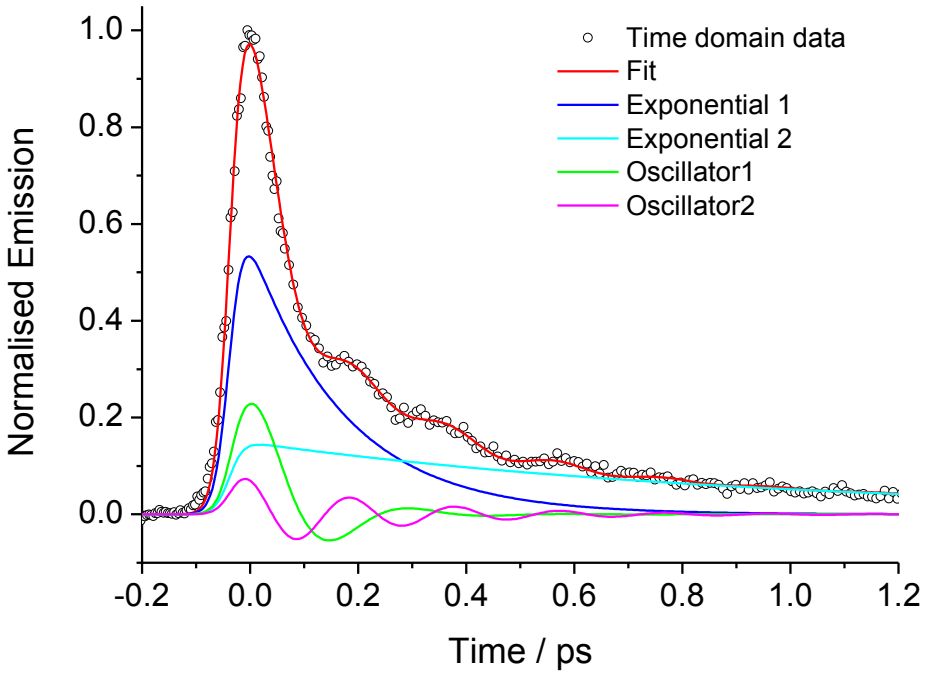

Figure 3.9 - *The individual components which comprise the overall fitting function for the fluorescence decay curve of 1-H in DCM measured at 556 nm.*

Table 3.2 - *Exponential components of the fluorescence lifetime of 1-H in DCM. Repeat fits to each measurement determined the error to be within 15% for each parameter.*

Emission λ / nm	τ_1 /ps	A_1	τ_2 /ps	A_2
455	0.11	0.88	0.87	0.12
465	0.13	0.86	0.89	0.14
472	0.14	0.84	0.93	0.16
480	0.14	0.85	0.93	0.15
488	0.16	0.84	1.00	0.16
497	0.18	0.83	1.08	0.17
506	0.19	0.82	1.12	0.18
516	0.21	0.83	1.38	0.17
525	0.20	0.82	1.20	0.18
535	0.23	0.80	1.21	0.20
545	0.25	0.81	1.37	0.19
556	0.29	0.81	1.48	0.19
576	0.31	0.83	1.31	0.17

Table 3.3 - *Damping (τ_D), frequency (ω), amplitude (A_ω) and phase (Φ) components of the two damped oscillator functions used to fit the oscillatory part of the time domain fluorescence decay data. Repeat fits to each measurement determined the error of each parameter to be within 25%.*

Emission λ / nm	**τ_{D1} / ps**	**ω_1 / THz**	**$A_{\omega 1}$**	**φ_1**	**τ_{D2} / ps**	**ω_2 / THz**	**$A_{\omega 2}$**	**φ_2**	**τ_{D3} / ps**	**ω_3 / THz**	**$A_{\omega 3}$**	**φ_3**
455	0.06	3.35	0.80	0.91	0.17	5.37	0.15	1.34	0.14	9.19	0.05	1.22
465	0.07	3.36	0.82	0.66	0.21	5.29	0.14	1.00	0.22	8.74	0.04	1.00
472	0.08	3.32	0.78	0.62	0.22	5.24	0.15	0.78	0.23	8.71	0.06	0.83
480	0.09	3.42	0.71	0.56	0.22	5.21	0.15	0.85	0.17	8.71	0.14	0.69
488	0.08	3.38	0.74	0.54	0.24	5.29	0.16	0.72	0.14	8.59	0.10	0.54
497	0.09	3.43	0.74	0.40	0.26	5.20	0.16	0.55	0.18	8.69	0.10	0.50
506	0.08	3.38	0.72	0.33	0.23	5.33	0.16	0.48	0.15	9.08	0.12	0.40
516	0.10	3.53	0.64	0.18	0.20	5.43	0.22	0.33	0.18	8.90	0.14	0.36
525	0.09	3.57	0.55	0.12	0.18	5.41	0.21	0.32	0.15	8.82	0.24	0.51
535	0.09	3.41	0.66	0.02	0.23	5.45	0.24	0.20	0.24	8.82	0.10	0.32
545	0.12	3.59	0.65	0.08	0.26	5.54	0.26	0.10	0.52	8.64	0.09	0.64
556	0.15	3.72	0.64	-0.14	0.30	5.49	0.24	0.04	0.64	8.76	0.12	0.50
576	0.17	3.95	0.65	-0.60	0.27	5.70	0.23	-0.30	0.65	9.16	0.12	0.60

An assessment was also made of the quality of fit obtained when fitting with a function comprised of a varied number of damped harmonic oscillator functions. The residual plots obtained by fitting the time-domain data (measured at 487 nm) with a sum of two exponential decay functions and 0, 1, 2 and 3 damped harmonic oscillators are shown in Figure 3.10. The data is not well fit by a bi-exponential only function (black) where an oscillation clearly remains in the residual plot, peaking at 0.2, 0.35 and 0.6 ps.

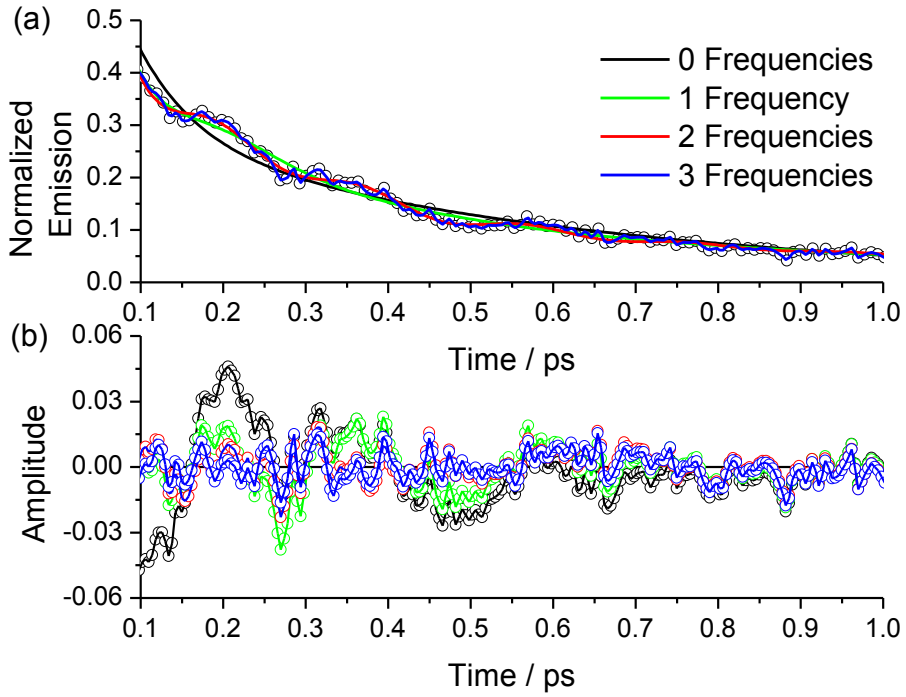

Figure 3.10 - *A comparison of the fit quality (a) and residual plots (b) obtained by fitting the time domain data with a function comprising the sum of a bi-exponential decay term and 0, 1, 2 and 3 damped harmonic oscillators.*

Addition of a single damped harmonic oscillator (3.5 THz) to the fitting function (green) greatly improves the quality of the fit around the first maximum of the oscillation (0.2 ps). However, the other maxima remain poorly fit by this function. Addition of a second oscillator (5.4 THz) to the fitting function (red) results in a further improvement to the fit quality and a near random residual plot. Addition of a third oscillator (~8.8 THz) did not result in a significant improvement to the fit quality. However, the third frequency does become important when studying substituted derivatives of 1-H (Chapter 4). Therefore, the parameters of the third frequency are reported in Table 3.3 to maintain continuity of the dataset. Thus, the sum of a bi-exponential decay function and three damped harmonic oscillators was deemed an appropriate function to provide a good fit to the data.

Further confirmation of the suitability of a two oscillator fitting function was gained by studying the Fourier transform of the time domain data. Figure 3.11 shows the Fourier transform of the time-resolved decay curve measured at 535 nm. Since the time-domain data is dominated by an ultrafast (~100 fs) exponential decay, this results in a dominant Lorentzian lineshape in the frequency domain. In order to resolve the time domain oscillation in the frequency domain, the exponential decay components were subtracted from the time domain fluorescence decay data of 1-H. Thus, only the oscillatory components of the time domain data remained. The Fourier transform of the raw time domain data (black line in Figure 3.11) resulted in two distinct bands in the frequency domain.

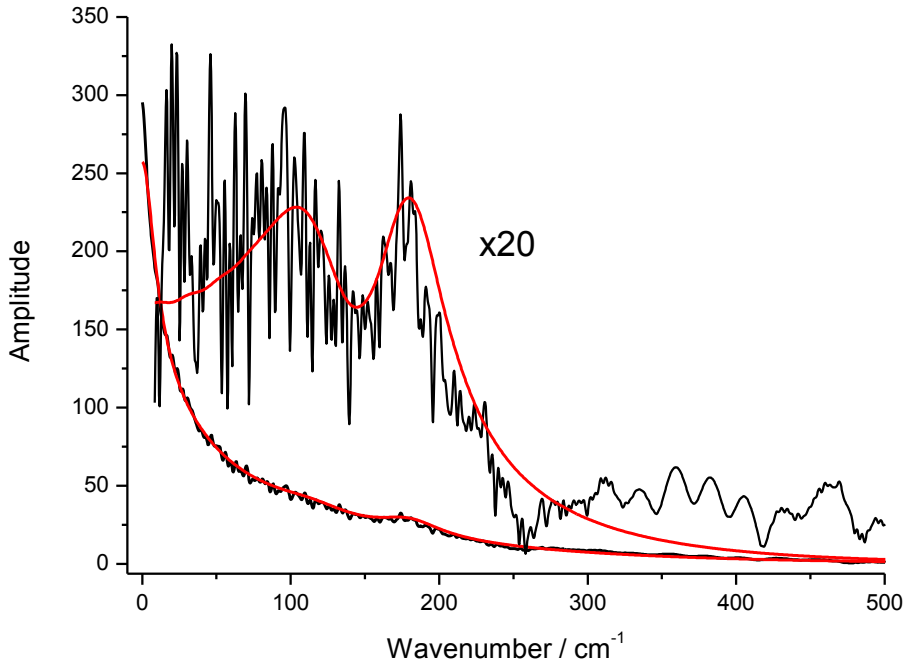

Figure 3.11 - *Fourier transform of the 1-H fluorescence lifetime data (emission measured at 535 nm). The raw data (black lines) is compared to the fitted function (red lines). The ultrafast component of the time domain data results in a dominant Lorentzian lineshape in the frequency domain. Subtraction of the exponential decay components from the time domain data leaves only the oscillatory components, the Fourier transform of which is magnified x20.*

The fitted function was also Fourier transformed (red line in Figure 3.11). This comparison shows that the peaks of the oscillation exhibited by the raw data correspond closely to the frequencies of the fitted function. Thus, the sum of a bi-exponential decay function and two damped harmonic oscillators is a suitable function to describe the time domain data.

3.3.2.1 Time-Dependent Emission Spectra

A more complete characterisation of the excited state dynamics is obtained by reconstructing time-dependent emission spectra. This procedure is described in detail in Chapter 2. Briefly, the area of the emission wavelength resolved time-domain decay curves (Figure 3.8) were normalized to the intensity in the steady state emission spectrum (Figure 3.5) at the corresponding wavelength. The resulting spectra for 1-H in DCM, where the data points have been fitted to a log-normal function, are shown in Figure 3.12. Since the broad nature of the emission spectrum did not allow fluorescence up-conversion measurements over the entire emission range, the log normal fits were constrained by assuming zero emission intensity at 350 nm and 800 nm (blue circles in Figure 3.5). The time-dependent emission spectra presented here were reconstructed from the deconvoluted fits to the raw time domain data. In order to ensure that neither the deconvolution nor the reconstruction procedure introduced any artefacts to the data, the reconstruction procedure was also conducted using the raw time-domain data. This is described in more detail in Chapter 2.

Reconstruction of the time dependent emission spectra allows a more comprehensive representation of the excited state relaxation dynamics both the time domain and frequency domain in the form of a contour plot (Figure 3.13). Such a plot holds all of the information regarding the time-dependence of the emission spectrum, where slicing along the time axis (y-axis) reveals frequency domain spectra and slicing along the frequency axis (x-axis) reveals time domain decay curves. Figure 3.13 clearly shows the oscillation observed in the time domain data represented as circles.

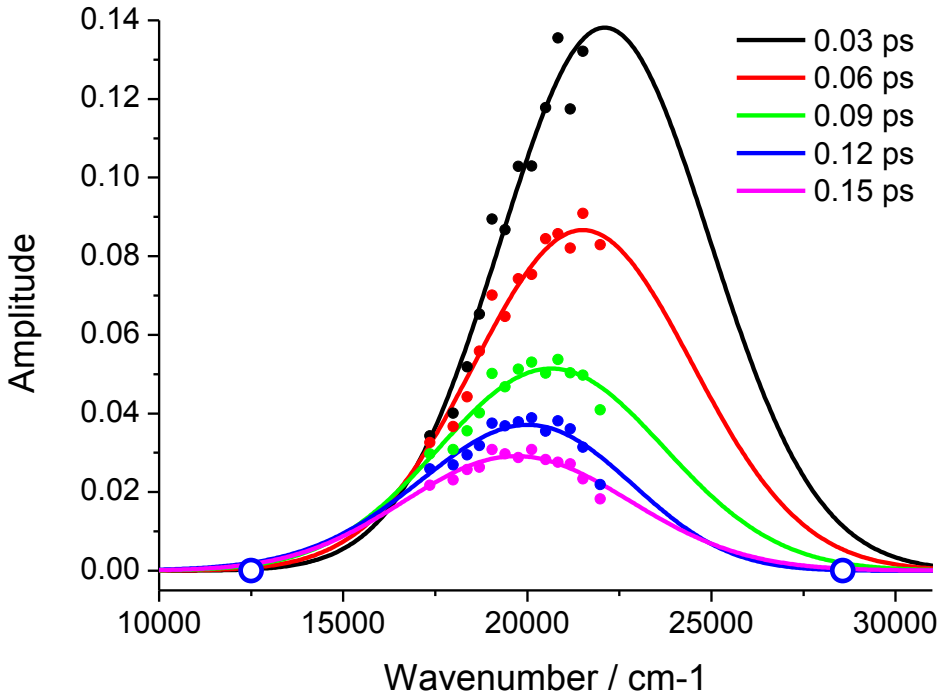

Figure 3.12 - *Time-dependent emission spectra of 1-H in DCM reconstructed from the deconvoluted wavelength resolved fluorescence decay (points) and fit to a log-normal function (lines).*

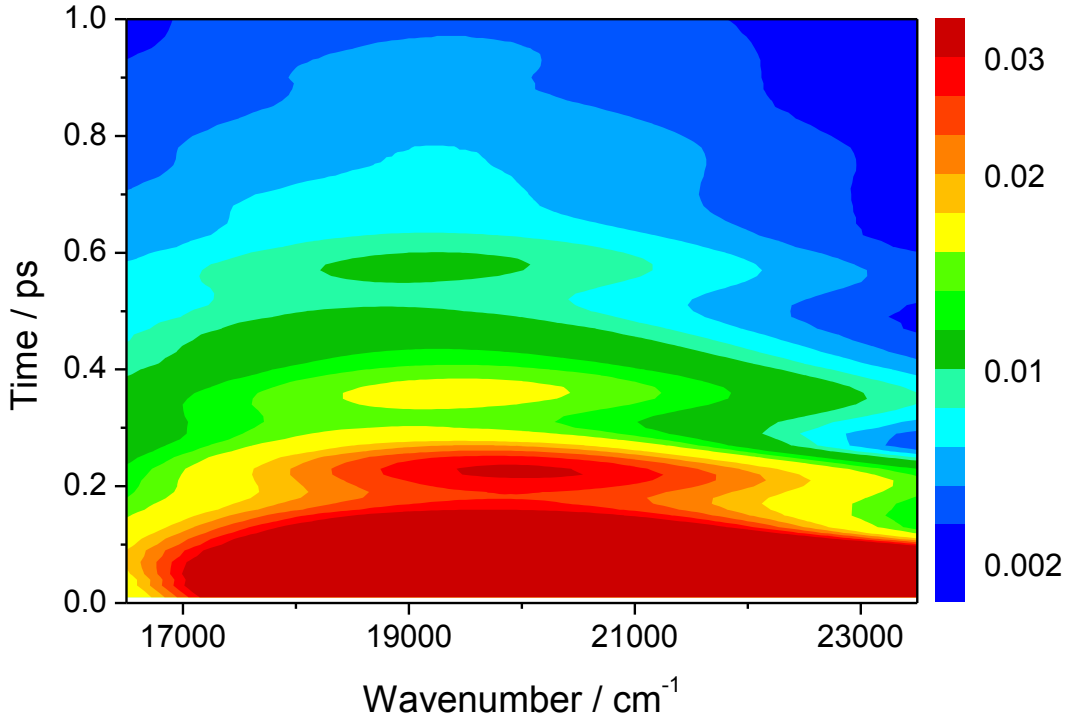

Figure 3.13 - *Contour plot representation of the time-dependent emission spectrum of 1-H in DCM. The ultrafast decay and oscillation are evident.*

The time dependence of the log-normal fit parameters can also be used to assess the temporal evolution of a number of important parameters of the emission spectrum. In particular, the time-dependent evolution of the integrated intensity, mean frequency and width of the emission spectrum are shown in Figure 3.14. The integrated intensity of the emission spectrum describes the excited state population dynamics independently of any emission wavelength dependence. This is particularly important for a system such as that studied here in which the fluorescence decay dynamics depend significantly upon the emission wavelength. Figure 3.14 reveals two interesting observations. Firstly, the integrated intensity (black line) of the emission spectrum is found to exhibit a non-single exponential decay. Secondly, the oscillation observed in the wavelength resolved time domain data (Figure 3.13) is also observed in the temporal evolution of both the integrated intensity (black line) and mean frequency (red line) of the emission spectrum. The bi-modal fluorescence decay and coherent oscillation are discussed in more detail in Section 3.3.2.2 and Section 3.3.2.3 respectively.

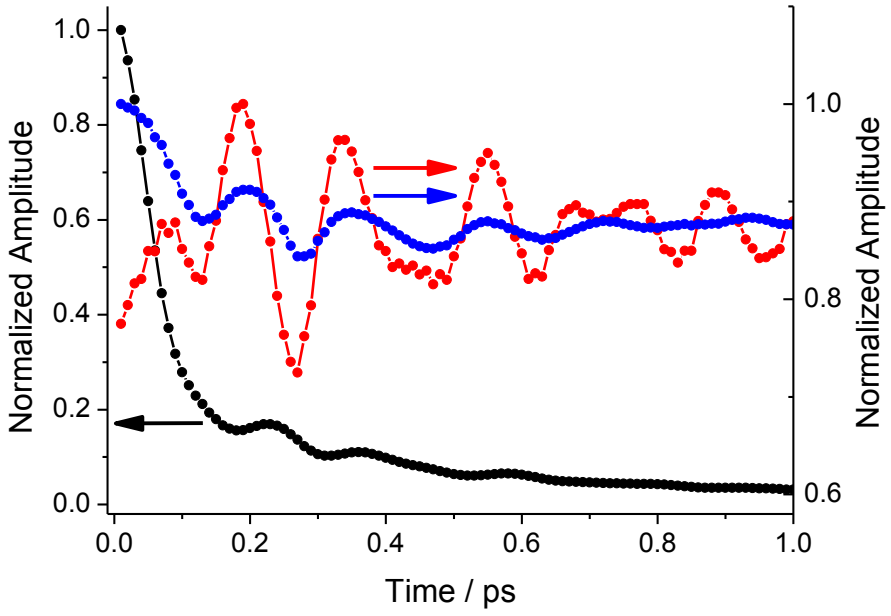

Figure 3.14 - *Time dependent integrated intensity (black, left axis), mean frequency (blue, right axis) and width (red, right axis) of the 1-H emission spectrum in DCM.*

3.3.2.2 Bi-modal Fluorescence Decay

The integrated intensity of the emission spectrum is found to exhibit a non-single exponential decay (black line in Figure 3.14). This decay is dominated by an ultrafast (~100 fs) component followed by a slower (~1 ps) relaxation. The mean frequency (blue line in Figure 3.14) reveals that the emission spectrum exhibits a red shift with time, which is due to the ultrafast collapse of the blue side of the spectrum. This is evident in the raw time domain data (Figure 3.8) where the excited state decay is considerably faster on the blue side of the emission spectrum. Since no rise time was observed on the red side of the emission spectrum, it is unlikely that solvent reorientation is responsible for the rapid decay of the excited state. The origin of dynamic red shifted spectra as a result of solvation dynamics is discussed in more detail in Chapter 1. Further analysis of solvent effects upon the excited state dynamics of this molecular motor system is presented in Section 3.3.4. The extraordinarily fast decay and red shift of the emission spectrum is ascribed to intramolecular structural motion of the molecular motor on the excited state potential energy surface.

The dominant ~100 fs decay component can be rationalised in terms of the highly strained ground state structure of the molecule. Excitation of 1-H is known to occur *via* a π-π^* transition of the central carbon-carbon double bond.[18,19] As a result, the highly strained structure is able to relax *via* intramolecular structural evolution. Previous calculations suggest that the non-radiative excited state decay of this class of molecular motor proceeds *via* structural evolution along both the pyramidalization (at C9, Figure 3.2) and rotational (rotor relative to stator about C1'=C9, Figure 3.2) co-ordinates.[18] Motion along these co-ordinates leads to a conical intersection where the excited state is able to undergo ultrafast internal conversion directly to the ground state. A more detailed discussion of excited state structural evolution leading to internal conversion at a conical intersection is presented in Chapter 1. Therefore, relief of the highly strained structure provides a strong driving force for excited

state structural evolution along the co-ordinate of radiationless decay. As a result, the timescale of this decay process is extremely fast, as reflected by the ~100 fs decay timescale observed experimentally. However, the longer ~1 ps component is not consistent with this assignment. If the excited state structural evolution were to lead directly to a conical intersection, such a distinctly bi-modal fluorescence decay would be not expected. Therefore, the mechanism of excited state relaxation must be more complex than simple barrierless structural evolution leading directly to a conical intersection. One possibility is that non-emissive excited states, which are not possible to detect *via* fluorescence measurements, could be involved in this mechanism. Transient absorption spectroscopy is ideally suited to probing non-emissive excited states and so was employed in an attempt to better understand the origin to the bi-modal fluorescence decay (Section 3.3.3).

3.3.2.3 Coherent Oscillation

Figure 3.14 reveals that the oscillation observed in the wavelength resolved time domain data (Figure 3.8) is also observed in the temporal evolution of both the integrated intensity and mean frequency of the emission spectrum. An oscillation in the mean frequency of the emission spectrum may arise by coherent excitation of a Franck-Condon active vibrational mode which modulates the energy of the ground to excited state electronic transition. This launches a wavepacket on the excited state potential energy surface which oscillates with the frequency of the vibrational mode.[20,21] Thus, the energy (and hence the frequency) of the fluorescence oscillates with a frequency matching that of the vibrational mode. The origin of coherent oscillations in time resolved spectra is discussed in detail in Chapter 1. In such a case, it is expected that the oscillation should exhibit an approximate phase shift of π when the emission is measured on the blue side compared to the red side of the emission spectrum (Chapter 1, Figure 1.8).[21,22] In addition, the amplitude of the oscillation is expected to be largest on the extreme edges of the emission spectrum.

In contrast, an oscillation in the integrated intensity of the entire emission spectrum suggests that an excited state vibrational mode is also coupled to the fluorescence transition moment. Such a coupling will result in the modulation of the probability of fluorescence and so an oscillation in the amplitude of the entire emission spectrum. In this case, no phase shift is expected to be observed when monitoring the emission on the red compared to the blue side of the spectrum.[23] In addition, the amplitude of the oscillation is not expected to be larger at the extreme edges of the emission spectrum .

In the case of 1-H, the extremely broad nature of the emission spectrum (Figure 3.5) does not allow access to the fluorescence decay dynamics on the blue side of the emission spectrum. However, an approximate $\pi/2$ phase shift is observed upon changing the emission wavelength monitored from the centre to the red edge of the emission spectrum (Table 3.3). This suggests that the vibrational modes are coupled to the energy of the transition and hence modulate the frequency of the emission. However, the amplitude of the oscillation was found to be largest at the central frequency of the emission spectrum. This indicates that the coherently excited vibrational modes are also coupled to the fluorescence transition moment of 1-H. Therefore, the time-resolved emission data indicates that electronic excitation of 1-H leads to coherent excitation of Franck-Condon active vibrational modes which modulates both the frequency and the transition moment of the S_1-S_0 electronic transition.

The assignment of these coherently excited modes can be made by using the damping times of each harmonic oscillator of the fitted function (Table 3.3). Of the three frequencies involved in this function, only the lowest frequency mode (113 cm^{-1}) is damped on a timescale comparable to that of the fast component of the fluorescence decay (~100 fs). This suggests that the molecular dynamics involved in this excited state relaxation process may also damp the vibrational mode. Thus, we suggest that the 113 cm^{-1} mode is directly coupled to the co-ordinate of excited state structural evolution and therefore assign it as a reactive

mode. In contrast, the higher frequency modes (~5.3 THz and ~8.8 THz) are damped on a slower timescale (~250 fs). This suggests that the excited state structural evolution does not result in the damping of these vibrational modes. Therefore, we suggest that these modes are not coupled to the co-ordinate of excited state structural evolution and so they are assigned as spectator modes.

In order to attempt further assignment of the reactive 113 cm^{-1}mode, resonance Raman spectroscopy was employed by our collaborators. Continuous wave Raman measurements are able to probe only ground state frequencies. However, by comparing the Raman spectra of a probe molecule in the absence and presence of a pump laser, it is possible to assess which modes are resonantly enhanced by electronic excitation. Therefore, it is possible to assess which ground state vibrational modes are displaced by electronic excitation. Comparison of the resonance Raman spectrum to a calculated ground state Raman spectrum can then allow assignment of which vibrational modes are coupled to the S_0-S_1 transition. Figure 3.15 shows a comparison of the calculated ground state Raman spectrum (c, black line), the measured ground state Raman spectrum (b, blue line) and the resonance Raman spectrum (a, red line) for 1-H recorded in cyclohexane. The solvent Raman bands of DCM precluded measurements in this solvent. No modes were found in the ground state Raman spectrum of 1-H which exactly match the frequencies observed experimentally. However, this is not surprising since electronic excitation results in a significantly altered electronic structure compared to the ground state (as indicated by the ultrafast excited state relaxation discussed in Section 3.3.2.2). As a result, it is likely that the ground state modes will be shifted in frequency in the excited state. Similar observations have been reported previously for cis-stilbene, a molecule which undergoes excited state isomerization involving pyramidalization and rotation.[24-26] Resonantly enhanced modes are observed for 1-H at 300 cm^{-1} (red line in Figure 3.15).

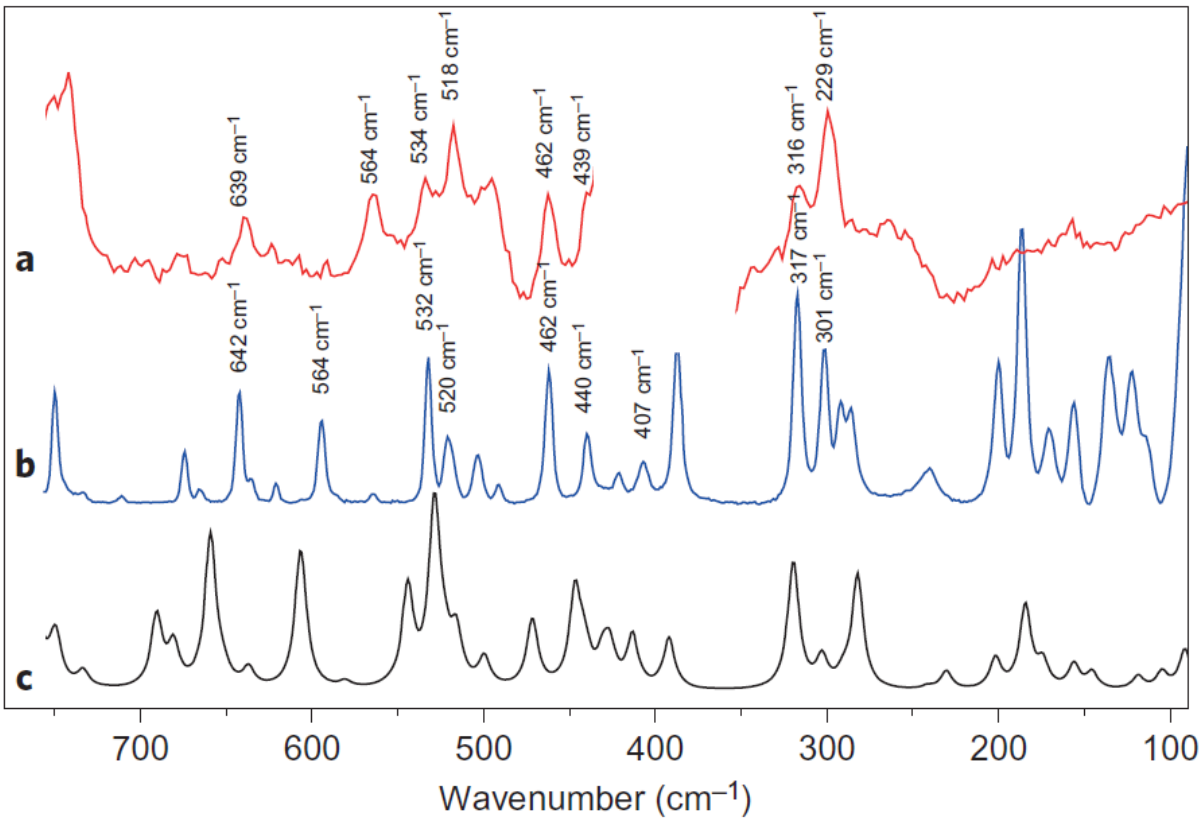

Figure 3.15 - *A comparison of (a) the resonance Raman spectrum, (b) the non-resonant Raman spectrum and (c) calculated ground state Raman spectrum of 1-H. Experimental spectra were measured in cyclohexane.*

The calculated Raman spectrum indicates that one of these modes involves out of plane nuclear displacement of the C9 atom (Figure 3.2). Such nuclear motion is involved in pyramidalization, a key component of the co-ordinate of excited state structural evolution. Therefore, the 113 cm^{-1} coherently excited vibrational mode is tentatively assigned to pyramidalization of the C9 atom.

The observation of a coherently excited vibrational mode which is directly involved in the excited state structural evolution co-ordinate raises the potential of coherent control. The use of appropriately shaped laser pulses to control photochemical reactions has been an area of intense interest.[13,14] For this class of molecular motor, it may be possible to selectively excite this vibrational mode and hence selectively induce excited state nuclear motion along the co-

ordinate of motor action. Therefore, the excited state population could be driven towards (by inducing the nuclear motion) or away from (by not inducing the motion) the conical intersection. Thus, control over the directionality and efficiency of the rotary motion of the molecular motor may be possible. However, the extremely fast damping (~100 fs) of the reactive vibrational mode means that such coherent control schemes would only be applicable for the first 100 fs after excitation. Thus, the ability to successfully implement such schemes on this timescale remains speculative.

3.3.3 Transient Absorption Spectroscopy

In order to investigate further the origin of the long fluorescence decay component, transient absorption spectroscopy was employed. Transient absorption probes excited states which are both emissive and non-emissive. In contrast, fluorescence up-conversion probes only fluorescent excited states. Therefore, transient absorption is ideally suited for determining the involvement of non-emissive excited state structures in the excited state decay mechanism of a probe molecule.

Transient spectra of 1-H in DCM (Figure 3.16) reveal two distinct transient features: a short lived absorption band centred at 560 nm and a significantly longer lived absorption band centred at 450 nm. This is consistent with a previous transient absorption study on a molecular motor analogous to 1-H. [27] After an initial decay, the 450 nm band remains unchanged over the lifetime of the measurement (>80 ps). Therefore, this band is assigned to ground state absorption of the metastable form of 1-H (1b in Figure 3.2). This is the product of the excited state isomerization reaction (Step 1 in Figure 3.2) and exhibits a half-life on the order of minutes (thermally activated decay).[16] The feature centred at 560 nm is comparatively short lived and is assigned to excited state absorption of 1-H (1a in Figure 3.2). Figure 3.17 shows a transient decay curve measured at 560 nm (black points) and fitted

to a bi-exponential function (red line) according to the procedure described previously (Chapter 2).

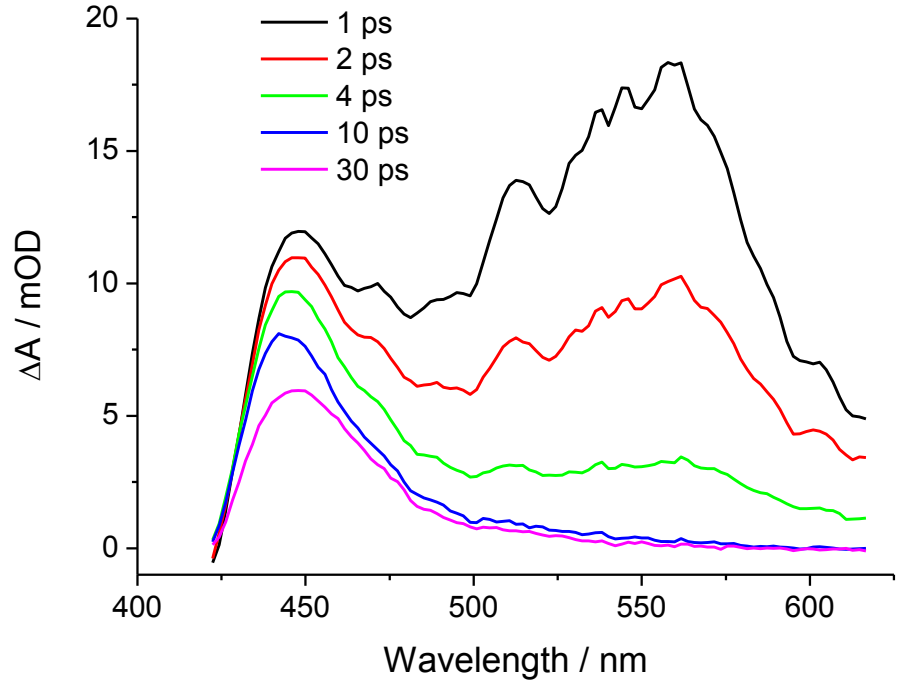

Figure 3.16 – *Time-dependent transient spectra of 1-H in DCM.*

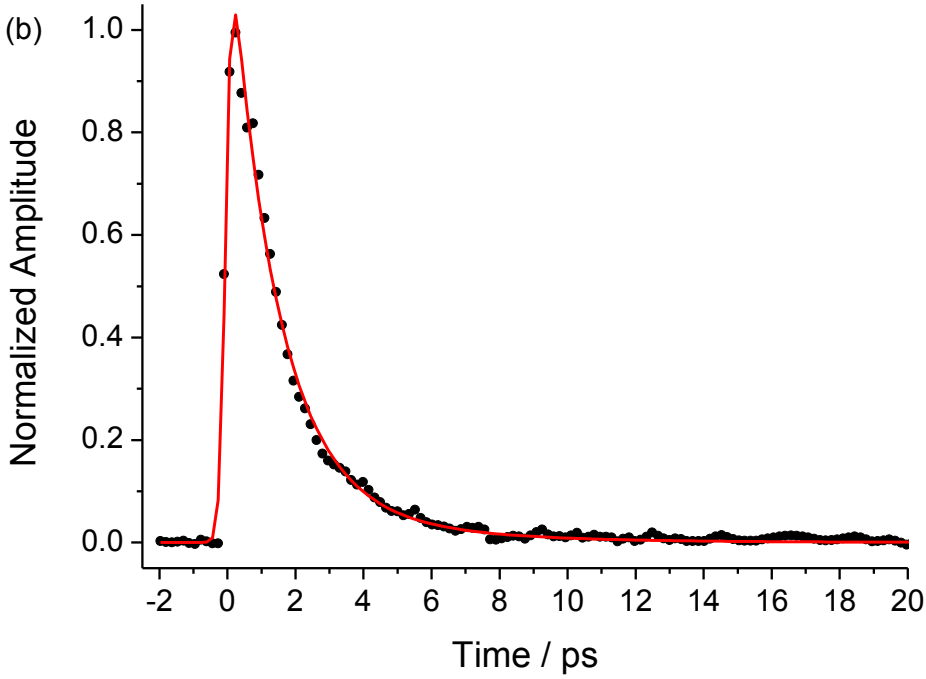

Figure 3.17 - *Time-domain decay of the 560 nm transient (black points) and corresponding fitted function (red line).*

The lifetime of this transient feature is thus revealed to 1.5 ps. This is in close agreement with the time constant of the longer exponential decay component of the integrated intensity of the time-dependent emission spectrum (~1 ps, Figure 3.14). Therefore, we suggest that the long component of the fluorescence decay and the decay of the 560 nm transient feature represent the same process: the relaxation of a 'dark' excited state to the ground state (most likely by internal conversion at a conical intersection). In contrast, we suggest that the ~100 fs fluorescence decay component represents an emissive excited state ('bright state') relaxing to the dark excited state. However, in order for the relaxation of the dark state to be detected in the fluorescence measurement (as the long component of the fluorescence decay), the dark state population must still be able to reach an emissive region of the excited state potential energy surface. Therefore, we suggest that the dark state population is able to repopulate the bright state by passing over a barrier on the excited state surface. Such a mechanism would give rise to a bimodal fluorescence decay profile as is observed for 1-H (Figure 3.14).

In order to provide further evidence for this assignment, we turned to calculations reported previously[18,19] for a molecular motor analogous to 1-H. As described previously, these calculations suggest that the initial electronic excitation is a π-π^* transition of the central double bond. The initially populated excited state (Franck-Condon state) then undergoes rapid structural evolution *via* simultaneous twisting about the 'axle' bond (C9-C1' in Figure 3.1) and extensive pyramidalization at the stator-axle linkage (C9 in Figure 3.1). An excited state potential energy surface was calculated, on which two conical intersections with the ground state surface were identified.[18,19] These conical intersections were reported to lie slightly above minimum energy and along the pyramidalization and rotation co-ordinates relative to the ground state structure. Thus, significant structural change in the excited state is required for these molecules to reach a conical intersection. This is consistent with the proposed bright to dark state model.

The calculated excited state potential energy surface[19] was used as a model surface on which to map the primary processes which occur after excitation of 1-H (Figure 3.18). The initial excitation leads to population of the Franck-Condon state (FC) on the excited state potential energy surface (represented by a diffuse circle). The FC state is emissive and so is termed the 'bright state'. This population undergoes rapid (~100 fs timescale) excited state structural evolution as a function of both pyramidalization and rotation to a position of minimum energy on the surface. The relaxed state has a significantly reduced fluorescence transition moment and so is termed a 'dark state'. Therefore, this bright to dark state relaxation is the origin of the ~100 fs fluorescence decay component. The initial excitation of 1-H also coherently excites three vibrational modes (113 cm^{-1}, 180 cm^{-1} and 294 cm^{-1}). This results in oscillations during the structural motion (as indicated by a broken arrow in Figure 3.18).

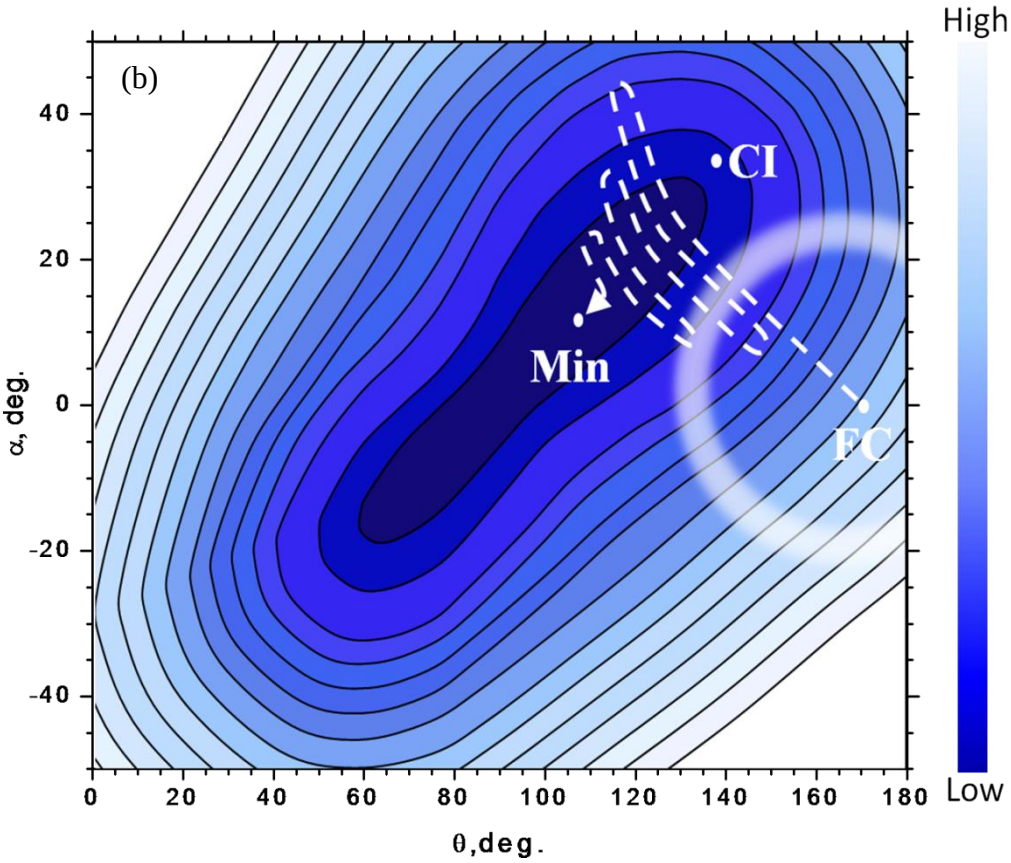

Figure 3.18 - *A schematic representation of the primary events on the excited state potential energy surface of **1**-H after electronic excitation.*

From the dark state, the excited state population decays *via* internal conversion at the conical intersection (CI). Since the conical intersection lies slightly above minimum energy, internal conversion occurs on a slower timescale (~1 ps). The dark state population is also able to return to the emissive region of the surface over the barrier which formed the downhill nature of the initial relaxation. Therefore, the relaxation of the dark state population to the ground state is the origin of both the ~1 ps fluorescence decay component and the ~1.5 ps lifetime of the 550 nm transient absorption band. Thus, the differing timescales of decay exhibited by the bright state and dark state is reflected by the distinctly bi-modal decay of the 1-H emission spectrum.

3.3.4 Solvent Dependence

In order to further probe the nature of the structural evolution undergone by 1-H on the excited state potential energy surface, the solvent dependence of the excited state decay dynamics was investigated. Particular attention was given to the effects of solvent polarity and viscosity. The polarity of the solvent can have a large effect upon excited state dynamics, particularly if the electronic structure of the ground and excited states of a probe molecule differ significantly (Chapter 1). Thus, the study of solvent polarity effects in this work can give an insight into the charge transfer character of the electronic excitation of the molecular motor. The viscosity of the solvent can affect the excited state dynamics since structural modifications involving large scale torsional motion, as may occur during cis-trans isomerisation reactions,[28] are generally expected to displace a significant volume of solvent. This leads to slower structural evolution and so a longer lived excited state (Chapter 1). As a result, the study of solvent viscosity effects upon the 1-H excited state decay dynamics can provide an insight into the nature of the motion along the pyramidalization and rotational co-ordinates. The effects of solvent polarity and viscosity upon the excited state dynamics were assessed by both fluorescence up-conversion and transient absorption spectroscopies.

The fluorescence decay curves of 1-H recorded at 556 nm (corresponding to the red side of the emission spectrum in all cases) in a series of solvents (of varied polarity and viscosity) are presented in Figure 3.19. The longer component of the fluorescence decay is best represented on a log intensity scale (Figure 3.19b). The raw data was fitted to a function comprising the sum of exponential decay and damped harmonic oscillator terms according to the procedure described previously (Chapter 2). The parameters of these fitting functions are shown in Table 3.4 (exponential decay terms) and Table 3.5 (oscillator components). An adequate fit to the data was achieved with a sum of 2 exponential terms and 3 oscillators for the measurements in acetonitrile, ethanol and cyclohexane (in line with the data recorded in DCM). However, an additional (intermediate) exponential term (τ_2 in Table 3.4) was required for the most viscous solvents (decalin and octanol). The time constant of τ_2 was found to be much closer to the short exponential term (τ_1 in Table 3.4) than that of the long exponential term (τ_3 in Table 3.4). Therefore, the weighted average of τ_1 and τ_2 was calculated ($<\tau_1>$ in Table 3.4) and taken as a representation of the fast exponential decay component for the measurements in decalin and octanol.

In all cases, the ultrafast decay is superimposed with a series of oscillations as observed previously for 1-H in DCM (Section 3.3.2). The frequency of each damped harmonic oscillator term does not vary with solvent within experimental error (Table 3.5). This is not a surprising observation since the excitation of a vibrational mode is an intramolecular process and thus is not expected to exhibit a solvent dependence. However, each mode is damped slightly more quickly in polar solvents. This suggests that the coherent nuclear motion induced by the vibrational modes is dephased more quickly in polar solvents. Polar solvents are able to support a broader distribution of initial frequencies of the coherently excited vibrational modes. This is because polar solvents are able to better stabilise the electronic structure of the excited state.

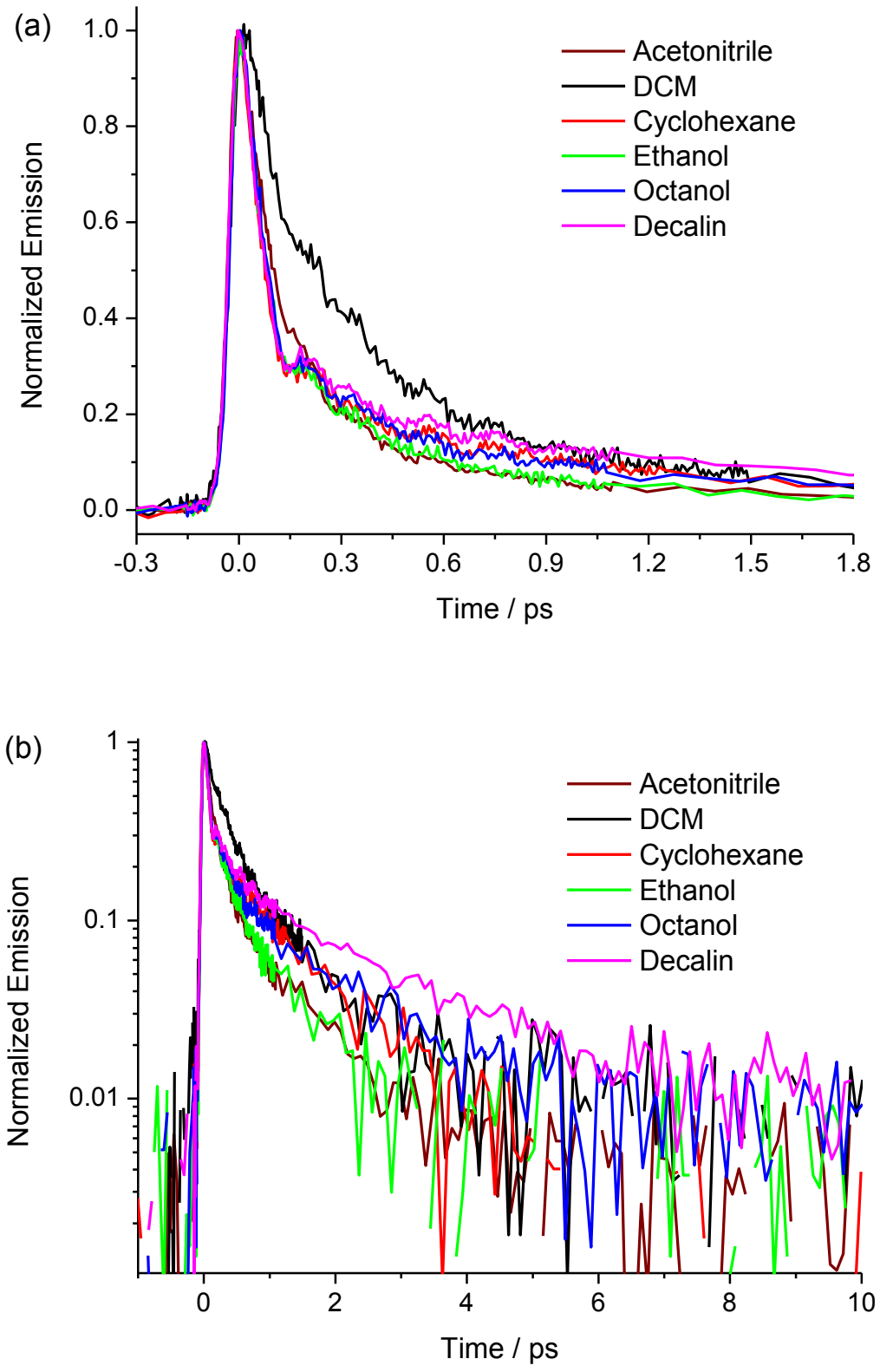

Figure 3.19 - *Solvent dependent fluorescence decay curves of 1-H measured at 556 nm on (a) a linear intensity scale and (b) a log-intensity scale.*

Table 3.4 - *Exponential components of the function fitted to the solvent dependent fluorescence decay data of 1-H. Repeat fits to each measurement determined the error of each parameter to be within 15%.*

Solvent	***Viscosity / mPa s***	τ_1 **/ps**	A_1	τ_2 **/ps**	A_2	$\langle\tau_1\rangle$ **/ps**	τ_3 **/ps**	A_3
Acetonitrile	0.369	0.14	0.88	-	-		1.12	0.12
DCM	0.431	0.29	0.81	-	-		1.48	0.19
Cyclohexane	0.894	0.10	0.76	-	-		1.15	0.24
Ethanol	1.074	0.17	0.78	-	-		1.02	0.22
Decalin	2.495	0.07	0.70	0.44	0.19	0.15	2.92	0.11
Octanol	7.288	0.12	0.65	0.62	0.27	0.27	2.68	0.08

Table 3.5 – *Damped harmonic oscillator components of the function fitted to the solvent dependent fluorescence decay data of 1-H. Repeat fits to each measurement determined the error of each parameter to be within 25%.*

Solvent	***Viscosity / mPa s***	τ_{D1} **/ ps**	ω_1 **/ THz**	$A_{\omega1}$	φ_1	τ_{D2} **/ ps**	ω_2 **/ THz**	$A_{\omega2}$	φ_2	τ_{D3} **/ ps**	ω_3 **/ THz**	$A_{\omega3}$	φ_3
Acetonitrile	0.369	0.09	3.17	0.54	0.56	0.23	5.47	0.23	0.38	0.20	8.53	0.25	1.41
DCM	0.431	0.15	3.72	0.64	0.14	0.30	5.49	0.24	0.04	0.64	8.76	0.12	0.50
Cyclohexane	0.894	0.14	3.50	0.77	0.94	0.32	5.28	0.14	0.47	0.28	8.67	0.09	0.56
Ethanol	1.074	0.09	3.17	0.73	0.68	0.17	5.43	0.17	0.18	0.16	8.50	0.10	1.19
Decalin	2.495	0.16	3.49	0.68	1.07	0.42	5.39	0.18	0.35	0.34	8.43	0.14	1.80
Octanol	7.288	0.08	3.21	0.78	0.84	0.19	5.78	0.12	-0.22	0.20	8.55	0.10	1.39

Therefore, a wider distribution of excited state electronic structures leads to a wider frequency distribution of the coherently excited vibrational modes in polar solvents. Thus, a broader distribution of frequencies contributes to the coherent nuclear motion. Therefore, the coherent nature of these vibrations is lost more quickly and so the oscillation in the time domain data is damped more quickly. In contrast, the damping time of the oscillator terms show no dependence upon solvent viscosity (for example, ethanol compared to octanol). This is not a surprising observation since the nuclear motion of a vibrational mode is very unlikely to displace a volume of solvent large enough to be influenced by the friction of the medium.

The bi-modal structure of the fluorescence decay curve described previously for 1-H in DCM (Figure 3.8) is retained in each solvent. In each case, a major amplitude fast decay term (τ_1 in Table 3.4) and a minor amplitude longer decay term (τ_3 in Table 3.4) are found. The decay time of the fastest exponential component (τ_1 and $< \tau_1 >$ in Table 3.4) was not found to exhibit any discernible solvent dependence. No dependence was found upon solvent polarity where the decay time in acetonitrile (140 fs) is comparable to that observed in cyclohexane (100 fs) within experimental error (Table 3.4). The lack of solvent polarity effects suggests that the initially populated excited state does not exhibit any significant charge transfer character relative to the ground state structure. Thus, the polarity of the solvent does not affect the stabilisation of the Franck-Condon bright state population. This is consistent with the lack of solvent polarity effect observed for the steady state spectroscopy of 1-H (Section 3.3.1).

Similarly, no dependence of the short exponential decay was found upon solvent viscosity where the decay time in ethanol (1 mPa s) is comparable to that observed in octanol (7.3 mPa s) within experimental error (170 fs and 120 fs respectively, Table 3.4). This shows that the relaxation of the bright state to the dark state is insensitive to friction of the medium. Two possible explanations can be invoked to explain this observation. Firstly, the excited state structural evolution is sufficiently strongly downhill (driven by the release of intramolecular

strain) such that any solvent friction effects are overcome by this driving force. Alternatively, the excited state structural evolution which facilities relaxation of the bright state to the dark state does not involve any large scale torsional motion. Such motion would be expected to displace a significant enough volume of solvent such that it is retarded in more viscous media (See Chapter 1 for a detailed discussion of solvent friction effects upon excited state molecular dynamics). Of the two co-ordinates believed to be involved in the excited state structural evolution of 1-H, pyramidalization is likely to displace a significantly smaller volume of solvent than rotation.[29-31] Therefore, the viscosity independent nature of the bright state to dark state relaxation dynamics suggests that pyramidalization may be the most significant co-ordinate of this relaxation process.

In contrast, the decay time of the longest exponential component (τ_3 in Table 3.4) exhibits no dependence upon solvent polarity (~1.1 ps in both acetonitrile and cyclohexane) but a clear dependence upon solvent viscosity (~1 ps in Ethanol compared to ~2.7 ps in octanol). The lack of solvent polarity dependence is consistent with an electronic excited state with no significant charge transfer character (as observed for τ_1). However, the dependence of τ_3 upon solvent viscosity is an observation which does offer better insight into the mechanism of excited state structural evolution of 1-H. This solvent viscosity dependence suggests that the relaxation of the dark state to the ground state proceeds *via* structural evolution which *does* require the displacement of a solvent volume large enough to be retarded by more viscous media. Therefore, it can be suggested that the approach of the dark state to the conical intersection (Figure 3.18) is facilitated by structural evolution which involves a more significant degree of torsional motion compared to that of the bright to dark state relaxation. However, the extent of the viscosity dependence remains far smaller than that expected of such sterically bulky groups undergoing large scale rotational motion.[32-34] In particular, τ_3 exhibits no difference (within experimental error) in octanol compared to decalin (a threefold

increase in viscosity, Table 3.4). Thus, although it is clear that relaxation of the dark state to the conical intersection does involve some motion along the rotational co-ordinate, this mechanism is more complex than simple torsional motion. It is most likely that a combination of torsion and pyramidalization facilitate the isomerization of 1-H in a manner which requires the displacement of only a small volume of solvent. Such a mechanism is employed as the rational for the viscosity independent excited state decay dynamics of the green fluorescent protein chromophore (discussed in detail in Chapter 1 and Chapter 7). Thus, some further insight has been gained into the mechanism of excited state structural evolution which facilitates the photochemical isomerization step of the 1-H motor cycle, but this mechanism remains far from fully resolved.

Figure 3.19 reveals that the fluorescence decay curve measured in DCM is anomalous. This is further highlighted by the timescale of the fastest decay component (τ_1 in Table 3.4) in DCM is significantly longer than the other solvents studied (approximately a factor of 2). This can clearly be seen in Figure 3.19 where the decay in DCM is obviously significantly longer over the first picosecond after excitation. A similar (but less significant) effect is observed for the timescale of the longest decay component (τ_3 in Table 3.4). Thus, the fluorescence decay dynamics of 1-H are uniquely affected by DCM. One possible explanation is a density effect. Of the solvents studied here, DCM has the significantly higher density. It is planned to investigate further the possible effects of solvent density upon the excited state dynamics of 1-H in the future. Thus, the rationale for the observed differences of the fluorescence decay dynamics in DCM currently remains unclear.

In order to further assess the excited state decay model proposed previously (Section 3.3.3) based upon the excited state decay dynamics of 1-H in DCM, the solvent dependence of the transient absorption spectroscopy was also assessed. Particular attention was given to the

comparison between the lifetime of the dark state transient absorption feature and the long component of the fluorescence decay (τ_3 in Table 3.4) in each solvent. In each solvent, as reported for 1-H in DCM (Figure 3.17), the transient spectra reveal two distinct transient states. Again, the faster decaying absorption band (centred at ~560 nm in all solvents) is assigned to absorption of the dark excited state of 1-H. The effect of solvent viscosity on the lifetime of the dark state was assessed by plotting the decay curves of the 560 nm transient in all solvents (Figure 3.20). The raw time-domain data (points) were fitted to a single exponential (in the case of acetonitrile, DCM, cyclohexane and ethanol) or bi-exponential function (in the case of decalin and octanol) represented by lines in Figure 3.2 . This is consistent with the fluorescence lifetime data where an additional (third) exponential term was required to fit the data recorded in decalin and octanol (Table 3.5). The parameters of the functions fitted to the dark state transient absorption decay data are summarised in Table 3.6. In the case of decalin and octanol, the weighted average of the two exponential terms was calculated as a representation of the lifetime of the dark state in these solvents ($<\tau>$ in Table 3.6).

The lifetime of the dark state from transient absorption ($<\tau>$ in Table 3.6) is compared directly to the long component of the fluorescence decay (τ_3 in Table 3.4) for each solvent in Figure 3.21. For each solvent, there is a good agreement between the lifetime of the dark state (from TA) and the long component of the fluorescence decay. Therefore, the model mechanism of excited state decay proposed for 1-H remains valid for each solvent studied.

The friction of the medium does not affect the rate of the bright to dark state decay (τ_1) but does have an effect upon the rate of the dark state decay to the ground state (τ_3). Thus, it can be suggested that the relaxation of the bright state to the dark state involves significantly less torsional motion than is required for the dark state population to reach the conical intersection and hence relax to the ground state.

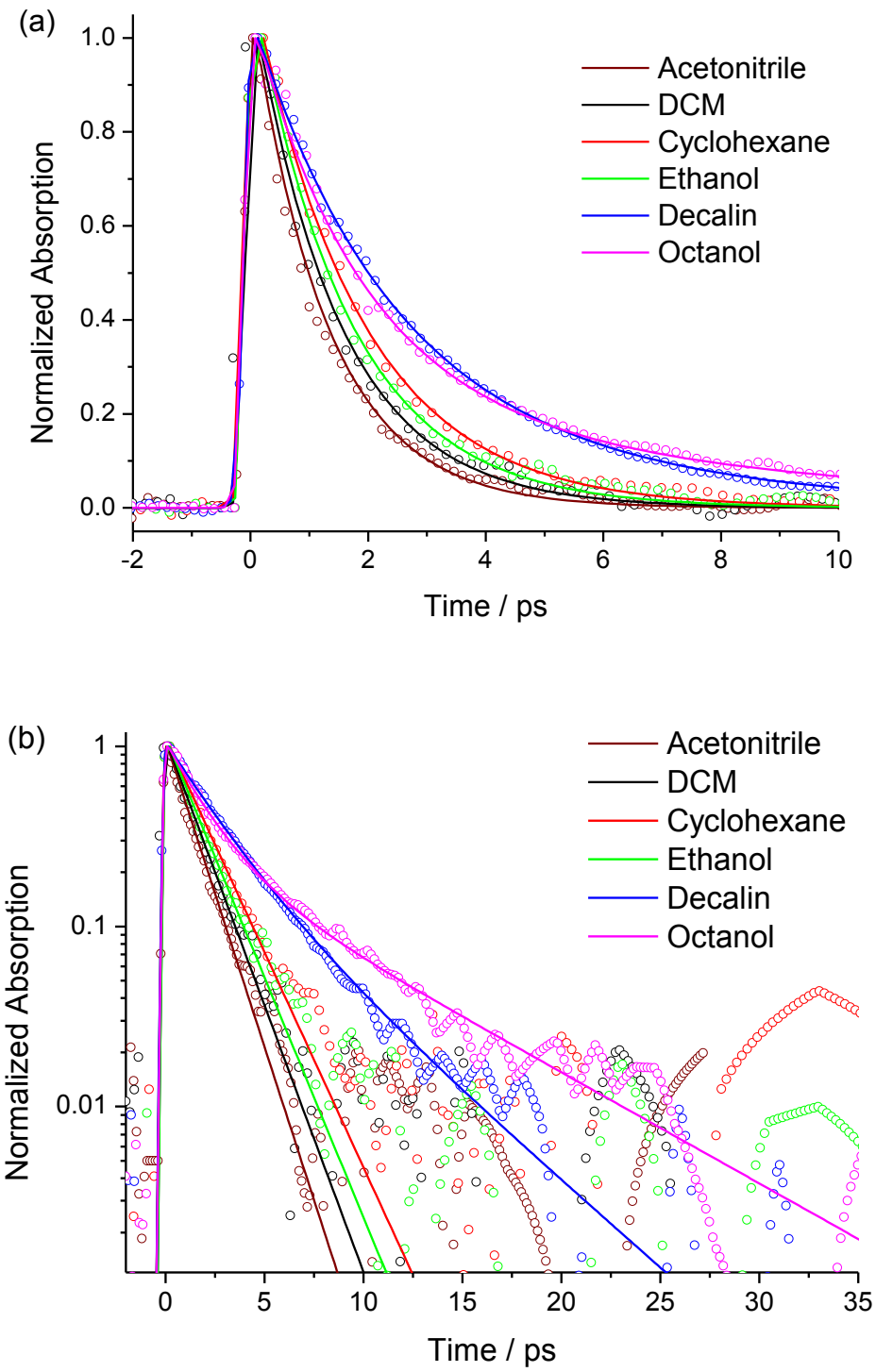

Figure 3.20 - *Solvent dependent decay of the dark state transient of 1-H at 560 nm on (a) a linear scale and (b) a log-scale. The raw data (points) were fitted to an exponential function (lines) in each case.*

Table 3.6 - *Parameters of the exponential fits to the solvent dependent dark state transient decay curves. Repeat measurements determined the error to be within 10% for each parameter.*

Solvent	***Viscosity / mPa s***	τ_1 **/ps**	A_1	τ_2 **/ps**	A_2	$\langle\tau\rangle$ **/ps**
Acetonitrile	0.369	1.28	1	-	-	-
DCM	0.431	1.47	1	-	-	-
Cyclohexane	0.894	1.82	1	-	-	-
Ethanol	1.074	1.60	1	-	-	-
Decalin	2.495	2.17	0.70	4.50	0.30	2.88
Octanol	7.288	1.72	0.73	6.61	0.27	3.03

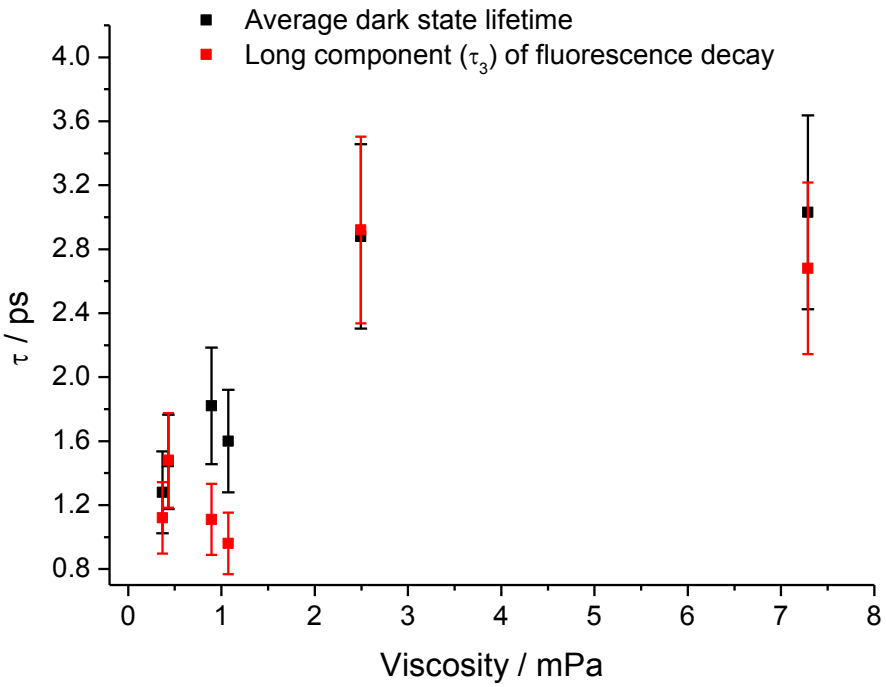

Figure 3.21 - *A comparison of the viscosity dependence of the dark state lifetime (from transient absorption) and the long exponential component of the fluorescence decay (from fluorescence up-conversion).*

3.4 Conclusion

The very earliest dynamics on the excited state potential energy surface of a unidirectional molecular rotary motor were probed by fluorescence up-conversion and transient absorption spectroscopies. An ultrafast bi-exponential fluorescence decay was observed, suggesting a possible bi-modal decay pathway of the excited state population. The fluorescence decay also exhibited a series of oscillations as a result of coherent excitation of Franck-Condon active vibrational modes. The time dependence of the reconstructed emission spectrum also revealed a bi-exponential decay, with oscillatory behaviour in the integrated intensity, mean frequency and width of the spectrum. This provides further evidence for a bimodal excited state relaxation, and also suggests that the coherently excited vibrational modes modulate both the transition moment (intensity) and frequency of the 1-H emission.

Transient absorption measurements revealed a transient absorption feature with a lifetime which matches the slowest component of the fluorescence decay. This allowed, with the aid of existing calculations on similar systems, the proposal of a model reaction scheme for the processes involved in the 'power stroke' of the motor molecule. We suggest that the initial excitation creates a 'bright' (Franck-Condon region) excited state population. Rapid relaxation (~100 fs) to a local minimum on the excited state potential energy surface creates an excited state population with a significantly reduced transition moment ('dark state'). This relaxation process was found to be solvent independent and so we suggest that structural motion along the pyramidalization co-ordinate may be more heavily involved in the bright to dark state decay. The dark state then decays to the ground state *via* internal conversion at a conical intersection. The dark state population is able to re-access the emissive region of the surface *via* a barrier and so the deactivation of the dark excited state to the ground state is represented by both the slower component of the fluorescence decay (~1 ps) and the decay of the transient absorption feature. The dark state lifetime was found to exhibit a dependence

upon solvent viscosity and so we suggest heavier role of torsional motion in the dark state decay co-ordinate in comparison to the decay of the bright state. Of the three coherently excited vibrational modes, the major amplitude mode (113 cm^{-1}) is suggested to be directly coupled to the pyramidalization co-ordinate whereas the minor modes (180 cm^{-1} and 294 cm^{1}) are ascribed to spectator modes. However, further evidence is required to provide definitive confirmation of these assignments.

3.5 References

(1) Balzani, V.; Credi, A.; Venturi, M. *Chem. Soc. Rev.* **2009**, *38*, 1542.

(2) Yoshida, M.; Muneyuki, E.; Hisabori, T. *Nat. Rev. Mol. Cell Biol.* **2001**, *2*, 669.

(3) Miller, R. J. *Nat. Chem.* **2012**, *4*, 523.

(4) Koumura, N.; Geertsema, E. M.; Meetsma, A.; Feringa, B. L. *J. Am. Chem. Soc.* **2000**, *122*, 12005.

(5) Koumura, N.; Zijlstra, R. W. J.; van Delden, R. A.; Harada, N.; Feringa, B. L. *Nature* **1999**, *401*, 152.

(6) Vicario, J.; Meetsma, A.; Feringa, B. L. *Chem. Commun.* **2005**, 5910.

(7) Pollard, M. M.; ter Wiel, M. K. J.; van Delden, R. A.; Vicario, J.; Koumura, N.; van den Brom, C. R.; Meetsma, A.; Feringa, B. L. *Chem. Eur. J.* **2008**, *14*, 11610.

(8) Pollard, M. M.; Klok, M.; Pijper, D.; Feringa, B. L. *Adv. Funct. Mater.* **2007**, *17*, 718.

(9) Klok, M.; Boyle, N.; Pryce, M. T.; Meetsma, A.; Browne, W. R.; Feringa, B. L. *J. Am. Chem. Soc.* **2008**, *130*, 10484.

(10) Klok, M.; Browne, W. R.; Feringa, B. L. *Phys. Chem. Chem. Phys.* **2009**, *11*, 9124.

(11) Cnossen, A., University of Groningen, 2013.

(12) Kay, E. R.; Leigh, D. A.; Zerbetto, F. *Angew. Chem.-Int. Edit.* **2007**, *46*, 72.

(13) Potter, E. D.; Herek, J. L.; Pedersen, S.; Liu, Q.; Zewail, A. H. *Nature* **1992**, *355*, 66.

(14) Wohlleben, W.; Buckup, T.; Herek, J. L.; Motzkus, M. *ChemPhysChem.* **2005**, *6*, 850.

(15) Heisler, I. A.; Kondo, M.; Meech, S. R. *J. Phys. Chem. B.* **2009**, *113*, 1623.

(16) Pollard, M. M.; Wesenhagen, P. V.; Pijper, D.; Feringa, B. L. *Org Biomol. Chem.* **2008**, *6*, 1605.

(17) Nakamura, T.; Takeuchi, S.; Suzuki, N.; Tahara, T. *Chem. Phys. Lett.* **2008**, *465*, 212.

(18) Kazaryan, A.; Kistemaker, J. C. M.; Schafer, L. V.; Browne, W. R.; Feringa, B. L.; Filatov, M. *J. Phys. Chem. A.* **2010**, *114*, 5058.

(19) Kazaryan, A.; Lan, Z.; Schäfer, L. V.; Thiel, W.; Filatov, M. *J. Chem. Theor. Comput.* **2011**, *7*, 2189.

(20) Chudoba, C.; Riedle, E.; Pfeiffer, M.; Elsaesser, T. *Chem. Phys. Lett.* **1996**, *263*, 622.

(21) Pollard, W. T.; Lee, S.-Y.; Mathies, R. A. *J. Chem. Phys.* **1990**, *92*, 4012.

(22) Mokhtari, A.; Chebira, A.; Chesnoy, J. *J. Opt. Soc. Am. B.* **1990**, *7*, 1551.

(23) Rubtsov, I. V.; Yoshihara, K. *J. Phys. Chem. A.* **1999**, *103*, 10202.

(24) Myers, A. B.; Mathies, R. A. *J. Chem. Phys.* **1984**, *81*, 1552.

(25) Ishii, K.; Takeuchi, S.; Tahara, T. *Chem. Phys. Lett.* **2004**, *398*, 400.

(26) Takeuchi, S.; Ruhman, S.; Tsuneda, T.; Chiba, M.; Taketsugu, T.; Tahara, T. *Science* **2008**, *322*, 1073.

(27) Augulis, R.; Klok, M.; Feringa, B. L.; van Loosdrecht, P. H. M. *Phys. Status. Solidi. C, Vol 6, No 1*; Itoh, T. T. K. S. M., Ed. 2009; Vol. 6, p 181.

(28) Waldeck, D. H. *Chem. Rev.* **1991**, *91*, 415.

(29) Chudoba, C.; Kummrow, A.; Dreyer, J.; Stenger, J.; Nibbering, E. T. J.; Elsaesser, T.; Zachariasse, K. A. *Chem. Phys. Lett.* **1999**, *309*, 357.

(30) Yoshihara, T.; Druzhinin, S. I.; Zachariasse, K. A. *J. Am. Chem. Soc.* **2004**, *126*, 8535.

(31) Grilj, J.; Buchgraber, P.; Vauthey, E. *J. Phys. Chem. A.* **2012**, *116*, 7516.

(32) Changenet, P.; Zhang, H.; van der Meer, M. J.; Glasbeek, M.; Plaza, P.; Martin, M. M. *J. Phys. Chem. A.* **1998**, *102*, 6716.

(33) van der Meer, M. J.; Zhang, H.; Glasbeek, M. *J. Chem. Phys.* **2000**, *112*, 2878.

(34) Espagne, A.; Paik, D. H.; Changenet-Barret, P.; Martin, M. M.; Zewail, A. H. *ChemPhysChem* **2006**, *7*, 1717.

4 Excited State Dynamics of Substituted Unidirectional Molecular Rotary Motors

In this chapter the effect of substituents on the excited state dynamics of the unidirectional molecular motor studied in Chapter 3 are reported. Particular focus is placed upon the sensitivity of the excited dynamics to electron donating and withdrawing substituents. After detailing the experimental conditions employed (Section 4.2), the first results section will consider steady state spectroscopy (Section 4.3.1). This will be followed by a description of ultrafast fluorescence up-conversion (Section 4.3.2) and ultrafast transient absorption (Section 4.3.3) measurements. In both cases the effect of solvent on the dynamics of the derivatives will be described. Finally, the substituent dependence will be discussed in terms of the model of excited state relaxation proposed for the parent motor in Chapter 3. The kinetic predictions of that model will be investigated by solving the system of rate equations for the scheme proposed and calculating the time-dependent populations of the states observed (Section 4.3.5). This reveals a systematic dependence of the reactive potential energy surface on the substituent.

4.1 Introduction

As determined in the previous chapter, the central carbon-carbon double bond, the 'axle', plays a key role in the excited state dynamics of the unidirectional molecular rotary motor. Theory and experiment suggest that excited state cis-trans isomerization occurs *via* simultaneous rotation about this bond and pyramidalization at the C9 carbon atom (Figure 4.1). These excited state structural changes give rise to fast non-radiative decay of the excited state.[1] Given the key role of the double bond in the excited state structural dynamics, modification of its properties may be expected to result in significant changes to the excited state decay.

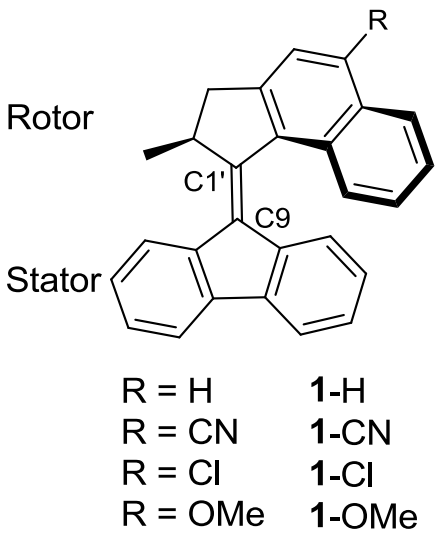

Figure 4.1 - *Structure of the substituted unidirectional molecular rotary motor derivatives.*

One way to achieve such a modification is by including electron withdrawing and donating substituents conjugated with the double bond. This is the topic of this chapter.

In earlier literature a number of studies have focused on substituent effects upon the cis-trans photoisomerization of stilbene and its derivatives.[2] Siewert and Spangler[3] found that electron donating substituents reduced the barrier to isomerization on the S_1 excited state potential energy surface. The substituents donate electron density to the delocalized system and thus stabilize the asymmetry in the electron density which forms in the excited state. King et al[4] found that the photoisomerization equilibria (photostationary state) of substituted stilbene, azobenzene and imine derivatives were also sensitive to the electron withdrawing and donating nature of the substituents. This study found that the nature of the substituents influenced the sensitivity of the photoisomerization to solvent polarity. In an attempt to gain further insight into the substituent dependence of the isomerization in stilbene, Dekhtyar and Rettig[5] modelled the ground and excited state structures of a series of electron donor-acceptor stilbene derivatives. The equilibrium bond lengths, electron density distributions and S_0-S_1 energy differences were found to be dependent upon the nature of the substituents.

These literature results suggested that modification of these structural parameters may also influence the molecular dynamics of photoisomerization in the motor systems. Therefore, a series of motors were prepared with electron donating and withdrawing substituents[6] (Figure 4.1). In comparison to the parent structure (1-H), these substituents are strongly electron donating (1-OMe), weakly electron withdrawing (1- Cl) and strongly electron withdrawing (1-CN). In each case the substituents were placed to be in direct conjugation with the central olefin. As a result, the electron donating or withdrawing character of the substituents can exert an influence over the electron density of the central olefin and indeed the entire delocalised system.[5] For 1-OMe and 1-CN the substituents are able to exert an influence *via* resonance effects.[7] In contrast, 1-Cl is expected to exert a much weaker influence *via* inductive effects.[7]

A previous study[6] was conducted to characterise the effects of these substituents upon the thermal helix inversion step in the ground state of the motor cycle (Step 2 Figure 3.2, Chapter 3). It was reported that the rate of this step was not sensitive to the electron donating or withdrawing nature of the substituent. However, the effects of these substituents upon the photochemical step of the motor cycle (Step 1 in Figure 3.2, Chapter 3) were not considered in any detail, although it was reported that the substituents significantly altered the photochemical quantum yield for formation of the metastable isomer[8] (1a compared to 1b in Figure 3.2, Chapter 3). The substituent dependence of the photochemical quantum yield is shown in Table 4.1 (reproduced from reference 6). As the electron withdrawing ability of the substituent was increased, the photochemical quantum yield increased. These data suggest that the excited state chemistry is affected more by the substituents than the ground state thermal helix inversion.

Table 4.1 – *The substituent dependent photochemical quantum yield (1a:1b in Figure 3.2, Chapter 3).This data is reproduced from Reference 8.*

Substituent	Quantum Yield
1-CN	0.2
1-Cl	0.15
1-H	0.14
1-OMe	0.048

To investigate this further, the substituent dependence of the excited state decay kinetics has been probed by ultrafast fluorescence up-conversion and transient absorption spectroscopies. The solvent dependence is also assessed, with particular focus placed upon the effects of viscosity and polarity. The data will be discussed in terms of the excited state mechanism proposed in the previous chapter.

4.2 Experimental

The molecular motor samples were supplied to us by the group of Prof. Ben Feringa (University of Groningen, The Netherlands). The experimental conditions employed for the steady state absorption and fluorescence, fluorescence up-conversion and transient absorption measurements are identical to those described previously for the parent molecule (1-H) in Chapter 3. Details regarding the measurement and fitting of the time-resolved data were given in Chapter 2.

Kinetic modelling was performed by integration of the rate equations using matrix methods.[9] The use of this procedure to determine analytical solutions of multi-step unimolecular kinetic schemes is well described in literature.[10-12] Briefly, a matrix was created based on the system of rate equations, for which eigenvalues and eigenvectors were calculated. The scalar coefficients, which relate the eigenvectors to the rate equation matrix, were then calculated. These three parameters provide a solution for the time dependent concentration of each

species in the model. In order to simplify the model, it was assumed that in each case the initial concentration (at time = 0 ps) of the excited state was equal to 1, so that details of oscillator strength, excitation pulse intensity and width are not required. Thus, the time dependent evolution (decay) of this initial excited state population was then calculated as a function of the rates of the remaining reaction pathways. The method was tested by solving a series of increasingly complex reaction schemes to which model solutions have previously been published.[9,13-17] The model reactions schemes and their calculated solutions (including the equations used and complete Mathematica scripts) are presented in Appendix 1.

4.3 Results and Discussion

4.3.1 Steady State Spectroscopy

The absorption and fluorescence spectra of each derivative in DCM are shown in Figure 4.2 and Figure 4.3 respectively. The absorption and emission maxima as well as the calculated Stokes shift in a range of solvents are summarised in Table 4.2.

In all cases, substitution leads to a red shift of absorption and emission relative to the parent molecule (1-H). Thus, both electron donating and withdrawing substituents lead to red shifted spectra. This is in line with previous studies of substituted stilbenes, where substitution at the para position resulted in red shifted spectra, with the magnitude of this red shift found to increase with the polarizability and size of the substituent.[2]

The Stoke's shift of each substituted motor derivative was found to be smaller in polar solvents (Table 4.2). This behaviour was observed previously for 1-H (Chapter 3) and is in contrast to that reported for substituted stilbenes.[2] Polar solvents were found to have a significant effect upon the steady state spectroscopy of donor/acceptor substituted stilbenes.[4]

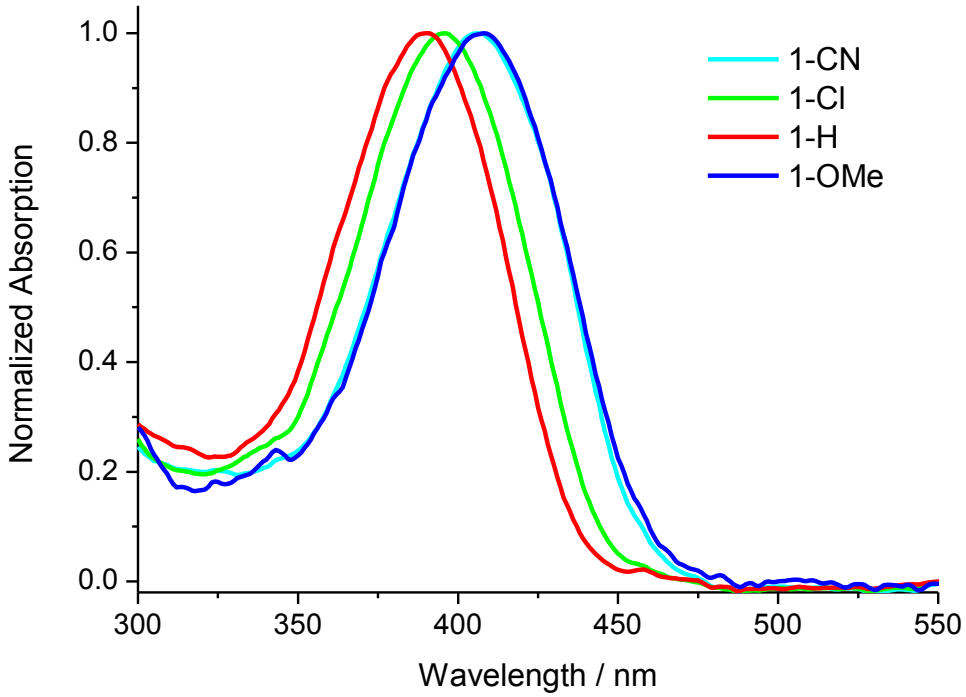

Figure 4.2 - *Steady state absorption spectra of each derivative in DCM.*

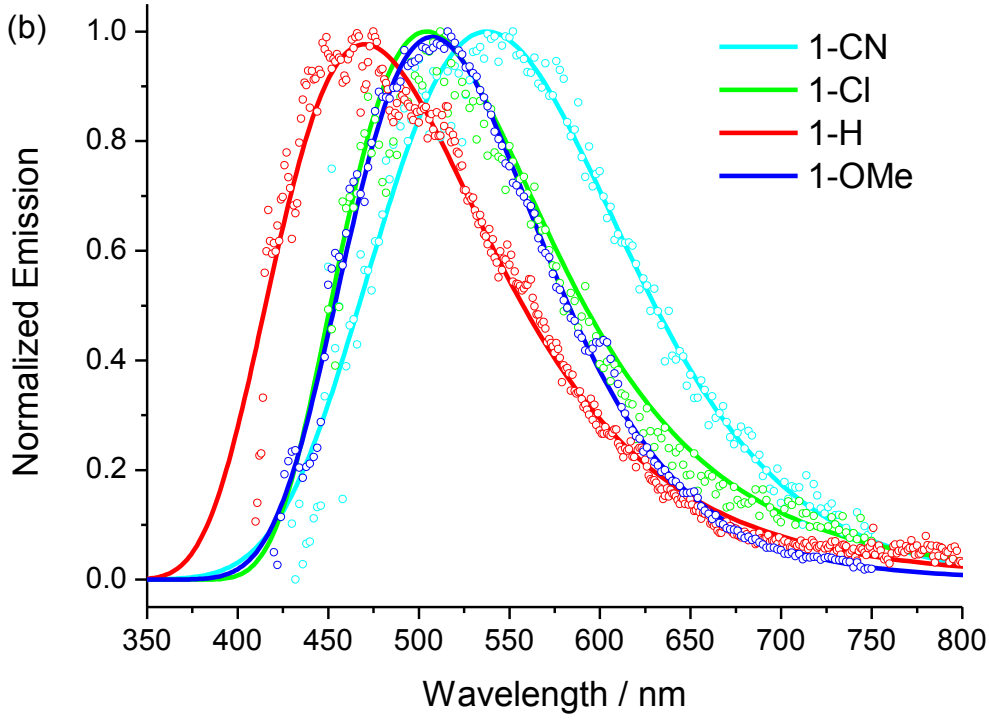

Figure 4.3 - *Steady state fluorescence spectra of each derivative in DCM.*

Table 4.2 - *Solvent dependence of the steady state absorption and fluorescence spectra of each derivative.*

Solvent	Viscosity / mPa s	Absorption Maximum / nm	Emission Maximum / nm	Stokes Shift / nm
1-CN				
Acetonitrile	0.37	403	515	112
DCM	0.43	406	538	132
Cyclohexane	0.89	402	525	123
Ethanol	1.07	402	510	108
Decalin	2.5	403	550	147
Octanol	7.29	404	542	138
1-Cl				
Acetonitrile	0.37	393	480	87
DCM	0.43	396	512	116
Cyclohexane	0.89	392	508	116
Ethanol	1.07	392	490	98
Decalin	2.5	393	507	114
Octanol	7.29	393	491	98
1-H				
Acetonitrile	0.37	386	465	79
DCM	0.43	390	475	85
Cyclohexane	0.89	387	489	102
Ethanol	1.07	386	470	84
Decalin	2.5	388	508	120
Octanol	7.29	388	472	84
1-OMe				
Acetonitrile	0.37	403	504	101
DCM	0.43	408	516	108
Cyclohexane	0.89	402	508	106
Ethanol	1.07	403	504	101
Decalin	2.5	403	508	105
Octanol	7.29	404	508	104

The stilbene data were interpreted in terms of a large change in dipole (charge transfer) between the ground and excited state of stilbene. As the polarity of the stilbene ground state is modified by donor/acceptor substituents, this charge transfer character became more significant.[5] Thus, polar solvents have a large effect upon stabilising the excited state of substituted stilbenes. The lack of solvent induced spectral shifts for the substituted molecular motor derivatives therefore suggests no large change between the electronic structures of the ground state and excited state population.

4.3.2 Ultrafast Fluorescence Up-Conversion Spectroscopy

To assess the substituent dependence of the excited state dynamics, the fluorescence decay of each substituted derivative in DCM was recorded by fluorescence up-conversion spectroscopy. For each derivative, the fluorescence decay was recorded at a series of emission wavelengths spanning the emission spectrum. The wavelength-resolved fluorescence decay curves of 1-CN, 1-Cl and 1-OMe are shown in Figure 4.4, Figure 4.5 and Figure 4.6 respectively. The general emission wavelength dependence exhibited by 1-H (Chapter 3) is retained for each substituted derivative. As the emission wavelength is tuned to the red, the lifetime of the excited state becomes longer. In each case, the raw data were fitted to a function comprising the sum of exponential and damped harmonic oscillator terms. The parameters of the fitted functions are shown for 1-CN in Table 4.3 and Table 4.4, for 1-Cl in Table 4.5 and Table 4.6 and for 1-OMe in Table 4.7 and Table 4.8 (exponential and oscillator terms respectively in each case). Two exponential terms were required to provide an adequate fit to the experimental data for 1-Cl and 1-OMe (as found for 1-H in Chapter 3). However, in the case of 1-CN an additional (intermediate) exponential term was required (τ_2 in Table 4.3). Therefore, the weighted average of τ_1 and τ_2 ($<\tau_1>$ in Table 4.3) was taken as a representation of the short component of the fluorescence decay for 1-CN.

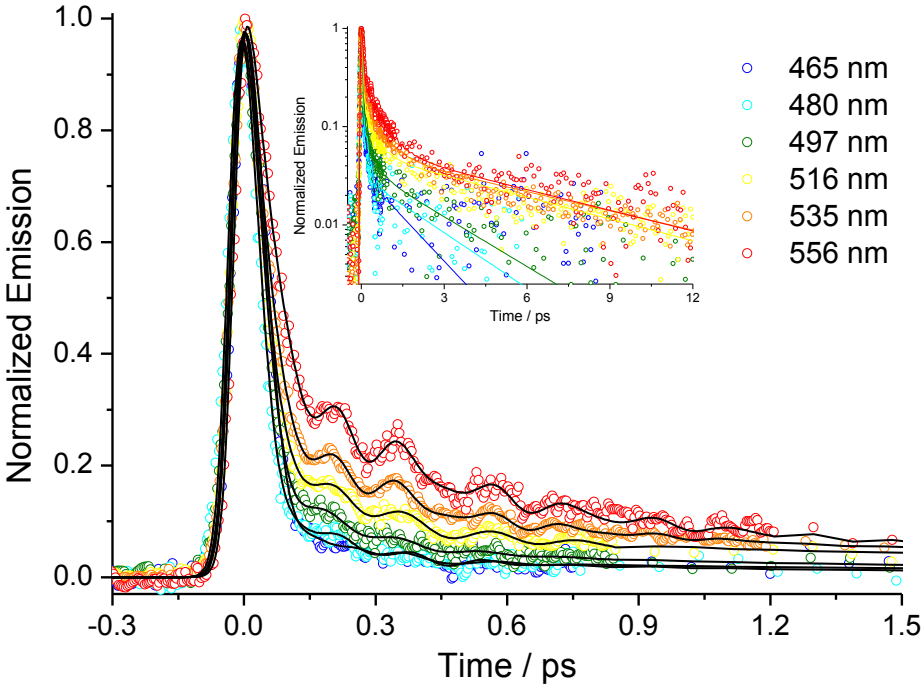

Figure 4.4 - *Wavelength-resolved fluorescence decay curves of 1-CN in DCM. Inset shows the data on a log intensity scale.*

Table 4.3 - *Exponential components of the functions fitted to the wavelength-resolved fluorescence decay curves of 1-CN in DCM. Repeat fits to each measurement determined the error of each parameter to be within 15%.*

Emission λ / nm	**τ_1 /ps**	**A_1**	**τ_2 /ps**	**A_2**	**$\langle\tau_1\rangle$ /ps**	**τ_3/ps**	**A_3**
464.8	0.07	0.91	0.19	0.06	0.077	1.37	0.04
472.4	0.06	0.89	0.23	0.09	0.076	1.95	0.02
480	0.07	0.87	0.16	0.10	0.079	2.61	0.03
487.7	0.07	0.86	0.30	0.10	0.094	3.03	0.04
496.9	0.08	0.84	0.27	0.11	0.10	2.63	0.05
506.1	0.09	0.83	0.38	0.11	0.12	3.94	0.06
515.5	0.09	0.80	0.40	0.13	0.13	5.75	0.07
525.1	0.10	0.73	0.40	0.19	0.16	5.95	0.08
534.7	0.11	0.73	0.55	0.20	0.20	6.36	0.07
544.5	0.11	0.65	0.45	0.26	0.21	6.47	0.09
555.9	0.12	0.59	0.53	0.33	0.27	6.11	0.08

Table 4.4 - *Damping (τD), frequency (ω), amplitude (Aω) and phase (Φ) components of the damped harmonic oscillator functions used to fit the oscillatory part of the* ***1****-CN fluorescence decay data. Repeat fits to each measurement determined the error of each parameter to be within 25%.*

Emission λ / nm	τ_{D1} / **ps**	ω_1 / **THz**	$A_{\omega 1}$	φ_1	τ_{D2} / **ps**	ω_2 / **THz**	$A_{\omega 2}$	φ_2	τ_{D3} / **ps**	ω_3 / **THz**	$A_{\omega 3}$	φ_3
464.8	0.08	3.62	0.80	0.17	0.19	5.41	0.12	0.41	0.16	7.86	0.08	-0.63
472.4	0.07	3.83	0.74	0.57	0.11	5.31	0.10	0.99	0.10	8.17	0.16	-0.23
480	0.08	3.68	0.73	0.51	0.19	4.99	0.11	1.15	0.09	8.48	0.16	-0.47
487.7	0.07	3.64	0.78	0.32	0.20	5.09	0.12	0.97	0.15	8.46	0.10	-0.45
496.9	0.07	3.68	0.88	0.51	0.18	5.36	0.11	0.93	0.12	8.34	0.01	0.32
506.1	0.07	3.54	0.83	0.68	0.24	5.33	0.09	0.96	0.15	8.49	0.07	0.37
515.5	0.08	3.39	0.84	0.84	0.38	5.15	0.07	1.14	0.11	8.20	0.08	1.07
525.1	0.08	3.34	0.88	0.83	0.35	5.30	0.08	0.92	0.29	8.29	0.04	1.11
534.7	0.08	3.33	0.86	0.68	0.34	5.36	0.09	0.84	0.39	8.20	0.05	1.48
544.5	0.08	3.52	0.82	0.54	0.45	5.46	0.09	0.65	0.41	8.35	0.09	1.32
555.9	0.09	3.36	0.81	0.47	0.50	5.33	0.10	0.77	0.35	8.25	0.10	1.41

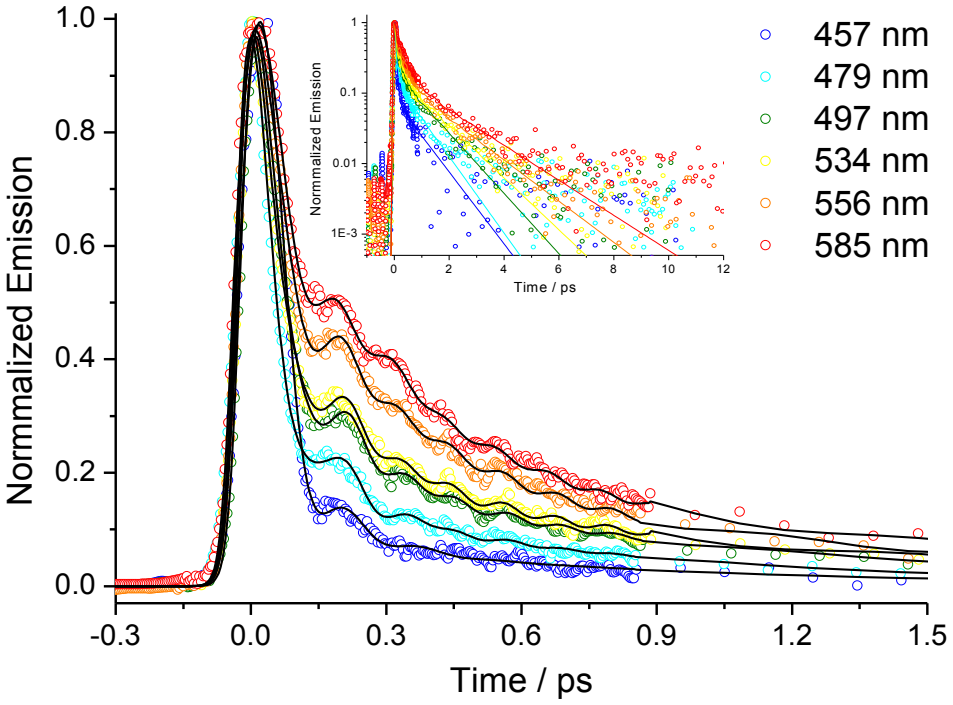

Figure 4.5 - *Wavelength-resolved fluorescence decay curves of 1-Cl in DCM. Inset shows the data on a log intensity scale.*

Table 4.5 - *Exponential components of the functions fitted to the wavelength-resolved fluorescence decay curves of 1-Cl in DCM. Repeat fits to each measurement determined the error of each parameter to be within 15%.*

Emission λ / nm	**τ_1 /ps**	**A_1**	**τ_2 /ps**	**A_2**
457.4	0.11	0.90	0.86	0.10
466.3	0.10	0.86	0.86	0.14
478.7	0.12	0.80	0.87	0.20
491.4	0.13	0.75	0.93	0.25
504.8	0.16	0.73	1.04	0.27
510.1	0.20	0.75	1.24	0.25
519	0.19	0.73	1.20	0.27
534.2	0.24	0.75	1.35	0.25
550.2	0.27	0.76	1.47	0.24
555.9	0.29	0.78	1.51	0.22
567.5	0.32	0.78	1.67	0.22
585.3	0.31	0.80	1.78	0.20

Table 4.6 - *Damping (τD), frequency (ω), amplitude (Aω) and phase (Φ) components of the damped harmonic oscillator functions used to fit the oscillatory part of the 1-Cl fluorescence decay data. Repeat fits to each measurement determined the error of each parameter to be within 25%.*

Emission λ / nm	τ_{D1} / **ps**	ω_1 / **THz**	$A_{\omega 1}$	φ_1	τ_{D2} / **ps**	ω_2 / **THz**	$A_{\omega 2}$	φ_2	τ_{D3} / **ps**	ω_3 / **THz**	$A_{\omega 3}$	φ_3
457.4	0.07	2.90	0.68	0.13	0.10	5.73	0.31	5.02	0.03	8.66	0.02	0.45
466.3	0.05	3.24	0.70	0.18	0.11	5.42	0.28	6.03	0.40	8.52	0.02	0.19
478.7	0.05	3.56	0.67	0.32	0.11	5.32	0.30	6.23	0.30	8.58	0.04	0.11
491.4	0.05	3.43	0.63	0.37	0.10	5.48	0.34	5.95	0.46	8.72	0.03	0.37
504.8	0.05	3.68	0.72	0.52	0.12	5.53	0.23	5.89	0.38	8.56	0.05	0.90
510.1	0.05	3.46	0.80	0.60	0.17	5.47	0.14	5.94	0.28	8.36	0.06	1.25
519	0.05	3.54	0.74	0.74	0.12	5.43	0.22	5.86	0.60	8.70	0.04	0.70
534.2	0.05	3.39	0.76	0.46	0.15	5.63	0.20	5.43	0.49	8.56	0.03	0.97
550.2	0.05	3.44	0.75	0.54	0.10	5.93	0.23	5.14	0.69	8.54	0.02	1.14
555.9	0.05	3.58	0.73	0.43	0.10	5.96	0.25	4.99	0.64	8.44	0.03	1.23
567.5	0.06	3.22	0.61	0.59	0.09	6.42	0.36	4.89	0.66	8.50	0.03	0.89
585.3	0.10	3.30	0.52	0.41	0.10	6.42	0.44	4.81	0.71	8.62	0.05	0.95

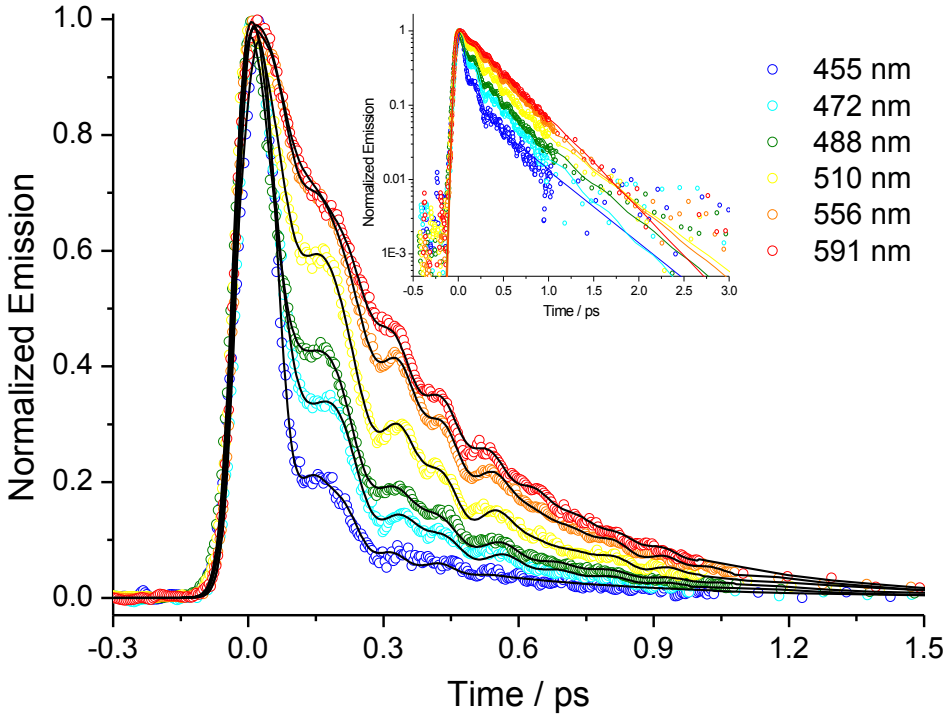

Figure 4.6 - *Wavelength-resolved fluorescence decay curves of 1-OMe in DCM. Inset shows the data on a log intensity scale.*

Table 4.7 - *Exponential components of the functions fitted to the wavelength-resolved fluorescence decay curves of 1-OMe in DCM. Repeat fits to each measurement determined the error of each parameter to be within 15%.*

Emission λ / nm	**τ_1 /ps**	**A_1**	**τ_2 /ps**	**A_2**
454.9	0.08	0.91	0.46	0.09
472.4	0.09	0.78	0.38	0.22
487.7	0.13	0.77	0.45	0.23
510.1	0.18	0.72	0.47	0.28
555.9	0.28	0.75	0.47	0.25
591.3	0.36	0.50	-	-

Table 4.8 - *Damping (τ_D), frequency (ω), amplitude ($A\omega$) and phase (Φ) components of the damped harmonic oscillator functions used to fit the oscillatory part of the 1-OMe fluorescence decay data. Repeat fits to each measurement determined the error of each parameter to be within 25%.*

Emission λ / nm	**τ_{D1} / ps**	**ω_1 / THz**	**$A_{\omega 1}$**	**φ_1**	**τ_{D2} / ps**	**ω_2 / THz**	**$A_{\omega 2}$**	**φ_2**	**τ_{D3} / ps**	**ω_3 / THz**	**$A_{\omega 3}$**	**φ_3**
454.9	0.10	4.91	0.30	0.18	0.12	7.94	0.30	3.53	0.11	10.05	0.39	3.69
472.4	0.16	5.07	0.55	0.84	0.29	8.15	0.18	2.64	0.12	10.12	0.27	3.62
487.7	0.17	5.13	0.53	0.60	0.33	8.05	0.17	2.65	0.13	9.86	0.30	3.80
510.1	0.23	5.02	0.45	1.11	0.29	8.22	0.31	2.37	0.26	10.06	0.24	3.12
555.9	0.25	5.05	0.37	1.28	0.30	8.27	0.37	2.40	0.36	10.29	0.27	2.92
591.3	0.10	4.52	0.41	1.34	0.25	8.42	0.35	2.25	0.40	10.12	0.24	3.40

In order to determine the substituent dependence of the excited state dynamics of the molecular motor, a comparison of the excited state decay kinetics of each derivative is required. The most suitable method is by direct comparison of the decay kinetics of the integrated intensity of the reconstructed time-dependent emission spectrum of each substituted derivative. This is because the decay of the integrated spectral intensity is independent of emission wavelength and so is unaffected by the significant emission wavelength dependence exhibited by the molecular motors. Therefore, the time-dependent emission spectra of each derivative were reconstructed from the wavelength-resolved time domain fluorescence decay curves (see Chapter 2 for a detailed description of this procedure). The resulting time-dependent spectra for 1-CN, 1-Cl and 1-OMe are shown in Figure 4.7 (a, b and c respectively). The time-dependent emission spectra of 1-H were presented previously in Chapter 3.

The time-domain evolution of the integrated spectral intensity was then calculated and compared directly for each derivative (Figure 4.8). In each case, an oscillation in the integrated intensity decay is observed (as found for 1-H, Chapter 3). Figure 4.8 shows that the most significant effect of substitution is upon the long component of the fluorescence decay. A clear trend is observed which follows the electron withdrawing/donating character of the substituents. As the electron withdrawing ability of the substituent becomes stronger (OMe < H < Cl < CN), the long decay component becomes significantly longer. In contrast, there is little effect upon the short component of the decay. For each derivative, the time-domain decay of the integrated intensity (points in Figure 4.8) was fitted to a function (lines in Figure 4.8) comprising the sum of exponential and damped harmonic terms. The parameters of the exponential components and oscillator components of these functions are shown in Table 4.9 and Table 4.10 respectively. A sum of three exponential and three damped oscillator terms were required to provide an adequate fit to the data for 1-CN, 1-Cl and 1-H. However, only two exponential terms were required for 1-OMe. As for the 1-CN wavelength resolved decay data, the weighted average of τ_1 and τ_2 ($<\tau_1>$ in Table 4.9) was taken as a representation of the 'short component of the fluorescence decay' (previously ascribed to the bright state decay of 1-H in Chapter 3) for 1-CN, 1-Cl and 1-H. In addition, subsequent discussion of the 'long component of the fluorescence decay' (ascribed to the dark state decay of 1-H in Chapter 3) will refer to τ_3 for each derivative (as for 1-H in Chapter 3).

Table 4.9 further highlights the significant effect of substitution upon the long component of the fluorescence decay. The lifetime of τ_3 is increased by a factor of more than 10 for 1-CN (4.46 ps) compared to 1-OMe (0.37 ps). Thus, the lifetime of the dark state is made significantly longer by a strong electron withdrawing substituent, where as a strong electron donating substituent results in a significant shortening of the dark state lifetime.

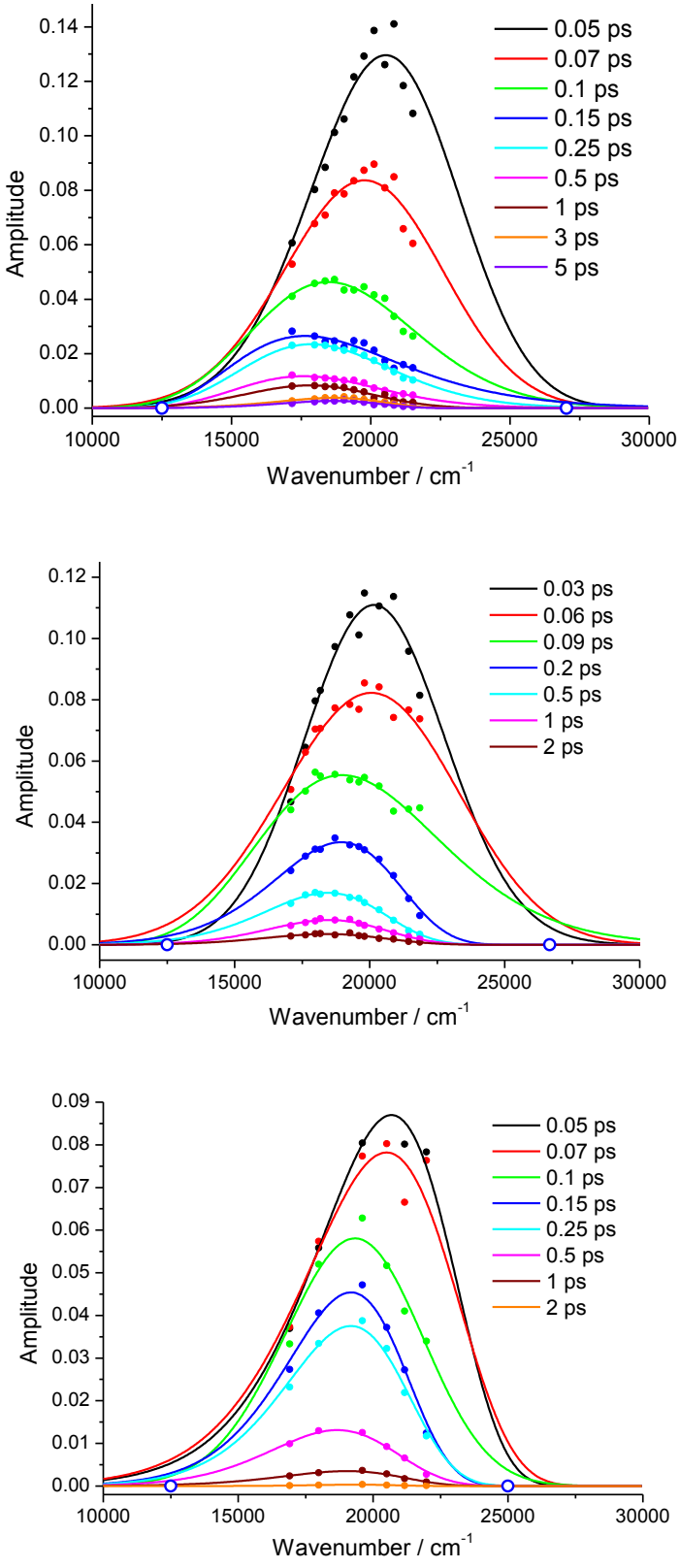

Figure 4.7 - *Time-dependent emission spectra of (a)* 1-*CN, (b)* 1-*Cl and (c)* 1-*OMe in DCM reconstructed from the deconvoluted wavelength-resolved fluorescence decays (points) and fitted to log-normal function (lines).*

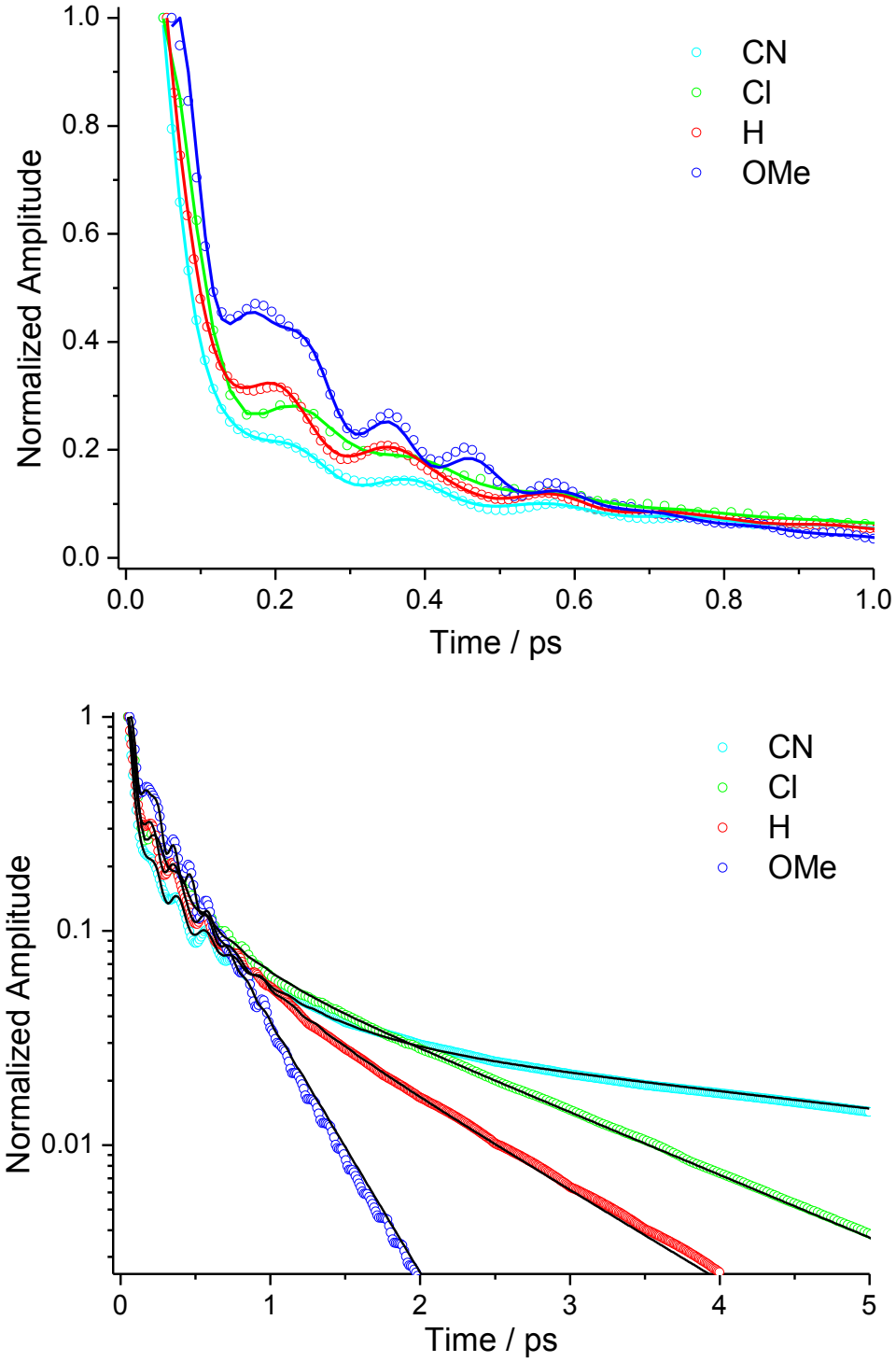

Figure 4.8 - *Time domain decay of the integrated intensity of the reconstructed time-dependent emission spectra of each derivative in DCM on (a) a linear scale and (b) a log scale. In each case, the time-domain data (points) was fitted with a function comprising the sum of exponential and damped harmonic oscillator terms (lines). Inset shows the data on a log intensity scale.*

Table 4.9 - *Exponential components of the function fitted to the decay of the integrated intensity of the time-dependent emission spectra of each derivative. Repeat fits to each measurement determined the error of each parameter to be within 15%.*

Substituent	τ_1 **/ps**	A_1	τ_2 **/ps**	A_2	$\langle\tau_1\rangle$ **/ps**	τ_3**/ps**	A_3
1-CN	0.07	0.77	0.44	0.19	0.14	4.46	0.04
1-Cl	0.10	0.67	0.33	0.24	0.16	1.55	0.09
1-H	0.08	0.77	0.32	0.16	0.12	1.02	0.07
1-OMe	0.11	0.54	-	-	-	0.37	0.46

Table 4.10 - *Damping (τD), frequency (ω), amplitude (Aω) and phase (Φ) components of the damped harmonic oscillator functions used to fit the oscillatory part of the decay of the integrated intensity of the time-dependent emission spectra of each derivative. Repeat fits to each measurement determined the error of each parameter to be within 25%.*

Substituent	τ_{D1} **/ ps**	ω_1 **/ THz**	$A_{\omega1}$	φ_1	τ_{D2} **/ ps**	ω_2 **/ THz**	$A_{\omega2}$	φ_2	τ_{D3} **/ ps**	ω_3 **/ THz**	$A_{\omega3}$	φ_3
1-CN	0.07	3.31	0.80	1.03	0.29	5.47	0.10	0.81	0.10	8.22	0.10	0.72
1-Cl	0.09	3.30	0.75	0.86	0.16	5.36	0.20	0.39	0.17	8.35	0.05	1.45
1-H	0.10	3.02	0.71	1.18	0.21	5.36	0.24	0.64	0.28	8.38	0.04	1.60
1-OMe	0.08	5.17	0.34	0.44	0.15	8.10	0.32	2.59	0.14	9.74	0.34	3.71

In the case of 1-Cl, the dark state lifetime is also longer than that of 1-H (by a factor of 1.5) but this is effect is far less significant than that of 1-CN. This is in line with the weak electron withdrawing nature of the Cl substituent.

In contrast to the long component, the short component of the fluorescence decay exhibits no significant substituent dependence (0.14 ps for 1-CN compared to 0.11 ps in 1-OMe). This suggests that the decay of the bright state to the dark state is not substituent dependent.

Turning to the effects of substitution upon the oscillatory component of the fluorescence decay, the most significant effect is observed for 1-OMe. The frequency of the oscillation differs for 1-OMe compared to the remaining derivatives. This can be seen in Figure 4.8 and is further highlighted by the frequencies of the oscillations recovered from fitting of the time domain data in Table 4.10. The frequencies of the coherently excited vibrational modes are identical (within experimental error) for 1-H, 1-Cl and 1-CN. However, in 1-OMe the lowest frequency mode (3.5 THz, 117 cm^{-1}) is no longer required to achieve an adequate fit to the data. Instead, it is replaced by a higher frequency mode (9.7 THz, 324 cm^{-1}). A similar result is apparent in the Fourier transform of the 1-OMe data. Figure 4.9 shows the Fourier Transform of the oscillatory part of the time domain data for 1-H (red line) and 1-OMe (blue line) compared to the Fourier transform of the fitted functions (black lines) for both derivatives.

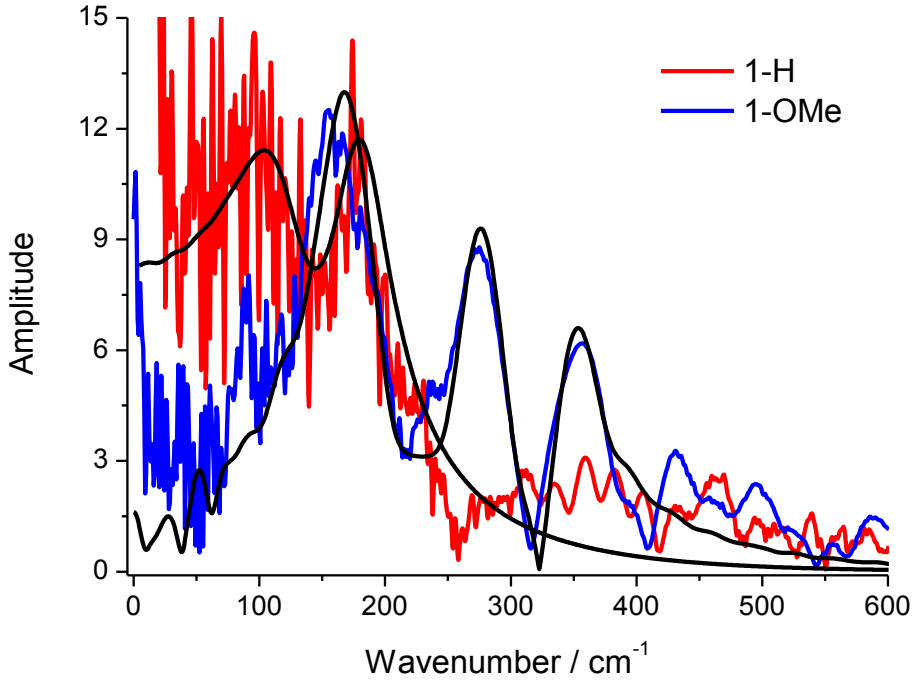

Figure 4.9 - *A comparison of the Fourier transform of the time-resolved fluorescence decay curves of 1-H and 1-OMe. The raw data (coloured lines) is compared to the fitted function (black lines) in both cases.*

1-OMe exhibits a significant high frequency mode (350 cm^{-1}, 10.5 THz) but no low frequency mode (105 cm^{-1}, 3.15 THz) when compared to 1-H. The disappearance of the lowest frequency mode is a potentially significant observation. This mode was previously assigned as a reactive mode (pyramidalization) for 1-H. The disappearance of the low frequency reactive mode suggests that either it is damped far more quickly for 1-OMe (faster than the time resolution of the experiment) or that it is not coherently excited (no wavepacket displaced between the ground and excited states as discussed in Chapter 1). However, both explanations suggest that the pyramidalization co-ordinate of 1-OMe may be significantly altered with respect to that of 1-H. Therefore, this may point towards a significantly altered excited state chemistry of 1-OMe. A key consideration is the extent to which an altered co-ordinate of excited state relaxation in 1-OMe correlates to the significantly faster decay of the 1-OMe dark state. This will be addressed further through transient absorption spectroscopy (Section 4.3.3).

To further investigate the origin of the observed differences in oscillation frequencies in the fluorescence decays of 1-OMe and 1-H, ground state Raman spectra were calculated using DFT. No significant differences were found between 1-OMe and 1-H. Therefore, the experimentally observed differences between the derivatives must arise in the excited state. This is not a surprising conclusion, since previous attempts to assign the coherently excited vibrational modes of 1-H by resonance Raman spectroscopy revealed that the ground state and excited state frequencies of 1-H differed significantly (Chapter 3). Thus, calculated excited state Raman spectra are required to assess further the origin of the observed coherently excited vibrational modes of 1-OMe. Such calculations are notoriously difficult and are outside our present capabilities. It is hoped that the experimental data reported here can provide a sound basis from which such calculations can be made in the future.

4.3.3 Ultrafast Transient Absorption Spectroscopy

To further probe the substituent effects upon the molecular motor dynamics, the substituent dependence of the transient absorption spectra was investigated. It was reported previously that two transient features were present in the transient spectra of 1-H (Chapter 3) and a closely related analogue.[20] A long lived band (>>200 ps) was assigned to formation of the photoproduct whereas a short lived band, which decayed on a timescale comparable to that of the long component of the fluorescence decay, was assigned to absorption of a dark excited state. Agreement between the long component of the fluorescence decay and the lifetime of the assigned dark state transient therefore underpins the bright to dark state model proposed for 1-H in Chapter 3. The relationship between these two parameters, and hence the validity of the model, was then tested for the substituted motor derivatives.

The time dependent transient spectra of each derivative measured in DCM are shown in Figure 4.10. The two transient features described previously for 1-H are retained in each case. The long lived blue shifted transient is again assigned to absorption of the photoproduct, with the shorter lived red shifted transient ascribed to absorption of a dark excited state. However, an additional feature is observed on the blue edge of the measured spectra in the case of 1-CN, 1-Cl and 1-OMe. Since the steady state absorption spectrum of each derivative is red shifted in comparison to 1-H (Figure 4.3), the transient bleach is also red shifted and thus becomes observable in our wavelength range (Figure 4.9). As a result it is possible to analyse the kinetics of the ground state recovery of each substituted derivative in addition to the decay of the dark state. The transient spectra of 1-Cl (Figure 4.10b) also reveal a negative ΔOD band on the red edge of the measured spectral region. A similar feature was found for the remaining derivatives when the measured spectral region was tuned further to the red (see Chapter 2 for experimental details). This transient feature is attributed to stimulated emission and is discussed in more detail in Section 4.3.3.1.

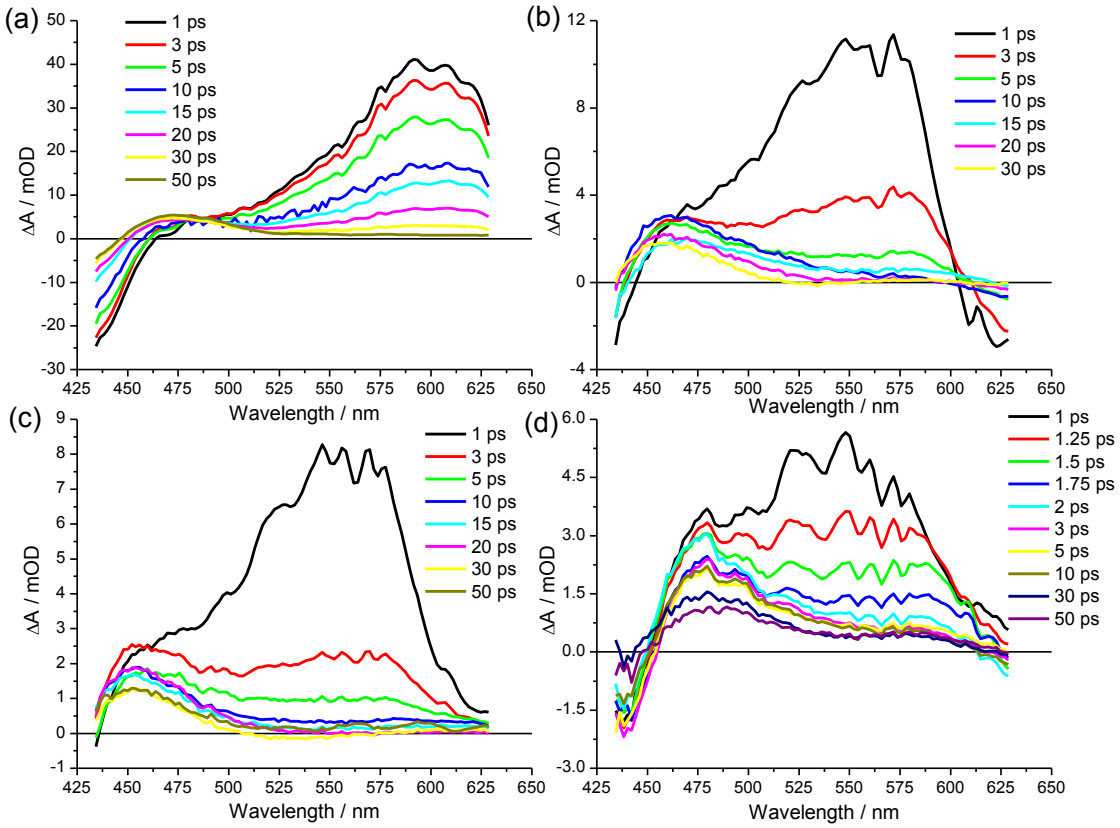

Figure 4.10 – *Time-dependent transient spectra of (a) 1-CN, (b) 1-Cl, (c) 1-H and (d) 1-OMe recorded in DCM.*

In order to determine any substituent dependent differences in the transient spectra, the transient spectrum of each substituted derivative recorded at a delay time of 1 ps (reproduced from Figure 4.10) is compared in Figure 4.11. This comparison reveals two interesting observations. Firstly, the transition moment of the dark state transient increases as the electron withdrawing strength of the substituent increases. Secondly, the dark state transient is red shifted as the electron withdrawing strength of the substituent increases. Thus, 1-OMe (strongly electron donating) exhibits the weakest and most blue shifted dark state transient whereas 1-CN (strongly electron withdrawing) exhibits the strongest and most red shifted dark state transient.

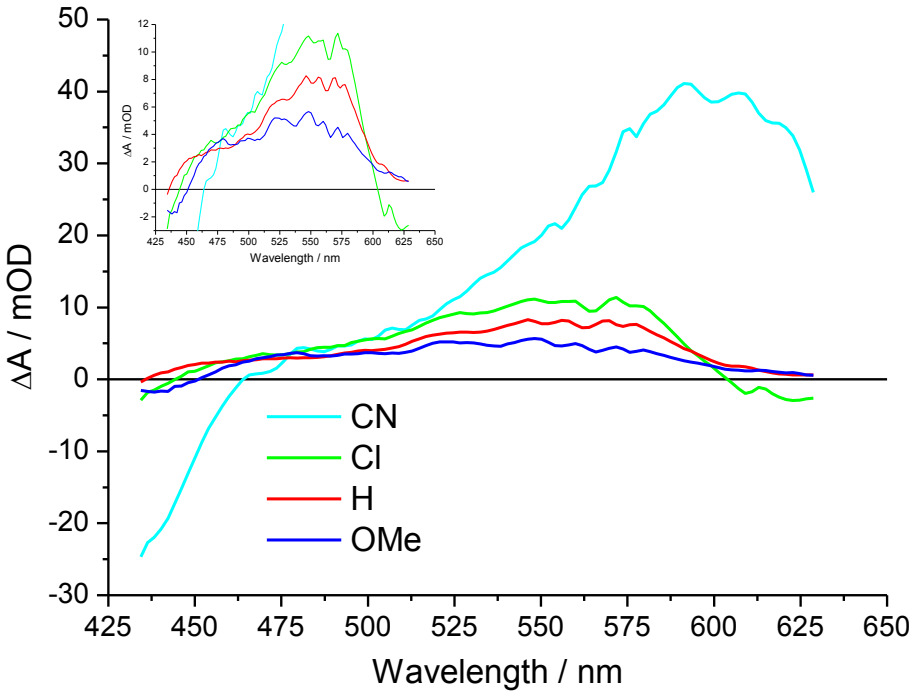

Figure 4.11 - *A comparison of the transient spectra of each substituted motor derivative recorded in DCM at a delay time 1 ps. Inset shows the 1-Cl, 1-H and 1-OMe data on an expanded scale.*

The substituent dependence of the dark state lifetime is assessed by comparing the dark state transient decay curves measured at the wavelength of maximum ΔA (~560 nm) for each derivative. This is shown in Figure 4.12 where the raw data (points) were fitted by an exponential function (lines). A single exponential function provided an adequate fit for 1-H, 1-Cl and 1-OMe, but a bi-exponential function was required for the 1-CN data (Table 4.11). A similar observation was made for the 1-CN fluorescence decay data whereby an additional (third) exponential term was required to provide an adequate fit to the raw data (Table 4.3). Therefore, the weighted average of the two exponential terms was calculated for the lifetime of the 1-CN dark state (<τ> in Table 4.11). Thus, the dark state lifetimes of 1-Cl, 1-H and 1-OMe are represented by τ_1 whereas the dark state lifetime of 1-CN is represented by <τ> (Table 4.11).

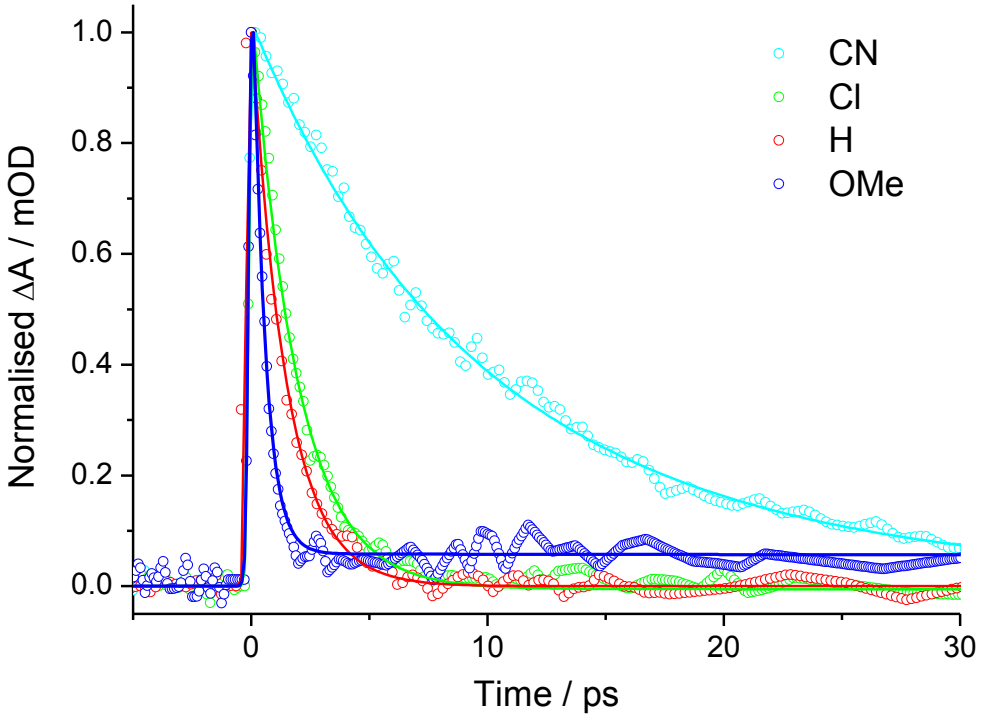

Figure 4.12 – *Time domain decay curves (recorded at the wavelength of maximum ΔA) of the dark state transient of each derivative measured in DCM.*

Table 4.11 - *Parameters of the exponential fitted to the dark state transient decay curve of each derivative in DCM. Repeat measurements determined the error to be within 10% for each parameter.*

Substituent	τ_1 **/ps**	A_1	τ_2 **/ps**	A_2	$\langle\tau\rangle$ **/ps**
1-CN	5.27	0.16	11.44	0.84	10.41
1-Cl	1.86	1	-	-	-
1-H	1.47	1	-	-	-
1-OMe	0.51	1	-	-	-

Similarly, the substituent dependence of the ground state recovery was assessed by comparing the transient bleach decay curve of each derivative (measured at 435 nm, the most blue shifted wavelength accessible in our measurements). This is shown in Figure 4.13 where again, the raw data (points) were fitted by an exponential function (lines). A single exponential was adequate for 1-Cl and 1-OMe but a bi-exponential function was required for 1-CN (Table 4.12). Again, the weighted average of the two exponential terms were calculated for 1-CN (<τ> in Table 4.12). Thus, the ground state recovery times of 1-Cl and 1-OMe are represented by τ_1 whereas 1-CN is represented by <τ> (Table 4.12).

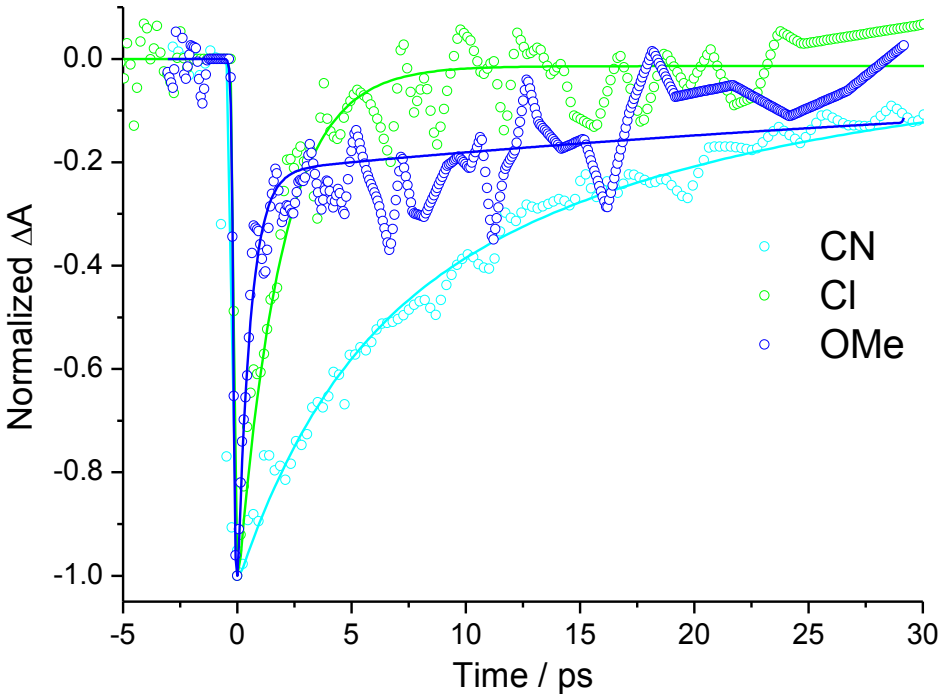

Figure 4.13 - *Time domain ground state bleach recovery curves (recorded at the wavelength of maximum ΔA) of each derivative measured in DCM. No data is reported for 1-H since the linear absorption spectrum of 1-H falls outside of our measured range.*

Table 4.12 - *Parameters of the exponential fitted to the ground state bleach recovery curve of each derivative in DCM. Repeat measurements determined the error to be within 10% for each parameter.*

Substituent	τ_1 **/ps**	A_1	τ_2 **/ps**	A_2	$\langle\tau\rangle$ **/ps**
1-CN	4.00	0.4	17.15	0.6	11.86
1-Cl	1.83	1	-	-	-
1-H	-	-	-	-	-
1-OMe	0.53	1	-	-	-

Table 4.11 reveals that 1-CN exhibits a significantly increased dark state lifetime that is approximately 7 times longer than for 1-H. This is qualitatively consistent with the fluorescence lifetime data described previously (Section 4.3.2, Table 4.9) where the long component of the fluorescence decay was found to be longest for 1-CN. In addition, Figure 4.12 and Table 4.11 also highlight the short lifetime of the dark state transient in 1-OMe (approximately 3 times shorter than 1-H). Again, this is in agreement with the fluorescence lifetime data whereby 1-OMe was found to exhibit the fastest fluorescence decay (Table 4.9). Figure 4.12 also reveals an anomalous feature of the excited state transient decay in 1-OMe where full relaxation to the baseline is not achieved even after ~100 ps. The origin of this feature is unknown, with no evidence of a long lived photoproduct evident in the steady state absorption spectrum of 1-OMe. This long lived signal was observed for 1-OMe in every solvent studied (See Section 4.3.6 for details of solvent dependence studies), as well as in the ground state recovery kinetics (Figure 4.13). Thus, it is assigned to a minor state which is populated by excitation, with a tentative suggestion of possible triplet state involvement. Finally, the dark state lifetime of 1-Cl is found to be slightly longer than that of 1-H. This is also consistent with the fluorescence lifetime data described previously.

Thus, a clear trend is present in the dark state lifetime data: the dark state lifetime becomes longer as the electron withdrawing strength of the substituent increases. This matches the trend observed for the long exponential component of the fluorescence decay. The same trend is also observed for the lifetime of the transient bleach (Figure 4.13, Table 4.12). Table 4.13 compares the time constant of the long exponential component of the fluorescence decay (from Table 4.9) and the lifetimes of the dark state (from Table 4.11) and ground state transients (from Table 4.12) for each derivative. Table 4.13 shows that for 1-H, 1-Cl and 1-OMe there is a close agreement between the lifetime of the dark state transient, the ground state transient and the long component of the fluorescence decay. In contrast, Table 4.13 reveals significant disparity between the long exponential component of the fluorescence decay (~ 4.5 ps) and the lifetime of the dark state transient from transient absorption (~12 ps) of 1-CN. However, close agreement is retained between the lifetimes of the dark state and ground state transients of 1-CN.

Table 4.13 - *A comparison of the long exponential component of the fluorescence decay, the dark state lifetime and ground state recovery of each derivative in DCM. Repeat measurements determined the error to be within 10% for the lifetimes of the dark state and ground state bleach transients and 15% for the long component of the fluorescence decay.*

Substituent	**Dark State Lifetime / ps**	**Ground State Recovery Time / ps**	**τ_3 Fluorescence / ps**
1-CN	10.41	11.86	4.46
1-Cl	1.86	1.83	1.55
1-H	1.47	-	1.02
1-OMe	0.51	0.53	0.37

Two possible explanations exist for such an observation. Firstly, the 1-CN 'dark' state (which we propose gives rise to the long fluorescence component through thermal repopulation of the 'bright state') could relax further to an additional deeper 'trapped' dark state which is unable to repopulate the 'bright' state. In this case, the long exponential component of the fluorescence decay would represent the relaxation of the 'dark' state to the 'trapped' state. The lifetime of the 560 nm transient would then represent the decay of the trapped state to the ground state. Although consistent with the observed kinetics, no experimental evidence was found to support the existence of an additional state (or states) in the excited state relaxation mechanism of 1-CN. If they exist they are shifted further to the red than our current measurements can observe.

Alternatively, the observed difference can be explained in terms of the signal to noise of the 1-CN fluorescence decay data. It was observed previously that the weight of the longest fluorescence component (τ_3 in Table 4.3) of 1-CN is small (< 9% at all emission wavelengths). In addition, the fluorescence quantum yield of the molecular motors is very low as described previously. Therefore, it is possible that the failure to observe a slow relaxation in the time resolved fluorescence measurement which is in agreement with the transient absorption data is simply due to the low signal of the 1-CN fluorescence – the longest component is simply not resolved. Significantly we find (Section 4.3.3.1) that the signal assigned to 1-CN stimulated emission actually decays with the same kinetics as the dark state transient absorption of 1-CN. This is consistent with the suggestion of a signal to noise limited long fluorescence decay time in 1-CN.

Therefore, we suggest that for each substituted motor derivative, the lifetime of the dark state transient, the recovery time of the ground state bleach and the long component of the fluorescence decay all represent the same process: the relaxation of a dark excited state to the ground state. Therefore, we suggest that the model proposed previously for the excited state

relaxation mechanism of 1-H (Chapter 3) remains valid for each derivative studied here. This model involves two parameters which may have a significant influence upon the excited state decay dynamics of the molecular motors: the energy of the barrier opposing the repopulation of the bright state from the dark state, and the energy of the conical intersection at which internal conversion leads to relaxation of the dark state to the ground state. Thus, the substituent dependence of the fluorescence decay dynamics and of the dark state lifetime must be considered in terms of the substituent dependence of these parameters. This is discussed further in Section 4.3.4.

4.3.3.1 Stimulated Emission

As described previously in Section 4.3.3, the transient spectra of each derivative were found to exhibit a negative ΔOD feature at significantly red shifted wavelengths compared to the ground state bleach. There is no ground state absorption in this region so the most likely cause is stimulated emission. Stimulated emission should reflect the fluorescence spectra which are known to extend beyond 700 nm (Figure 4.3). The stimulated emission decay is expected to closely follow that of the fluorescence decay. Our transient absorption time resolution does not allow observation of the fastest fluorescence components (τ_1 in Table 4.9), but we expect the long fluorescence component (τ_3 in Table 4.9) to match the stimulated emission decay. Since the long component of the fluorescence decay has previously been assigned to the decay of a dark excited state, the stimulated emission decay is also expected to match the lifetime of the dark state measured by transient absorption (Table 4.11). Figure 4.14 and Figure 4.15 show the transient spectra (measured between 550 nm and 700 nm using a sapphire window to generate the probe as detailed in Chapter 2) and a comparison of the dark state transient decay to the stimulated emission transient decay for 1-H and 1-CN respectively. The transient spectrum of 1-Cl presented previously (Figure 4.10b) was

adequate to time-resolve the decay of the stimulated emission transient and a comparison to the dark state decay of 1-Cl is shown in Figure 4.16.

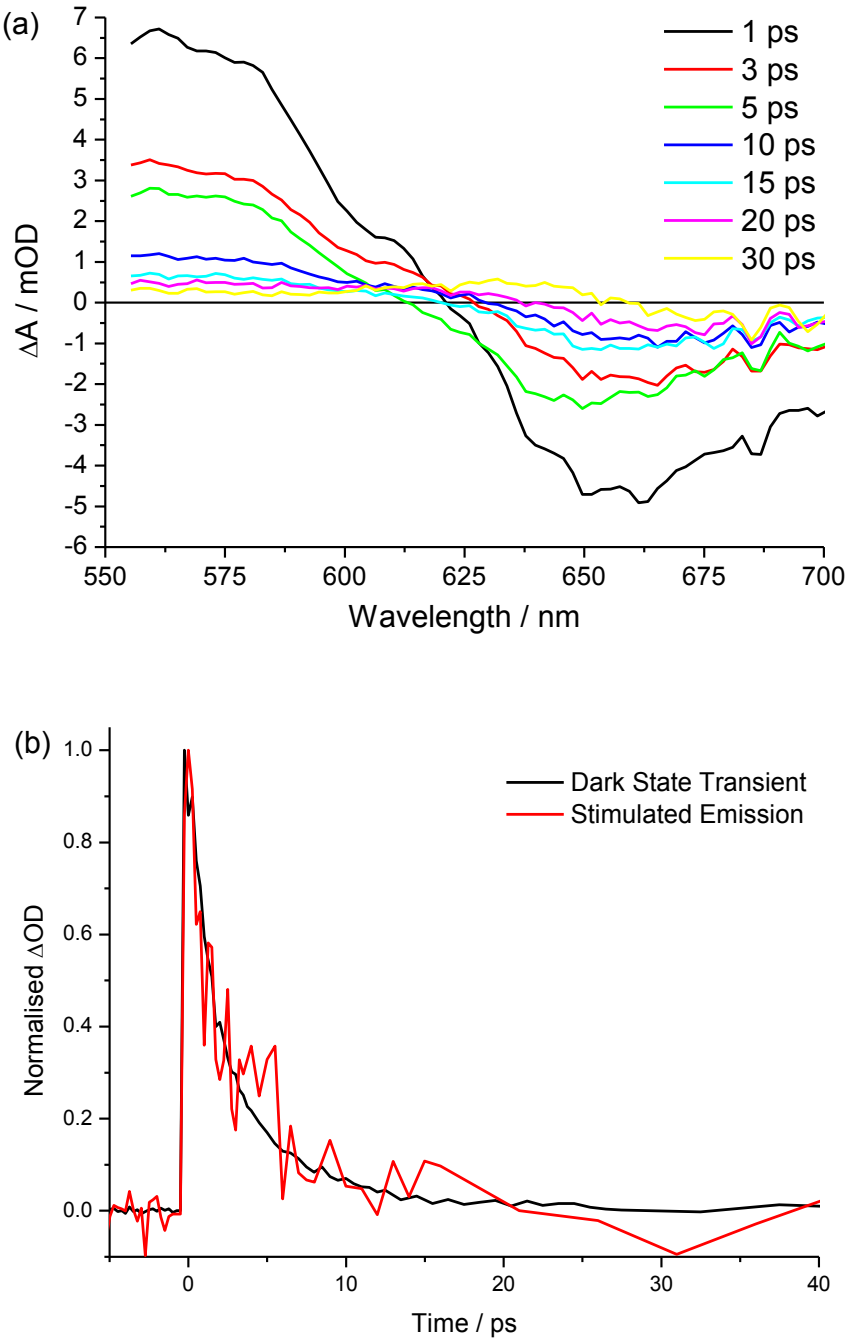

Figure 4.14 - *(a) Transient spectra of 1-H recorded in octanol recorded between 550 nm and 700 nm. The transient centred at ~660 nm is assigned to stimulated emission. (b) A comparison of the time resolved decay of the dark state transient (black) and stimulated emission transient (red).*

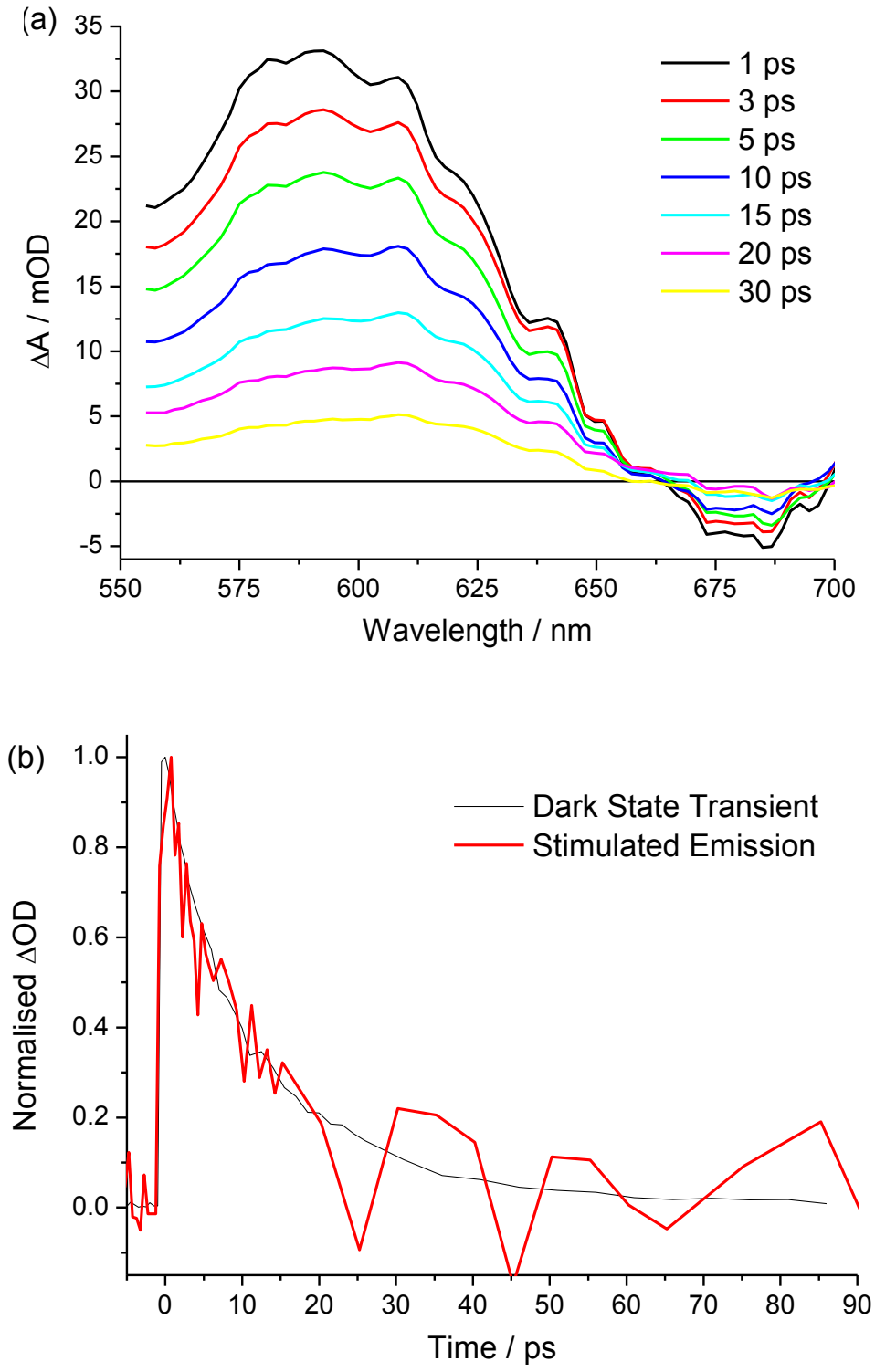

Figure 4.15 – *(a) Transient spectra of 1-CN recorded in ethanol recorded between 550 nm and 700 nm. The transient centred at ~680 nm is assigned to stimulated emission. (b) A comparison of the time resolved decay of the dark state transient (black) and stimulated emission transient (red).*

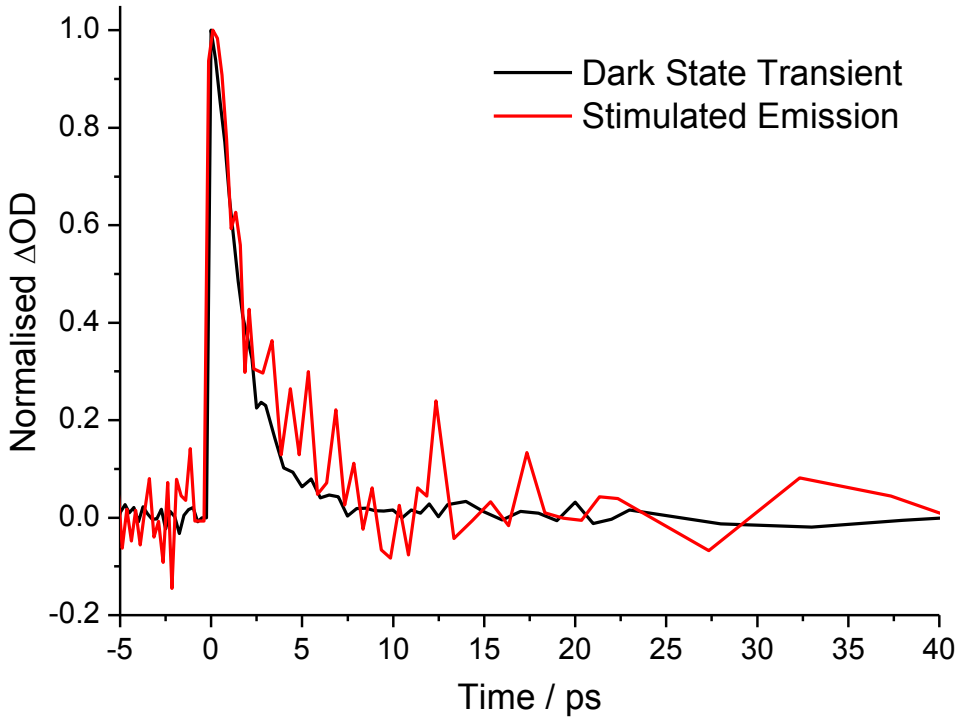

Figure 4.16 - *A comparison of the time resolved decay of the 1-Cl dark state transient (black) and stimulated emission transient (red recorded in DCM).The transient spectra are shown in Figure 4.10b.*

In the case of 1-OMe, low signal to noise (due to the low transition moment of 1-OMe as shown in Figure 4.11), precluded the determination of the decay timescale of the 1-OMe stimulated emission transient.

In each case, there is a clear agreement between the decay kinetics of the dark state transient and the stimulated emission transient (Figure 4.14b, Figure 4.15b and Figure 4.16). This supports the suggestion that the long component of the fluorescence decay and the lifetime of the dark state transient both represent the same process: the decay of the dark state to the ground state. This is a particularly important conclusion for 1-CN where the long component of the fluorescence decay is shorter than the lifetime of the dark state measured by transient absorption. The close agreement of the stimulated emission and dark state transient decay timescales suggests that this disparity between the long component of the fluorescence decay

and the dark state lifetime of 1-CN is due to signal to noise limitations of the time resolved fluorescence measurement. It is possible that the long component of the fluorescence decay is significantly longer than observed in the measured data, but that the signal to noise of the measurement does not allow this to be resolved. Therefore, it may possible that the 1-CN dark state is able to reach the emissive region of the excited state potential energy surface, but with such small amplitude such that it is not detected by the fluorescence up-conversion measurement. This emission may however be detected by transient absorption since time resolved fluorescence measures a decaying signal whereas stimulated emission is detected as a gain by transient absorption. These are distinctly different measurements which are therefore subject to differing signal to noise limitations, meaning the detection of a gain may be possible where a decaying signal has fallen below the signal to noise level. Therefore, we suggest that despite the experimentally observed differences, the long component of the fluorescence decay and the decay of the dark state transient of 1-CN both represent the decay of the 1-CN dark excited state to the ground state.

4.3.4 A One-Dimensional Model for Substituent Dependent Motor Dynamics

A model scheme of excited state potential energy surfaces was proposed previously (Chapter 3) in order to explain the observed substituent dependence of the excited state relaxation dynamics of the 1-H molecular motor. The potential energy surface was proposed to consist of two distinct regions – the initially populated emissive Franck-Condon 'bright' state and the non-emissive 'dark' state (Chapter 3, Figure 3.18). The 'bright' state relaxes to the 'dark' state *via* barrierless (or almost barrierless) structural evolution primarily along the C9-pyramidalization co-ordinate (represented experimentally by the fast component of the fluorescence decay). The 'dark' state population is then able to thermally repopulate the 'bright' state over an energy barrier, as well as relax to the ground state *via* internal

conversion at a conical intersection (represented by the long component of the fluorescence decay and the lifetime of the dark state transient).

For the substituted molecular motor derivatives, a general trend is apparent in the excited state decay data which follows the electron donating/withdrawing strength of the substituents. The lifetime of the dark state is made significantly longer by a strong electron withdrawing substituent (1-CN) and, in contrast, significantly shorter by a strong electron donating substituent (1-OMe) relative to 1-H.

We propose that two substituent dependent parameters of this model could give rise to the observed substituent dependence of the excited state decay dynamics. Firstly, the lifetime of the dark state in this scheme is governed by the energy of the conical intersection at which internal conversion of the dark state population to the ground state occurs. If the conical intersection is raised in energy above the local minimum of the dark state (corresponding to a larger barrier to internal conversion), the rate of deactivation to the ground state will decrease. Therefore, we suggest that the energy difference between the local minimum of the dark state and the conical intersection is increased as the electron withdrawing strength of the substituent increases. A schematic representation of the proposed substituent dependent model potential energy surfaces is shown in Figure 4.17.

In the case of 1-OMe (strong electron donor), we propose that the conical intersection is at or is very close to the minimum energy of the dark state (blue line in Figure 4.17). This results in very rapid (~500 fs) relaxation of the 1-OMe dark state. In comparison, we suggest that the conical intersection of 1-H (no electronic properties) lies slightly above the minimum energy of the 1-H dark state (red line in Figure 4.17). This leads to an increased dark state lifetime of 1-H compared to 1-OMe. Following on, we propose that the conical intersection of 1-Cl (weakly electron withdrawing) is even slightly higher above minimum energy (green line in

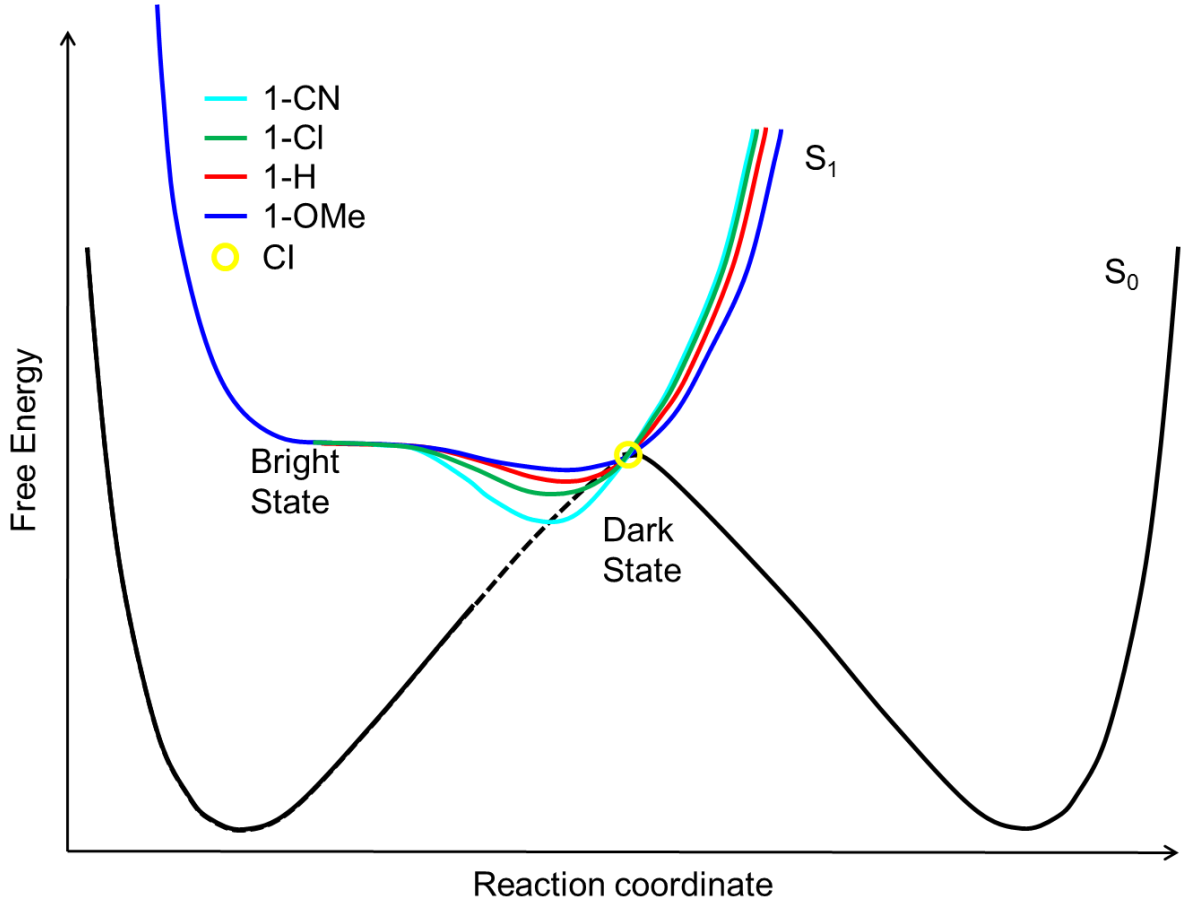

Figure 4.17 - *A schematic representation of the proposed substituent dependence of the excited state potential energy surface of the molecular motor. The dark state population relaxes directly to the ground state via internal conversion at a conical intersection (yellow circle). The energy of the conical intersection relative to the local minimum of the dark state (the barrier to internal conversion) increases as the electron withdrawing strength of the substituent is increased. In addition, the energy barrier opposing the dark state population from returning to the bright state becomes larger as the electron withdrawing strength of the substituent is increased.*

Figure 4.17) thus leading to a further increase to the 1-Cl dark state lifetime compared to 1-OMe and 1-H. Finally, we propose that the conical intersection of 1-CN lies significantly above the minimum energy of the 1-CN dark state (cyan line in Figure 4.17). Therefore, the lifetime of the 1-CN dark state is significantly longer than the remaining derivatives.

The second parameter of the model which will affect the measured excited state decay dynamics is the energy of the barrier on the excited state potential energy surface which opposes the repopulation of the bright state from the dark state. As described previously (Chapter 2), this barrier was proposed as the origin of the bimodal nature of the 1-H fluorescence decay. If the energy of the barrier is increased, the dark state population would be less able to repopulate the emissive region of the surface. This corresponds to a greater separation between the bright and dark states and would thus lead to a smaller amplitude of the long fluorescence decay component (and therefore a more distinctly bimodal fluorescence decay curve). Therefore, we propose that the substituent dependence of the fluorescence decay dynamics can be explained in terms of the energy of this barrier. We suggest that the dark to bright state barrier becomes larger as the electron withdrawing strength of the substituent is increased. This is illustrated in Figure 4.17.

We propose a deeper dark state for 1-CN (cyan line in Figure 4.17) compared to 1-H (red line in Figure 4.17), corresponding to a larger dark to bright state barrier. This would lead to a lower amplitude of the long fluorescence decay component of 1-CN (and thus a much more distinctly bimodal fluorescence decay profile). This in agreement with the experimental data (Figure 4.8 and Table 4.9). In addition, a larger barrier to repopulation of the emissive region of the surface is consistent with the failure to fully resolve the long component of the fluorescence decay of 1-CN.

In contrast, we suggest that the barrier is smaller for 1-OMe (blue line in Figure 4.17) compared to 1-H (red line in Figure 4.17), corresponding to a less significant separation between the bright and dark states. This would lead to a larger amplitude of the long fluorescence decay component (and thus a much less significantly bimodal fluorescence decay). Again, this is in agreement with the experimental data (Figure 4.8 and Table 4.9). Finally, in the case of 1-Cl (green line in Figure 4.17), no differences were observed (within

experimental error) between the amplitudes of the long fluorescence decay components of 1-H and 1-Cl. (Table 4.9). This suggests that any modification of the 1-Cl dark to bright state barrier relative to 1-H is minor. This is in line with the very weak electron withdrawing effect of the Cl substituent. Thus, we propose that the barrier of 1-Cl is slightly higher than that of 1-H (but significantly less so than 1-CN).

In order to test the proposed substituent dependence of the dark to bright state energy barrier, kinetic modelling was performed. The scheme of kinetic rate equations which arise from the proposed model was solved and the population of the 'bright' state was modelled as a function of the 'dark' to 'bright' state energy barrier for each derivative. This is discussed in detail in the next section.

4.3.5 Model Scheme of Excited State Relaxation and Solution of Kinetic Rate Equations

The kinetic scheme which arises from the proposed model is shown in Figure 4.18. The initial ground state structure 'A' is excited to the 'bright' excited state 'B*'. This population undergoes excited state structural evolution along the reaction co-ordinate (pyramidalization and rotation[1,21]) to the relaxed 'dark' excited state 'D*' ($k_{B\text{-}D}$). The population can then return by thermal excitation to the bright state ($k_{D\text{-}B}$), relax directly to the initial ground state structure 'A' ($k_{D\text{-}A}$) or relax directly to the ground state metastable photoproduct 'M' ($k_{D\text{-}M}$). The kinetic solution for each species was calculated by integration using matrix methods [9] as outlined in Section 4.2 and detailed in Appendix 1. For each derivative, the experimental data provides a quantitative representation of several of the rate constants involved in this scheme.

The experimental data measured in DCM was used as the basis of the model. The rate of the bright to dark state relaxation ($k_{B\text{-}D}$) is represented by the fast component of the fluorescence decay (τ_1 in Table 4.9).

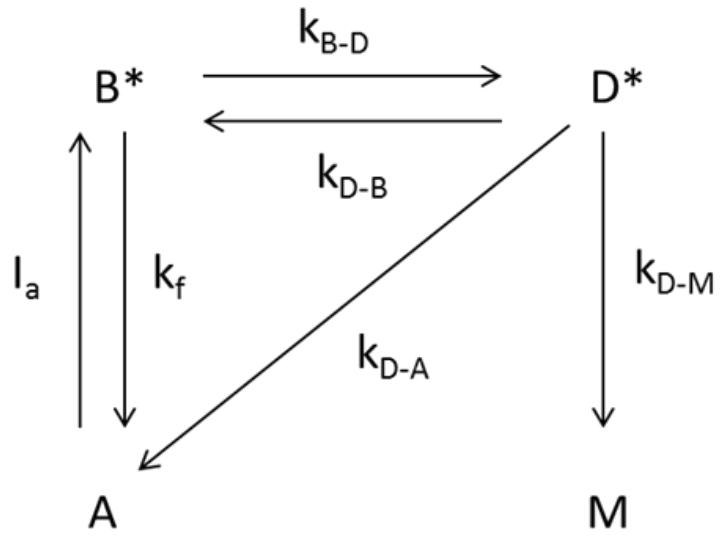

Figure 4.18 – *Kinetic scheme of the proposed model of excited state relaxation.*

The rate of the 'dark' state relaxation to the ground state 'A' (k_{D-A}) is represented by the long component of the fluorescence decay (τ_3 in Table 4.9). In addition, the rate of the 'dark' state relaxation to the metastable product 'M' (k_{D-M}) can be assessed by the photochemical quantum yield (A:M in Figure 4.10) of each derivative (Table 4.1). Therefore, the only component of the model which is not accessible from experiment is the rate at which the dark state repopulates the bright state (k_{D-B}), and this was treated as a fitting parameter in the simulation. Since this repopulation process must overcome the energy barrier which separates the dark state from the bright state, the rate of this process can be taken as a direct representation of the magnitude of this energy barrier. Thus, a slower rate represents a larger barrier and vice versa. Therefore, an assessment was made as to the extent to which the substituent dependent experimental data could be reproduced by varying only the rate of this step (k_{D-B}), and hence the size of this energy barrier in the reaction scheme. The time domain evolution of the 'bright' state population (B*) of each derivative was modelled as a function of k_{D-B} and compared to the corresponding experimentally measured fluorescence decay curves. Figure 4.19 shows this comparison for each derivative.

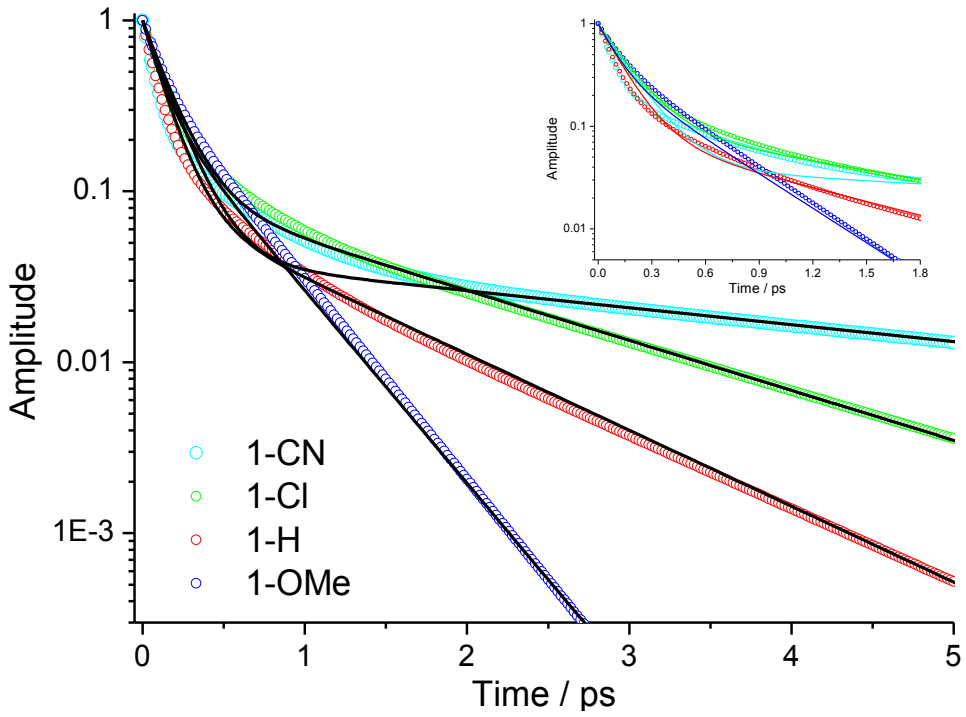

Figure 4.19 - *A comparison of the time-domain decay of the integrated intensity of the time-dependent emission spectra (circles) to the calculated time evolution of the 'bright' state population (solid lines) of each derivative in DCM.*

The decay of the integrated intensity of the time-dependent emission spectra of each derivative (points) is compared to the modelled time-domain evolution of the bright state population (solid lines). Only the exponential components of the integrated intensity decay are compared since the oscillatory terms do not represent relaxation of the excited state population. The rate constants which were extracted from the experimental data are summarized in Table 4.14, along with the $k_{D\text{-}B}$ values used to calculate the time dependent concentration curves of 'B*' in Figure 4.19.

In each case, the experimental data is well reproduced by the model. Therefore, this simulation is consistent with the hypothesis that an energy barrier must be crossed in order for the relaxed 'dark' excited state population to repopulate the emissive 'bright' state on the excited state potential energy surface.

Table 4.14 - *Rate constants used to solve the system of kinetic rate equations which arise from the proposed model of excited state relaxation.* $k_{B\text{-}D}$*,* $k_{D\text{-}A}$ *and* $k_{D\text{-}M}$ *were calculated from experimental data,* $k_{D\text{-}B}$ *was modelled as a representation of the size of the energy barrier opposing the relaxed 'dark' state from returning to the emissive 'bright' state on the excited state potential surface.*

Substituent	$\mathbf{k_{B\text{-}D}}$ **/ ps^{-1}**	$\mathbf{k_{D\text{-}A}}$ **/ ps^{-1}**	$\mathbf{k_{D\text{-}M}}$ **/ ps^{-1}**	$\mathbf{k_{D\text{-}B}}$ **/ ps^{-1}**
1-CN	6	0.19	0.038	0.24
1-Cl	5.8	0.65	0.09	0.51
1-H	7.2	0.97	0.136	0.5
1-OMe	7.4	3.35	0.165	1.7

Table 4.14 shows that the $k_{D\text{-}B}$ rate constant decreases as the electron withdrawing strength of the substituent is increased. This corresponds to an increasing energy barrier to repopulation of the bright state as the electron withdrawing ability of the substituent is increased. Therefore, the observed substituent dependence of the fluorescence decay data can be qualitatively well explained by a single parameter, the size of the dark to bright state energy barrier. However, simulation of the experimental data in the first picosecond proved problematic for 1-CN, 1-Cl and 1-H (inset Figure 4.19). As described previously, the decay of the integrated intensity of the time-dependent emission spectra of these derivatives required three exponential terms to provide an adequate fit to the data. This suggests that the excited state decay dynamics of these derivatives are complex and not well represented by a single rate constant. Thus, taking the weighted average of τ_1 and τ_2 ($<\tau_1>$ in Table 4.9) of the experimental fluorescence decay as a representation of $k_{B\text{-}D}$ for the calculated fluorescence curve may oversimplify the relaxation processes. The simulation method implemented in this study is not easily extended to allow the use of non-exponential decay processes. However, the general trend of the experimental data is well reproduced by the calculation.

In the case of 1-H and 1-Cl, the k_{D-B} rate constant is very similar for both derivatives, reflecting the relatively minor electron withdrawing effect of the Cl substituent. This is consistent with the experimental data (Table 4.9).

In the case of 1-OMe, the k_{D-B} rate constant is faster than for 1-H (3 fold increase) corresponding to a reduced energy barrier separating the 'dark' and 'bright' states on the excited state potential energy surface. This is consistent with the experimental data in which the amplitude of the long fluorescence decay component (representing decay of the dark state) is significantly larger for 1-OMe than the remaining derivatives. This suggests that the dark state of 1-OMe is more able to access the emissive region of the surface, as would be the case for a smaller barrier separating the dark and bright states.

Turning to 1-CN, the model reproduces the experimental data: - a low amplitude, long lived fluorescence decay component is observed. The k_{D-B} rate constant is twofold smaller than that for 1-H, corresponding to a larger barrier opposing repopulation of the bright state from the dark state.

4.3.6 Solvent Dependence

The solvent dependence of the excited state decay dynamics of each derivative was probed in order to gain further insight into the nature of the substituent dependent excited state decay dynamics. As for 1-H in the previous chapter, particular focus was placed upon the effects of solvent polarity and viscosity. Solvent polarity effects can give an insight into the differences between the electronic structures of the ground and excited states whereas viscosity effects probe the nature of the structural evolution in the excited state (Chapter 1).

The solvent dependent fluorescence decay curves (emission recorded at 556 nm) of 1-CN (Figure 4.7), 1-Cl (Figure 4.8) and 1-OMe (Figure 4.9) are shown below. The solvent

dependence of 1-H has been discussed previously (Chapter 2). The raw data were fitted to functions comprising the sum of exponential decay terms and damped harmonic oscillators. These parameters are summarized in Table 4.15 (exponential components) and Table 4.16 (oscillator components). For the 1-Cl data, two exponential terms provided an adequate fit for each solvent except for the two most viscous solvents (decalin and octanol) which required a third intermediate exponential term. This is in line with the 1-H data described in the previous chapter (Chapter 3).

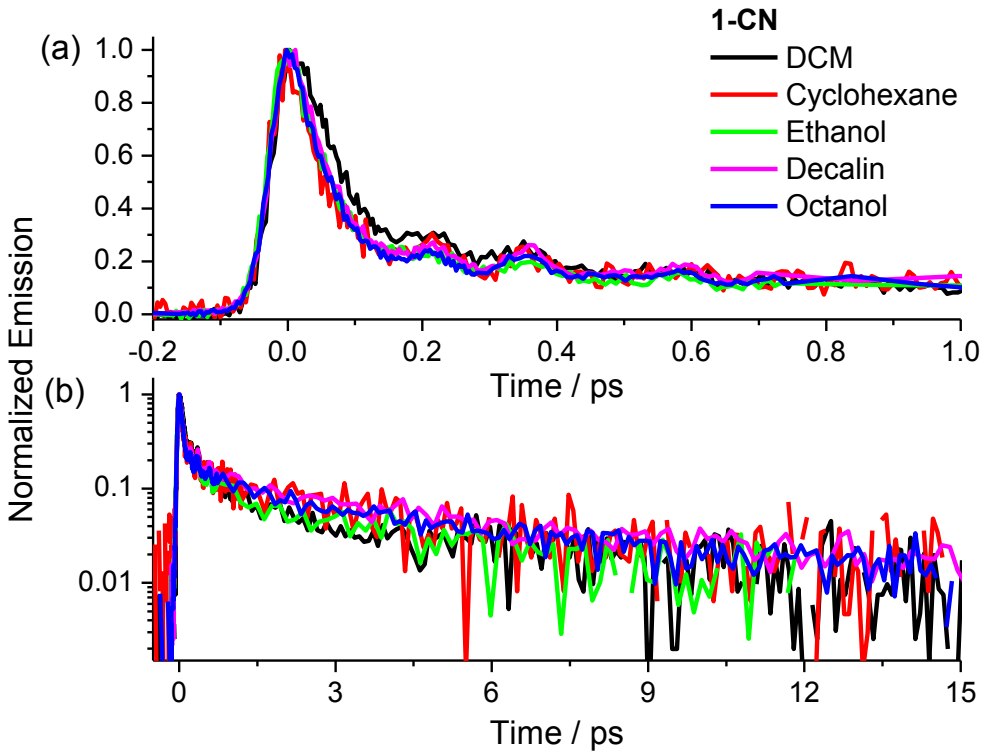

Figure 4.20 - *Solvent dependent fluorescence decay curves of 1-CN on (a) a linear intensity scale and (b) a log intensity scale.*

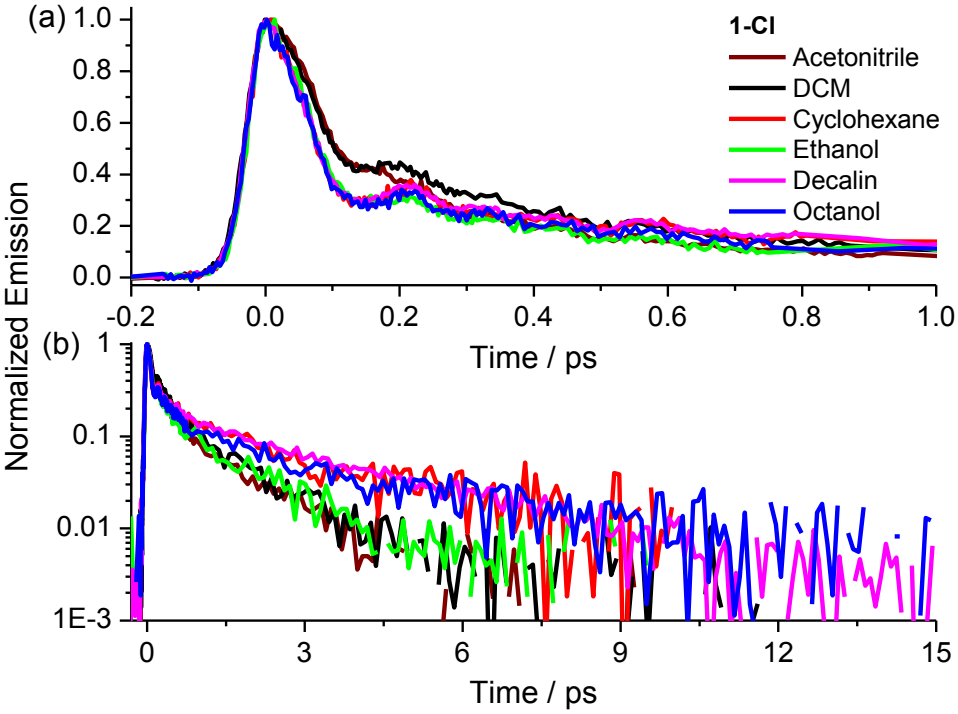

Figure 4.21 - *Solvent dependent fluorescence decay curves of 1-Cl on (a) a linear intensity scale and (b) a log intensity scale.*

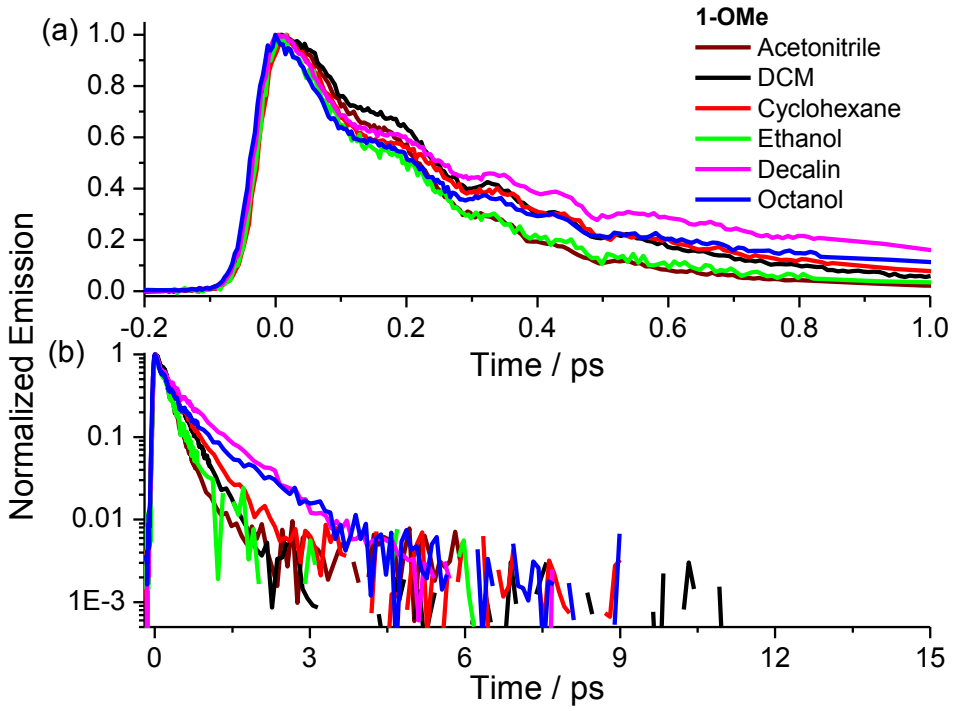

Figure 4.22 - *Solvent dependent fluorescence decay curves of 1-OMe on (a) a linear intensity scale and (b) a log intensity scale.*

Table 4.15 - *Exponential components of the function fitted to the solvent dependent fluorescence decay data of each derivative. Repeat fits to each measurement determined the error to be within 15% for each parameter.*

Solvent	Viscosity / mPa s	τ_1 / ps	A_1	τ_2 / ps	A_2	$\langle\tau_1\rangle$ / ps	τ_3 / ps	A_3
1-CN								
DCM	0.43	0.12	0.6	0.53	0.32	0.26	6.11	0.08
Cyclohexane	0.89	0.14	0.6	0.57	0.18	0.24	4.4	0.22
Ethanol	1.07	0.14	0.58	0.49	0.26	0.25	4.31	0.16
Decalin	2.5	0.09	0.65	0.58	0.22	0.21	8.03	0.13
Octanol	7.29	0.1	0.66	0.67	0.22	0.24	7.67	0.12
1-Cl								
Acetonitrile	0.37	0.18	0.82	-	-	-	1.47	0.18
DCM	0.43	0.29	0.78	-	-	-	1.51	0.22
Cyclohexane	0.89	0.28	0.65	-	-	-	2.34	0.35
Ethanol	1.07	0.24	0.7	-	-	-	1.41	0.3
Decalin	2.5	0.12	0.56	0.54	0.23	0.24	3.05	0.21
Octanol	7.29	0.11	0.48	0.5	0.38	0.28	4.18	0.14
1-H								
Acetonitrile	0.37	0.14	0.88	-	-	-	1.12	0.12
DCM	0.43	0.29	0.81	-	-	-	1.48	0.19
Cyclohexane	0.89	0.1	0.76	-	-	-	1.15	0.24
Ethanol	1.07	0.17	0.78	-	-	-	1.02	0.22
Decalin	2.5	0.07	0.71	0.44	0.18	0.14	2.92	0.11
Octanol	7.29	0.12	0.66	0.62	0.27	0.27	2.68	0.07
1-OMe								
Acetonitrile	0.37	0.19	0.85	-	-	-	0.4	0.15
DCM	0.43	0.28	0.75	-	-	-	0.47	0.25
Cyclohexane	0.89	0.28	0.76	-	-	-	0.7	0.24
Ethanol	1.07	0.25	0.97	-	-	-	0.44	0.03
Decalin	2.5	0.21	0.54	-	-	-	0.91	0.46
Octanol	7.29	0.18	0.67	-	-	-	0.82	0.33

Table 4.16 - *Damped harmonic oscillator components of the function fitted to the solvent dependent fluorescence decay data of each derivative. Repeat fits to each measurement determined the error of each parameter to be within 25%.*

Solvent	**Viscosity / mPa s**	τ_{D1} **/ ps**	ω_1 **/ THz**	$A_{\omega 1}$	φ_1	τ_{D2} **/ ps**	ω_2 **/ THz**	$A_{\omega 2}$	φ_2	τ_{D3} **/ ps**	ω_3 **/ THz**	$A_{\omega 3}$	φ_3
1-CN													
DCM	0.43	0.09	3.36	0.80	0.47	0.50	5.33	0.10	0.77	0.35	8.25	0.10	1.41
Cyclohexane	0.89	0.06	3.11	0.81	0.82	0.6	5.4	0.07	0.45	0.34	8.06	0.12	1.29
Ethanol	1.07	0.06	2.93	0.90	0.81	0.51	5.05	0.05	1.36	0.3	8.04	0.05	1.44
Decalin	2.50	0.09	3.40	0.80	0.66	0.61	5.15	0.10	1.33	0.62	8.08	0.10	1.21
Octanol	7.29	0.08	3.14	0.84	0.76	0.48	5.19	0.08	1.29	0.55	8.15	0.08	1.25
1-Cl													
Acetonitrile	0.37	0.03	3.24	0.80	0.43	0.11	6.09	0.18	4.81	0.75	8.25	0.02	2.37
DCM	0.43	0.05	3.58	0.72	0.43	0.10	5.96	0.25	4.99	0.64	8.44	0.03	1.23
Cyclohexane	0.89	0.04	3.68	0.90	0.34	0.22	5.49	0.08	5.38	0.66	8.37	0.02	1.74
Ethanol	1.07	0.05	3.34	0.90	0.38	0.14	5.73	0.09	5.40	0.67	8.61	0.01	0.93
Decalin	2.50	0.07	3.68	0.85	0.88	0.27	5.63	0.11	5.46	0.79	8.43	0.04	1.75
Octanol	7.29	0.06	3.79	0.75	0.42	0.10	5.87	0.21	5.27	0.65	8.50	0.04	0.97
1-H													
Acetonitrile	0.37	0.09	3.17	0.52	0.56	0.23	5.47	0.23	0.38	0.20	8.53	0.25	1.41
DCM	0.43	0.15	3.72	0.64	0.14	0.30	5.49	0.24	0.04	0.64	8.76	0.12	0.50
Cyclohexane	0.89	0.14	3.50	0.77	0.94	0.32	5.28	0.14	0.47	0.28	8.67	0.09	0.56
Ethanol	1.07	0.09	3.17	0.72	0.68	0.17	5.43	0.17	0.18	0.16	8.50	0.11	1.19
Decalin	2.50	0.16	3.49	0.68	1.07	0.42	5.39	0.18	0.35	0.34	8.43	0.14	1.80
Octanol	7.29	0.08	3.21	0.78	0.84	0.19	5.78	0.12	-0.22	0.20	8.55	0.10	1.39
1-OMe													
Acetonitrile	0.37	0.09	4.59	0.31	1.89	0.26	8.49	0.07	1.76	0.05	10.00	0.62	2.99
DCM	0.43	0.25	5.05	0.37	1.28	0.30	8.27	0.37	2.40	0.36	10.29	0.27	2.92
Cyclohexane	0.89	0.13	5.40	0.68	-0.03	0.49	8.46	0.18	1.37	0.41	10.31	0.14	2.35
Ethanol	1.07	0.16	5.06	0.64	0.72	0.64	8.5	0.18	1.72	0.65	10.65	0.18	1.88
Decalin	2.50	0.13	5.47	0.74	-0.15	0.64	8.52	0.15	1.15	0.61	10.38	0.11	2.28
Octanol	7.29	0.23	5.09	0.56	0.62	0.56	8.14	0.22	2.49	0.47	10.08	0.22	3.13

The 1-CN data required three exponential terms for every solvent, in line with the DCM data (Section 4.3.2). Finally, the 1-OMe data required only two exponential terms in each case. In line with the treatment of the 1-CN time resolved fluorescence data in DCM (Section 4.3.2), the weighted average of τ_1 and τ_2 was calculated ($<\tau_1>$ in Table 4.15) for the fitted functions comprised of three exponential terms. The weighted average ($<\tau_1>$) was then taken as a representation of the short component of the fluorescence decay for these data.

As described in Chapter 2, the shortest exponential component of the 1-H fluorescence decay was found to be independent of both solvent polarity and viscosity. This is true for each derivative studied here. It is interesting to compare τ_1 values in cyclohexane and ethanol in each case (Table 4.15) as they are of similar viscosity (0.89 mPa s and 1.07 mPa s respectively at 25 ^{o}C) but different polarities (0 D and 1.69 D respectively). Thus, the decay of the FC state is independent of polarity, suggesting that solvation dynamics are not an important driving force (as it may be in the case of a significant increase in charge transfer character between bright and dark states). Similarly τ_1 (or $<\tau_1>$) is independent of viscosity – it becomes slightly shorter in more viscous solvents, but we suggest that this most likely reflects the effect of fitting to the exponential terms. A viscosity independent nature of τ_1 can arise either if the structural evolution represented by this relaxation is volume conserving in nature or if the strong downhill driving force is sufficient to overcome the solvent friction effects. This is consistent with the hypothesis (Chapter 3) that this component of the fluorescence decay represents an ultrafast relaxation of the excited state to a dark state intermediate, primarily *via* volume conserving energetically downhill pyramidalization of the C9 atom[1,21] (Figure 4.1).

The longest exponential component (τ_3) of the fluorescence decay of each derivative does not exhibit a dependence upon solvent polarity but does depend upon the viscosity (Table 4.15). Recall that τ_3 is associated mainly with the decay of the dark state (Section 4.3.2). This

follows the τ_3 solvent dependence discussed previously for 1-H (Chapter 3). In the low viscosity regime (<1 mPa s), increasing the viscosity of the solvent (~3 fold for acetonitrile to ethanol), has no effect upon τ_3. A further increase in viscosity (threefold increase from ethanol to decalin) results in an increased time constant of τ_3. However, a further increase in viscosity (8 fold from decalin to octanol) does not result in a further increase in the τ_3 time constant. Therefore, each derivative exhibits some dependence upon solvent viscosity, but the extent of this viscosity dependence remains far smaller than that expected of a system undergoing excited state structural evolution *via* large scale torsional motion.[19,22,23] Complete rotation of the bulky rotor/stator groups of the motor molecule is expected to displace a significant volume of solvent and so a more significant viscosity dependence would be expected. Thus, the nature of this co-ordinate must be more complex than simple torsional motion. Pyramidalization is also likely to be heavily involved in this co-ordinate.

The solvent dependence of the transient absorption spectroscopy of each derivative was also assessed. In particular, the effects of solvent viscosity and polarity upon the lifetime of the dark state and ground state bleach transients were considered. These data were fitted to exponential functions (Table 4.17 and Table 4.18 respectively). 1-CN required two exponential terms in all solvents, 1-H and 1-Cl required two exponential terms only in the most viscous solvents (decalin and octanol) and 1-OMe required only a single exponential term in all solvents. For the bi-exponential fitted functions, the weighted average of the two exponential terms was calculated as a representation of the lifetime of the dark state and ground state bleach transients ($<\tau>$ in Table 4.17 and Table 4.18 respectively). This is consistent with the fluorescence and transient absorption measurements described previously for DCM (Section 4.3.3). The lifetimes of the dark state and ground state bleach transients were then compared directly to the long exponential component of the fluorescence decay data (τ_3) as shown in Table 4.19.

Table 4.17 – *Solvent dependent parameters of the exponential fit to the dark state decay curves of each derivative. Repeat measurements determined the error to be within 10% for each parameter.*

Solvent	Viscosity / mPa s	τ_1 / ps	A_1	τ_2 / ps	A_2	$\langle\tau\rangle$ / ps
1-CN						
Acetonitrile	0.37	1.09	0.19	10.4	0.81	8.68
DCM	0.43	5.27	0.16	11.44	0.84	10.41
Cyclohexane	0.89	2.7	0.33	12.55	0.67	9.35
Ethanol	1.07	4.41	0.35	15.94	0.65	11.92
Decalin	2.5	4.48	0.12	22.21	0.88	19.99
Octanol	7.29	7.32	0.20	31.96	0.80	26.98
1-Cl						
Acetonitrile	0.37	1.6	1	-	-	
DCM	0.43	1.86	1	-	-	
Cyclohexane	0.89	2.49	1	-	-	
Ethanol	1.07	2.21	1	-	-	
Decalin	2.5	2.5	0.50	5.57	0.50	4.02
Octanol	7.29	2.34	0.57	8.55	0.43	4.99
1-H						
Acetonitrile	0.37	1.28	1	-	-	
DCM	0.43	1.47	1	-	-	
Cyclohexane	0.89	1.82	1	-	-	
Ethanol	1.07	1.6	1	-	-	
Decalin	2.5	2.17	0.70	4.5	0.30	2.88
Octanol	7.29	1.72	0.73	6.61	0.27	3.03
1-OMe						
Acetonitrile	0.37	0.5	1	-	-	
DCM	0.43	0.51	1	-	-	
Cyclohexane	0.89	0.65	1	-	-	
Ethanol	1.07	0.5	1	-	-	
Decalin	2.5	1.08	1	-	-	1.08
Octanol	7.29	0.83	1	-	-	0.83

Table 4.18 - *Solvent dependent parameters of the exponential fitted to the ground state recovery curves of each derivative. Poor signal to noise precluded this measurement for 1-Cl in cyclohexane. Repeat measurements determined the error to be within 10% for each parameter.*

Solvent	Viscosity / mPa s	τ_1 / ps	A_1	τ_2 / ps	A_2	$\langle\tau\rangle$ / ps
1-CN						
Acetonitrile	0.37	2.79	0.48	19.35	0.52	11.34
DCM	0.43	4.00	0.40	17.15	0.60	11.86
Cyclohexane	0.89	7.37	0.61	13.59	0.39	9.77
Ethanol	1.07	5.91	0.25	13.81	0.75	11.82
Decalin	2.5	15.42	0.68	31.29	0.32	20.51
Octanol	7.29	16.9	0.56	50.13	0.44	31.61
1-Cl						
Acetonitrile	0.37	1.41	1	-	-	1.41
DCM	0.43	1.83	1	-	-	1.83
Cyclohexane	0.89	-	-	-	-	-
Ethanol	1.07	2.11	1	-	-	2.11
Decalin	2.5	3.95	1	-	-	3.95
Octanol	7.29	4.59	1	-	-	4.59
1-OMe						
Acetonitrile	0.37	0.51	1	-	-	0.51
DCM	0.43	0.53	1	-	-	0.53
Cyclohexane	0.89	0.74	1	-	-	0.74
Ethanol	1.07	0.47	1	-	-	0.47
Decalin	2.5	1.11	1	-	-	1.11
Octanol	7.29	0.85	1	-	-	0.85

Table 4.19 – *Solvent dependence of the ground state recovery time, the dark state lifetime and the long component of the fluorescence decay of each derivative. Repeat measurements determined the error to be within 10% for both the ground state recovery time and the dark state lifetime, and 15% for the long component of the fluorescence decay.*

Solvent	Viscosity / mPa s	<τ> Ground State / ps	<τ> Dark State / ps	τ_3 Fluorescence / ps
1-CN				
Acetonitrile	0.37	11.34	8.68	-
DCM	0.43	11.86	10.41	6.11
Cyclohexane	0.89	9.71	9.35	4.62
Ethanol	1.07	11.82	11.92	4.27
Decalin	2.5	20.51	19.99	8.03
Octanol	7.29	31.61	26.98	7.67
1-Cl				
Acetonitrile	0.37	1.41	1.6	1.43
DCM	0.43	1.83	1.86	1.51
Cyclohexane	0.89	-	2.49	2.34
Ethanol	1.07	2.11	2.21	1.41
Decalin	2.5	3.95	4.02	3.05
Octanol	7.29	4.59	4.99	4.18
1-H				
Acetonitrile	0.37	-	1.28	1.12
DCM	0.43	-	1.47	1.48
Cyclohexane	0.89	-	1.82	1.11
Ethanol	1.07	-	1.6	0.96
Decalin	2.5	-	2.88	2.92
Octanol	7.29	-	3.03	2.68
1-OMe				
Acetonitrile	0.37	0.51	0.5	0.4
DCM	0.43	0.53	0.51	0.47
Cyclohexane	0.89	0.74	0.65	0.7
Ethanol	1.07	0.47	0.5	0.46
Decalin	2.5	1.11	1.08	0.91
Octanol	7.29	0.85	0.83	0.82

A clearer comparison is gained by plotting the viscosity dependence of each kinetic component (average lifetimes of the dark state and ground state bleach transients and the long component of the fluorescence decay) for each derivative (Figure 4.23). Figure 4.23 reveals that the correspondence between the lifetimes of the dark state and ground state bleach transients, and the long exponential component of the fluorescence observed in DCM remains valid for each solvent studied. In the case of 1-CN, the disparity between the dark state lifetime measured by transient absorption and the long component of the fluorescence decay is retained in each solvent studied. Possible reasons for this were discussed above (Section 4.3.3.1). The dark state decay of 1-CN also remains significantly slower than for the other derivatives in every solvent. Turning to 1-OMe, the excited state dynamics of this derivative are significantly faster than the remaining derivatives. In every solvent studied, there is close agreement between the timescale of ground state recovery, dark state relaxation and the long exponential component of the fluorescence decay of 1-OMe.Thus, the lifetime of the 1-OMe dark state is viscosity dependent, but remains significantly shorter than the remaining derivatives in every solvent studied. In the case of 1-Cl, there is also good agreement between the lifetimes of the dark state and ground state bleach transients and the long exponential component of the fluorescence decay in each solvent. In comparison to 1-H, the dark state lifetime of 1-Cl is slightly longer, but this remains a far smaller effect than that observed for 1-CN. This is consistent with the data described previously and is not surprising since the Cl substituent has only a very small effect upon the electron density of the molecule.

Therefore, the substituent dependent trend observed previously in DCM (Section 4.3.3) is retained in each solvent studied in this work. Thus, the picture developed above for DCM appears equally applicable to a range of solvents. The dynamics are independent of solvent polarity and are only weakly dependent on viscosity.

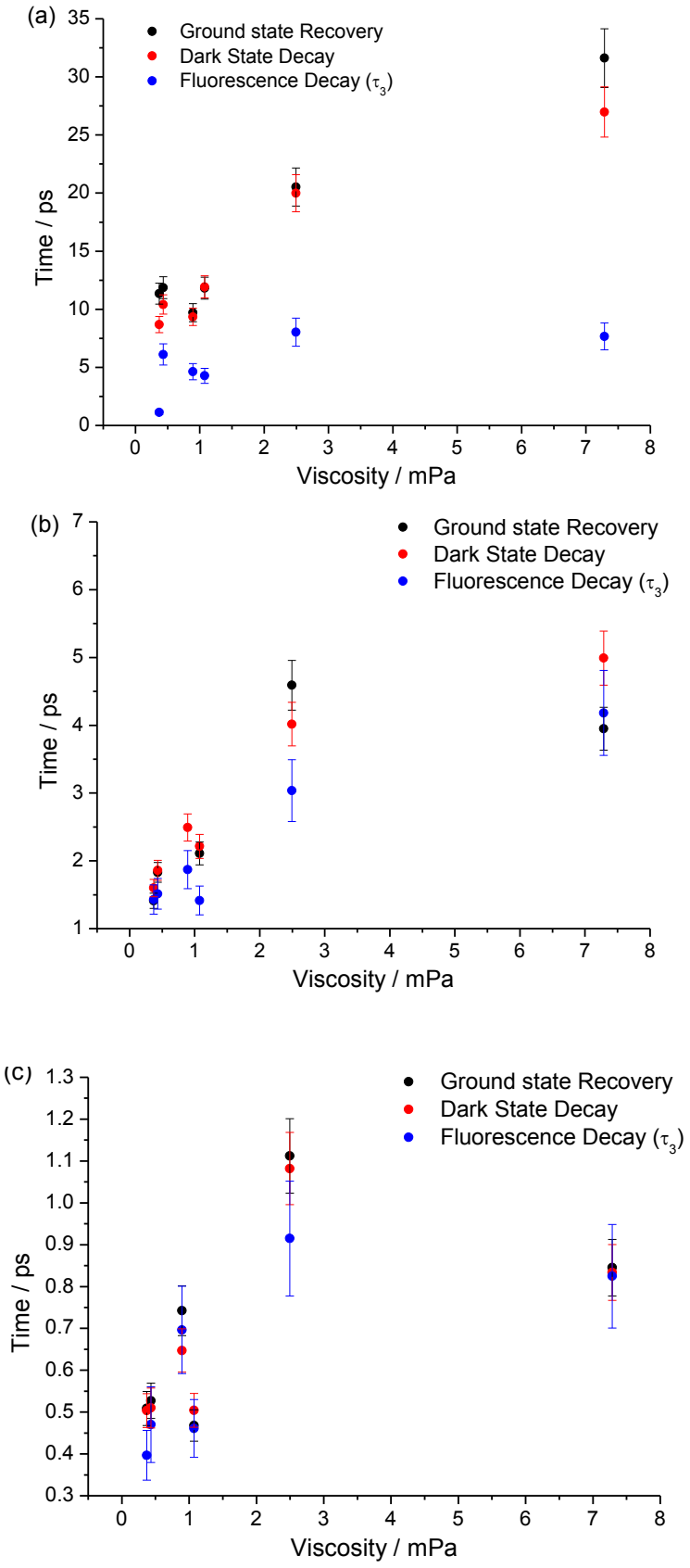

Figure 4.23 - *A comparison of the solvent dependent ground state recovery time, dark state lifetime and long component of the fluorescence decay for (a) 1-CN, (b) 1-Cl and (c) 1-OMe.*

4.4 Conclusion

The substituent dependence of the excited state dynamics of a rotary molecular motor was probed with ultrafast fluorescence up-conversion and transient absorption spectroscopies. A significant substituent dependence was discovered, with both electron withdrawing and donating substituents influencing the molecular dynamics on the excited state potential energy surface. This is in marked contrast to the minor effect of the substituents on the thermal ground state dynamics.

The model invoked previously for the 1-H excited state dynamics (Chapter 2) was applied to the substituted derivatives. This model involves an initially populated emissive excited state (bright state), which relaxes to a non-emissive excited state (dark state). The dark state population then relaxes to the ground state *via* internal conversion at a conical intersection. The dark state is also able to repopulate the bright state *via* a barrier on the excited state potential energy surface. No substituent dependence was observed for the bright to dark state relaxation. In contrast, the lifetime of the dark state was found to be highly sensitive to the nature of the substituent. As the electron withdrawing strength of the substituent is increased, the lifetime of the dark state becomes longer. We propose that the observed substituent dependent dynamics of the molecular motor can be explained in terms of two parameters of the excited state potential energy surface: the energetic position of the conical intersection relative to the dark state minimum and the size of the dark to bright state energy barrier. We suggest that the conical intersection becomes higher in energy relative to the local minimum of the dark state as the electron withdrawing strength of the substituent is increased. This leads to the longest lived dark state for the strongest electron withdrawing substituent is (1-CN) and the shortest lived dark state for the strongest electron donating substituent (1-OMe). We also suggest that the energy barrier opposing repopulation of the bright state by the dark state population increases as the electron withdrawing strength of the substituent is increased.

This leads to the lowest amplitude dark state decay signal in the fluorescence decay curves of 1-CN and the highest amplitude dark state decay signal in the fluorescence decay curves of 1-OMe. This proposal was supported by kinetic modelling of the bright state population as a function of the size of the dark to bright state energy barrier.

The solvent dependence of each substituted motor derivative was found to be similar. Solvent polarity was found to have no effect upon either the steady state spectroscopy or the excited state relaxation dynamics of each derivative. This suggests that no significant charge redistribution occurs between the ground state and Franck-Condon bright state of each derivative. The kinetics of the bright to dark state relaxation (ascribed to the short component of the fluorescence decay of each derivative) were also found to be independent of solvent viscosity for each derivative. This supports the suggestion that this relaxation proceeds primarily *via* volume conserving energetically downhill pyramidalization. In contrast, the kinetics of the dark excited state to ground state relaxation (ascribed to the longest component of the fluorescence decay of each derivative) were found to exhibit some dependence upon solvent viscosity. However, this dependence was found to be far less significant than that expected of a system undergoing large scale torsion (such as that typical of an isomerization reaction). Therefore, this suggests that the mechanism of the dark to ground state relaxation is more complex than simple torsional motion, with pyramidalization also likely to play a large role in this process.

In order to obtain a deeper insight into why such a significant substituent dependence is observed, theoretical studies, particularly in which the potential energy surfaces are modelled as a function of substituent, are required. It is hoped that the experimental data presented here can serve as a solid basis from which such calculations can be made in the future.

4.5 References

(1) Kazaryan, A.; Kistemaker, J. C. M.; Schafer, L. V.; Browne, W. R.; Feringa, B. L.; Filatov, M. *J. Phys. Chem. A.* **2010**, *114*, 5058.

(2) Waldeck, D. H. *Chem. Rev.* **1991**, *91*, 415.

(3) Siewert, S. S.; Spangler, L. H. *J. Phys. Chem.* **1995**, *99*, 9316.

(4) King, N. R.; Whale, E. A.; Davis, F. J.; Gilbert, A.; Mitchell, G. R. *J. Mater. Chem.* **1997**, *7*, 625.

(5) Dekhtyar, M.; Rettig, W. *Phys. Chem. Chem. Phys.* **2001**, *3*, 1602.

(6) Pollard, M. M.; Wesenhagen, P. V.; Pijper, D.; Feringa, B. L. *Org. Biomol. Chem.* **2008**, *6*, 1605.

(7) Clayden, J.; Greeve, N.; Warren, S.; Wothers, P. *Organic Chemistry, Oxford University Press* **2001**.

(8) Cnossen, A., University of Groningen, 2013.

(9) Berberansantos, M. N.; Martinho, J. M. G. *J. Chem. Educ.* **1990**, *67*, 375.

(10) Pogliani, L.; BerberanSantos, M.; Martinho, J. M. G. *J. Math. Chem.* **1996**, *20*, 193.

(11) Sauder, J. M.; MacKenzie, N. E.; Roder, H. *Biochemistry* **1996**, *35*, 16852.

(12) Xu, M.; Beresneva, O.; Rosario, R.; Roder, H. *J. Phys. Chem. B.* **2012**, *116*, 7014.

(13) van Boekel , M. A. J. S. In *Kinetic Modeling of Reactions In Foods*; CRC Press: 2008.

(14) Robson Wright, M. In *An Introduction to Chemical Kinetics*; John Wiley & Sons, Ltd: 2005, p 43.

(15) Steiner, E.; Knovel *The Chemistry MathsBbook*; Oxford University Press: Oxford ; New York, 2008.

(16) Matsen, F. A.; Franklin, J. L. *J. Am. Chem. Soc.* **1950**, *72*, 3337.

(17) In *Comprehensive Chemical Kinetics*; Bamford, C. H., Tipper, C. F. H., Eds.; Elsevier: 1969; Vol. Volume 2, p II.

(18) Martin, M. M.; Plaza, P.; Changenet, P.; Meyer, Y. H. *J. Photochem. Photobiol. A.* **1997**, *105*, 197.

(19) Changenet, P.; Zhang, H.; van der Meer, M. J.; Glasbeek, M.; Plaza, P.; Martin, M. M. *J. Phys. Chem. A.* **1998**, *102*, 6716.

(20) Augulis, R.; Klok, M.; Feringa, B. L.; van Loosdrecht, P. H. M. In *Phys. Status. Solidi. C, Vol 6, No 1*; Itoh, T. T. K. S. M., Ed. 2009; Vol. 6, p 181.

(21) Kazaryan, A.; Lan, Z.; Schäfer, L. V.; Thiel, W.; Filatov, M. *J. Chem. Theory. Comput.* **2011**, *7*, 2189.

(22) van der Meer, M. J.; Zhang, H.; Glasbeek, M. *J. Chem. Phys.* **2000**, *112*, 2878.

(23) Espagne, A.; Paik, D. H.; Changenet-Barret, P.; Martin, M. M.; Zewail, A. H. *ChemPhysChem* **2006**, *7*, 1717.

5 Excited State Dynamics of a tri-phenylacetylene Substituted Molecular Motor

In this chapter, the excited state dynamics of a tri-phenylacetylene substituted derivative of the molecular motor system are investigated. The effect of the substitution is to give the motor some features of a propeller, and our aim is to investigate the effect of this on the photophysics. After detailing the experimental conditions employed (Section 5.2), the steady state spectroscopy of the system will be described (Section 5.3.1). Following this, ultrafast fluorescence up-conversion (Section 5.3.2) and transient absorption (Section 5.3.3) measurements will be discussed. The solvent dependence of each measurement is also considered.

5.1 Introduction

As an extension of the molecular motor project, a tri-phenylacetylene substituted derivative of the molecular motor was synthesised (CCPh, Figure 5.1). In comparison to the electron donating/withdrawing substituents studied in Chapter 4, CCPh is a very weak electron donor[1-3] but is significantly larger. Thus, the electronic properties of CCPh are not expected to alter significantly compared to the 1-H molecular motor system (by analogy with the very weak electron withdrawing Cl substituent in Chapter 4). Therefore, this structure allows an assessment of the effects of sterically large substituents upon the excited state decay dynamics of the molecular motor. It is envisaged that the extended chain phenyl substituents may act as 'paddles' whereby additional friction is experienced to rotational motion of the molecule. In principle it is expected that any such additional friction will lead to slower reorientational motion.[4] Since excited state structural evolution along the rotational (and pyramidalization) co-ordinate is believed to facilitate non-radiative excited state decay (Chapter 3), slower rotational motion is expected to lead to a longer lived excited state.

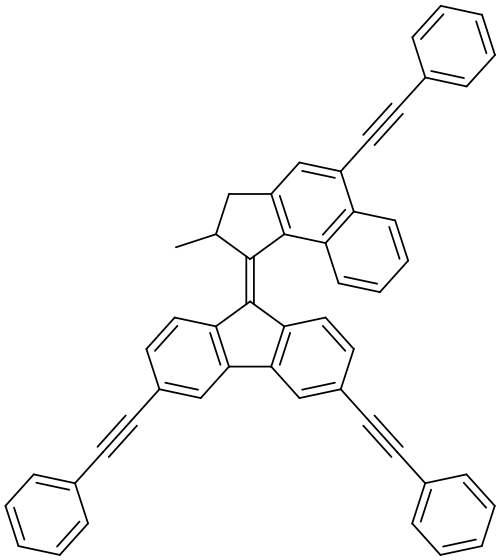

Figure 5.1 - *Molecular structure of the tri-phenylacetylene substituted molecular motor (CCPh).*

This can be detected *via* fluorescence up-conversion and transient absorption spectroscopies, as described in preceding chapters. Any such retardation effects are likely to be enhanced in more viscous media, and so the effect of solvent viscosity will be investigated. Thus, by comparing the measured excited state kinetics of CCPh to that of the parent molecule (1-H, Chapter 3) we hope to gain a new insight into the coupling of excited state relaxation to the environment in this class of molecular motor.

5.2 Experimental

The synthesis of CCPh is described in Chapter 2.[5] The experimental conditions employed for all steady state (absorption and emission) and transient absorption measurements are identical to those described previously for 1-H (Chapter 3). Fluorescence up-conversion measurements were conducted with the excitation beam centred at 415 nm (corresponding to 830 nm fundamental beam) for CCPh and as described in Chapter 4 for the other derivatives. All other parameters are identical to those described previously.

5.3 Results and Discussion

5.3.1 Steady State Spectroscopy

The steady state absorption and fluorescence spectra of CCPh (recorded in DCM) are shown in Figure 5.2. In comparison to the electron donating/withdrawing substituted molecular motor derivatives studied in Chapter 4, CCPh exhibits a significant red shift in both the maximum of absorption and emission. However, the Stokes shift of CCPh (102 nm) is larger than that of the parent molecule 1-H (85 nm) but smaller than that of 1-OMe (108 nm), 1-CN (132 nm) and 1-Cl (116 nm). Thus, the steady state spectroscopy of CCPh is consistent with a weak electron donor substituent, with an intermediate Stokes shift between 1-H (no electronic effect) and 1-OMe (strong electron donor).

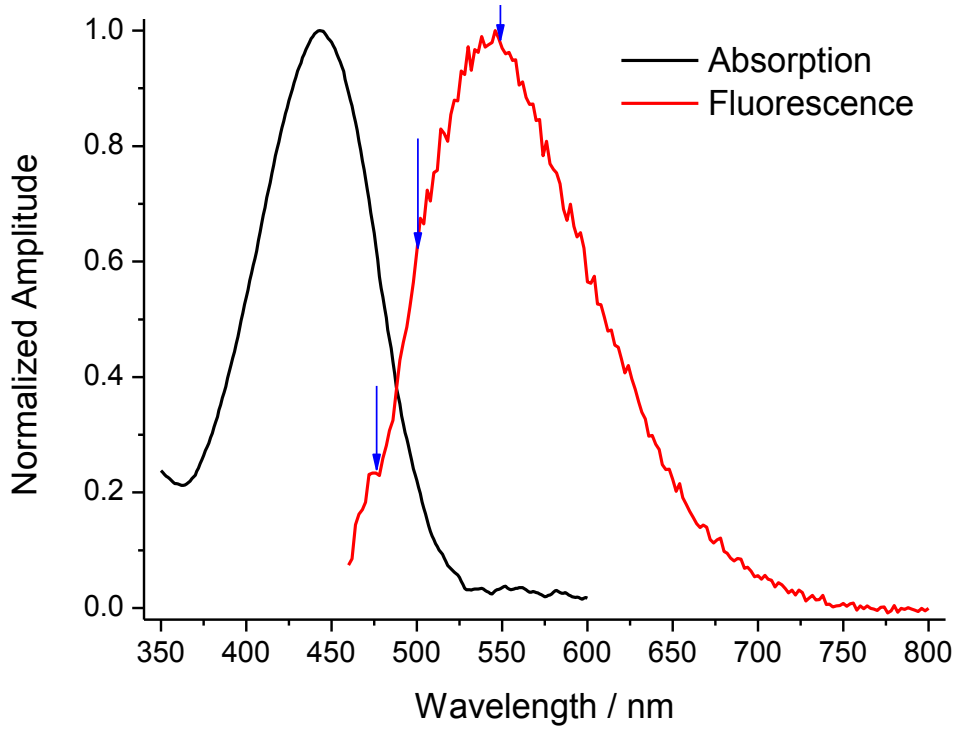

Figure 5.2 - *Steady state absorption (black) and emission (red) spectra of CCPh in DCM. The emission spectrum was recorded by excitation at 450 nm (peak of absorption). The blue arrows show the wavelengths at which the fluorescence lifetime was measured by fluorescence up-conversion.*

In order to probe the effect of the tri-phenylacetylene substituents upon the excited state dynamics of the molecular motor, time-resolved spectroscopy measurements were employed.

5.3.2 Ultrafast Fluorescence Up-conversion Spectroscopy

The fluorescence decay dynamics of CCPh were studied as a function of emission wavelength and solvent viscosity. Figure 5.3 shows the fluorescence decay curves of CCPh in DCM recorded at 3 emission wavelengths on the blue side of the spectrum (marked by blue arrows in Figure 5.2). The raw data (points) were fitted to a sum of three exponential decay terms and three damped harmonic oscillator functions (lines). The parameters of the exponential and oscillator components of the fitted functions are summarized in Table 5.1 and Table 5.2 respectively.

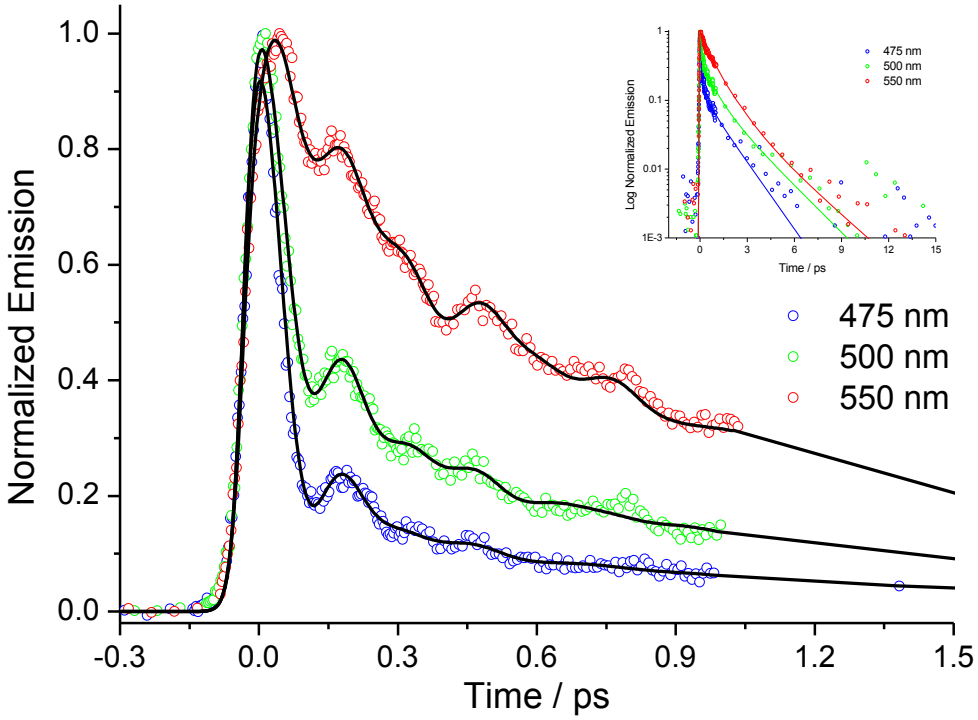

Figure 5.3 - *Time-resolved fluorescence decay curves of CCPh in DCM measured at an emission wavelength of 550 nm (red), 500 nm (green) and 475 nm (blue). The raw data (points) were fitted to a function (lines) comprising the sum of three exponential and three damped harmonic oscillator terms. Inset shows the data on a log-intensity scale.*

Table 5.1 – *Exponential components of the function fitted to the emission wavelength dependent fluorescence decay data of CCPh in DCM. Repeat fits to each measurement determined the error to be within 15% for each parameter.*

Emission λ / nm	τ_1 /ps	A_1	τ_2 /ps	A_2	τ_3 /ps	A_3
475	0.07	0.82	0.27	0.07	1.24	0.11
500	0.09	0.70	0.62	0.19	1.94	0.11
550	0.11	0.35	0.93	0.53	2.17	0.12

Table 5.2 – *Damping (τ_D), frequency (ω), amplitude (A_ω) and phase (Φ) components of the damped harmonic oscillator functions used to fit the oscillatory part of the time domain fluorescence decay data of CCPh in DCM. Repeat fits to each measurement determined the error of each parameter to be within 25%.*

Excitation λ / nm	τ_{D1} / ps	ω_1 / THz	$A_{\omega1}$	φ_1	τ_{D2} / ps	ω_2 / THz	$A_{\omega2}$	φ_2	τ_{D3} / ps	ω_3 / THz	$A_{\omega3}$	φ_3
475	0.15	2.04	0.21	2.83	0.20	3.99	0.18	1.57	0.11	6.41	0.61	5.40
500	0.15	1.98	0.26	3.12	0.24	3.99	0.18	1.81	0.14	6.65	0.56	4.98
550	0.10	2.49	0.66	4.66	0.57	3.87	0.11	0.85	0.25	6.86	0.23	4.67

From Figure 5.3 it is evident that CCPh retains the general fluorescence decay profile exhibited by the molecular motor derivatives studied in the previous chapters. The decay remains ultrafast and superimposed with a series of oscillations. The decay consists of a short (< 110 fs) component (with increasing weight as the emission wavelength is blue shifted) and a minor amplitude (12 %) longer (>1 ps) decay component. An intermediate decay component (with decreasing weight as the emission wavelength is blue shifted) was also required to provide an adequate fit to the data. The decay of each exponential component becomes faster as the emission wavelength is blue shifted, as observed for 1-H (Chapter 3).

The significant wavelength dependence of the sub-picosecond fluorescence decay dynamics is also exhibited by the damped harmonic oscillator terms. The two highest frequency terms (τ_{D2} and τ_{D3} in Table 5.2) become more strongly damped as the emission wavelength is blue shifted. This is in contrast to the lowest frequency term (τ_{D1} in Table 5.2) which is independent of the emission wavelength. The frequency of each oscillator term is also wavelength independent (within experimental error).

The effect of the weak electron donating ability of the tri-phenylacetylene substituents upon the fluorescence decay dynamics should be considered. To do so, a comparison was made between the fluorescence decay curves of CCPh (very weak electron donor), 1-OMe (strong electron donor) and 1-H (no electronic effect). This is shown in Figure 5.4 and Table 5.3 (exponential decay terms only). In each case, the decay curves were recorded in DCM at the wavelength of maximum emission (550 nm, 500 nm and 475 nm for CCPh, 1-OMe and 1-H respectively). Figure 5.4 shows that the fluorescence decay curve of CCPh (clearly non-single exponential) is significantly different from that of 1-OMe and more similar to that of 1-H (also non-single exponential). This is supported by the parameters extracted from the fitting (Table 5.3). The significant shortening of the long component of the fluorescence decay (τ_3 in Table 5.3) of 1-OMe compared to 1-H (by a factor of ~3) was previously assigned as an effect of the electron donating ability of the OMe substituent (Chapter 4). In the case of CCPh, the long exponential decay term (~2.2 ps) is actually longer than that of 1-H (~ 1ps). Therefore, the fluorescence decay of CCPh is more like that of 1-H rather than 1-OMe. This is consistent with the very weak electron donating ability of the phenylacetylene substituents. Therefore, the observed differences between the excited state decay kinetics of CCPh and 1-H can be ascribed to the effect of the sterically bulky phenylacetylene substituents, rather than any electronic effects.

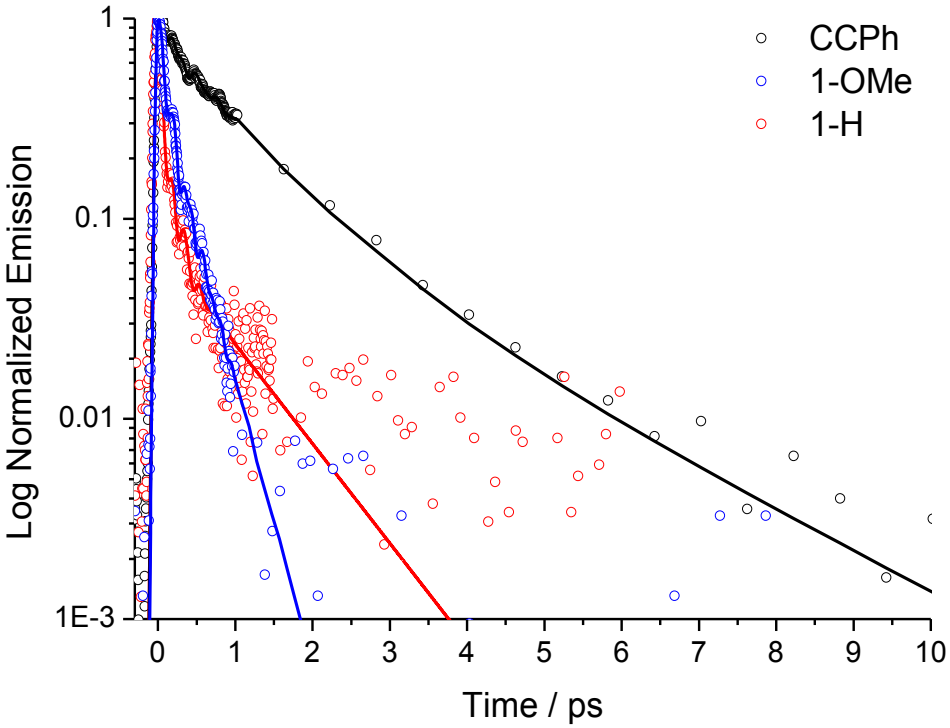

Figure 5.4 - *A comparison of the fluorescence decay curves of CCPh (black), 1-OMe (blue) and 1-H (red), measured at the wavelength of maximum emission in each case. The raw data (points) were fitted to a function (lines) comprising the sum of exponential decay terms (up to three) and two damped harmonic oscillators. Inset shows the data on a log-intensity scale.*

Table 5.3 - *A comparison of the exponential decay terms of the functions fitted to the fluorescence decay curves of CCPh, 1-OMe and 1-H. Repeat fits to each measurement determined the error to be within 15% for each parameter*

Substituent	τ_1 **/ps**	A_1	τ_2 **/ps**	A_2	τ_3**/ps**	A_3
CCPh	0.11	0.35	0.93	0.53	2.17	0.12
1-OMe	0.08	0.74	-	-	0.34	0.26
1-H	0.14	0.84	-	-	0.93	0.16

Table 5.3 shows that increasing the size of the rotor (CCPh compared to 1-H) increases only the lifetime of the long fluorescence decay component (τ_3), with no effect upon the short fluorescence decay component (τ_1). The CCPh decay also exhibits an additional dominant (~ 50 %) ~1 ps decay term. Previously, only the long component of the fluorescence decay of 1-H (Chapter 3) and a series of substituted molecular motors (Chapter 4) was found to be dependent upon solvent viscosity. Therefore, the effect of the sterically bulky phenylacetylene substituents upon the viscosity dependence of the excited state decay dynamics of the motor is an important consideration.

The fluorescence decay curves of CCPh recorded in a series of increasingly viscous solvents are shown in Figure 5.5. In each case, the emission wavelength was tuned to 550 nm corresponding to approximately the wavelength of maximum emission. The raw data (points) was fitted to a function (lines) comprising three exponential decay terms and three damped harmonic oscillators. The parameters of the exponential and oscillator terms are summarized in Table 5.4 and Table 5.5 respectively.

The fluorescence decay dynamics of CCPh exhibit a clear dependence upon solvent viscosity. Table 5.4 reveals that the lifetime of the longest exponential component of the decay (τ_3) increases as the viscosity of the medium is increased. In contrast, the time constant of the fastest exponential component (τ_1) is independent of viscosity (within experimental error). This is in agreement with the fluorescence decay dynamics of 1-H described previously (Chapter 3). The intermediate exponential term (τ_2) also shows some viscosity dependence, but this less significant than that observed for τ_3. For example, increasing the viscosity by a factor of ~7 (ethanol to octanol) increases the time constant of τ_3 by a factor of 3.3, but only a factor of 1.5 for τ_2.

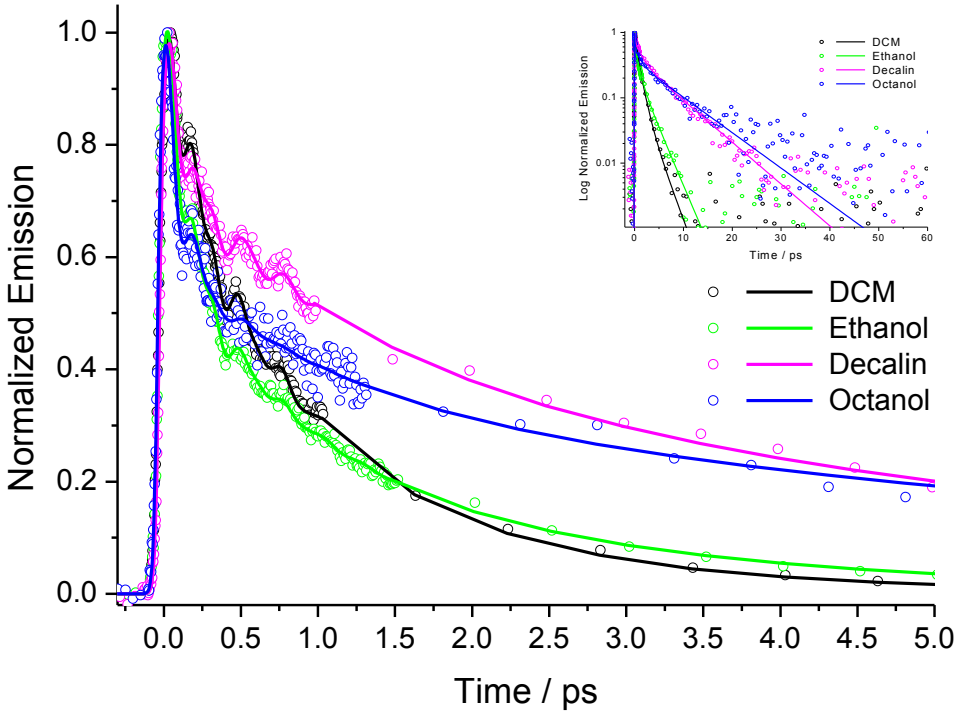

Figure 5.5 - *Solvent dependent fluorescence decay curves of CCPh measured at 550 nm. The raw data (points) were fitted to a function (lines) comprising the sum of three exponential decay terms and three damped harmonic oscillators. Inset shows the data on a log-intensity scale.*

Table 5.4 - *Exponential components of the function fitted to the solvent dependent fluorescence decay data of CCPh measured at 550 nm. Repeat fits to each measurement determined the error to be within 15% for each parameter.*

Solvent	***Viscosity / mPa s***	**τ_1 /ps**	**A_1**	**τ_2 /ps**	**A_2**	**τ_3 /ps**	**A_3**
DCM	0.43	0.11	0.35	0.93	0.53	2.17	0.12
Ethanol	1.07	0.10	0.54	0.82	0.27	2.44	0.19
Decalin	2.5	0.09	0.37	1.46	0.31	6.94	0.32
Octanol	7.29	0.09	0.53	1.22	0.20	8.10	0.27

Table 5.5 *Damping (τ_D), frequency (ω), amplitude (A_ω) and phase (Φ) components of the damped harmonic oscillator functions used to fit the oscillatory part of the time domain fluorescence decay data of CCPh measured at 550 nm. Repeat fits to each measurement determined the error of each parameter to be within 25%.*

Solvent	***Viscosity / mPa s***	τ_{D1} **/ ps**	ω_1 **/ THz**	$A_{\omega 1}$	φ_1	τ_{D2} **/ ps**	ω_2 **/ THz**	$A_{\omega 2}$	φ_2	τ_{D3} **/ ps**	ω_3 **/ THz**	$A_{\omega 3}$	φ_3
DCM	0.43	0.10	2.49	0.66	4.66	0.57	3.87	0.11	0.85	0.25	6.86	0.23	4.67
Ethanol	1.07	0.10	2.13	0.60	4.63	0.40	3.89	0.13	0.56	0.20	6.85	0.27	4.64
Decalin	2.5	0.10	2.33	0.56	5.05	0.65	3.83	0.13	0.66	0.17	6.91	0.31	4.48
Octanol	7.29	0.12	2.08	0.36	4.94	0.23	3.68	0.14	0.91	0.11	6.29	0.50	4.99

In addition, the lifetime of τ_3 exhibits a larger dependence upon viscosity for 1-CCPh than 1-H. For example, increasing the solvent viscosity by a factor of ~7 (ethanol to octanol) results in an increased τ_3 time constant by a factor of ~3.3 for 1-CCPh compared to ~2.6 for 1-H. Therefore, as the size of the rotor of the molecular motor is increased (CCPh compared to 1-H), the lifetime of the long fluorescence decay component (previously assigned to the relaxation of the dark excited state to the ground state) becomes more sensitive to the viscosity of the medium. Thus, a larger rotor results in greater retardation of motion along the dark to ground state relaxation co-ordinate. This shows that the coupling between the medium and the molecule can be modified by altering the size of the rotor in the molecular structure of the motor. However, the observed viscosity dependence remains small for such a bulky system undergoing large scale torsion. Typically a viscosity dependence of η^1 or $\eta^{2/3}$ is expected for cis-trans isomerization reactions[6-8] (See Chapter 1 for a detailed discussion of viscosity dependent isomerization reactions). This is consistent with the previous assignment (Chapter 4) of a combination of both torsional motion and pyramidalization to the co-ordinate of the dark to ground state decay. In contrast, the insensitivity of τ_1 (previously ascribed to relaxation of the bright excited state to the dark excited state) to the tri-phenylacetylene

substitution suggests that sterically bulky substituents do not influence the bright to dark state relaxation co-ordinate. Thus, since no such retardation is observed, this suggests that volume displacing torsional motion is not required for bright to dark state relaxation to proceed. This is consistent with the previous assignment (Chapter 4) of pyramidalization to the co-ordinate of bright to dark state relaxation, with little or no torsional motion involved.

5.3.3 Ultrafast Transient Absorption Spectroscopy

Transient absorption was employed successfully in the previous chapters to study further the excited state decay dynamics of the molecular motor derivatives. As a result, the transient absorption spectra of CCPh were measured with a particular focus on the relationship between the dark state lifetime (measured by transient absorption) and the fluorescence decay data.

The transient spectra of CCPh were measured in the same series of solvents as that used to probe the fluorescence decay. An example of the time dependent absorption spectra is shown in Figure 5.6 for CCPh measured in decalin. Two dominant transient features are found in the transient absorption spectrum of CCPh: the ground state bleach (~440 nm) and an excited state absorption band (~515 nm) which is ascribed to absorption of the dark excited state. The dark state transient decays to a weak band centred at ~500 nm which then remains unchanged for the duration of the measurements (over 300 ps). This corresponds to the steady state absorption maximum of the photoproduct and so this weak permanent (for the measurement duration) band is ascribed to ground state absorption of the CCPh photoproduct. Of most significance is the solvent viscosity dependence of the lifetime of the CCPh dark state transient. Figure 5.7 shows the time-domain relaxation of the dark state transient for each solvent studied. In each case, the raw data (points) were fitted to a bi-exponential function (lines), the parameters of which are summarized in Table 5.6.

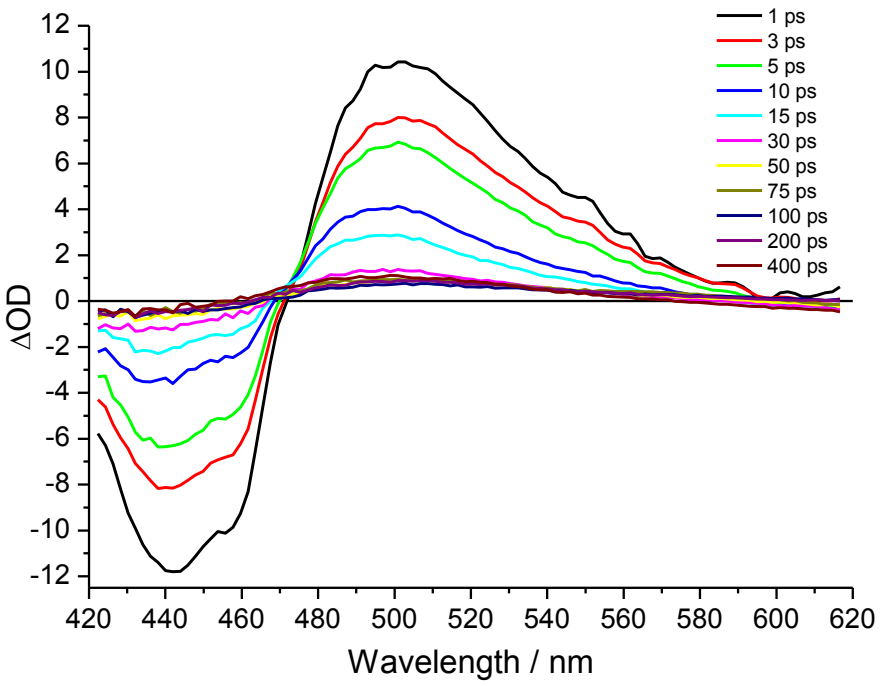

Figure 5.6 - *Transient absorption spectra of CCPh in Decalin.*

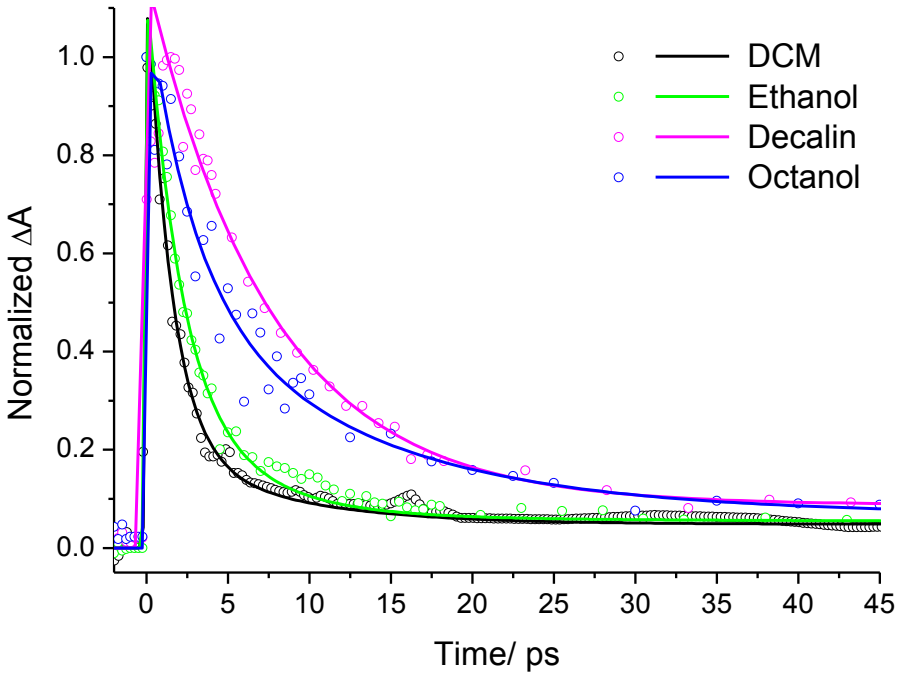

Figure 5.7 - *Solvent dependent decay of the dark state transient of CCPh (~515 nm). The raw data (points) were fitted to a bi-exponential function (lines).*

Table 5.6 - *Parameters of the bi-exponential function fitted to the solvent dependent dark state transient decay curves of CCPh. Repeat measurements determined the error to be within 10% for each parameter.*

Solvent	***Viscosity / mPa s***	**τ_1 /ps**	**A_1**	**τ_2 /ps**	**A_2**	**$\langle\tau\rangle$ /ps**
DCM	0.43	1.35	0.83	6.73	0.17	2.25
Ethanol	1.07	1.94	0.74	6.03	0.26	2.99
Decalin	2.5	4.62	0.15	7.36	0.85	6.95
Octanol	7.29	2.83	0.55	12.28	0.45	7.02

The long-lived photoproduct absorption feature at ~500 nm resulted in a permanent (for the duration of the measurement) positive baseline in the decay curves (Figure 5.7).To account for this, an arbitrary long (1 ns) exponential component of fixed lifetime but freely varying amplitude was included in the fit.

The dark state lifetime of CCPh follows a similar trend to that described previously for the fluorescence up-conversion measurements. There is little difference between the dark state lifetime measured in solvents in the low viscosity regime (DCM and Ethanol), but a significant increase is observed in the high viscosity regime (Decalin and Octanol). However, little difference is observed between decalin and octanol despite an approximate threefold increase in viscosity. As observed for the long fluorescence decay component, the measured viscosity dependence is smaller than that expected of a system undergoing large scale torsional motion, where typically a η^1 or $\eta^{2/3}$ dependence is expected for cis-trans isomerization reactions [6-8] This is in agreement with the data reported previously for the substituted molecular motor derivatives (Chapter 4) and suggests that the excited state structural evolution is more complex than just simple torsional motion. Instead, it is most likely that a combination of torsion and pyramidalization facilitate non-radiative excited state decay in these systems.[9,10] Thus, increased friction does retard the torsional component of the

molecular dynamics, but not the pyramidalization. Therefore, the dark state lifetime does not continue to increase with increasing solvent viscosity. It is also possible that the sheer (macroscopic) viscosity of the solvent is not the most suitable measure of solvent friction for this system. A detailed discussion of solvent friction and its experimental measures is given in Chapter 1. Thus, the non-linearity of the solvent viscosity dependence may arise due to the approximation of sheer viscosity as a representation of the effects of solvent friction.

A key consideration is the comparison of the dark state transient lifetime and the long exponential component of the fluorescence decay. This is because the timescale of both should be in agreement for an excited state decay mechanism in which a 'dark' excited state decays to the ground state and couples thermally to the bright state during its lifetime (as observed for 1-H in Chapter 3). The time constant of the longest exponential component of the fluorescence decay curves (measured at the maximum wavelength of emission) and the dark state transient lifetime of CCPh measured in each solvent are summarized in Table 5.7. A plot of these parameters on the same axes (as a function of viscosity) allows a more direct comparison and is shown in Figure 5.8. Thus, it is clear that the timescale of the longest component of the fluorescence decay is in agreement with the lifetime of the dark state transient (within experimental error) for every solvent studied. This is consistent with the assignment of a 'dark' excited state in the excited state decay mechanism of this class of molecular motor.

A further important consideration is the comparison between the lifetime of the dark state transient and the recovery of the ground state. Figure 5.9 shows the time domain relaxation of the ground state bleach measured in each solvent. Again, in each case the raw data (points) were fitted to a bi-exponential function plus an arbitrary 1 ns component (lines), the parameters of which are summarized in Table 5.8.

Table 5.7 - *A comparison of the solvent viscosity dependent dark state transient lifetime and long exponential fluorescence decay component (τ_3) of CCPh. Repeat measurements determined the error of the dark state transient lifetime and long exponential fluorescence decay component to be within 10 % and 15 % respectively.*

Solvent	Viscosity / mPa s	<τ> Excited State / ps	τ_3 Fluorescence / ps
DCM	0.43	2.25	2.17
Ethanol	1.07	2.99	2.44
Decalin	2.5	6.95	6.94
Octanol	7.29	7.02	8.10

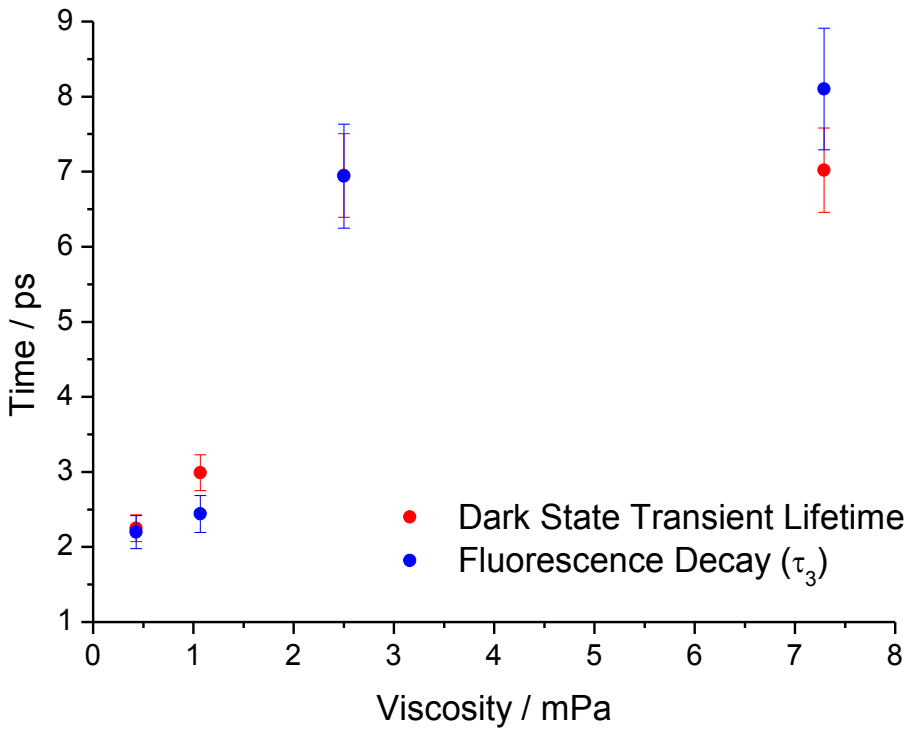

Figure 5.8 - *A comparison of the solvent viscosity dependent dark state transient lifetime and long exponential fluorescence decay component (τ_3) of CCPh.*

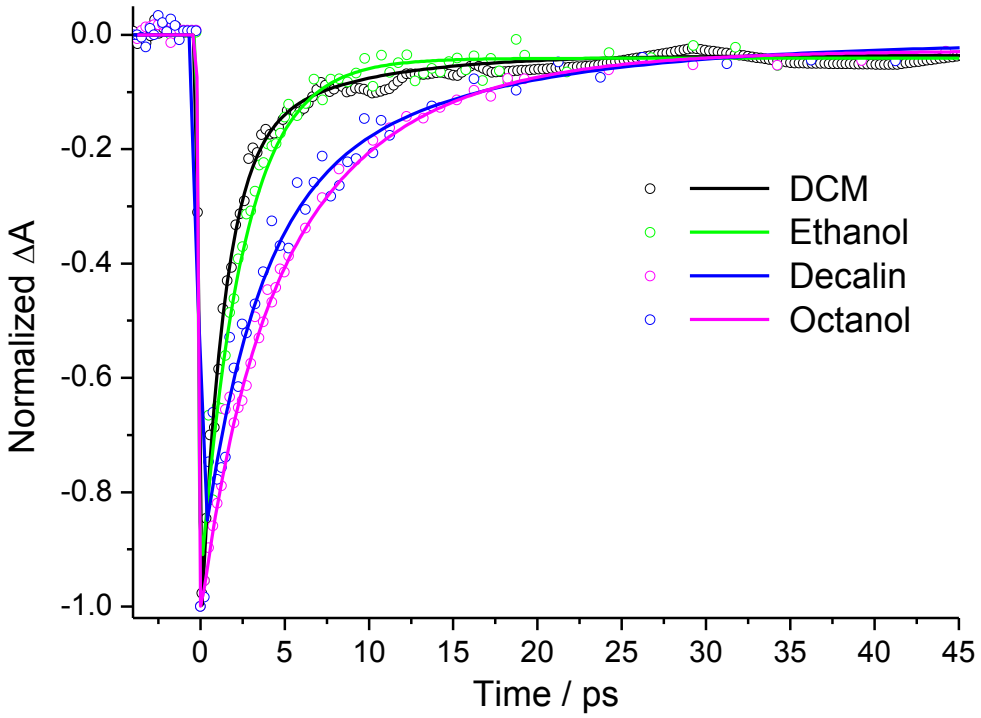

Figure 5.9 - *Solvent dependent decay of the ground state bleach (~440 nm) of CCPh. The raw data (points) were fitted to a bi-exponential function (lines).*

Table 5.8 - *Parameters of the bi-exponential function fitted to the solvent dependent decay curves of the CCPh ground state bleach. Repeat measurements determined the error to be within 10% for each parameter.*

Solvent	***Viscosity / mPa s***	**τ_1 /ps**	**A_1**	**τ_2 /ps**	**A_2**	**$\langle\tau\rangle$ /ps**
DCM	0.43	1.47	0.86	7.57	0.14	2.33
Ethanol	1.07	2.43	0.92	3.63	0.08	2.54
Decalin	2.5	2.87	0.42	7.89	0.58	5.78
Octanol	7.29	3.37	0.59	10.54	0.41	6.28

Table 5.8 shows that the ground state recovery kinetics follow the same trend exhibited by the dark state relaxation kinetics. A direct comparison of the dark state decay and ground state recovery kinetics is shown in Figure 5.10, where the lifetimes of the dark state and ground state transient features are plotted as a function of viscosity on the same axes. From Figure 5.10 it is clear that within experimental error, the dark state relaxation of CCPh occurs on the same timescale as the ground state recovery in all solvents. Therefore, this suggests that the excited state of CCPh relaxes directly to the ground state with no further intermediate states observed, as expected for 'dark' excited state relaxation directly to the ground state.

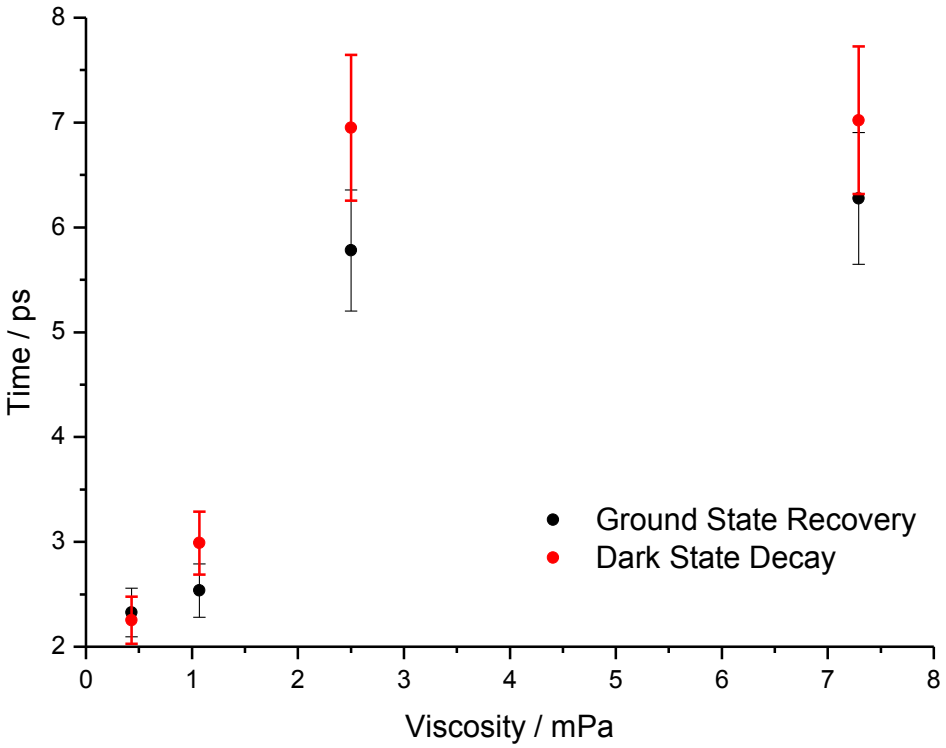

Figure 5.10 - *A comparison of the solvent viscosity dependent ground state recovery time and dark state transient lifetime of CCPh.*

5.4 Conclusion

In this chapter the excited state dynamics of a tri-phenylacetylene substituted molecular motor (CCPh) were investigated. The phenylacetylene substituent is sterically bulky and a very weak electron donor. A comparison of the fluorescence decay dynamics of CCPh and 1-OMe (strong electron donor) revealed no significant effects associated with the weak electron donating ability of the tri-phenylacetylene substituents. Thus, it was concluded that any observed differences in the exited state decay dynamics between CCPh and 1-H can be attributed to the steric bulkiness of the tri-phenylacetylene substituents.

The fluorescence decay of CCPh in DCM was found to exhibit similar features to that of 1-H, with a short exponential component (~ 100 fs) and a long exponential component (~2 ps). An additional intermediate exponential component (~1 ps) was also observed for CCPh. Transient absorption spectroscopy revealed that the timescales of the dark state transient decay, repopulation of the ground state and long exponential component of the fluorescence decay were in close agreement. Thus, it was concluded the excited state decay dynamics of CCPh remain consistent with the mechanism of excited state decay proposed for the molecular motor derivatives in Chapter 3 and Chapter 4.

This mechanism suggests that the 'dark' excited state to ground state relaxation (ascribed to the long exponential fluorescence decay term, τ_3) proceeds *via* internal conversion at a conical intersection promoted by both pyramidalization and torsional co-ordinates. As a result, it was envisaged that addition of sterically bulky phenylacetylene substituents would lead to increased friction opposing the rotational motion, and hence a longer lived dark state. This was found to be true, with both the long exponential fluorescence decay term and dark state transient exhibiting an increased lifetime compared to 1-H. In addition, the dark state lifetime of CCPh was found to exhibit a more significant dependence upon solvent friction

compared to 1-H. This provides further evidence for a coupling between torsional motion and the decay of the dark excited state of this molecular motor system.

In contrast, the independence of the short exponential decay term (τ_1, ascribed to bright to dark state relaxation), to the tri-phenylacetylene substituents, even in the most viscous media, provides strong support for the non-involvement of rotation in this reaction co-ordinate. Therefore, further evidence is provided for the assignment of pyramidalization as the primary co-ordinate by which bright to dark excited state relaxation occurs in this molecular motor system.

5.5 References

(1) Flors, C.; Oesterling, I.; Schnitzler, T.; Fron, E.; Schweitzer, G.; Sliwa, M.; Herrmann, A.; van der Auweraer, M.; de Schryver, F. C.; Muellen, K.; Hofkens, J. *J. Phys. Chem. C.* **2007**, *111*, 4861.

(2) Kleiman, V. D.; Melinger, J. S.; McMorrow, D. *J. Phys. Chem. B.* **2001**, *105*, 5595.

(3) Clayden, J.; Greeve, N.; Warren, S.; Wothers, P. *Organic Chemistry, Oxford University Press* **2001**.

(4) Velsko, S. P. *J. Chem. Phys.* **1983**, *78*, 249.

(5) Cnossen, A., University of Groningen, 2013.

(6) Changenet, P.; Zhang, H.; van der Meer, M. J.; Glasbeek, M.; Plaza, P.; Martin, M. M. *J. Phys. Chem. A.* **1998**, *102*, 6716.

(7) van der Meer, M. J.; Zhang, H.; Glasbeek, M. *J. Chem. Phys.* **2000**, *112*, 2878.

(8) Espagne, A.; Paik, D. H.; Changenet-Barret, P.; Martin, M. M.; Zewail, A. H. *ChemPhysChem* **2006**, *7*, 1717.

(9) Kazaryan, A.; Kistemaker, J. C. M.; Schafer, L. V.; Browne, W. R.; Feringa, B. L.; Filatov, M. *J. Phys. Chem. A.* **2010**, *114*, 5058.

(10) Kazaryan, A.; Lan, Z.; Schäfer, L. V.; Thiel, W.; Filatov, M. *J. Chem. Theor. Comput* **2011**, *7*, 2189.

6 Excited State Dynamics of 9-9-bifluorenylidene

In this chapter, the excited state dynamics of 9,9'-bifluorenylidene (BiF) will be investigated. After describing the experimental conditions employed (Section 6.2), the steady state spectroscopy of BiF will be presented (Section 6.3.1). Ultrafast fluorescence up-conversion (Section 6.3.2) and transient absorption (Section 6.3.3) measurements will then be discussed. Particular attention will be given to the solvent dependence of each measurement. Finally, the data are used to propose two possible model schemes of excited state decay (Section 6.3.3).

6.1 Introduction

9,9'-bifluorenylidene (BiF) is a byproduct of the synthesis of the molecular motors studied in this work. The molecular structure of BiF is similar to that of 1-H (Chapter 3), but is constructed of two fluorenyl groups (the lower half 'stator' of 1-H) connected by a central carbon double bond (Figure 6.1). Thus, BiF is comprised of two 'stator' groups rather than a 'stator' and 'rotor' group as for 1-H. Therefore, BiF does not possess any molecular motor properties and so can be considered as a more conventional cis/trans photoisomerizing system, and perhaps, when suitably substituted, a candidate for a molecular switch.

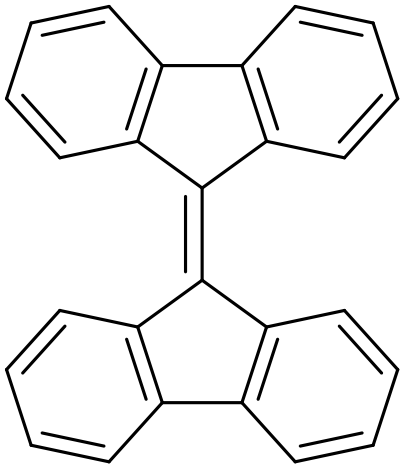

Figure 6.1 - *Molecular structure of 9,9'-bifluorenylidene (BiF).*

BiF has been the subject of study elsewhere due to its potential application as an electron acceptor in the design of organic photovoltaic devices (OPVs).[1-4] However, some controversy exists in the literature regarding the ground state structure of BiF. Brunetti et al report that BiF adopts a co-planar (non-twisted) structure in the ground state.[1] However, Pogodin et al[5] and Sun et al[2,3] report that BiF is significantly twisted (~34^{o}) about the central olefin due to steric overcrowding either side of the central double bond. This is supported by the crystal structure which revealed a 32^{o} twist about this bond.[6] In order to avoid such controversy, we used DFT to calculate the optimized ground state structure of BiF independently of these previous studies. We also found that the ground state structure of BiF is twisted (34.4^{o}) about the central double bond. A highly twisted ground state structure thus means that the ground state of BiF is likely to be highly strained, since a planar structure would be preferred for a delocalized system. [5,7] It is this highly strained ground state structure which is reported to be responsible for the strong electron accepting ability of BiF.[1-3] Addition of a single electron across the central olefin significantly reduces the double bond character. It is reported that the strain held by the ground state structure is then relieved by torsion about the central bond. Thus, there is a strong driving force for BiF to accept an electron. This makes BiF a particularly attractive candidate for the starting structure of the electron acceptor components of OPV devices.

In this study, we aim to characterize the excited state dynamics of BiF. Electronic excitation of BiF will induce a π- π^* transition largely localised on the central olefin, as occurs for the motor molecules.[8,9] Thus, the double bond character of this central olefin will be significantly reduced in a manner similar to that which occurs upon the addition of an electron. Therefore, it was envisaged that BiF would undergo torsional motion in the excited state to release the strain in the ground state structure. Such behaviour would be revealed in the excited state dynamics of BiF. To achieve this, ultrafast fluorescence up-conversion and

transient absorption spectroscopies were employed. An important aspect of this study was the effect of solvent viscosity upon the excited state relaxation kinetics of BiF. This is because any such torsional motion would be expected to be slowed down in more viscous media. Thus, the viscosity dependence of the excited state lifetime of BiF was hoped to give some insight into the nature and extent of excited state structural evolution.

6.2 Experimental

The synthesis of BiF is described in Chapter 2.[10] The experimental conditions employed for all steady state (absorption and emission) and transient absorption measurements are identical to those described previously for 1-H (Chapter 3). Fluorescence up-conversion measurements were conducted with the excitation beam centred at 415 nm (corresponding to 830 nm fundamental beam). All other parameters are identical to those described previously.

6.3 Results and Discussion

6.3.1 Steady State Spectroscopy

The solvent dependent steady state absorption spectra of BiF are shown in Figure 6.2. The absorption spectrum of BiF exhibits neither a significant solvent polarity dependence (ethanol compared to cyclohexane) nor viscosity dependence (cyclohexane compared to decalin). This is in line with the steady state spectroscopy of fluorene, where the position and shape of the absorption spectrum is reported to exhibit no solvent dependence.[11] However, the absorption spectrum of fluorene is significantly blue shifted in comparison to BiF and consists of three bands between 200 – 310 nm.[11] Therefore, the dimerization of fluorene to form BiF results in significant spectroscopic changes. When attempting to record a steady state emission spectrum of BiF, no emission was detected above the solvent (Raman) background even in the most viscous solvents. This is in contrast to fluorene where a clear emission band (centred at ~320 nm) is observed.[11]

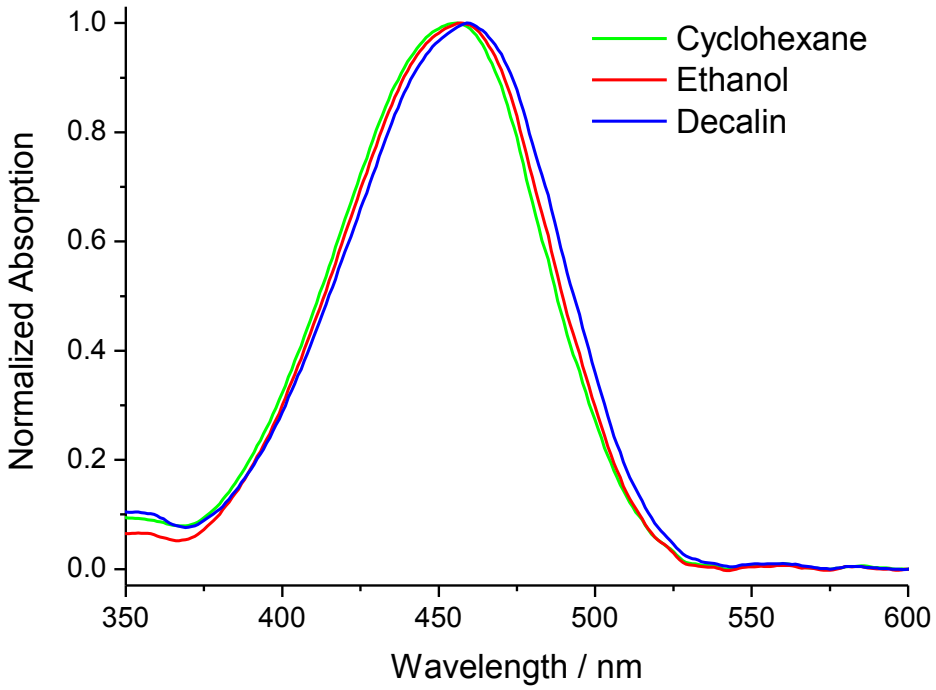

Figure 6.2 - *Solvent dependent steady state absorption spectra of BiF*

Further attempts were made to record BiF emission spectra at low temperature, but again no emission was detected even in an ethanol glass at 80 K. Such observations were reported previously for BiF by Sinoy and Donckt.[12] The low temperature data suggests that large scale evolution of the molecular structure is not required for non-radiative excited state relaxation of BiF. At temperatures as low as 80 K, such structural motion would be almost entirely prohibited and so would lead to enhanced fluorescence. No enhancement is observed at low temperature suggesting torsional dynamics of the fluorene rings are not essential for radiationless decay. This is a surprising result since large scale excited state structural evolution was anticipated due to the highly strained nature of the ground state structure.

6.3.2 Ultrafast Fluorescence Up-conversion Spectroscopy

The time-resolved fluorescence decay of BiF was recorded at an emission wavelength of 520 nm in each solvent are shown in Figure 6.3. The raw data (points) were fitted to a function (lines) comprising the sum of 3 exponential and 3 damped harmonic oscillator terms. The

parameters of these functions are summarized in Table 6.1 and Table 6.2 (exponential and damped harmonic oscillator terms respectively).

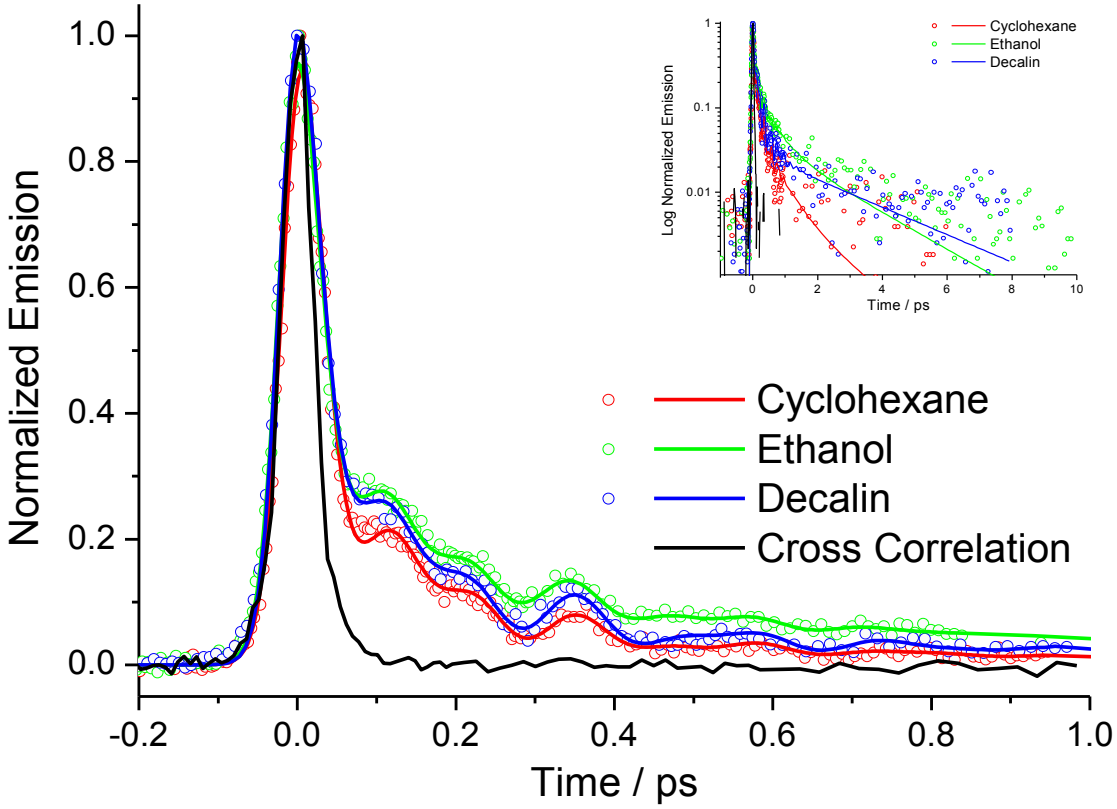

Figure 6.3 - *Solvent dependent fluorescence decay curves of BiF recorded at 520 nm. The raw data (points) were fitted to a function (lines) comprising the sum of 3 exponential terms and 3 damped harmonic oscillators. Inset shows the data on a log intensity scale.*

Table 6.1 – *Parameters of the exponential terms of the functions fitted to the solvent dependent fluorescence decay curves of BiF. Repeat fits to each measurement determined the error to be within 15% for each parameter.*

Solvent	**Viscosity / mPa s**	**τ_1 / ps**	**A_1**	**τ_2 / ps**	**A_2**	**τ_3 / ps**	**A_3**	**$\langle\tau\rangle$ / ps**
Cyclohexane	0.89	0.09	0.91	0.48	0.08	1.56	0.01	0.13
Ethanol	1.07	0.08	0.82	0.48	0.14	2.16	0.04	0.22
Decalin	2.5	0.09	0.90	0.36	0.07	2.40	0.03	0.19

Table 6.2 - *Damping (τ_D), frequency (ω), amplitude (A_ω) and phase (Φ) components of the damped harmonic oscillator functions used to fit the oscillatory part of the time domain fluorescence decay data of BiF. Errors were calculated to be within 25% by repeat fits to each measurement.*

Solvent	**Viscosity / mPa s**	τ_{D1} **/ ps**	ω_1 **/ THz**	$A_{\omega 1}$	φ_1	τ_{D2} **/ ps**	ω_2 **/ THz**	$A_{\omega 2}$	φ_2	τ_{D3} **/ ps**	ω_3 **/ THz**	$A_{\omega 3}$	φ_3
Cyclohexane	0.89	0.05	2.71	0.85	2.21	0.25	4.88	0.05	2.57	0.17	8.38	0.10	1.16
Ethanol	1.07	0.06	2.83	0.79	2.05	0.19	4.88	0.11	2.72	0.20	8.38	0.10	1.18
Decalin	2.5	0.06	2.70	0.78	2.07	0.27	4.98	0.09	2.43	0.19	8.17	0.13	1.45

Figure 6.3 reveals an extremely fast decay superimposed with a series of oscillations. The absence of a scattered light or Raman signal contribution to the measured decay was confirmed by comparison with the experimental time resolution (cross correlation measured by up-converting the Raman scattering of Heptane as described in Chapter 2) shown by the black line in Figure 6.3.. This shows that although extremely fast, the BiF decay is slower than the time resolution of the experiment. In addition, no solvent Raman scattering was detected at 520 nm, thus confirming that the measured data is not influenced by scattered light or Raman scattering of the solvent.

Table 6.2 shows that the parameters of the oscillation observed in the fluorescence decay curves of BiF are independent of solvent (within experimental error). Three frequencies were required to provide an adequate fit to the raw data. The Fourier transform of the raw time domain data (subject to subtraction of the exponential components as described in Chapter 2) is shown in Figure 6.4. This confirms the validity of a fitted function comprised of three damped harmonic oscillator terms, as three frequencies are clearly present in the experimental data. Of these frequencies, only one exhibits a damping time comparable to that of the exponential decay components.

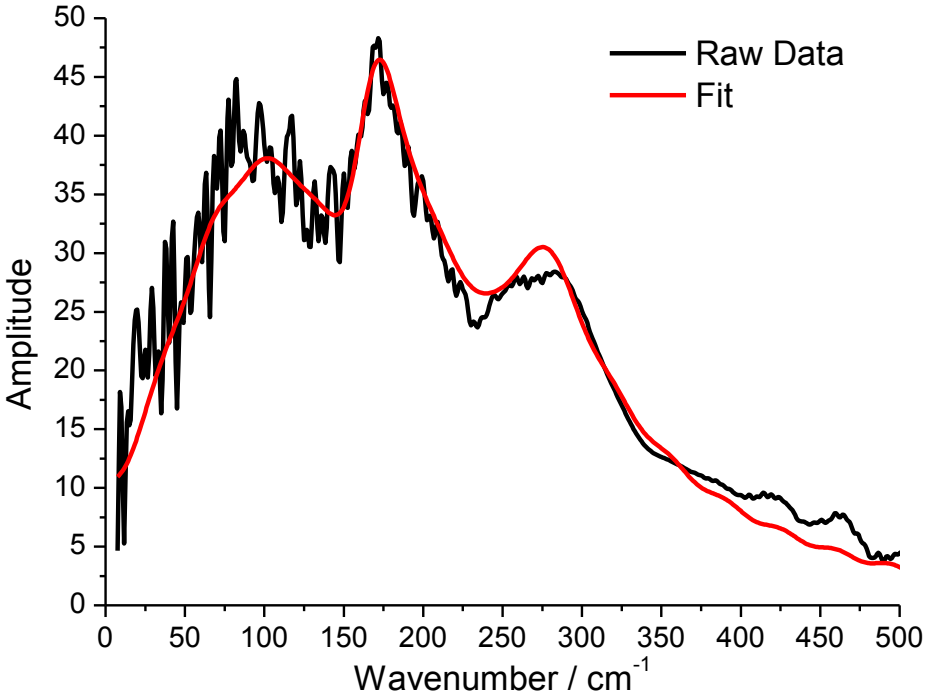

Figure 6.4 - *Fourier transform of the BiF time domain fluorescence decay data recorded in decalin. The raw data (black) is compared to the fitted function (red) after subtraction of the exponential decay components in each case.*

The lowest frequency mode (~2.7 THz, 90 cm^{-1}) has a damping constant of ~60 fs which is comparable to the fastest component of the exponential decay function (~90 fs).Thus, this lowest frequency mode may be coupled to the co-ordinate of excited state structural evolution which promotes ultrafast fluorescence decay (as discussed for the molecular motor 1-H in Chapter 3). In contrast, the remaining vibrational modes are damped on a far slower timescale and so are assigned as spectator modes.

In order to attempt to assign the vibrational modes, the DFT calculated Raman spectrum of BiF was compared to the frequencies of the damped harmonic oscillator terms of the fitted function. However, no modes were found in the calculated spectrum which match the experimentally observed frequencies. This suggests that the excited state structure is significantly different to that of the ground state. A similar observation was made for the

molecular motors in Chapter 3 and Chapter 4. Thus, in order to assign further the coherently excited vibrational modes, detailed excited state calculations are required. Such data is not currently available.

The extremely fast fluorescence decay (average fluorescence lifetime < 250 fs) revealed by Figure 6.3 is consistent with the absence of fluorescence observed in the steady state spectroscopy of BiF (Section 6.3.1). Table 6.1 reveals the most significant component of the decay (~85 %) is a sub 100 fs exponential term. The decay is also composed of a smaller amplitude (~ 10 %) ~400 fs decay term and a minor amplitude (< 5%) long (>1.5 ps) decay component. The fluorescence decay kinetics of BiF exhibit very little viscosity dependence (Table 6.1). Only the minor (less than 5% amplitude) slowest exponential component is longer lived in more viscous media. This suggests that the primary mechanism of non-radiative excited state decay does not involve structural evolution along a co-ordinate in which large scale torsional motion is involved. This is because any such co-ordinate is expected to displace a large volume of solvent and thus would be retarded in viscous media. This observation is in agreement with the lack of emission at temperatures as low as 80K.

A similar conclusion has previously been reached for the aromatic molecule azulene. The S_1 state of azulene was found to be essentially non-fluorescent (quantum yield ~10^{-6}) with a sub picosecond fluorescence lifetime in solution.[13] Even in the crystal at 4.2 K, the fluorescence lifetime of the azulene S_1 state was found to be less than 3.5 ps.[14,15] Therefore, the Franck-Condon state of azulene must undergo ultrafast deactivation to the ground state without significant volume displacing structural dynamics. Detailed quantum mechanical calculations revealed a conical intersection between the S_0 and S_1 states of azulene.[15] It was reported that this conical intersection was reached from the Franck-Condon S_1 state by means of two reactive co-ordinates: the shortening of the transannular bond (red arrows in Figure 6.5) and the lengthening of the adjacent C-C bonds (blue arrows in Figure 6.5).

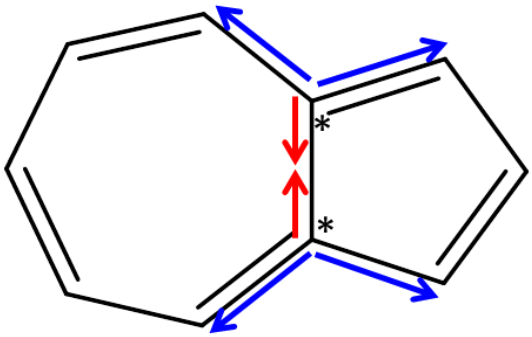

Figure 6.5 - *The co-ordinates of excited state structural evolution invoked for the ultrafast excited state decay of azulene. DFT calculations reveal that an S_1/S_0 conical intersection is reached by simultaneous shortening of the transannular bond (red arrows) and lengthening of the adjacent C-C bonds (blue arrows). Ultrafast deactivation of the excited state to the ground state is thus achieved via almost entirely volume conserving excited state molecular dynamics. This figure is reproduced from Reference* 15.

This evolution of the molecular structure leads to an intersection of the S_1 and S_0 surfaces, as well as distortion of the electronic structure of azulene, including breaking of the central π bond.[14] Quantum mechanical simulations found that ultrafast internal conversion would occur in the region of this conical intersection with an efficiency approaching 100 %. The co-ordinates invoked require only very small scale molecular structural dynamics and so explain both the viscosity independent nature of the azulene S_1 excited state decay in solution, and the ultrafast fluorescence lifetime observed in the crystal. Thus, the case of azulene serves as a clear example of a molecular system in which excited state decay can occur on an ultrafast timescale with only small and volume conserving changes to the molecule structure. Thus, it may be possible to invoke a similar mechanism in order to explain the observed decay dynamics of BiF, if a conical intersection were approached *via* co-ordinates which required only very small scale changes to the molecular structure. One such co-ordinate known to be involved in isomerization reactions (e.g. the molecular motors studied in previous chapters) is

pyramidalization. Therefore, in the case of BiF it may be possible to invoke pyramidalization of the central C=C atoms as a co-ordinate which promotes ultrafast internal conversion of the excited state.

However, an alternative mechanism may also be proposed to explain the data. It is possible that the extremely fast timescale of fluorescence decay may arise from the relaxation of the emissive Franck-Condon excited state ('bright' state) to a position on the excited state potential energy surface from which no emission occurs (a 'dark' state). A similar mechanism was invoked for the molecular motors in Chapter 3 and Chapter 4. In such a case, the fluorescence decay would not represent relaxation of the excited state directly to the ground state. Such an intermediate state would suggest a ground state recovery slower than the fluorescence decay. In order to investigate this further, transient absorption spectroscopy was used to probe the excited state decay and ground state repopulation dynamics.

6.3.3 Transient Absorption Spectroscopy

The time dependent transient spectra of BiF were recorded in the same series of solvents reported previously for the time-resolved fluorescence measurements (Section 6.3.2). The transient spectra recorded in decalin are shown in Figure 6.6. No solvent dependent spectral differences were observed, in line with the solvent independence of the steady state absorption spectra (Figure 6.2). In each case, a broad positive ΔOD feature is observed on the red side of the measured spectral region. This broad feature relaxes rapidly to reveal a longer lived positive feature centred at ~510 nm. The ground state bleach is also observed centred at ~470 nm. This is in close agreement with the steady state absorption spectrum of BiF in decalin with the maximum of absorption observed at ~460 nm (Figure 6.2). The relaxation kinetics of each of these transient features were then compared. Firstly, the relaxation kinetics of the broad feature were determined by plotting the decay of the transient signal at the furthest red shifted wavelength in the measured range (620 nm).

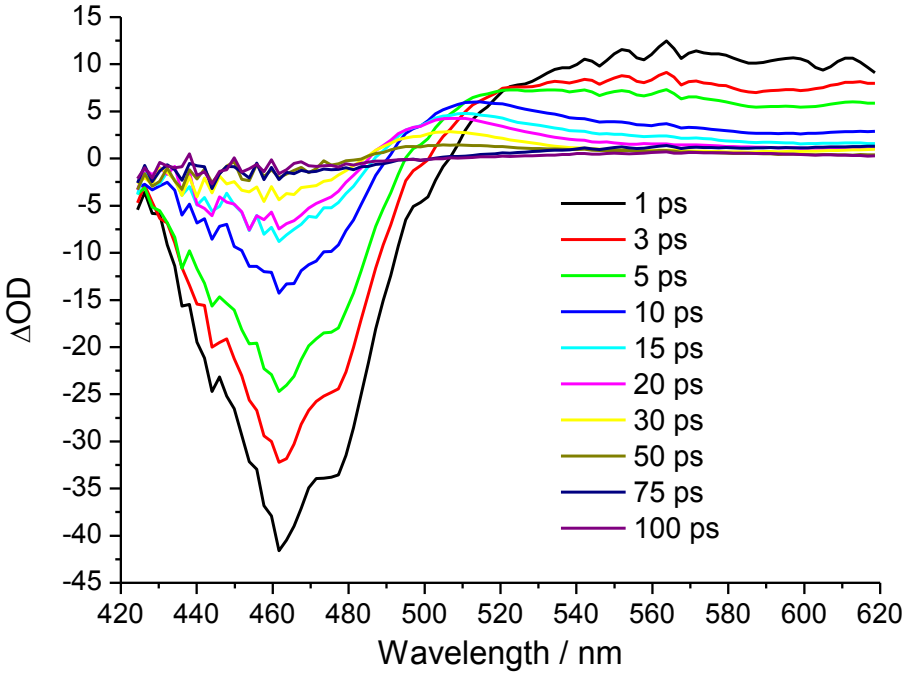

Figure 6.6 - *Time dependent transient absorption spectra of BiF in decalin.*

This wavelength was chosen to ensure that neither the transient feature at 510 nm nor the ground state bleach interfered with the measured decay kinetics of this broad feature. The ground state recovery kinetics were then assessed by plotting the decay of the transient signal at the furthest blue shifted wavelength measured. Again, this wavelength was chosen in order to avoid interference with the relaxation kinetics of any other transient feature. Figure 6.7 compares the decay kinetics at both wavelengths in decalin. The solvent dependent decay of each transient feature is shown in Figure 6.9. In each case, the raw data (points) were fitted to a bi-exponential function (lines). The parameters of these exponential functions are summarized for the ground state recovery (435 nm) and broad transient (620 nm) in Table 6.3 and Table 6.4 respectively.

Figure 6.7 shows that the broad transient (620 nm) decays on a faster timescale than the recovery of the ground state. The relaxation timescale of both transients is independent of solvent within experimental error (Figure 6.8, Figure 6.9, Table 6.3 and Table 6.4).

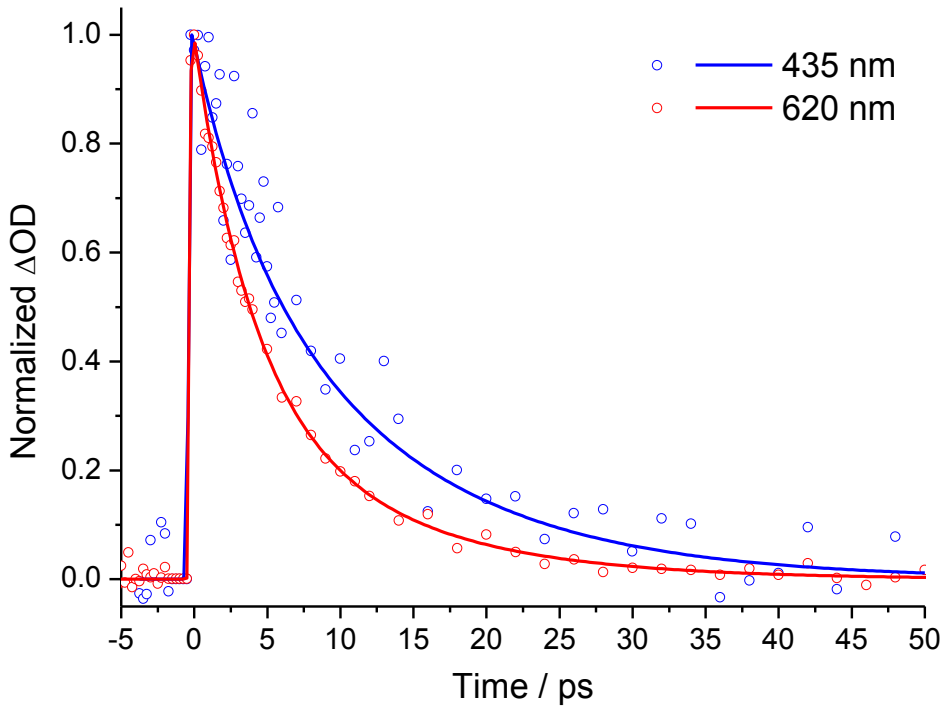

Figure 6.7 - *A comparison of the transient decay kinetics of BiF in decalin measured at 435 nm and 620 nm. Both curves were normalized and the data recorded at 435 nm was inverted.*

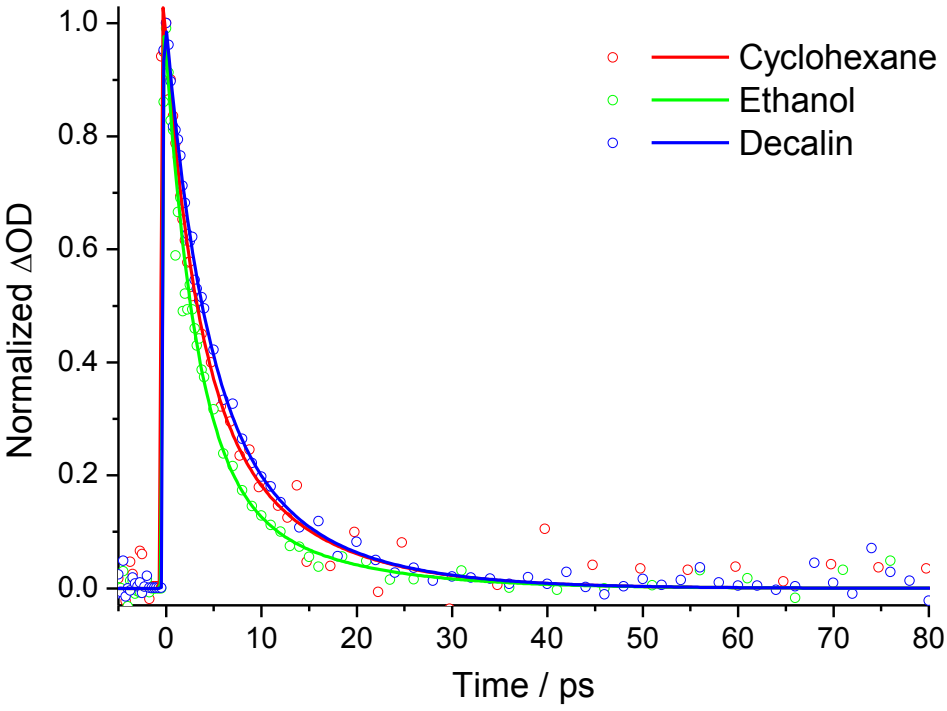

Figure 6.8 - *Solvent dependent transient decay curves of BiF measured at 620 nm.*

Table 6.3 - *Parameters of the bi-exponential functions fitted to the solvent dependent transient decay curves of BiF in decalin measured at 620 nm. Repeat measurements determined the error to be within 10% for each parameter.*

Solvent	Viscosity / mPa s	τ_1 / ps	A_1	τ_2 / ps	A_2	$\langle\tau\rangle$ / ps
Cyclohexane	0.89	3.28	0.63	11.34	0.37	6.25
Ethanol	1.07	3.24	0.77	11.69	0.23	5.13
Decalin	2.5	3.84	0.61	10.57	0.39	6.46

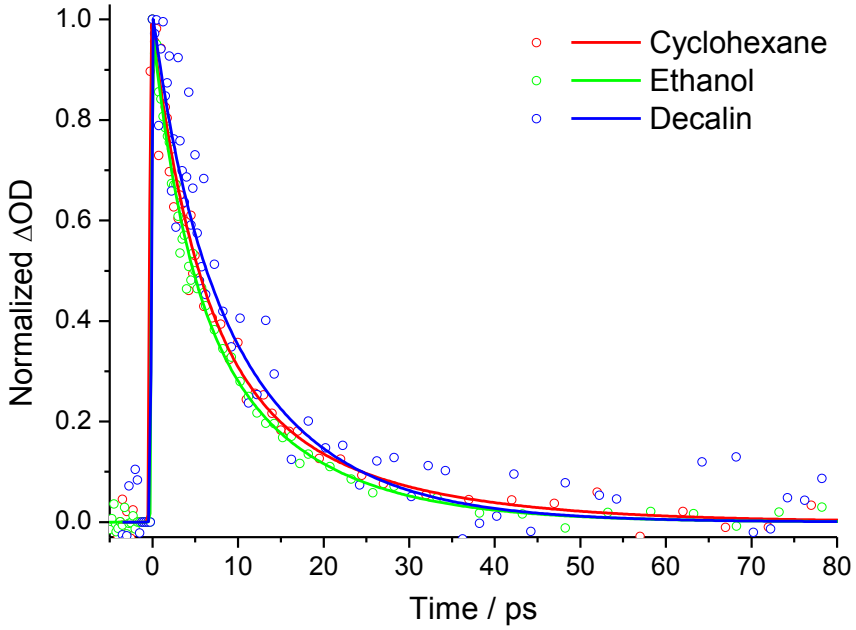

Figure 6.9 - *Solvent dependent transient decay curves of BiF measured 435 nm. In each case, the data has been inverted.*

Table 6.4 - *Parameters of the bi-exponential functions fitted to the solvent dependent transient decay curves of BiF in decalin measured at 435 nm. Repeat measurements determined the error to be within 10% for each parameter.*

Solvent	Viscosity / mPa s	τ_1 / ps	A_1	τ_2 / ps	A_2	$\langle\tau\rangle$ / ps
Cyclohexane	0.89	5.42	0.62	17.57	0.38	10.04
Ethanol	1.07	4.99	0.60	17.61	0.40	10.00
Decalin	2.5	4.28	0.29	12.32	0.71	10.01

This is in line the solvent independent nature of the time-resolved fluorescence spectroscopy of BiF (Section 6.3.2). However, in comparison to the fluorescence data (Table 6.1), the decay timescales of both transients are significantly slower. This shows that the fluorescence decay occurs on a much faster timescale than the recovery of the ground state population. As described previously (Section 6.3.2), such an observation would be expected for a system in which a bright excited state relaxes to a non-emissive dark excited state. However, the disparity between the decay timescales of ground state recovery (435 nm transient) and the decay of the broad transient (620 nm) preclude the simple assignment of this broad transient feature to absorption of a dark excited state. Since the ground state recovery is slower than the decay of the broad transient, the relaxation of the broad transient cannot represent relaxation of the excited state directly to the ground state. Instead, the relaxation of this transient feature must represent a different process.

One possibility is that the relaxation of the broad 620 nm transient leads to the growth of the 510 nm transient, and it is then the decay of the 510 nm transient which corresponds to the recovery of the ground state. In order to assess this further, the decay kinetics of the 510 nm transient were measured. However, the kinetics at this wavelength are more difficult to resolve due to the close overlap of the ground state bleach and the broad transient feature in this region of the measured range. The extent of this overlap can be seen by overlaying the steady state absorption spectrum of BiF with the transient spectra (Figure 6.10). This shows that the ground state absorption of BiF extends beyond 520 nm, thus overlapping with the 510 nm transient. This makes a true assessment of the decay kinetics of the 510 nm transient difficult. The time domain decay curve at 510 nm (Figure 6.11) shows a rise time in the transient signal at 510 nm followed by a slow decay. The raw data (points) were fitted to a function comprising the sum of a negative amplitude single exponential term (rise time) and a

(positive amplitude) single exponential term (decay). The parameters of this fit are shown in Table 6.5.

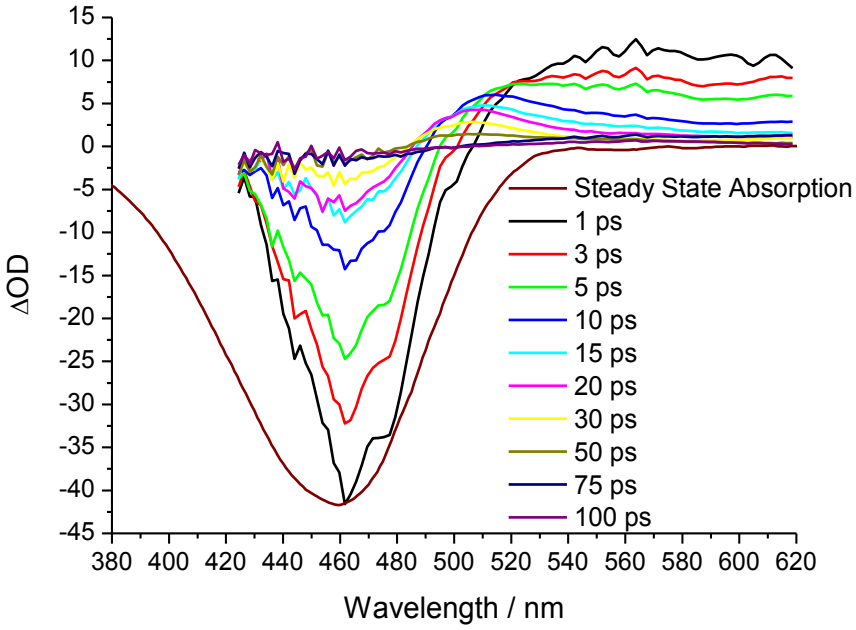

Figure 6.10 - *Transient absorption spectra of BiF in decalin overlaid with the (inverted) steady state absorption spectrum. The kinetics at 510 nm are complicated by the strong ground state absorption in this region.*

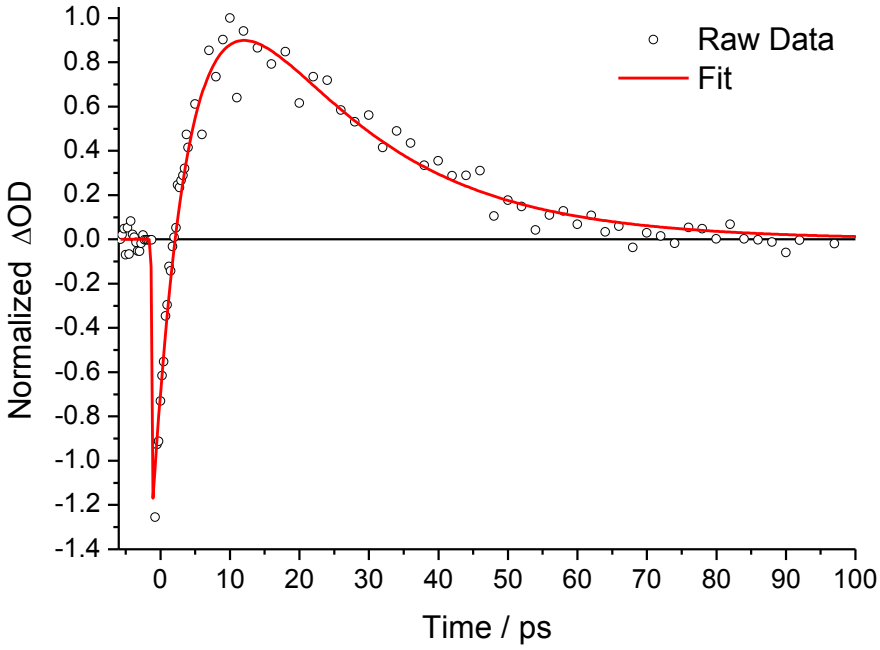

Figure 6.11 - *Transient decay curve of BiF measured at 510 nm in decalin.*

Table 6.5 - *Parameters of the exponential function fitted to the 510 nm transient decay curve of BiF in decalin. Repeat measurements determined the error to be within 10% for each parameter.*

Wavelength / nm	τ_1 / ps	A_1	τ_2 / ps	A_2
510	6.12	-4.077	18.31	2.84

Thus, the rise of the 510 nm transient (~6 ps) occurs with a similar time constant to that of the decay of the broad transient feature (~6.5 ps). This provides some evidence to support the suggestion that the relaxation of the broad transient feature could lead to population of the 510 nm transient state. However, although such a suggestion remains tentative due to the complex nature of the spectra in the 510 nm region, this idea can be used to support both of the possible mechanisms of excited state relaxation mentioned previously (Section 6.3.2). In both mechanisms, we propose that the 510 nm transient represents a thermalized vibrationally hot ground state which is populated by the decay of the broad transient feature (620 nm). Vibrationally hot ground states have been observed by transient absorption spectroscopy in a number of systems including DNA base pairs,[16-18] the green fluorescent protein,[19] and electron transfer reactions.[20] However, the assignment of the broad transient feature differs between each mechanism.

In the first possible mechanism (Figure 6.12), the broad transient represents a dark excited state. In this mechanism, the measured fluorescence decay represents relaxation of the Frank-Condon 'bright' excited state population to a non-emissive 'dark' excited state. This occurs on an extremely fast timescale due to the highly strained nature of the ground state structure. Thus, upon electronic excitation, release of this strain serves as a strong driving force which results in the extraordinarily fast relaxation of this initial populated excited state.

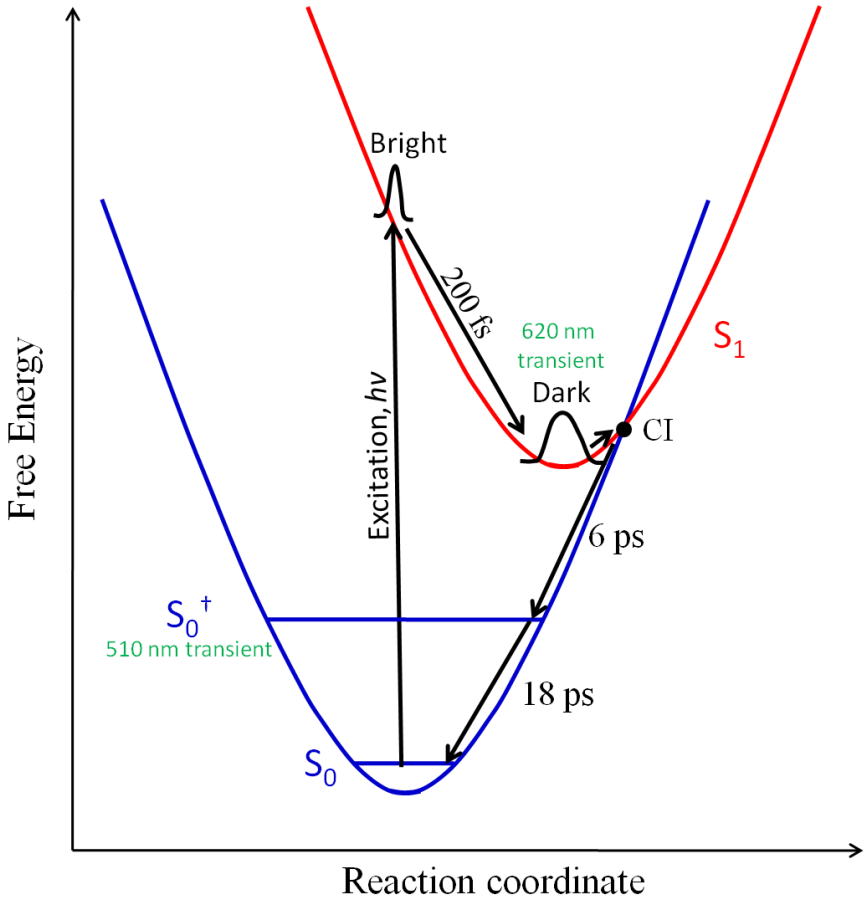

Figure 6.12 - *A proposed excited state decay mechanism for BiF in which a 'dark' state is involved. The initially populated Franck-Condon state is assigned as an emissive 'bright' state. This population relaxes to a non-emissive 'dark' excited state in ~200 fs. The 'dark' excited state population relaxes to the ground state via an S_1/S_0 conical intersection (CI) in ~6 ps. The low frequency modes of the initially repopulated ground state ($S_0^{\dagger}$) are vibrationally hot (thermalized). The excess energy is then transferred from the low frequency modes of the molecule to the low frequency modes of the solvent (vibrational cooling) in ~18 ps. This corresponds to repopulation of the equilibrium ground state structure (S_0).*

The population of a dark excited state would then account for the observed broad red shifted transient absorption feature. The dark excited state population could then relax to the ground state, corresponding to the decay of the broad transient feature. We suggest that the dark state to ground state relaxation process occurs *via* internal conversion at an S_1/S_0 conical

intersection (CI in Figure 6.12). However, the reaction co-ordinates which promote relaxation of the Franck Condon population to the dark state (and hence towards the CI) must be largely volume conserving. This is because the non-radiative decay of BiF is not inhibited even in an ethanol glass at 80 K (Section 6.3.1). Thus, we suggest that small changes to the bond lengths and/or molecular shape (such as occurs in pyramidalization), as described for azulene (Figure 6.5), could form the reaction co-ordinates which promote this relaxation. However, since the electronic structure of the excited state is suggested to be significantly displaced from that of the equilibrium ground state structure (Section 6.3.2), relaxation of the excited state could lead to a vibrationally hot ground state ($S_0^{\dagger}$ in Figure 6.12). We suggest that this is the origin of the formation of the ~510 nm transient feature. This suggestion is supported by the kinetics of each transient feature. The 510 nm feature grows with a ~6 ps time constant (Table 6.5) which is in close agreement with the average decay time of the transient signal at 620 nm (~6 ps, Table 6.3). Since the dark state population would be significantly relaxed compared to the Franck-Condon state, we suggest that thermalization of the population is completed prior to formation of the vibrationally hot ground state. Therefore it would be the low frequency modes of the ground state which are vibrationally excited. Therefore, the excess energy of the thermalized vibrationally hot ground state ($S_0^{\dagger}$ in Figure 6.12) can be transferred directly to the low frequency modes of the solvent (vibrational cooling) in tens of picoseconds. This corresponds to the repopulation of the equilibrium ground state structure (S_0 in Figure 6.12). This process is attributed to the decay of the ~510 nm transient.

Further evidence exists for this assignment in the ground state recovery kinetics. In this proposed mechanism, the fast exponential component of the ground state recovery will reflect the relaxation of the 'dark' excited state to the thermalized vibrationally hot ground state ($S_0^{\dagger}$ in Figure 6.12). This fast component (~5 ps, Table 6.4) is comparable (within experimental error) to the lifetime of the broad transient (~6 ps, Table 6.3). In addition, the long

exponential component of the ground state recovery would reflect the vibrational cooling of the thermalized vibrationally hot ground state ($S_0^{\dagger}$ to S_0 in Figure 6.12). Indeed, the time constant of this long component (~17ps, Table 6.4) is in close agreement with the decay of the 510 nm transient (~18 ps, Table 6.5). Therefore, the measured data does support an excited state decay mechanism for BiF in which a dark excited state relaxes to a thermalized vibrationally hot ground state.

In the related but alternative mechanism (Figure 6.13), the broad transient may itself represent a non-thermalized vibrationally hot ground state. In this case, the fluorescence decay timescale would represent the relaxation of the excited state directly to the hot ground state (with no dark excited state involved). Again, the very fast nature of this decay would be driven by the release of the highly strained molecular structure by molecular reorganisation upon electronic excitation leading directly to ground state relaxation by internal conversion at an S_1/S_0 conical intersection. Again, we suggest that this relaxation is promoted *via* motion along highly volume conserving reaction co-ordinates. These are likely to involve bond lengthening/shortening corresponding to volume conserving changes to the molecular shape and electronic structure (most likely pyramidalization) akin to that described for azulene[14,15] and proposed previously for the molecular motors (Chapters 3-5). Excited state decay on this extremely fast timescale (sub 200 fs) populates a specific set of modes in the ground state ($S_0^{\ddagger}$ in Figure 6.13) rather than a thermal distribution. This is in contrast to the proposed alternative dark state model, where the slower decay of the dark excited state allows the excess energy to be populate a thermal (albeit 'hot') distribution in the ground electronic state. Absorption by the $S_0^{\ddagger}$ state is then attributed to the observed broad red shifted transient feature. Since the high frequency modes hold the excess energy of the vibrationally hot ground state, this energy cannot easily be transferred to the solvent.

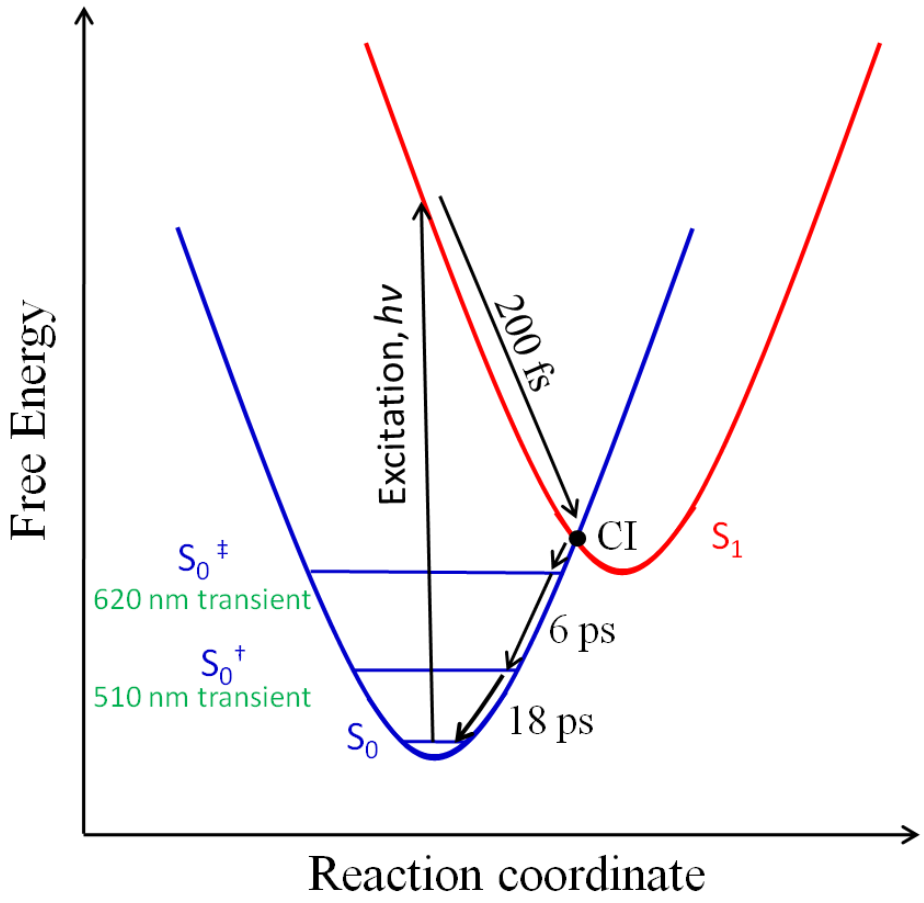

Figure 6.13 - *A proposed excited state decay mechanism for BiF in which no 'dark' state is involved. The initially populated Franck-Condon state relaxes directly to the ground state via an S_1/S_0 conical intersection (CI). The high frequency vibrational modes of the initially repopulated ground state ($S_0^{\ddagger}$) are vibrationally hot (non-thermalized). The excess energy is dissipated amongst the low frequency modes via fast intramolecular vibrational redistribution to form a thermalized ground state with vibrationally hot low frequency modes ($S_0^{\dagger}$).The excess energy is then transferred from the low frequency modes of the molecule to the low frequency modes of the solvent. This corresponds to repopulation of the equilibrium ground state structure (S_0).*

This is because of the lack of overlap with the low frequency modes of the solvent to which heat is transferred most efficiently in solution.[21,22] Instead, the excess energy must first be

dissipated amongst the lower frequency modes of the BiF solute by fast intramolecular vibrational redistribution. This results in the population of a thermalized vibrationally hot ground state ($S_0^{\dagger}$ in Figure 6.13), in which the low frequency modes are vibrationally excited. The absorption by this state is assigned to the ~510 nm transient feature. The excess energy held in the low frequency modes can then be transferred to the solvent (vibrational cooling) and the equilibrium ground state structure is repopulated (S_0 in Figure 6.13). This corresponds to the decay of the 510 nm transient.

Thus, two plausible mechanisms of excited state decay exist for BiF. A detailed theoretical study of the BiF excited state would be required to provide more definitive evidence to support either model. It is hoped that the data presented in this study could form the basis of detailed quantum mechanical calculations in the future.

6.4 Conclusion

The ultrafast excited state decay dynamics of 9,9'-bifluorenylidene (BiF) were studied.

BiF was found to be essentially non-fluorescent, even in an ethanol glass at a temperature of 80 K. This is consistent with the measured fluorescence lifetime data where the fluorescence of BiF is quenched on a sub 200 fs timescale, even in viscous media. This viscosity independence and lack of emission at low temperature suggests that non-radiative excited state decay of BiF is achieved without significant large scale excited state structural evolution. Instead, we suggest that an almost entirely volume conserving co-ordinate promotes internal conversion to the ground state at an S_0/S_1 conical intersection, in a scheme analogous to that proposed previously for azulene. Evidently, such volume conserving excited state processes are common. Calculations suggest that pyramidalization at the C=C bond is a candidate. Transient absorption spectroscopy revealed a more complex picture of the excited state relaxation dynamics. It was found that the ground state of BiF recovers on a

much slower timescale (~10 ps) than the quenching of fluorescence (~200 fs). In addition, a broad, red shifted transient feature was observed. Two possible mechanisms of excited state relaxation are proposed for BiF. In the first, the initially populated excited state structure undergoes ultrafast (200 fs) relaxation to a non-emissive 'dark' excited state. This 'dark' excited state population then relaxes (~6 ps) to a thermalized vibrationally hot ground state with the excess energy in low frequency modes. The thermalized hot ground state population then undergoes vibrational cooling (energy transfer to the solvent) to repopulate the equilibrium ground state in tens of picoseconds. Alternatively, the initially populated excited state structure undergoes ultrafast relaxation (200 fs) directly to a non-thermalized vibrationally hot ground state with the excess energy in vibrationally excited non-thermally distributed high frequency modes. This excess energy cannot be transferred directly to the solvent and so fast intramolecular vibrational redistribution dissipates (6 ps) the excess energy amongst the low frequency modes of the molecule. The excess energy is then transferred to the low frequency modes of the solvent (vibrational cooling) in order to repopulate the equilibrium ground state structure in tens of picoseconds. A detailed theoretical study of the BiF excited state is required to provide more definitive evidence to support either model. It is hoped that the data presented in this study could form the basis of such quantum mechanical calculations in the future.

6.5 References

(1) Brunetti, F. G.; Gong, X.; Tong, M.; Heeger, A. J.; Wudl, F. *Angew. Chem.-Int. Edit.* **2010**, *49*, 532.

(2) Sun, G.-Y.; Li, H.-B.; Geng, Y.; Su, Z.-M. *Theor. Chem. Acc.* **2012**, *131*.

(3) Sun, G.-Y.; Wu, S.-X.; Geng, Y.; Li, H.-B.; Wu, Y.; Su, Z.-M. *Theor. Chem. Acc.* **2012**, *131*.

(4) Carlotto, S.; Orian, L.; Polimeno, A. *Theor. Chem. Acc.* **2012**, *131*.

(5) Pogodin, S.; Rae, I. D.; Agranat, I. *Eur. J. Org. Chem.* **2006**, 5059.

(6) Lee, J. S.; Nyburg, S. C. *Acta Crystallogr. Sect C. Cryst. Struc. Commun.* **1985**, *41*, 560.

(7) Brunetti, F. G.; Gong, X.; Tong, M.; Heeger, A. J.; Wudl, F. *Angew. Chem.* **2010**, *49*, 532.

(8) Kazaryan, A.; Kistemaker, J. C. M.; Schafer, L. V.; Browne, W. R.; Feringa, B. L.; Filatov, M. *J. Phys. Chem. A.* **2010**, *114*, 5058.

(9) Kazaryan, A.; Lan, Z.; Schäfer, L. V.; Thiel, W.; Filatov, M. *J. Chem.Theor. Comp.* **2011**, *7*, 2189.

(10) Cnossen, A., University of Groningen, 2013.

(11) Redzimski, T.; Heldt, J. R. *J. Fluoress.* **2003**, *13*, 393.

(12) Donckt, E. V.; Toussaint, P.; Van Vooren, C.; Van Sinoy, A. *J. Chem. Soc., Faraday Trans. 1* **1976**, *72*, 2301.

(13) Wurzer, A. J.; Wilhelm, T.; Piel, J.; Riedle, E. *Chem. Phys. Lett.* **1999**, *299*, 296.

(14) Diau, E. W. G.; De Feyter, S.; Zewail, A. H. *J. Chem. Phys.* **1999**, *110*, 9785.

(15) Bearpark, M. J.; Bernardi, F.; Clifford, S.; Olivucci, M.; Robb, M. A.; Smith, B. R.; Vreven, T. *J. Am. Chem. Soc.* **1996**, *118*, 169.

(16) McGovern, D. A.; Quinn, S.; Doorley, G. W.; Whelan, A. M.; Ronayne, K. L.; Towrie, M.; Parker, A. W.; Kelly, J. M. *Chem. Commun.* **2007**, 5158.

(17) Doorley, G. W.; McGovern, D. A.; George, M. W.; Towrie, M.; Parker, A. W.; Kelly, J. M.; Quinn, S. J. *Angew. Chem.-Int. Edit.* **2009**, *48*, 123.

(18) Towrie, M.; Doorley, G. W.; George, M. W.; Parker, A. W.; Quinn, S. J.; Kelly, J. M. *Analyst* **2009**, *134*, 1265.

(19) Vengris, M.; van Stokkum, I. H. M.; He, X.; Bell, A. F.; Tonge, P. J.; van Grondelle, R.; Larsen, D. S. *J. Phys. Chem. A.* **2004**, *108*, 4587.

(20) Kambhampati, P.; Son, D. H.; Kee, T. W.; Barbara, P. F. *J. Phys. Chem. A.* **2000**, *104*, 10637.

(21) Middleton, C. T.; Cohen, B.; Kohler, B. *J. Phys. Chem. A.* **2007**, *111*, 10460.

(22) Braem, O.; Penfold, T. J.; Cannizzo, A.; Chergui, M. *Phys. Chem. Chem. Phys.* **2012**, *14*, 3513.

7 Photodynamics of Alkyl Substituted Derivatives of the GFP Chromophore

In this chapter, the excited state dynamics of a series of alkyl substituted derivatives of *p*-hydroxybenzilideneimidazolinone (HBDI), the synthetic chromophore of the green fluorescent protein, will be investigated. After detailing the experimental conditions employed (Section 7.2), the steady state absorption (Section 7.3.1) and emission (7.3.2) spectroscopy will be studied. Following this, ultrafast fluorescence up-conversion measurements will be discussed (Section 7.3.3) with a focus placed upon the emission wavelength dependence (Section 7.3.3.1) and solvent viscosity dependence (7.3.3.2). Finally, DFT ground state calculations will be described and employed to provide a rationale for the experimental data (Section 7.3.4).

7.1 Introduction

The realisation that the synthetic analogue, *p*-hydroxybenzilideneimidazolinone (HBDI), of the green fluorescent protein (wt-GFP) chromophore is essentially non-fluorescent in free solution[1] continues to generate significant debate regarding the exact function of the protein matrix. Clearly the protein environment plays a key role in the photodynamics of wt-GFP and acts to suppress the rate of radiationless decay of the excited state of the chromophore. This leads to enhanced fluorescence in the protein compared to the chromophore in solution. Significant interest has been generated in the pH dependence of the GFP photophysics. This is because wt-GFP was found to exhibit pH dependent absorption and fluorescence spectra.[2,3] Significantly, it was found that wt-GFP undergoes an excited state protein transfer (ESPT) reaction.[4] Thus, it is the anionic state of the chromophore which is actually responsible for the emission of wt-GFP. As a result, the pH dependence of the photophysics of HBDI has been extensively characterised.[5] It is possible to generate a cationic form (protonation of the unsubstituted N-atom) or an anionic form (deprotonation of OH) by addition of acid or base

respectively (Figure 7.1). Both the cationic and anionic forms result in red shifted absorption and emission spectra. Each state remains non-fluorescent, but the anionic state exhibits a slightly longer excited state lifetime (increased by a factor of ~2 compared to the neutral state).[6] In order to assess whether ESPT occurs for HBDI, the site of deprotonation (OH) was methylated (OMe-HBDI) in order to prevent formation of the anion.[7] This would prevent any ESPT reaction from occurring. No effect was observed upon the excited state relaxation dynamics and so it was concluded that ESPT is not involved in the non-radiative decay mechanism of the HBDI excited state.

Additional evidence was gained from studying the effects of structural modifications to HBDI upon the excited state dynamics. Particular focus has been placed upon varying the location of the OH group from the para position (p-HBDI) to the meta position (m-HBDI).[8,9] The position of the OH group was found to significantly affect the excited state decay dynamics, whereby the m-HBDI derivative exhibited a longer excited state lifetime. This was largely attributed to the ability of m-HBDI to support an intramolecular excited state proton transfer which is not possible in the case of p-HBDI. Thus, the protein environment of GFP plays a significant role and serves to facilitate ESPT and suppress the non-radiative decay pathway of the chromophore.

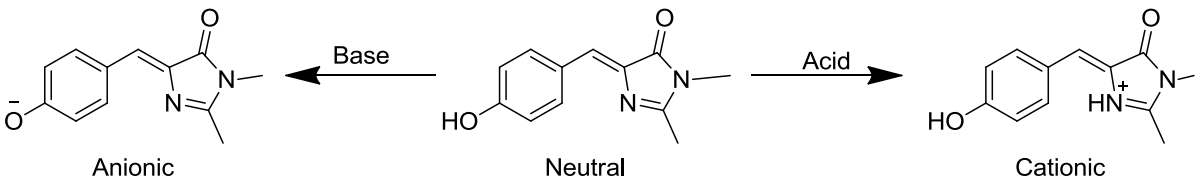

Figure 7.1 - *The anionic, neutral and cationic forms of HBDI.*

In order to improve understanding of these key protein-chromophore interactions, one must first understand better the factors which affect the radiationless decay of the chromophore in solution. It has been established that the radiationless relaxation of the HBDI excited state occurs *via* an ultrafast internal conversion mechanism, promoted by torsional motion along a volume conserving and almost barrierless co-ordinate (See Chapter 1). Thus, an excited state isomerization reaction is hypothesized as the most likely co-ordinate of structural evolution which leads to the radiationless relaxation of HBDI. However, the exact nature of this co-ordinate has been the subject of much debate with a number of possibilities suggested. Extensive theoretical studies have been performed to simulate a number of potential co-ordinates for HBDI isomerization. Weber et al[10] considered the excited state isomerization of HBDI (in three charge states) proceeding *via* three possible torsional co-ordinates (Figure 7.2 reproduced from Reference 10). Rotation about each individual bridging bond (τ and φ) as well as concerted rotation about both bonds (hula-twist, HT) was considered. The hula-twist model was originally proposed by Liu and Hammond[11] as an isomerization mechanism in which large scale (solvent displacing) torsional motion does not occur. This was proposed in order to explain the experimental observations that the excited state lifetime of HBDI did not significantly increase in viscous solvents.[12] A detailed discussion of the effects of solvent friction upon the dynamics of excited state isomerization reactions is given in Chapter 1. As shown by Figure 7.2, it was found that only torsion about the individual bridging bond was barrierless for all charge states (although no conical intersection was found for the anionic state *via* this pathway). Subsequent theoretical studies have also concluded that torsion about only one of the bridging bonds (as opposed to concerted torsion of both) is the co-ordinate of HBDI isomerization.[13-18] However, torsion about which of the two possible bridging bonds remains not entirely proven.[5]

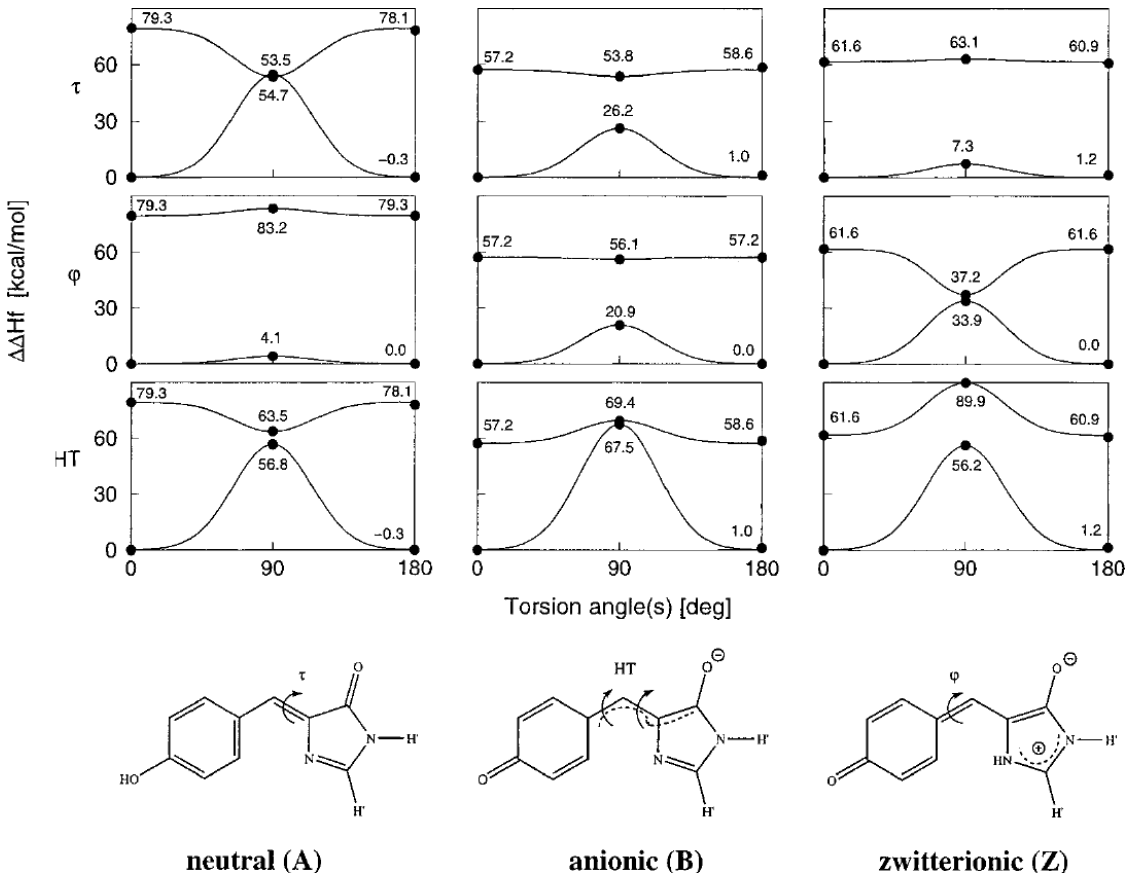

Figure 7.2 - *Calculated potential energy surfaces for the isomerization of three charge states of HBDI via torsion about the bridging double bond (τ), single bond (φ) and a concerted rotation of both (HT, hula-twist). This figure is reproduced directly from Reference 10.*

Liquid phase theoretical studies (as opposed to gas phase) which are the closest representation of the experimental conditions (measured in solution) currently available, suggest that it is rotation about the bridging double bond (τ in Figure 7.2) which facilitates the isomerization of HBDI.[13] However, the small viscosity dependence observed experimentally suggests that such simple large scale torsional motion is not an adequate description of the isomerization mechanism. Instead, the molecular dynamics on the excited state potential energy surface must be more complex. Thus, uncertainty remains regarding the exact nature of the non-radiative excited state decay mechanism of HBDI.

It is thus the aim of this work to improve our understanding of this mechanism. To do so, the excited state decay dynamics of a series of alkyl substituted HBDI derivatives will be studied (Figure 7.3). The effect of structural modifications to HBDI upon the excited state dynamics has previously been shown to be significant. The addition of substituted phenyl substituents to the chromophore was found to significantly alter the photophysical properties of the excited state.[19] In particular, the decay dynamics were shown to be highly dependent upon the electron donating/withdrawing properties and size of the substituents. Thus, it has been established that the photophysics of HBDI are highly sensitive to the structure of the molecule. Therefore, studying the excited state decay dynamics of the alkyl substituted HBDI derivatives allowed this dependence to be probed further. In particular, it is possible to assess the effects of the steric and electronic properties of the substituents upon the radiationless decay pathway. The nature of the torsional motion can also be investigated in detail by assessing the effects of sterically bulky substituents (35Bu and 35BuBz, Figure 7.3) upon the excited state decay dynamics. It is expected that large scale torsional motion would be retarded by sterically bulky substituents. Thus, it is hoped to gain a further insight into the extent and nature of the torsional motion which is involved in the non-radiative excited state of HBDI.

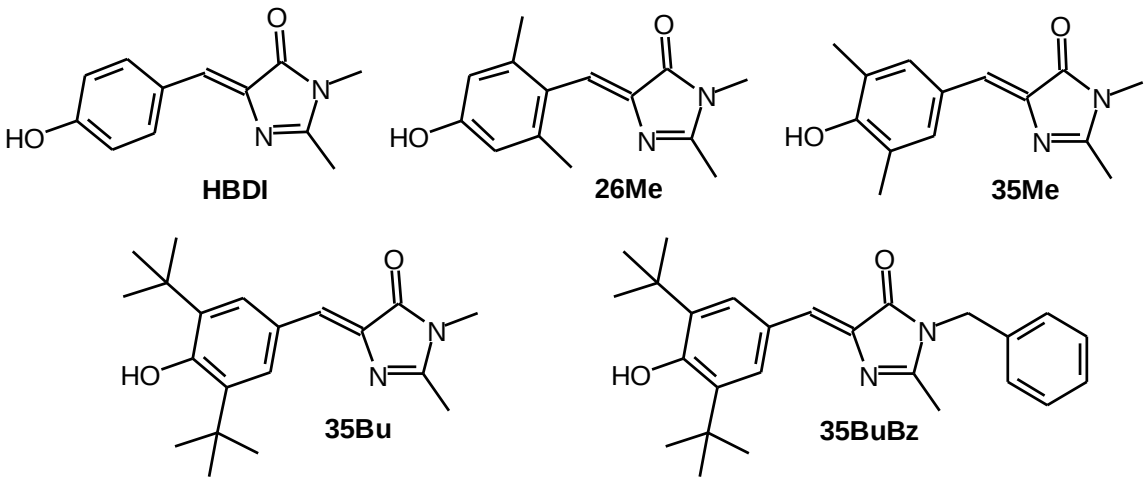

Figure 7.3 - *Molecular structures of the alkyl HBDI derivatives.*

The pH dependent photophysics were also investigated for these derivatives, since the anionic form of the chromophore is known to play such a key role in wt-GFP. Thus, it was also hoped to gain an insight into possible mechanisms by which the protein is able to suppress the radiationless decay pathway of the chromophore in such an effective manner.

7.2 Experimental

The synthesis of the HBDI derivatives is detailed in Chapter 2.[20] Steady state absorption spectra were recorded using a PerkinElmer Lambda XLS spectrophotometer as a function of pH, measured with a calibrated pH meter (Thermo Scientific Orion). pK_a values were determined from the Henderson-Hasselbalch equation:

$$pH = pK_a - \log\left[\left(A - A_0\right)/\left(A_f - A\right)\right] \qquad (7\text{-}1)$$

Where A is the absorbance at a chosen wavelength, A_0 is the absorbance of the pure neutral species and A_f is the absorbance of the final fully deprotonated or protonated sample. The intercept of a plot of pH against $\log\left[\left(A - A_0\right)/\left(A_f - A\right)\right]$ yields the pK_a with accuracy better than 0.5 units. Three separate wavelengths were used in each determination and the results averaged.

Steady state fluorescence spectra were recorded using a PerkinElmer LS Fluorescence Spectrometer with 10 nm excitation and emission bandwidths. All steady state measurements were made with a sample concentration ~10 μM (corresponding to 0.25OD at the wavelength of maximum absorption) in a 1 cm path length cell.

The time-resolved fluorescence decay curves were measured as a function of wavelength by fluorescence up-conversion (described in Chapter 2). The laser excitation pulse was centred at 405 nm or 415 nm for blue or red-shifted absorption bands respectively. All time-resolved

measurements were made with a sample concentration ~100 μM (corresponding to 0.3 OD at the excitation wavelength) in a 1 mm path length cell.

7.3 Results

7.3.1 Steady State Absorption of HBDI derivatives

The absorption spectra of the HBDI derivatives in basic, neutral and acidic ethanol can be seen in Figure 7.4 (a, b and c respectively). A summary of the absorption wavelength maxima is shown in Table 7.1. These measurements were also conducted in water, with a summary of the pK_a (neutral to cation and neutral to anion), wavelength of maximum absorption and extinction coefficient for each derivative (with the exception of 35BuBz due to poor solubility) presented in Table 7.2.

For the neutral form (in water), the largest effect of substitution can be seen for dimethyl substituents at the 2,6 position (26Me) where the spectrum exhibits a large blue shift (22 nm) and the extinction coefficient is halved relative to HBDI. In contrast, substitution of the neutral state at the 3,5 position (Methyl or t-butyl) has a much less significant effect with a small red shift (6 nm) and almost no change to the extinction coefficient.

The pH dependence of each derivative was investigated by conversion of the neutral form to the cationic and anionic forms, by addition of acid and base respectively. This was done in pH steps of approximately 0.5, an example of which can be seen for 35Bu (in water) in Figure 7.5. Here, as with all derivatives studied, a clear isosbestic point is observed in both the neutral to cation and neutral to anion conversions. This suggests that an equilibrium exists between only two charged species in all cases. The pK_a values determined for each derivative show no significant variation with substituent within the experimental error (Table 7.2). Therefore, these substituents have little effect on the ability of HBDI to stabilise a cationic or anionic charge.

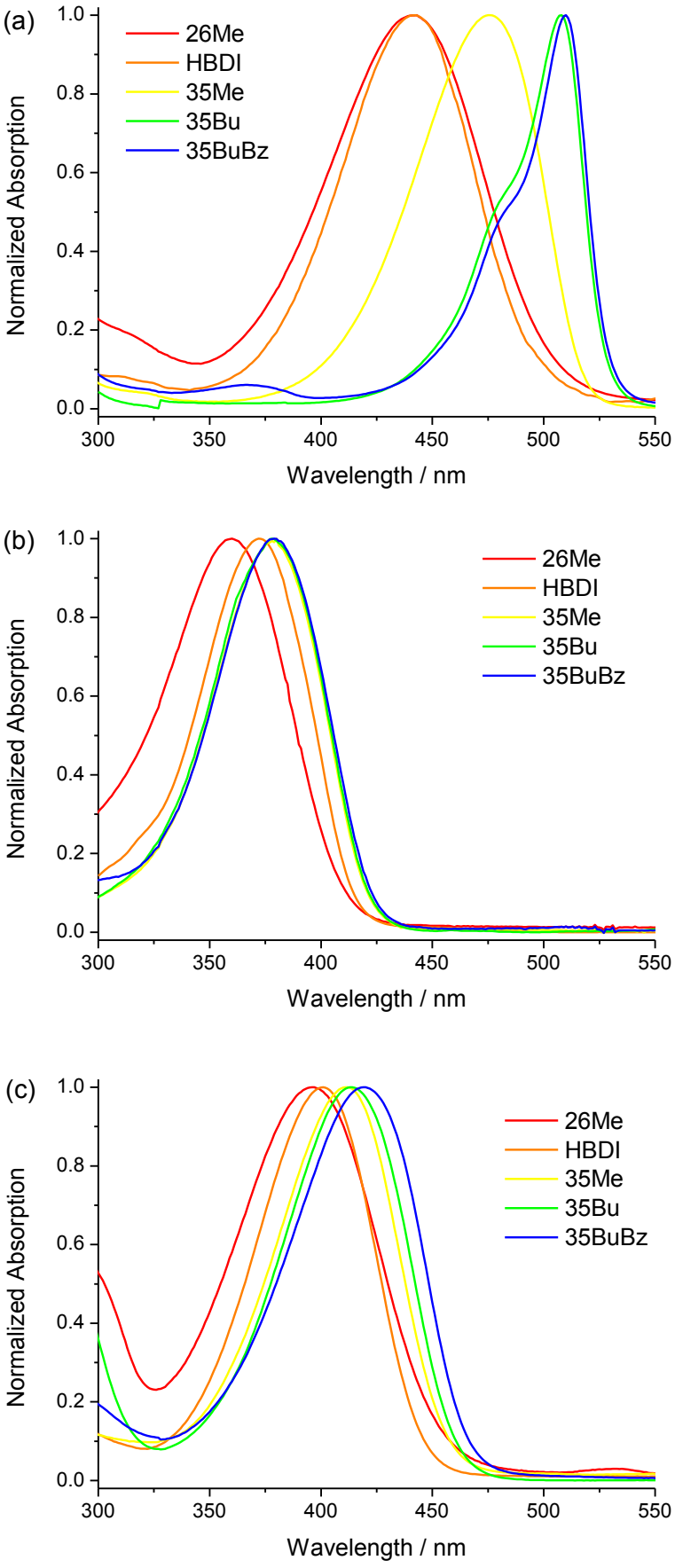

Figure 7.4 - *Absorption spectra of the alkyl HBDI derivatives in (a) basic, (b) neutral, and (c) acidic ethanol.*

Table 7.1 - *Absorption maxima for HBDI and its alkyl derivatives in ethanol.*

		HBDI	26Me	35Me	35Bu	35BuBz
λ_{max}/nm	Anion	442	442	476	508	510
	Neutral	372	360	380	378	379
	Cation	401	396	411	414	419

Table 7.2 - *pK_a, absorption maxima and extinction coefficient for HBDI and its alkyl derivatives in water. Repeat measurements determined the errors to be within 10%.*

		HBDI	**26Me**	**35Me**	**35Bu**
pK_a	Neut/An	7.8	8.8	7.5	8.3
	Neut/Cat	2.7	3.2	3.0	3.2
λ_{max}/nm	Anion	425	411	450	492
	Neutral	370	348	376	376
	Cation	393	384	401	403
ε / $10^3 M^{-1}cm^{-1}$	Anion	32.4	14.6	38.8	46.7
	Neutral	23.9	10.7	25.9	22.9
	Cation	24.8	10.2	29.7	23.1

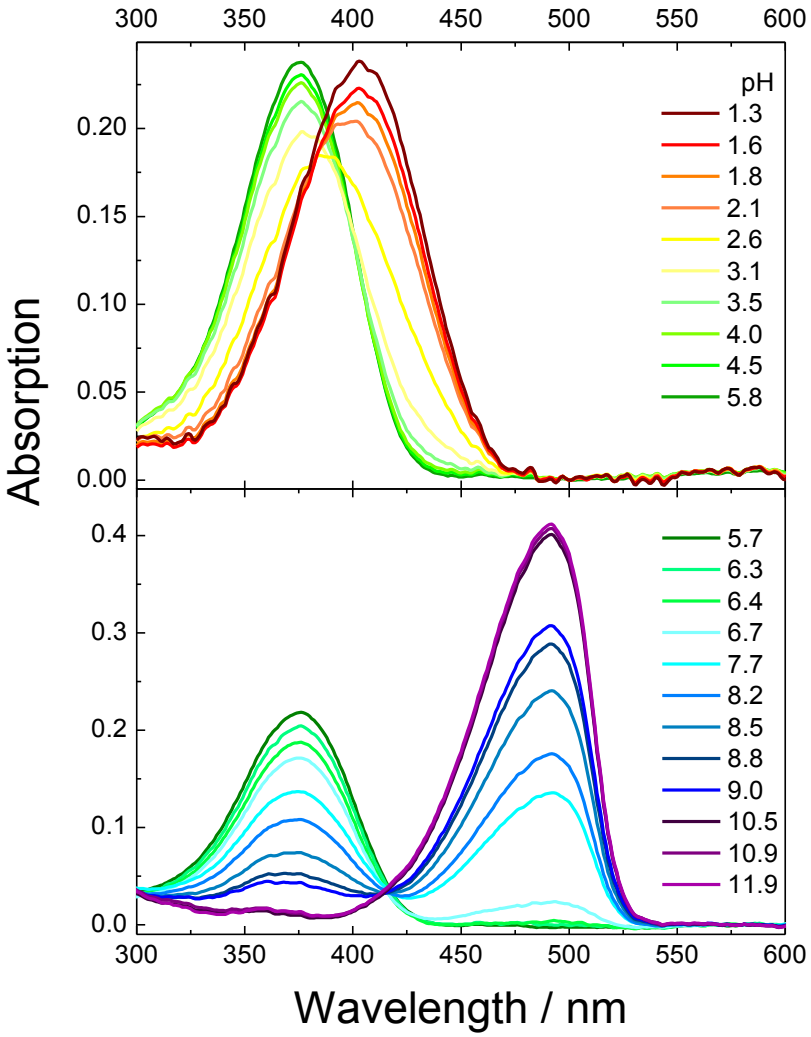

Figure 7.5- *Absorption Spectra of 35Bu in water as a function of pH.*

As previously established for HBDI,[7] generation of the cation of each derivative in water results in a red shifted absorption spectrum (~25 nm) compared to its neutral state. As for the neutral state, the absorption band of the 26Me cation is also blue shifted relative to HBDI and the low extinction coefficient is retained. Similar behaviour for all derivatives was also observed in acidified ethanol (Table 7.1).

A far more remarkable effect is observed when the anionic states of the HBDI derivatives are formed. As established previously, generation of the anionic form of HBDI in water results in a significant red shift (55 nm) compared to the neutral form.[7] The neutral to anion red shift

observed in water for the 35Me derivative was larger than for HBDI (74 nm), and the effect of 35Bu substitution was even greater still (116 nm). Again, as observed for the neutral state, the 26Me anion is blue shifted relative to the HBDI anion, and exhibits a smaller extinction coefficient. The spectral shifts observed for the neutral to anion conversion were even larger in basic ethanol. HBDI exhibited a red shift of 70 nm, 35Me substitution resulted in a red shift of 96 nm and 35Bu substitution led to a red shift of 130 nm. However, the anionic form of 26Me did not exhibit a blue shift relative to anionic HBDI in ethanol. Instead, the wavelength of maximum absorption was identical for each.

The observation of large spectral shifts between the absorption bands of the neutral and anionic states of these derivatives is potentially of great significance. Clearly, even small modifications to the electronic structure of the chromophore result in significantly altered photophysics. Thus, small changes to the chromophore, induced and stabilised by the protein matrix, could certainly give rise to the observed differences between the photophysics of wt-GFP and HBDI. In addition, the observation that these chromophore derivatives exhibit such remarkably large spectral shifts makes the synthesis of fluorescent proteins (FPs), through the use of artificial amino acid residues for example,[21,22] a worthwhile objective. If a FP incorporating such a chromophore were to undergo an excited state proton transfer reaction (as occurs in wt-GFP), the anionic form generated by the reaction would show a giant Stokes-shift (corresponding to the neutral to anionic red shift of the chromophore). Systems in which large Stokes shifts occur have been important for enhancements in bioimaging by shifting the emission wavelength further from the excitation wavelength (scatter) and allowing greater tunability of the colour of the emission.[23,24] The extension of such systems is important for the continued development of these fields.

A clear trend is observed in this data with regards to the inductive effect of the substituents. Alkyl groups substituted directly onto a phenyl ring are able to donate electron density to the

delocalised system *via* an inductive pathway. Alkyl substituents with greater branching are able to donate greater electron density.[25] Therefore, 35Bu is the strongest electron donating substituent in this series of HBDI derivatives. Thus, the magnitude of the observed red shift for all pH conditions follows the trend of electron donating ability of the substituent (HBDI < 35Me < 35Bu). This suggests that the electron donating substituents stabilise the energy of the excited state and so lead to a lower energy absorption (red shift). However, this does not explain the anomalous behaviour of the 26Me derivative. Clearly, the spectroscopy of this molecule is more complex and must be investigated further (Section 7.3.4).

7.3.2 Steady State Fluorescence

The steady state fluorescence spectra of the anionic, neutral and cationic states of the HBDI derivatives measured in ethanol at room temperature can be seen in Figure 7.6 (a, b and c respectively). The peak wavelengths of the emission spectra and Stokes shifts (calculated from the absorption data shown in Table 7.1) are summarised in Table 7.3. The emission in all cases was extremely weak and obscured by Raman scattering from the solvent (ethanol in this case). The spectra presented in Figure 7.6 were subjected to a subtraction of the Raman scattering (determined by measuring the emission spectrum of pure ethanol under identical conditions in each case). As a result of this procedure, the exact profile of the weak emission is somewhat uncertain but the general trends are reproducible.

The emission spectra of the neutral HBDI derivatives largely follow the trend set by the absorption spectra. The emission spectrum of 26Me is blue shifted compared to HBDI, 35Me is red shifted and 35Bu is red shifted even further. However, one exception is the case of 35BuBz which exhibits a larger Stokes shift than 35Bu. This is a surprising observation which suggests a possible influence of the phenyl ring upon the excited state despite not being involved directly in the delocalised system. A better insight could be gained by studying the time-resolved excited state dynamics as discussed in Section 7.3.3.

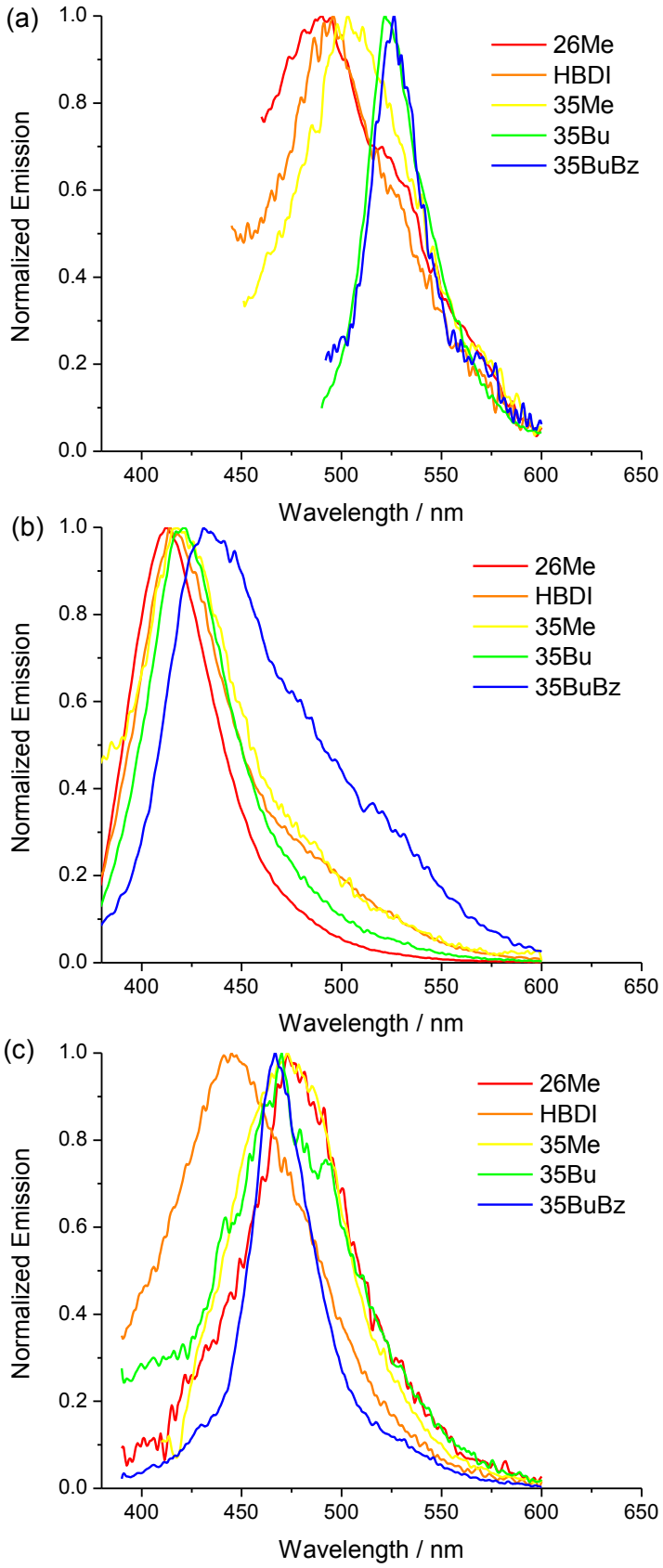

Figure 7.6 – *Steady state fluorescence spectra of the alkyl HBDI derivatives in (a) basic, (b) neutral, and (c) acidic ethanol after subtraction of the solvent Raman scattering. Excitation was at the absorption maximum in each case.*

Table 7.3 - *Emission maxima and Stokes shifts of HBDI and its alkyl derivatives measured in ethanol.*

		HBDI	**26Me**	**35Me**	**35Bu**	**35BuBz**
λ_{max}/nm	Anion	494	490	504	522	525
	Neutral	416	412	418	420	434
	Cation	444	474	473	469	466
Stokes Shift / nm	Anion	52	48	28	14	15
	Neutral	44	52	38	42	55
	Cation	43	78	62	55	47

The emission spectra of the anionic HBDI derivatives also largely follow the absorption spectra. 35BuBz and 35Bu are most red shifted, show a close mirror image to their respective absorption spectra and do not exhibit a large Stokes shift (15 nm and 14 nm, respectively). In addition, 35Me is red shifted relative to HBDI but less significantly than 35BuBz and 35Bu. However, 35Me does exhibit a larger Stokes shift (28 nm) than both 35BuBz (15 nm) and 35Bu (14 nm) although it is still significantly smaller than that of HBDI (52 nm) and 26Me (48 nm). The shape of the spectra must also be considered. The anionic states of both 35Bu and 35BuBz exhibit much narrower emission spectra than the remaining derivatives. Broad emission (and absorption) spectra suggest electronic ground and excited state structures which are significantly geometrically different. In such cases, the initial excitation occurs to a wider distribution of the excited state surface (broader absorption spectrum), and emission occurs to a wider distribution of the ground state surface (broader emission). As a result, the absorption and emission maxima are much less clearly defined and so a larger Stokes shift is observed. Therefore, the narrow spectra and smaller Stokes shifts of 35Bu and 35BuBz suggest that the ground and excited states of these derivatives exhibit a much smaller

geometric difference. In addition, if the electronic structure of a molecule is significantly different between the ground and excited state, solvation dynamics may be observed. Time resolved spectroscopy is particularly adept at the determination and study of such effects (See Chapter 1) and these considerations are discussed in Section 7.3.3.1.

The emission spectra of the cationic HBDI derivatives also largely reflect the behaviour of the cationic absorption spectra. However, the notable exception in this case is 26Me, the emission spectrum of which is significantly red shifted compared to cationic HBDI (30 nm). In addition, the Stokes shift of cationic 26Me is notably larger than that of HBDI (78nm compared to 43 nm respectively). The origin of this effect is somewhat unclear, but it is again obvious that the photophysics of the 26Me derivative appear to differ from the other derivatives. Further investigation was required to establish the reasoning behind these differences (Section 7.3.4).

7.3.3 Ultrafast Time-Resolved Fluorescence

In order to gain a better understanding of the excited state dynamics of the chromophore derivatives, we turned to ultrafast time-resolved fluorescence spectroscopy. This technique allows the unambiguous measurement of the lifetime of the excited state. The fluorescence decay curves measured for HBDI and its alkyl derivatives in ethanol are shown in Figure 7.7 (neutral and anionic forms). These measurements were made at the wavelength of maximum emission in each case (as detailed in Table 7.3). The decay curves were subjected to the fitting procedure described previously (Chapter 2), where a sum of two exponential functions was adequate to provide a good fit to the data in all cases. A summary of the fitting parameters is shown in Table 7.4.

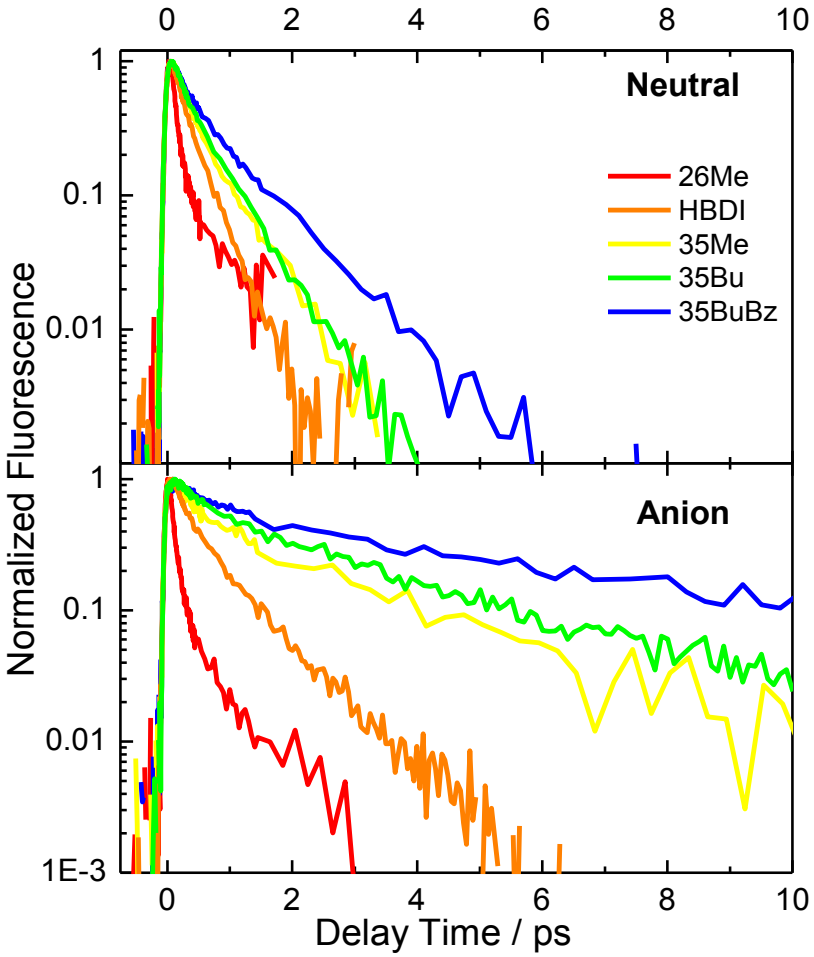

Figure 7.7 - *Fluorescence decay curves of alkyl HBDIs in neutral and basic ethanol measured at the emission maxim (Neutral: λ_{ex} 405 nm. Basic: λ_{ex} 415 nm).*

The decay of every derivative is ultrafast, with a sub 2 ps calculated average fluorescence lifetime in all cases except the anionic form of 35BuBz (4.18 ps). Such a fast decay has been previously reported for HBDI, and ascribed to an ultrafast structural reorganisation in the excited state along a near barrierless co-ordinate.[12,26] This reorganisation leads the excited state population to an S_1-S_0 conical intersection where internal conversion repopulates the ground state on an ultrafast timescale (See Chapter 1). The decay of each derivative is bi-exponential, reflecting a distribution of geometries in the ground state facilitated by structural flexibility about both bridging bonds of HBDI.[27] However, the decay of 26Me is unique compared to the other derivatives.

Table 7.4 - *Fit parameters for fluorescence decay data of HBDI and its alkyl derivatives in ethanol. Repeat measurements determined the error to be within 10% for each parameter.*

	τ_1 / ps	A_1	τ_2/ps	A_2	$<\tau>$ /ps
Neutral					
HBDI	0.18	0.54	0.41	0.46	0.29
26Me	0.09	0.96	1.36	0.04	0.15
35BuBz	0.25	0.51	0.94	0.49	0.58
35Me	0.22	0.51	0.61	0.49	0.39
35Bu	0.27	0.53	0.66	0.47	0.45
Anionic					
HBDI	0.25	0.55	0.87	0.45	0.53
26Me	0.07	0.91	0.49	0.09	0.11
35BuBz	1.12	0.51	7.40	0.49	4.18
35Me	0.44	0.57	2.71	0.43	1.41
35Bu	0.59	0.44	2.97	0.56	1.94

The decay of 26Me is significantly faster than the remaining derivatives, and is dominated by a ~100 fs component (96 % amplitude). This almost single exponential decay is no longer characteristic of a system in which a distribution of ground state geometries contributes to the excited state decay. It is thus possible that the mechanism of non-radiative decay of 26Me is different to the remaining derivatives. One possibility is the formation of a trapped 'dark' state, such as that observed for the molecular motor systems described previously in this work (Chapters 3 – 5). Transient absorption measurements may provide a further insight, but these measurements were not performed as part of this study.

Thus, it was found that 26Me is the only derivative to exhibit a shorter average fluorescence lifetime than HBDI. This suggests that 2,6 methyl substitution of HBDI actually results in an enhancement of the radiationless relaxation pathway rather than suppression. The anomalous behaviour of 26Me is consistent with the steady state spectroscopy described previously whereby 26Me was the only derivative to exhibit blue shifted absorption (Section 7.3.1) and emission (Section 7.3.2) spectra compared to HBDI. Thus, the time-resolved data, coupled with the anomalous behaviour of the 26Me steady state spectra, suggests that the 26Me derivative has a potentially significantly different photochemistry compared to the other derivatives. This prompted a more detailed investigation from a theoretical viewpoint in an attempt to discern the differences between 26Me and the remaining derivatives (Section 7.3.4).

Table 7.4 shows that the remaining derivatives (35BuBz, 35Me and 35Bu) exhibit a longer fluorescence lifetime compared to HBDI in both the neutral and anionic forms. Therefore, this suggests that the radiationless decay pathway is suppressed in these derivatives relative to HBDI. Importantly, there is a clear correlation between a longer average excited state lifetime and increasingly large alkyl substituents (HBDI < 35Me < 35Bu < 35BuBz). This trend is observed in both the neutral and anionic states, but is more pronounced for the anionic forms. The enhancement of the excited state lifetime could arise from two possible contributions. Firstly, the electronic structure of the chromophore is significantly altered by inductive donation of electron density from the substituents (as discussed in Section 7.3.1). Alternatively, the increasingly large substituents may increase the friction opposing motion along the isomerization co-ordinate in the excited state. The effects of solvent friction upon the molecular dynamics of isomerization reactions are described in detail in Chapter 1. If the isomerization co-ordinate involves large scale torsional motion, sterically bulky substituents may slow down the molecular dynamics. As a result, non-radiative excited state decay can be

hindered and so a longer excited state lifetime is observed experimentally. In order to separate the electronic and sterics effects upon the excited state dynamics, a viscosity dependence study was conducted for 35BuBz and 35Bu. This analysis is discussed in detail in Section 7.3.3.2.

7.3.3.1 Emission Wavelength Dependence

An investigation of the emission wavelength dependence of the decay dynamics was conducted for each derivative. As described previously (Chapter 1), significantly emission wavelength dependent decay dynamics can be indicative of a system in which solvent dynamics stabilise the electronic structure of the excited state. Thus, such an analysis can be used to determine the extent to which the electronic structure of a molecule is displaced between the electronic ground and excited states. An example of the emission wavelength dependence of the fluorescence decay dynamics is shown for cationic 35Bu in pentanol in Figure 7.8. The emission was measured on the blue side (460 nm), centre (480 nm) and red side (500 nm) of the emission spectrum. The decay curves were fitted with a bi-exponential function and the resulting fit parameters are shown in Table 7.5. The decay curves are superimposed, and the fit parameters are identical (within experimental error). Therefore, it was concluded that the HBDI derivatives investigated here do not exhibit an emission wavelength dependence. This is consistent with the behaviour of HBDI reported previously.[28] In addition, in no case was a rise time found on the red side of the emission spectrum. This indicates that there is no time-dependent shift of the excited state to lower energy after excitation. Such an effect may be observed in the excited state decay profile of a molecule which exhibits significant excited state solvation dynamics, or in which a new species is formed (i.e. the product of an excited state proton transfer reaction). This suggests that the excited state dipole moment of each HBDI derivative does not differ significantly from its corresponding ground state and no excited state reactions occur in any case. A detailed

discussion of excited state reactions and the role of solvent dynamics in the stabilisation of electronic excited state structures is given in Chapter 1.

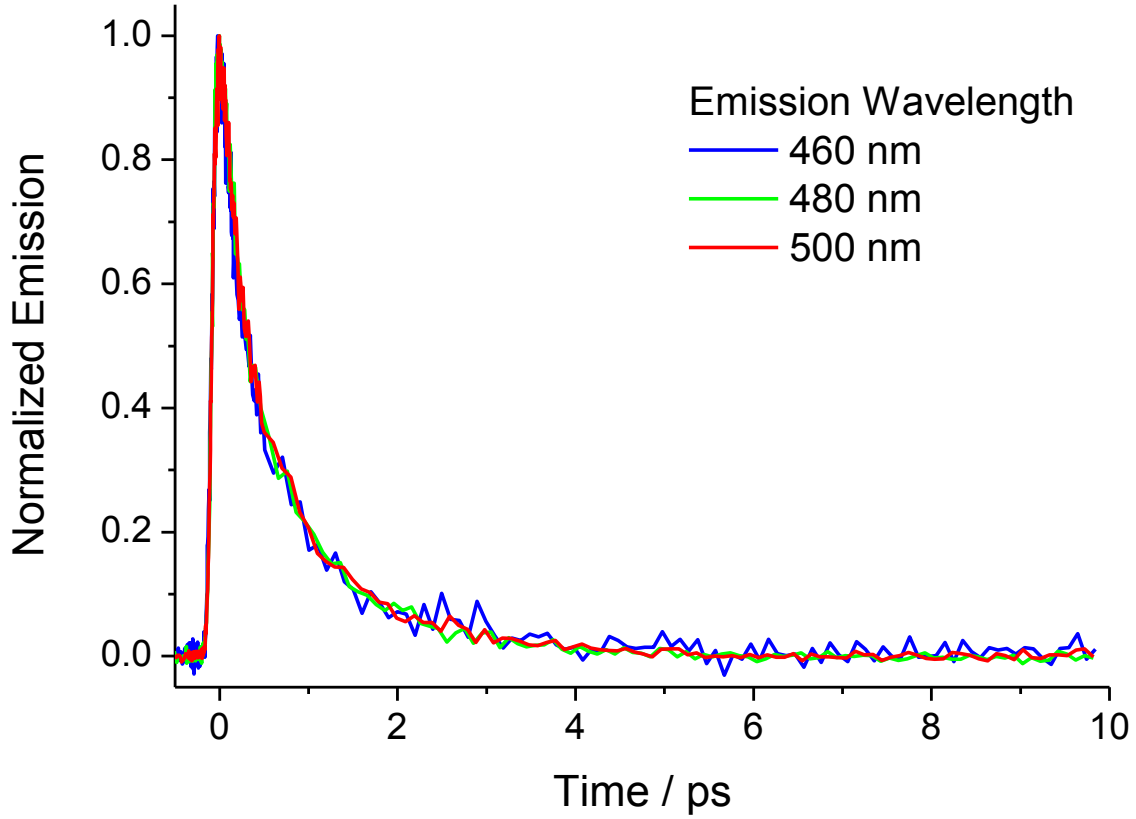

Figure 7.8 - *Emission wavelength dependence of the fluorescence decay of cationic 35Bu in Pentanol.*

Table 7.5 - *Parameters of fit to the cationic 35Bu fluorescence decay curves measured in pentanol as a function of emission wavelength. Repeat measurements determined the error to be within 10% for each parameter.*

Wavelength / nm	τ_1 / **ps**	A_1	τ_2/**ps**	A_2	$<\tau>$ /**ps**
460	0.26	0.66	1.28	0.34	0.61
480	0.22	0.56	1.00	0.44	0.57
500	0.26	0.56	1.06	0.44	0.61

7.3.3.2 Viscosity Dependence

In order to separate the electronic and friction effects of the substituents on the excited state dynamics, we measured the excited state lifetime of two derivatives as a function of viscosity in a series of similar solvents. The influence of solvent viscosity (taken as an approximation of friction) upon excited state molecular dynamics is discussed in detail in Chapter 1. The non-radiative excited state decay of HBDI is proposed to occur *via* barrierless excited state structural evolution along the torsional co-ordinate of the central bridging olefin.[3,5] This structural evolution leads the excited state population to a conical intersection where ultrafast internal conversion to the ground state occurs. A detailed discussion of the non-radiative decay mechanism of HBDI is given in Section 7.1. It is generally expected that torsional motion would be greatly retarded in high solvent friction conditions. However, only a weak friction dependence is observed experimentally for HBDI.[3,5] Thus, although torsion may be involved in the radiationless decay co-ordinate, it is not simply large scale torsional motion which promotes non-radiative decay. However, it is expected that more sterically bulky substituents (such as those studied in this work) would result in an even greater retardation of the torsional motion and so an even longer excited state lifetime. Thus, a larger dependence upon solvent friction may be observed experimentally for the alkyl substituted derivatives of HBDI. Therefore, by measuring the excited state lifetime of the substituted derivatives as a function of solvent viscosity, it is possible to assess the extent to which torsional motion is involved in the co-ordinate of non-radiative excited state decay of HBDI.

Since 35Bu and 35BuBz have the strongest electron donating substituents (t-butyl) and differ only by the bulky phenyl substituent of 35BuBz, these derivatives were chosen for this analysis. The neutral form of each derivative was measured at the corresponding wavelength of maximum emission. The fluorescence decay curves of the derivatives in alcohol solvents of increasing viscosity are shown in Figure 7.9 (a,b and c for HBDI, 35Bu and 35BuBz

respectively). Each decay curve was subjected to the fitting procedure described previously (Chapter 2), and the average excited state lifetime was calculated. A summary of the fitting parameters is shown in Table 7.6.

In order to assess the viscosity dependence of each derivative in a quantitative manner, the Stokes-Einstein equation can be used:

$$k = \frac{k_B T}{\eta V} \qquad (7\text{-}2)$$

Where k is the rate constant of excited state decay, k_B is the Boltzmann constant, T is the temperature, η is the viscosity and V is the volume.

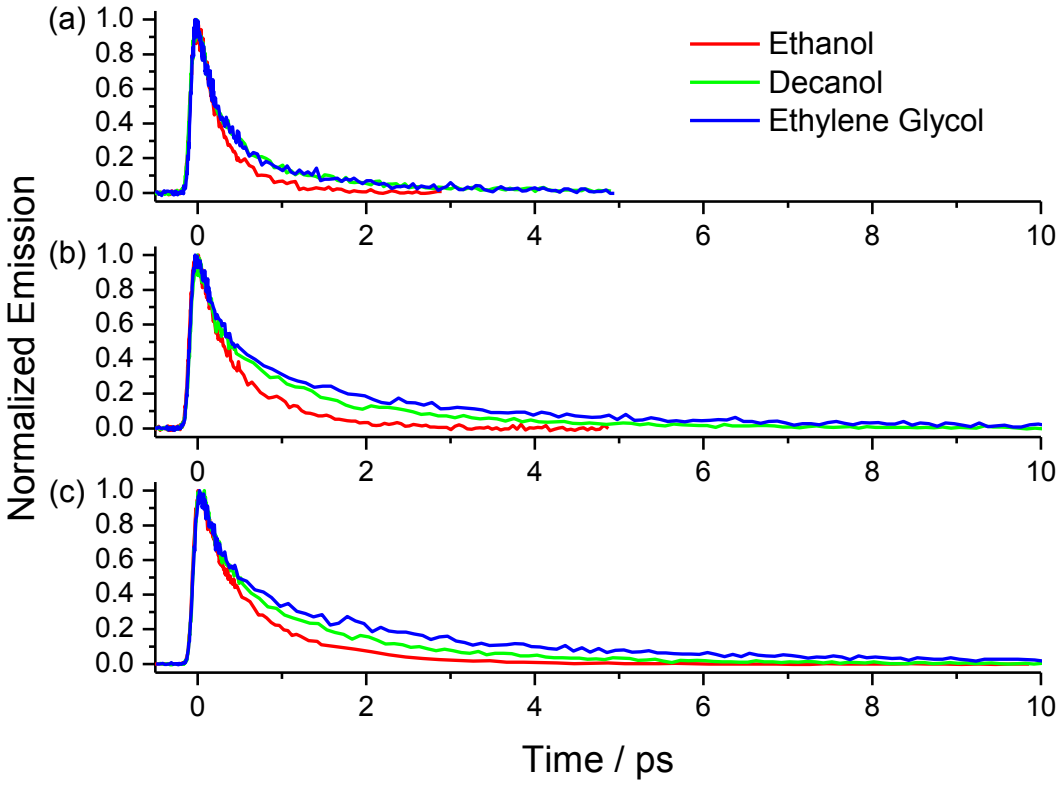

Figure 7.9 - *Fluorescence decay curves measured in alcohol solvents of increasing viscosity for (a) HBDI, (b) 35Bu and (c) 35BuBz.*

Table 7.6 - *Fit parameters for HBDI, 35Bu and 35BuBz in a series of increasingly viscous alcohol solvents. Repeat measurements determined the error to be within 10% for each parameter.*

	Viscosity / cP	τ_1 /ps	A_1	τ_2/ps	A_2	τ_3/ps	A_3	$<\tau>$ /ps
HBDI								
Ethanol	1.1	0.18	0.54	0.41	0.46	-	-	0.29
Decanol	10.9	0.25	0.76	1.29	0.24	-	-	0.50
Ethylene Glycol	16.1	0.24	0.76	1.33	0.24	-	-	0.49
35Bu								
Ethanol	1.1	0.27	0.53	0.66	0.47	-	-	0.45
Decanol	10.9	0.21	0.56	1.12	0.40	2.95	0.09	0.78
Ethylene Glycol	16.1	0.2	0.62	1.1	0.32	4.06	0.15	1.00
35BuBz								
Ethanol	1.1	0.25	0.51	0.94	0.49	-	-	0.58
Decanol	10.9	0.32	0.57	1.66	0.57	-	-	0.9
Ethylene Glycol	16.1	0.34	0.59	2.53	0.41	-	-	1.24

Therefore, by plotting k (calculated by the inverse of the average fluorescence lifetime) against $1/\eta$, a straight line can be fitted to the data with a gradient of k_BT/V. Thus, the volume (V) of solvent displaced during the excited state relaxation can be calculated. This volume can then be used to assess the extent to which torsional motion is involved in the excited state structural evolution co-ordinate. Figure 7.10 shows this plot for HBDI (orange), 35Bu (green) and 35BuBz (blue). The gradient of the fitted straight line along with the subsequent calculated displaced volume is shown in Table 7.7.

Table 7.7 shows that as HBDI is loaded with more sterically bulky substituents, the volume of solvent displaced by the structural evolution which promotes non-radiative decay is

increased. However, this volume is far smaller than that expected of a phenyl ring undergoing large scale torsion. [29-31] A benzene ring has a hydrodynamic volume of approximately 80 Å^3.[32] Thus, although some viscosity dependence is evident, it is far less significant than that expected if simple excited state torsion about a central bridging bond were invoked as the co-ordinate of the radiationless decay of HBDI.

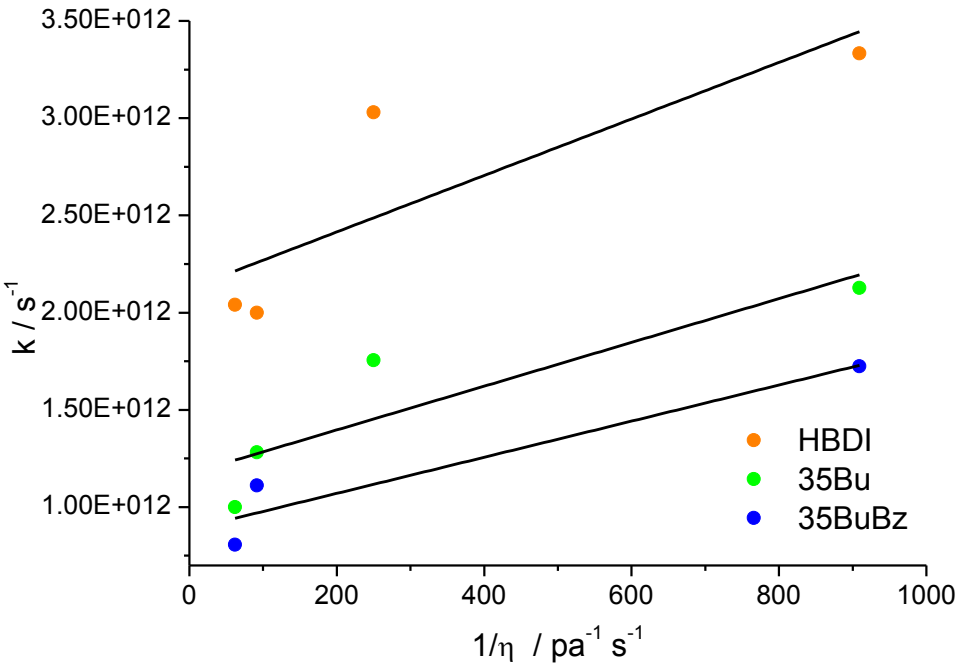

Figure 7.10 - *Viscosity dependence of the average fluorescence lifetime of HBDI, 35Bu and 35BuBz.*

Table 7.7 – *Gradient of the straight line plot fitted to the viscosity dependent excited state relaxation of each derivative (Figure 7.10) and calculated volume of solvent displaced by each derivative. Linear regression determined the error to be within 35 % in each case.*

Derivative	***Gradient***	***Volume*** / Å^3
HBDI	1.45×10^9	2.79
35Bu	1.13×10^9	3.59
35BuBz	9.29×10^8	4.36

This is in line with previous reports where it was found that the excited state decay of HBDI exhibits a weak dependence upon solvent viscosity.[28] Therefore, this suggests that the radiationless decay pathway proceeds to the conical intersection *via* a co-ordinate which does not involve simple large scale torsional motion about a central bridging bond. However, it is clear than torsional motion does indeed play some role in the radiationless excited state relaxation of HBDI. Thus, the true co-ordinate of structural evolution must involve torsion, but in a manner which does not displace large volumes of solvent. This is in line with previous reports for HBDI,[2] and a number of theoretical studies have been conducted to investigate the possible mechanism of a 'volume conserving' co-ordinate. A more detailed discussion of this work is presented in Section 7.1. Thus, further evidence for the involvement of torsional motion in the non-radiative decay of HBDI was found, but the exact nature of this torsional motion in terms of a weak solvent friction dependence remains unclear.

7.3.4 DFT Calculations

In order to gain a better insight into the anomalous behaviour of the 26Me derivative, we turned to ground state DFT calculations. This allows us to model the ground state structure of the chromophore in order to determine if any substituent dependent differences arise. Interestingly, 26Me was the only derivative to exhibit a non-planar optimised ground state structure (Figure 7.11). The proximity of the methyl substituents to the imidazolinone ring forces the molecule to adopt a non co-planar structure between the imidazolinone and phenyl rings. This is likely to result in a reduced π-electron delocalisation and may affect the charge transfer character of the ground to excited state transition. A non-planar ground state structure may significantly affect the excited state dynamics of 26Me.

As described previously (Chapter 1), a number of calculations have shown that the non-radiative excited state decay of HBDI occurs *via* an S_1-S_0 conical intersection.

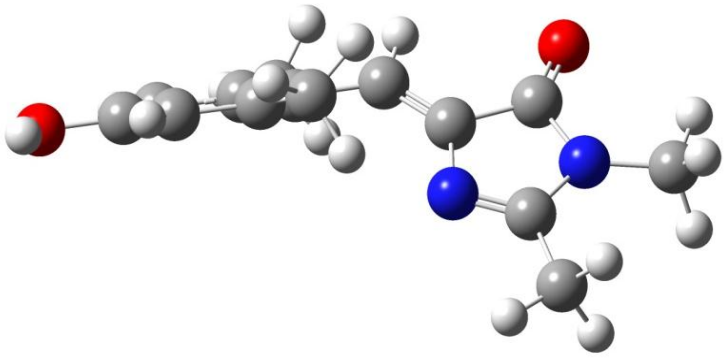

Figure 7.11 - *DFT calculated (gas phase) ground state structure of 26Me.*

This is reached by excited state structural reorganisation in which a 90^{o} twist about the central double carbon-carbon bridging bond is a key step.[13,33] Therefore, if the ground state structure of the molecule was pre-positioned such that the structure of the excited state was already appropriately twisted, this could place the population of the excited state adjacent to the conical intersection directly after excitation. A schematic representation of how the ground state potential energy surface could be affected by a twisted ground state structure is shown in Figure 7.12.

The twisted structure (green) results in an asymmetric ground state surface compared to the planar structure (blue). As a result, excitation leads to a Franck-Condon population which is significantly closer to the conical intersection (Orange). As a result, very little (or even no) structural reorganisation in the excited state would be required before internal conversion can occur at the conical intersection. Therefore, the lifetime of the excited state would be significantly shorter than that of a molecule in which the ground state structure is not pre-loaded to arrive on the excited state surface directly adjacent to the conical intersection. Thus, it is possible that the twisted nature of the 26Me ground state structure results in a Frank-Condon state which is sufficiently close to the conical intersection so as to allow internal conversion with little or no structural reorganisation required. Thus, ultrafast decay of the excited state is promoted on a timescale significantly faster than the remaining derivatives.

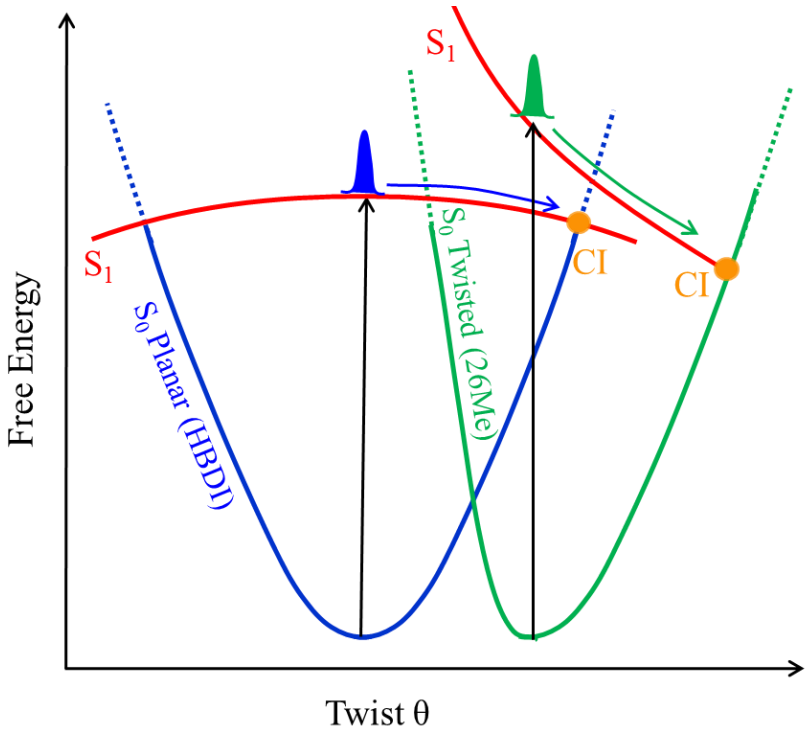

Figure 7.12 - *A schematic representation of the effect of a non-planar ground state structure upon the mechanism of non-radiative excited state decay of HBDI.*

7.4 Conclusion

Alkyl substitution of the GFP chromophore has been shown to result in significantly altered photophysics compared to the unsubstituted parent HBDI. The position and size of the substituents exert a significant influence over the steady state spectra and ultrafast decay of the excited state. 26Me substitution results in blue shifted absorption and fluorescence spectra and a significant quenching of the fluorescence lifetime (relative to HBDI). DFT calculations reveal a non-planar ground state structure for 26Me as a result of steric crowding. Thus, it is hypothesized that the twisted ground state structure gives rise to a Frank-Condon excitation onto a point on the excited state potential energy surface which is much closer to the S_1-S_0 conical intersection than for the other derivatives. This promotes direct ultrafast internal conversion to the ground state without significant excited state structural reorganisation, thus leading to a shortened excited state lifetime. This adds further weight to the notion that the

radiationless decay pathway of HBDI is accessed by twisting of the chromophore along the reaction co-ordinate (excited state structural reorganisation).

In contrast, substitution at the 3,5 positions results in red shifted absorption and fluorescence spectra accompanied by a longer fluorescence lifetime. This effect scales with the steric size of the substituent where 35BuBz exhibits the most red shifted spectra and the longest fluorescence lifetime. Thus, the largest substituents have the largest retardation effect upon the non-radiative decay of the HBDI excited state. Thus, further experimental evidence has been found which suggests that torsional motion is involved in the co-ordinate of radiationless relaxation. However, a detailed viscosity analysis found that the effect of these large substituents remains significantly smaller than that expected of a system undergoing conventional excited state isomerization. Thus, although evidence was found to support the involvement of torsion, it is clear that the nature of the co-ordinate is far more complex than simple large scale rotation about a bridging bond.

The pH dependence established previously for HBDI,[7] whereby both the absorption and fluorescence spectra of the anionic and cationic forms are red shifted relative to the neutral form, is retained for each substituent. In each case, the anionic form is most red shifted. However, the magnitude of this red shift for the alkyl derivatives, particularly 35Bu (130 nm in ethanol), was much larger than that observed in the pH dependence of HBDI. This raises the possibility of custom engineering FP systems in which a neutral to anionic transformation of the chromophore (as occurs in an excited state proton transfer reaction, for example) results in a giant Stokes shift. There is significant potential for such systems in a number of applications in bioimaging and related fields. However, a greater understanding of the effects of substituents upon the photophysics of FP chromophores is first required. Future investigations may include the study of a wider range of substituents. Detailed quantum

mechanical calculations of the ground and excited state potential energy surfaces may be particularly important.

7.5 References

(1) Niwa, H.; Inouye, S.; Hirano, T.; Matsuno, T.; Kojima, S.; Kubota, M.; Ohashi, M.; Tsuji, F. I. *Proc. Natl. Acad. Sci. USA* **1996**, *93*, 13617.

(2) Meech, S. R. *Chem. Soc. Rev* **2009**, *38*, 2922.

(3) Tonge, P. J.; Meech, S. R. *J. Photochem. Photobiol. A.* **2009**, *205*, 1.

(4) Chattoraj, M.; King, B. A.; Bublitz, G. U.; Boxer, S. G. *Proc. Natl. Acad. Sci. USA* **1996**, *93*, 8362.

(5) Meech, S. R. *Chem. Soc. Rev.* **2009**, *38*, 2922.

(6) Litvinenko, K. L.; Webber, N. M.; Meech, S. R. *Chem. Phys. Lett.* **2001**, *346*, 47.

(7) Dong, J.; Solntsev, K. M.; Tolbert, L. M. *J. Am. Chem. Soc.* **2006**, *128*, 12038.

(8) Dong, J.; Solntsev, K. M.; Poizat, O.; Tolbert, L. M. *J. Am. Chem. Soc.* **2007**, *129*, 10084.

(9) Solntsev, K. M.; Poizat, O.; Dong, J.; Rehault, J.; Lou, Y.; Burda, C.; Tolbert, L. M. *J. Phys. Chem. B.* **2008**, *112*, 2700.

(10) Weber, W.; Helms, V.; McCammon, J. A.; Langhoff, P. W. *Proc. Natl. Acad. Sci. USA* **1999**, *96*, 6177.

(11) Liu, R. S.; Hammond, G. S. *Chemistry (Weinheim an der Bergstrasse, Germany)* **2001**, *7*, 4537.

(12) Litvinenko, K. L.; Webber, N. M.; Meech, S. R. *J. Phys. Chem. A.* **2003**, *107*, 2616.

(13) Altoe, P.; Bernardi, F.; Garavelli, M.; Orlandi, G.; Negri, F. *J. Am. Chem. Soc.* **2005**, *127*, 3952.

(14) Martin, M. E.; Negri, F.; Olivucci, M. *J. Am. Chem. Soc.* **2004**, *126*, 5452.

(15) Levine, B. G.; Martinez, T. J. *Annu. Rev. Phys. Chem.* **2007**, *58*, 613.

(16) Olsen, S.; Manohar, L.; Martinez, T. J. *Biophys. J.* **2002**, *82*, 359A.

(17) Toniolo, A.; Granucci, G.; Martinez, T. J. *J. Phys. Chem. A.* **2003**, *107*, 3822.

(18) Toniolo, A.; Olsen, S.; Manohar, L.; Martinez, T. J. *Faraday Discuss.* **2004**, *127*, 149.

(19) Petkova, I.; Dobrikov, G.; Banerji, N.; Duvanel, G.; Perez, R.; Dimitrov, V.; Nikolov, P.; Vauthey, E. *J. Phys. Chem. A.* **2010**, *114*, 10.

(20) Baldridge, A.; Kowalik, J.; Tolbert, L. M. *Synthesis-Stuttgart* **2010**, 2424.

(21) Kent, K. P.; Childs, W.; Boxer, S. G. *J. Am. Chem. Soc.* **2008**, *130*, 9664.

(22) Wang, L.; Xie, J. M.; Deniz, A. A.; Schultz, P. G. *J. Org. Chem.* **2003**, *68*, 174.

(23) Chudakov, D. M.; Matz, M. V.; Lukyanov, S.; Lukyanov, K. A. *Physiol. Rev.* **2010**, *90*, 1103.

(24) Kogure, T.; Kawano, H.; Abe, Y.; Miyawaki, A. *Methods* **2008**, *45*, 223.

(25) Clayden, J.; Greeve, N.; Warren, S.; Wothers, P. *Organic Chemistry, Oxford University Press* **2001**.

(26) Mandal, D.; Tahara, T.; Meech, S. R. *J. Phys. Chem. B.* **2004**, *108*, 1102.

(27) Gepshtein, R.; Huppert, D.; Agmon, N. *J. Phys. Chem. B.* **2006**, *110*, 4434.

(28) Mandal, D.; Tahara, T.; Webber, N. M.; Meech, S. R. *Chem. Phys. Lett.* **2002**, *358*, 495.

(29) Changenet, P.; Zhang, H.; van der Meer, M. J.; Glasbeek, M.; Plaza, P.; Martin, M. M. *J. Phys. Chem. A.* **1998**, *102*, 6716.

(30) van der Meer, M. J.; Zhang, H.; Glasbeek, M. *J. Chem. Phys.* **2000**, *112*, 2878.

(31) Espagne, A.; Paik, D. H.; Changenet-Barret, P.; Martin, M. M.; Zewail, A. H. *ChemPhysChem* **2006**, *7*, 1717.

(32) Bondi, A. *J. Phys. Chem.* **1964**, *68*, 441.

(33) Olsen, S.; Smith, S. C. *J. Am. Chem. Soc.* **2008**, *130*, 8677.

8 Summary and Outlook

In this thesis, we describe research probing the excited state reaction dynamics of two important molecular systems: light-driven unidirectional molecular rotary motors and the model chromophore of the green fluorescent protein.

The molecular motors were found to exhibit bimodal fluorescence decays (sub-picosecond and picosecond) superimposed with oscillations attributed to the coherent excitation of vibrational modes. One such vibrational mode was suggested to be directly coupled to the reaction co-ordinate which promotes ultrafast internal conversion. This is of potential significance for aspirations to apply coherent control schemes to these motors. However, the extent to which this can be realised, particularly with the experimental challenges presented by the observed sub-100 fs dephasing time of the mode in question, remains to be seen. Combining experimental data with existing calculations allowed the proposal of a coupled two-state model for dynamics on the excited state potential energy surface. We proposed that population of an emissive Frank-Condon state is followed by ultrafast relaxation (100 fs) to a non-emissive dark state. The dark state can repopulate the emissive state *via* a barrier, or decay to the ground state *via* internal conversion at a conical intersection (1 ps).

The study was extended to the effects of electron withdrawing and donating substituents upon the excited state dynamics. The dynamics of the ultrafast bright to dark state decay were insensitive to the nature of the substituent. In contrast, a substituent dependence was observed for the dynamics of the dark to ground state decay. It was found that electron withdrawing substituents resulted in an increased lifetime of the dark state whereas electron donating substituents led to a shorter lifetime. We attributed this to a substituent dependence of the barrier opposing both repopulation of the bright state, and a related barrier to the S_1/S_0 conical intersection. We proposed that both barriers become larger as the electron

withdrawing strength of the substituent is increased. This was supported by a kinetic model obtained by solving the rate equations which arise from the proposed reaction scheme. This result has significance for the design and optimization of synthetic molecular motors. The optimization of the photochemical quantum yield, and hence the efficiency, of the system is significantly dependent upon the dynamics on the excited state surface. Thus, a means by which these dynamics can be influenced and ultimately controlled synthetically is vital for the continued development of these systems towards functional molecular machines.

These studies were extended to a 'molecular propeller'. Phenylacetylene substituents were found to exert no influence over the dynamics of the bright to dark state relaxation, but did result in a longer lifetime of the dark state. However, the extent of the retardation effect upon the non-radiative decay of the excited state was smaller than expected for a large molecular system undergoing a conventional isomerization reaction *via* a single bond rotation mechanism. This led to the suggestion that such motion is far less involved in the mechanism of bright to dark state decay, but plays a more significant (albeit still small) role in the dark to ground state decay mechanism. This provides further insight into the molecular dynamics on the excited state potential energy surface.

An important consideration for the future of these molecular motor systems is the effect of immobilising the molecular motor on a surface. In order to harness the kinetic energy of the rotational motor motion for functional purposes, the stator must be fixed with respect to the rotor. A study of the excited state dynamics of such a system may provide an invaluable insight into the nature of the excited state surface in a structure which is significantly closer to a functional molecular machine than free molecules in solution. Such a study, with molecular motor molecules bound to nanoparticles, is planned. In addition, the study of a wider range of substituted molecular motors (limited to only three in this study) may give a deeper insight into the substituent dependent nature of the excited state surface. Finally,

detailed excited state quantum mechanical calculations of the substituted derivatives, particularly with reference to the substituent dependence of the excited state surface and the low frequency modes, could be invaluable. Such data, in combination with the experimental data presented in this study, will provide a comprehensive characterization of the excited state dynamics in this class of molecular motor.

This study was finally extended to probe the excited state dynamics of the chromophore of the green fluorescent protein, HBDI. The ultrafast viscosity independent decay of this molecule was confirmed and extended to studies of the substituent dependence. Alkyl substitution was found to have a profound effect on the electronic spectra, suggesting a route to controlling the wavelength of the protein emission, important for applications. However, even very bulky substituents did not slow the decay, consistent with a volume conserving coordinate. These studies will be extended to probe a wider range of fluorescent protein chromophores, relevant to understanding the photophysics of second generation fluorescent proteins.